Onslow Bay Physical / Dynamical Experiments

Summer / Fall 1975
Data Report

By L. J. Pietrafesa, D. A. Brooks
R. D'Amato and L. P. Atkinson

UNC Sea Grant Publication UNC-SG-77-07

ONSLOW BAY

PHYSICAL/DYNAMICAL EXPERIMENTS

SUMMER-FALL, 1975

DATA REPORT

by

L. J. Pietrafesa,

D. A. Brooks,

R. D'Amato

North Carolina State University

and

L. P. Atkinson

Skidaway

This work was partially supported by the Department of Energy under Contract No. E(38-1)-902 and the Office of Sea Grant, NOAA, U.S. Dept. of Commerce, under Grant No. 04-6-158-44054, and the North Carolina Dept. of Administration. The U.S. Government is authorized to produce and distribute reprints for governmental purposes notwithstanding any copyright that may appear hereon. The Center for Marine and Coastal Studies, NCSU, provided additional support for transportation and supplies.

Department of Energy
Contract No. E(38-1)-902

UNC Sea Grant Publication
UNC -SG-77-07

Center for Marine and Coastal Studies
Report No. 78-04

April, 1978

Acknowledgments

The authors would like to thank all those who have participated in this project to date. These include the Captain, Art Jordan, and crew, particularly, Mitch Malpus, of the R/V Advance II. Also, much credit is given to the scientists, technicians and graduate and undergraduate students without whose assistance, both at sea and back at the University, the existing data could not have been collected and processed. The list includes:

Larry Atkinson
John Bane
Paul Blankinship
Dave Brooks
Rich D'Amato
Kuang-Lung Fan
Ian Hartwell
Eileen Hofmann
John Klinck
Ernie Knowles
Dave Leech
Chuck McClain
Kerry Parker
Marcus Bowen
Nancy Bowen
Jerry Sawyer
Len Pietrafesa
Jim Singer
Charles Gabriel

Table of Contents

List of Tables

List of Figures

List of Figures (Cont'd)

List of Figures (Cont'd)

List of Figures (Cont'd)

List of Figures (Cont'd)

List of Figures (Cont'd)

List of Figures (Cont'd)

List of Figures (Cont'd)

List of Figures (Cont'd)

List of Figures (Cont'd)

List of Figures (Cont'd)

List of Figures (Cont'd)

List of Figures (Cont'd)

List of Figures (Cont'd)

List of Figures (Cont'd)

List of Figures (Cont'd)

List of Figures (Cont'd)

List of Figures (Cont'd)

I. Introduction

The objectives of this data report are to provide a commentary on the logistics and methodology of, and also to serve as a documentation of, the experimental/observational data sets obtained during the Summer and Fall/Winter of 1975. Beyond the inclusion of the reduced, i.e., computer processed and filtered, data no interpretation is provided. It is anticipated that this report will serve as an effective guidebook for future field programs.

This report includes data from four cruises (two deployment, two retrieval) of the R/V Advance II during the Summer through Fall/Winter, 1975.

These cruises constituted part of the North Carolina State University (NCSU) - Skidaway Institute of Oceanography (SKIO) combined efforts to contemporaneously measure: the temperature and salinity, i.e., hydrography; the current speeds and direction at several locations; and sea level and meteorology local and regional to Onslow Bay, North Carolina. Personnel from SKIO also measured various biological parameters along the hydrographic grid (cf. Figure 3). This work constitutes the initial effort of a multi-discipline, multi-institutional program partially sponsored by the Department of Energy and in part by the National Oceanographic and Atmospheric Administration and the University of North Carolina - Sea Grant College Program, to study the continental shelf processes affecting the oceanography of the South Atlantic Bight. The immediate problems being addressed were those of understanding the processes by which nutrients are transported onto the North Carolina Shelf from offshore and to establish possible transport pathways for effluents discharged into North Carolina coastal waters.

The purpose of these cruises was to deploy (retrieve) fixed position current meter moorings (Figure 2) and to make detailed hydrographic and biological parametric measurements in Onslow Bay. The results of the latter surveys are presented in a series of SKIO data reports. (Atkinson, Singer and Pietrafesa, 1976 a, b)

Endeco 105 current meters were used to measure speed and direction at specified temporal intervals and spatial locations.

A reporting of the raw, i.e., unprocessed and unfiltered, data was made in a separate and preliminary data report (Pietrafesa, Brooks, Atkinson, D'Amato and Bane, 1976).

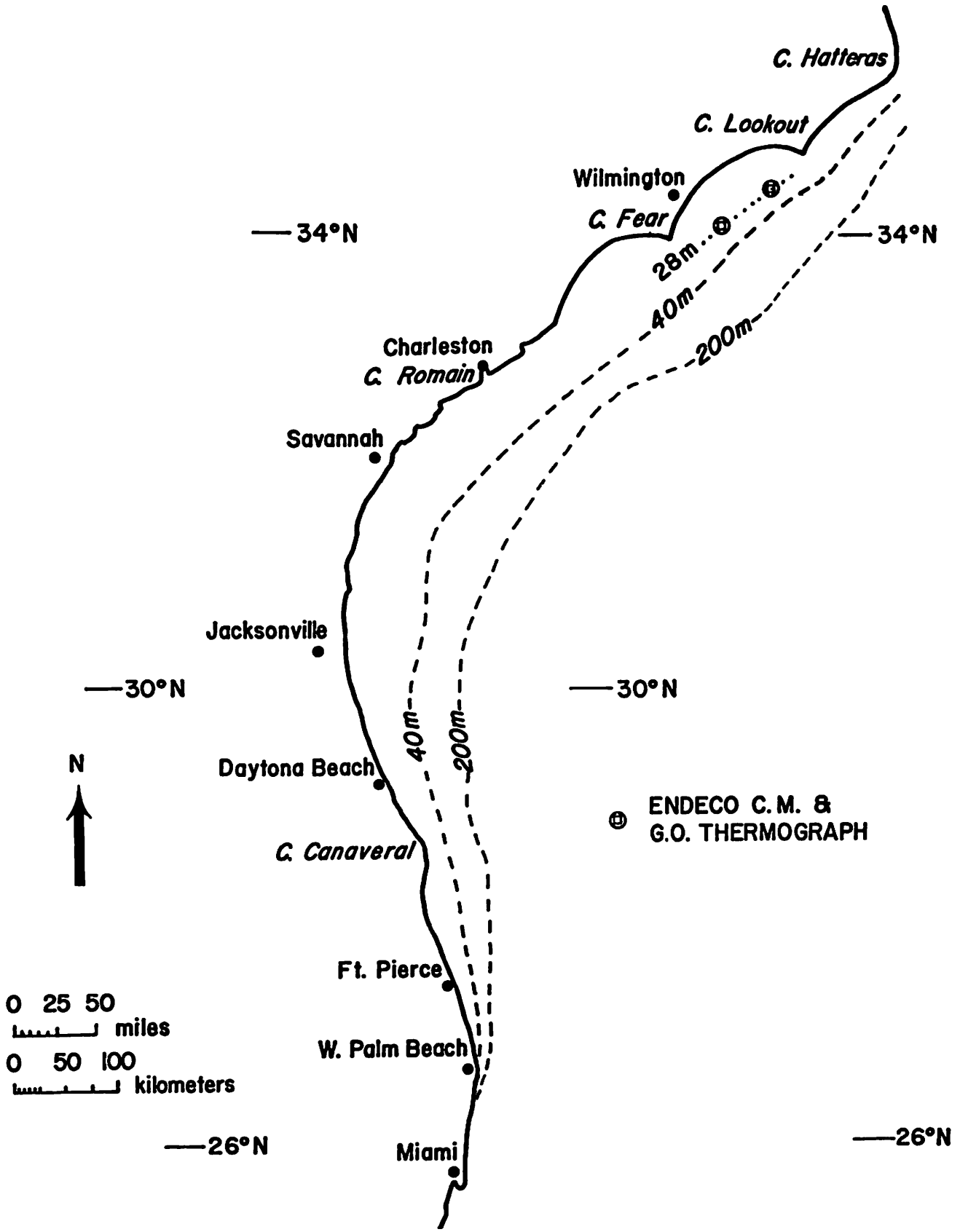

Figure 1 South Atlantic Bight

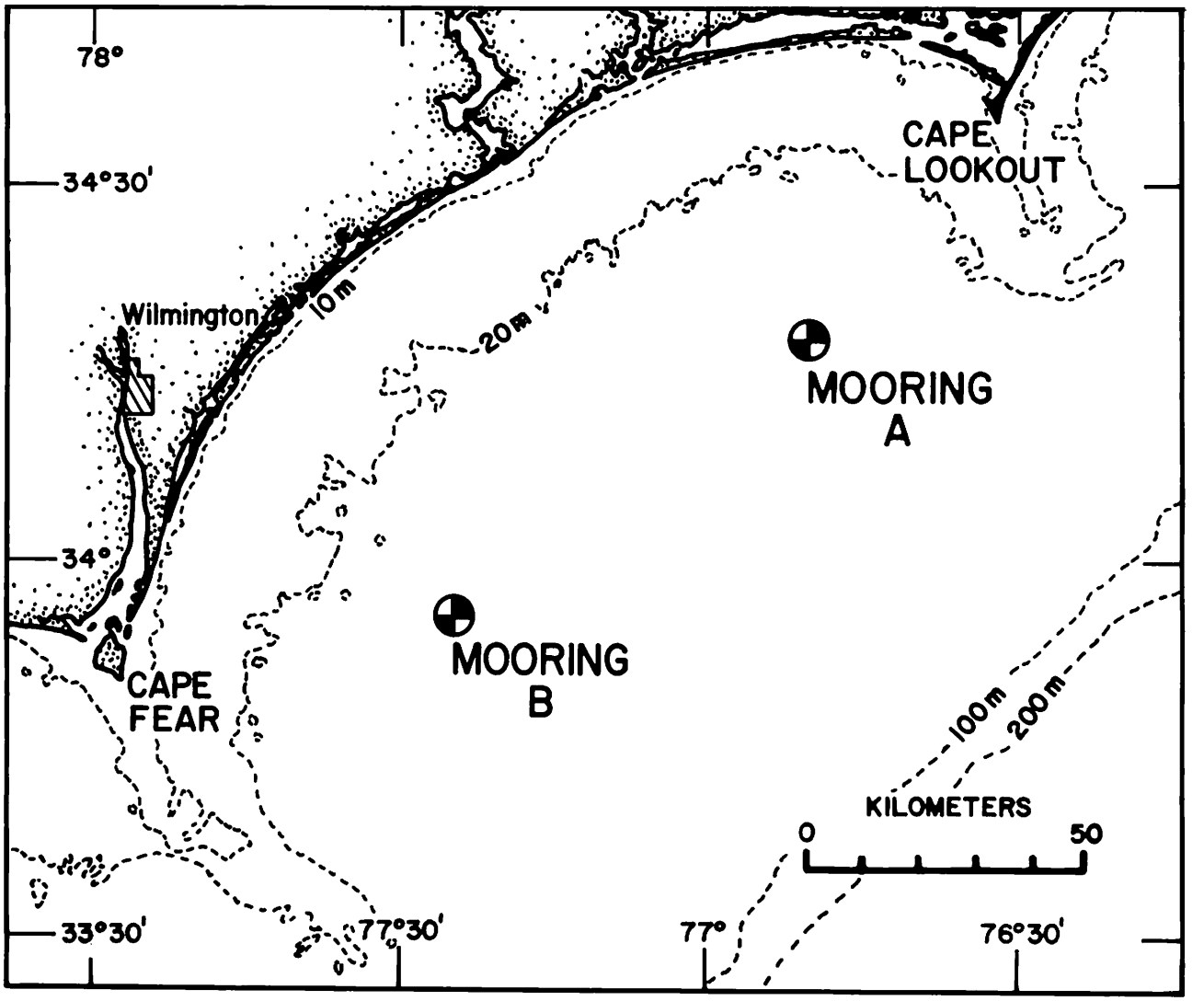

Figure 2 Onslow Bay, North Carolina study area

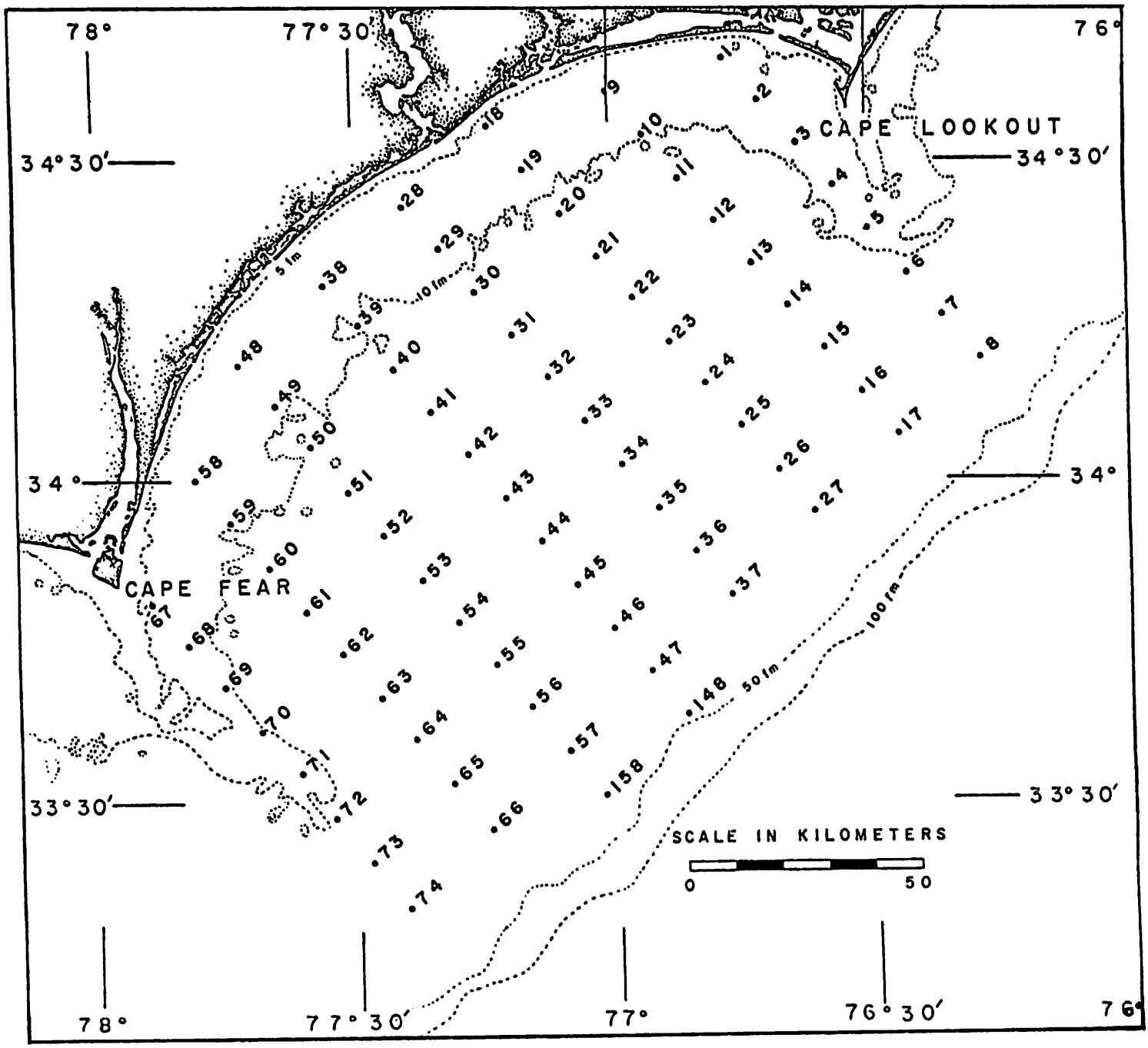

Figure 3 SKIO/NCSU hydrography grid (also SKIO biological sampling grid)

II. Purpose/Description of 1975 Experiment

The essential part of the 1975 Summer-Fall Experiment was a fixed-level array of 4 Endeco 105 - film recording current meters and 4 General Oceanics film - recording thermographs. Specifications of both types of instruments are given in pages 13 - 15 of this report. Two moorings were set at the "focal points" of the cuspate shaped Onslow Bay (cf. Figure 2). The current meters were set two to a mooring at depths of 10 and 25 meters from the surface in 28 meters of water, at each of the mooring sites, A and B (Figure 4). The array was designed to observe the propagation of phenomena across and along the inner to mid-shelf and to establish insights into the physics of the vertical and horizontal modal structure of the horizontal currents.

The data from the upper part of the water column were collected to address the "possibility of siting ocean-outfalls" problem (Pietrafesa, 1974) while the lower elements were specific to the "intrusion" (Pietrafesa and Atkinson, 1975) problem. More generally, Onslow Bay was chosen as an initial study site in the context of a study of the whole of the continental margin of the South Atlantic Bight because it is the more densely populated region of the North Carolina coast and, consequently, the waste disposal problem is more critical there than elsewhere. The reason for siting the study of the intrusion of nutrients onto the continental shelf of the South Atlantic Bight in Onslow Bay was primarily based on the fact that there is/has been more historical data, i.e., background information needed to plan such a study, collected in Onslow Bay than anywhere else in the South Atlantic Bight. Given the cuspate nature of the embayment, the fact of potential outfall sites at either end of the bay and the obvious horizontal and vertical plane (three dimensional) character of the property distributions in Onslow Bay (Stefannson, Atkinson and Bumpus, 1971), the initial moorings were located at sites A and B.

The initial periods of study; August - September, 1975 and October - December, 1975 were intended to offer quasi-seasonal time series of current observations. These time series were intended to be used, not only for understanding the physical/dynamical character of the observational period but also as a guide for future larger field studies, such as the planned (and completed) Summer-Fall-Winter, 1976-1977 and Summer, 1977 field programs planned in the same area under ERDA and NOAA-U.N.C. Sea Grant sponsorship (cf. Figures 5-7).

III. Equipment and Mooring Description

The moorings, established at sites A and B during both of the 1975 experiments, i.e., Summer and Fall/Winter, had a taut line (wire) configuration. A subsurface float was used to keep

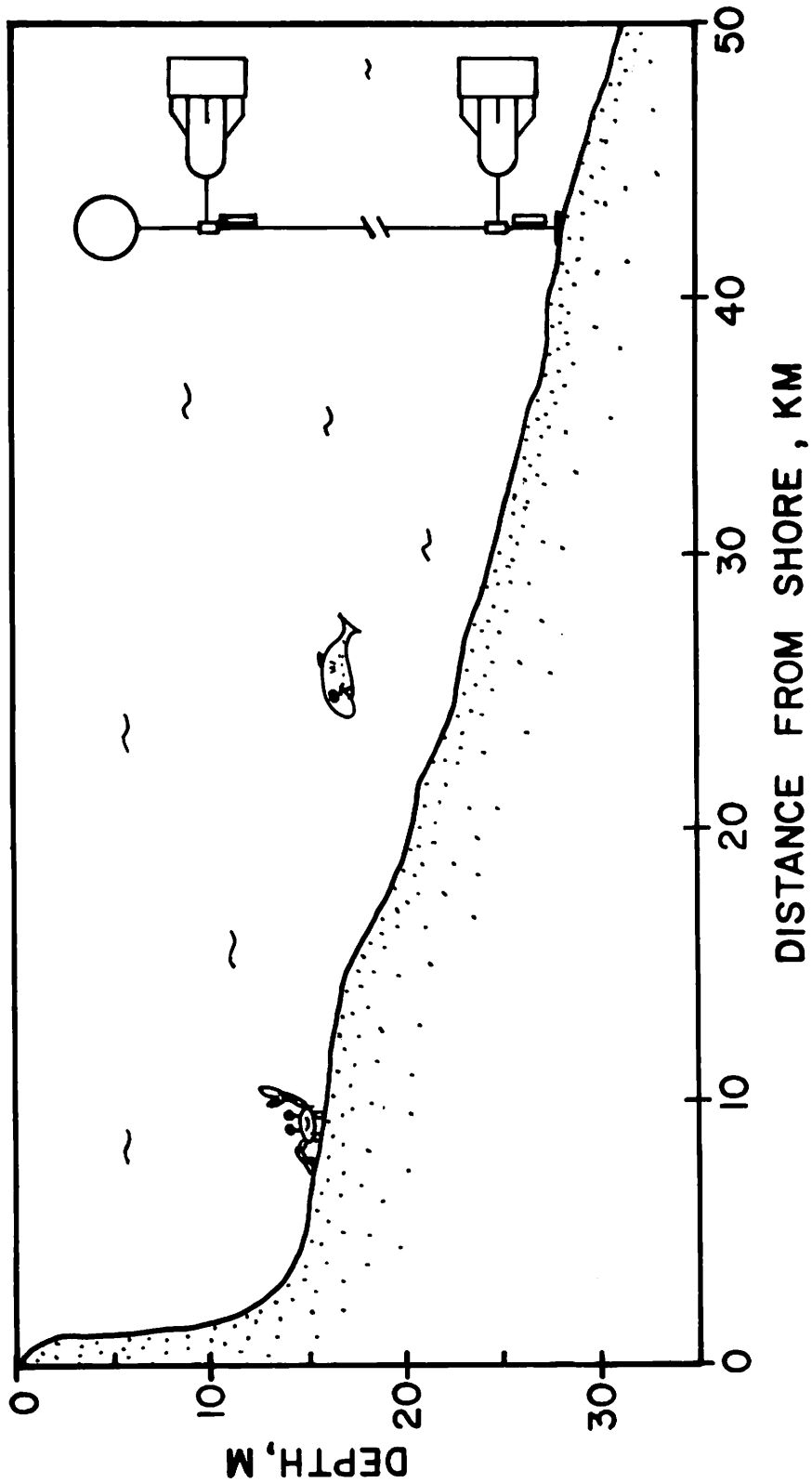

Figure 4 Vertical Section of instrument depths at sites A and B

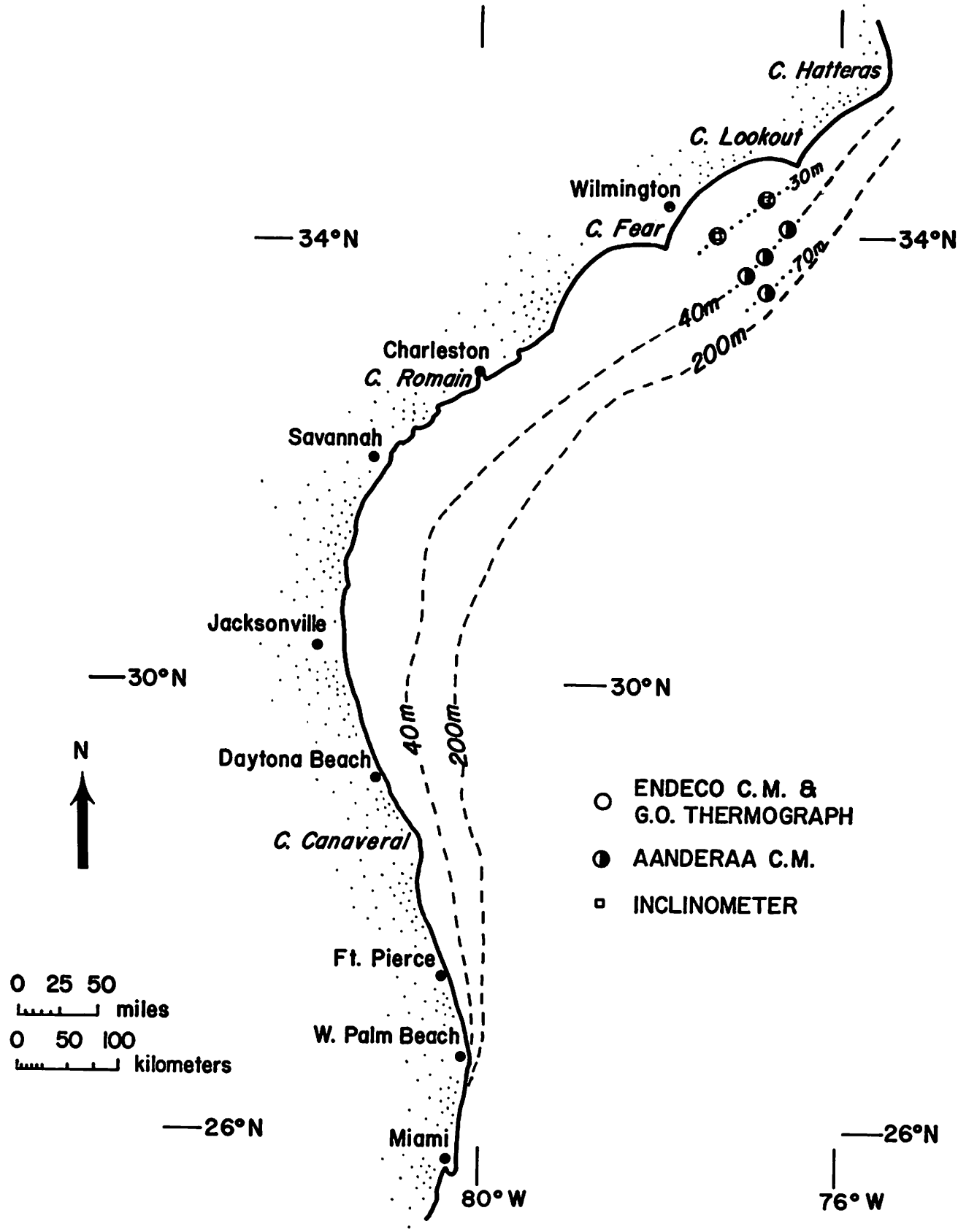

Figure 5 Mooring site locations for Summer, 1976 experiment (OBIS V)

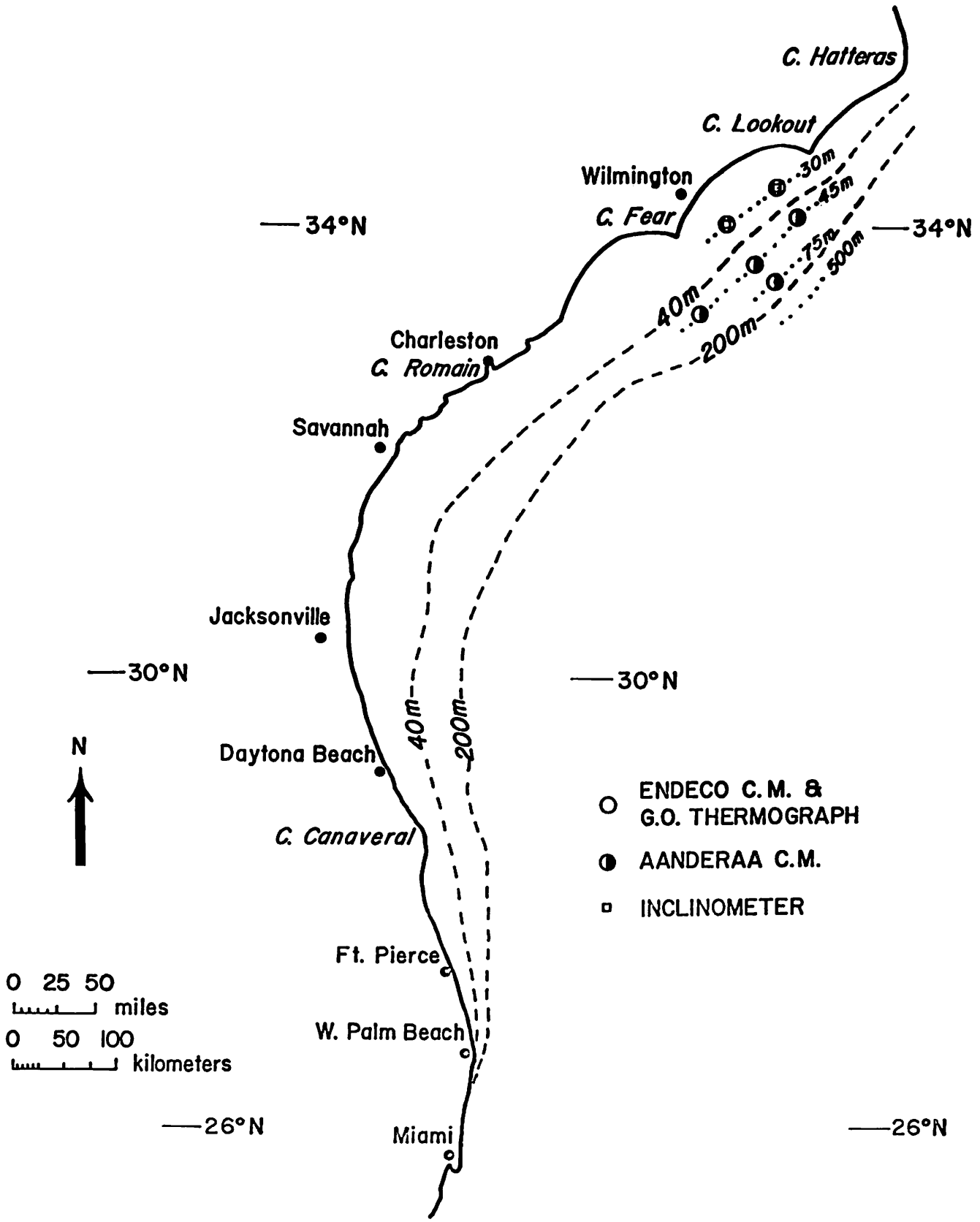

Figure 6 Mooring site locations for Fall-Winter, 1976 experiment

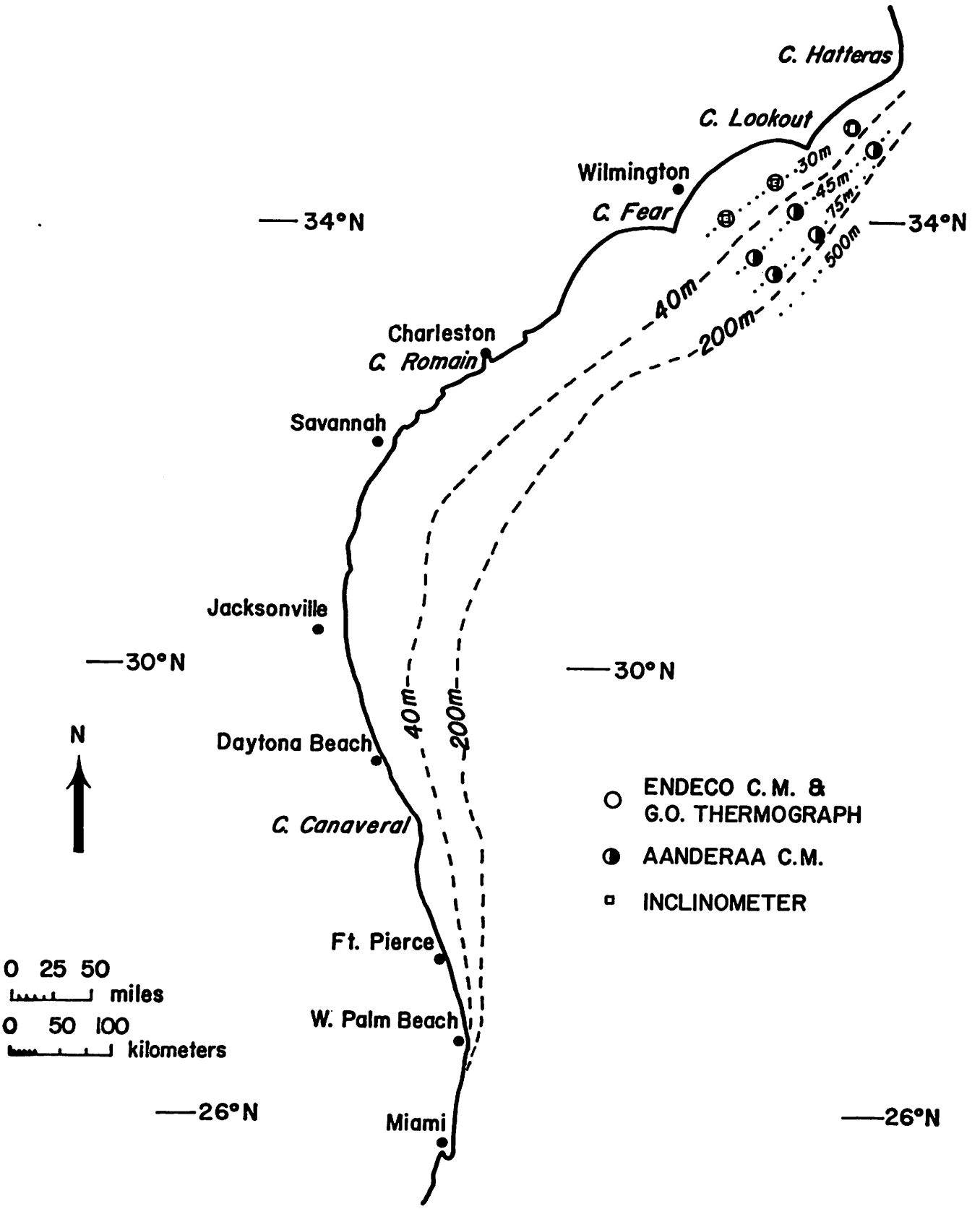

Figure 7 Mooring site locations for Summer, 1977 experiment

a bottom anchored cable taut. Fixed level recording equipment was attached to and suspended (away) from the cable. Additionally, a bottom anchored, auxiliary surface marker was located 190 meters from the main mooring line. The bottom "auxiliary" anchor was connected to the "main" anchor by a 200 meter polypropylene ground line, which floats approximately a meter from the ocean floor. The mooring configuration is depicted in Figure 8.

The operational logistics of installing moorings A and B were initiated in such a way as to maximize repeatability of location in subsequent experiments. The R/V Advance II was used during all deployment and retrieval phases of these 1975 experiments and mooring position locations (Table 1) were taken by the ship's Loran A system at the time of installation. The absolute error (accuracy) of the position is estimated to be less than ± 1 minute of latitude and longitude. The relative error (precision) is estimated to be less than ± 0.5 minute in either co-ordinate. Depths were taken by fathometer and are accurate to within ± 0.5 meters.

The recording instruments used on these moorings were Endeco-105 film recording current meters and General Oceanics 3070 film recording thermographs. The specifications of the instruments are given in Table 2. This current meter is of the axial flow, ducted impeller, film recording type and is tethered to the taut line mooring. It is specifically designed for continental shelf and estuarine environmental monitoring. The E-105 (Figure 8) records analog signals from direction and speed transducers on 16 millimeter photographic film. The ducted impeller acts as the speed sensor with an internal conversion of its rotation converted to a light trace on the film. The light trace, which is generated by sensor output, is lengthened or shortened at a rate proportional to the speed of the current. A light bar, whose length is representative of the current speed integrated over the timing interval, is produced by the advancing light trace. The length of the displacement of the light trace divided by the time interval yields the speed, averaged over the timing interval. Consecutive thirty-minute time exposures are taken of the continuous light traces and a timing pulse is provided by a crystal timer (accuracy of 1 part in 420) every 24 hours. Instantaneous instrument direction is given by the displacement of a light trace from a datum line. The directional light trace is generated by a magnetic compass coupled with an analog encoder. The time integrated signal appears as a bar of light which varies in intensity along its length as a function of the length of time that the instrument is aligned in a particular direction. The displacement of the point of maximum intensity from the datum line then yields the average direction for the thirty minute period of actual recording.

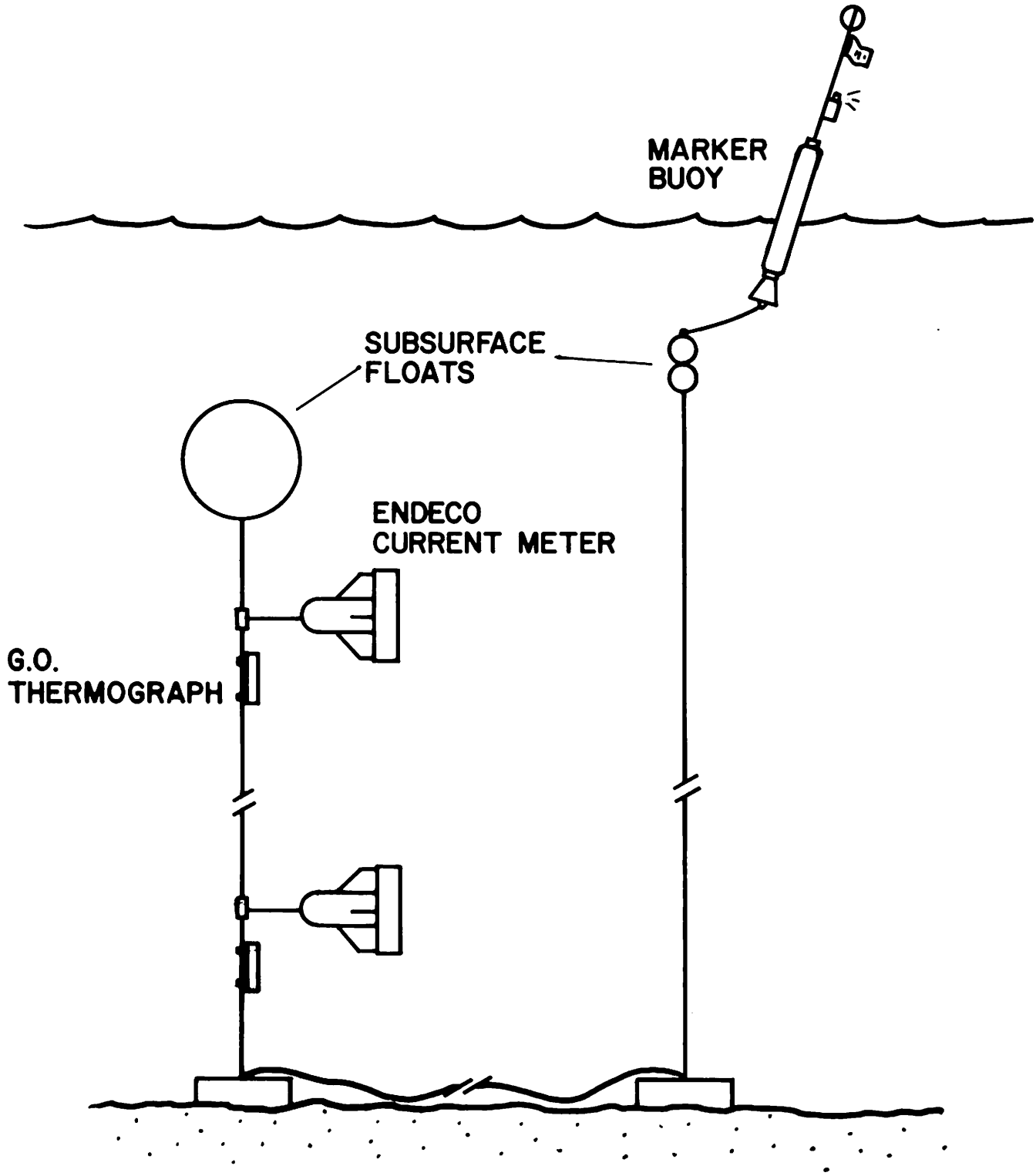

Figure 8 Fixed position current meter mooring

Table 1*

Experiment	Mooring	Latitude-Longitude Location	Loran A Location	Water Depth	Meter Depth	Meter No.	Meter Notation
(1) 6 August - 26 September, 1975	A	34° 17.6'N 76° 51'W	4856 2056	28 m	10 m	(E-105) 318	$A1_{top}$
	A				25 m	(E-105) 317	$A1_{bot}$
	B	33° 56.7'N 77° 25.0'W	4889 2495	28 m	11 m	(G.O.3070) 3	$B1_{top}$
	B				25 m	(E-105) 247	$B1_{bot}$
(2) 14 October - 9 December, 1975	A	34° 17.6'N 76° 50.8'W	4854 2060	28 m	10 m	(E-105) 316	$A2_{top}$
	A				23 m	(E-105) 247	$A2_{bot}$

* Note: Only instruments that functioned are recorded here. Each mooring (A & B) had, for each experiment, 2 Endecos and 2 Thermographs.

Table 2

SPECIFICATIONS: ENDECO Type 105 in-situ Tethered Current Meter

1. CURRENT VELOCITY	
Sensor Type:	Ducted Impeller
Sensitivity:	53.7 RPM/knot
Speed Range:	0 - 1.75 knots (0-90.1 cm/sec) at one Reading/ 60 minutes
	0 - 3.5 knots (0.180.2 cm/sec) at one Reading/ 30 minutes
	0 - 7.0 knots (0-360.4 cm/sec) at one Reading/ 15 minutes
Impeller Threshold:	Less than .05 knot (2.57 cm/sec)
Resolution:	.05 knot
Speed Accuracy:	$\pm$3 percent of Full Scale
2. CURRENT DIRECTION	
Magnetic Direction:	0 - 360^{o}
Sensitivity:	$\pm$5^{o} at 0.05 knot (2.57 cm/sec)
Resolution:	$\pm$1^{o}
Accuracy:	2 percent above 0.05 knot, when referenced to computer calibration

3. TILT
The instrument orients to the flow thus eliminating the need for tilt indication or correction.

4. RECORDING TIME AND RATE	
Number of Readings:	3600
Recording Rate:	1 Reading/15 minutes 1 Reading/30 minutes 1 Reading/60 minutes
Time Reference Mark:	24-hour Light Emitting Diode indication provided by timer
Maximum Recording Period:	75 days at 1 Reading/30 minutes
Time Stability:	$\pm$1.5 second/day at 20^{o}C $\pm$4 second/day from -5 to +30^{o}C
Timer Type:	ENDECO Type 124 Crystal Timer

Table 2 (Cont'd)

5. RECORDER	
Method:	Direct photographic time exposure of sensor outputs
Light Source:	Light Emitting Diodes continuously energized
Format:	Analog/Bar Graph
Film Type:	50 feet - 16 mm Tri-Z Cine Kodak Magazine, Modified
Power:	Four, 1-1/2 volt standard "D" size cells (Use only carbon-zinc batteries in non-ferrous cases)
6. OPERATING ENVIRONMENT	
Operating Medium:	Salt, fresh, or polluted water
Operating Temperature Range:	-2° to 45°C (28° to 113°F
Storage Temperature Range:	-24° to 65°C (-29° to 149°F)
Maximum Depth:	500 feet (pressure cases to 10,000 psi available)
7. INSTRUMENT HOUSING	
Material:	P.V.C. Plastic
Finish:	All surfaces painted for resistance to marine growth
Hardware:	300 Series Stainless Steel and Plastic
8. PHYSICAL SIZE	
Weight:	27 pounds (in air)
Buoyancy:	Approximately neutral; adjustable for salt, fresh, or polluted water
Dimensions:	30" long X 16" diameter
Shipping Weight:	45 pounds
Shipping Crate Dimensions:	38" long X 22" diameter

Specifications: General Oceanics Model 3070 Film Recording Thermograph

WEIGHT:	3 kgs. (6½ lbs.) in air; approximately 1 kg. (2.2 lbs.) positively buoyant in water
EXPOSED MATERIALS:	Rigid polyvinyl chloride (PVC) housing, end caps, and thermometer bulb guard; stainless steel hardware and thermometer bulb

Table 2 (Cont'd)

DIMENSIONS:	11.4 cm. (4½") O.D.x 38 cm. (15") overall length less thermometer bulb guard piece.
DEPTH RATING:	50 meters (72 psi)
TEMPERATURE RANGE:	0° to 55°
ACCURACY:	±1% of full scale (.55°C)
TIME REFERENCE:	Battery powered calendar watch with second, minute and hour hands plus date window
WATCH ACCURACY:	±0.0035% (30 seconds per 24 hours)
DATE INTERVAL:	Selectable at 5, 15, 30, or 60 minutes. Timing intervals chosen by changing timing plugs in data logger circuit. A 15 minute range was used in this study.
MAIN BATTERY SUPPLY:	16 manganese-alkaline penlight cells. (Mallory MN 1500, size AA, or equal).
OPERATING LIFE:	5 months or, if sooner, 11,000 camera operations. (Watch battery, one year).

The General Oceanics Model 3070 Film Recording Thermograph is a self-contained instrument for measurement and recording of air and water temperatures over extended periods of time. The Model 3070 sensor is a large dial thermometer mounted on one end cap of the cylindrical instrument housing. The bimetallic sensing element of the thermometer protrudes through the end cap out into the environment for quick response to temperature changes. This thermometer bulb is protected by a small guard piece with a number of through-holes for easy circulation of air or water. The thermometer dial is photographed at periodic intervals (15 min. interval used) by a film data logger at the opposite end of the housing. A battery powered calendar watch is mounted in the center of the thermometer dial to provide an accurate time and date reference for each film frame.

IV. Data Processing

Data from three different sources are included in this report. Each data set presented unique processing problems and each is discussed separately. Most of the computer programs used to process and analyze the data are members of a time series analysis library known as FESTSA (Brooks, 1976).

Current Meters. Endeco type 105 film-recording current meters were used in the 1975 Onslow Bay observational program. The sampling interval was 0.5 hours. The film magazines were transcribed by Endeco to 9-track magnetic tapes containing files of speed and direction. The speed and direction values were converted to u and v components in several ways. The Carolina Cape region is defined by an irregular, cuspate, scallop like coastline which extends into shoals and consequently it is difficult to specify a spatial co-ordinate system. Coherency and phase relationships between components of a vector time series are functions of the co-ordinate system in which the components are specified. The natural tendencies are to choose either a north-south, east-west horizontal axis or to assume a straight coastline of uniform cross-section so that the horizontal co-ordinate system axes lie parallel to and perpendicular to the straight isobaths. Unfortunately, however, the isobaths in the Carolina Capes region are not uniform or straight and the choice of a co-ordinate system is less than obvious. Two tacts were taken herein. The first co-ordinate system chosen is one based on the direction of the local bathemetric contours at approximately mid shelf to the shelf break, which tend to run southwest to northeast at an angle 55.6^{o} clockwise from North (cf. Figure 9). The second co-ordinate system used is one oriented on a basis determined by the characteristics of the data itself. A co-ordinate system which maximizes the variance in any given direction gives the so-called "Principal Axis" of variance. This system, in which the estimated phase difference between u

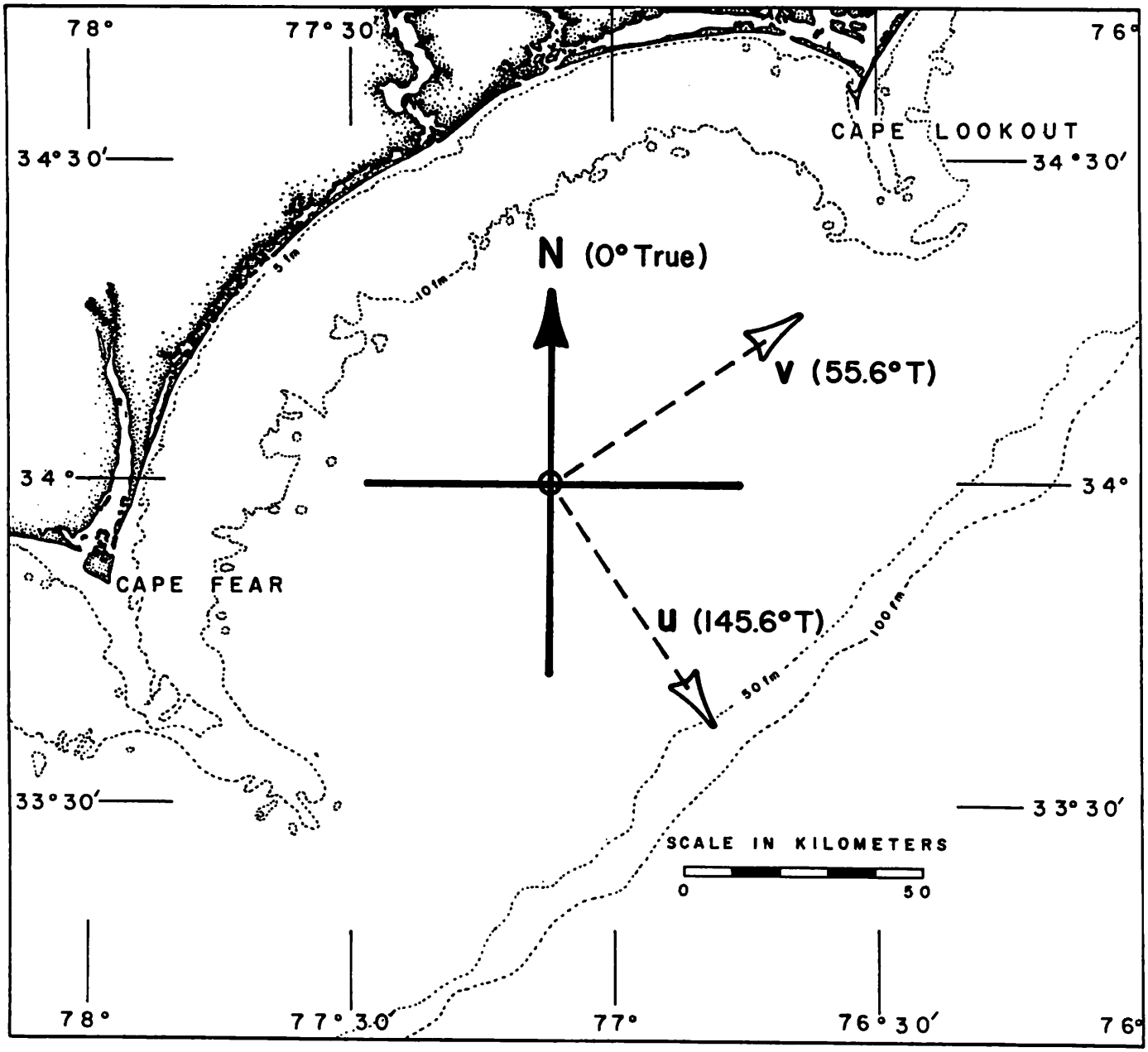

Figure 9 Rotated Co-ordinate system for Onslow Bay

and v is identically $\pm 90^{o}$ is also called the "Normal" system (Fofonoff, 1969) and the "Hodograph" system (Mooers, 1970). As a function of the physical, dynamical processes causing the measured hydrodynamics, the principal axis of variance may vary with frequency and geographic location. The "Principal Axis" for a given vector time series is obtained by rotating the covariance matrix until the cross-covariance between orthogonal velocity components is zero. The rotation of the co-ordinate system into the principal axis does not fix the sign of the 90^{o} phase shift between u and v. This is determined by the data. Since the principal axis for a given vector time series will vary with frequency, we can construct, hodographs which will allow for the vector time series to be decomposed into cyclonic and anticyclonic rotating motions of different amplitude and phase. The sum of these two polarized motions yields an ellipse whose semi-major axis is oriented along the principal axis of variance at that particular frequency. The principal axis herein is given as a function of frequency rather than as an average over a large frequency band.

Within this report, the vector time series have been variously represented in the different possible ways described above. The figure captions indicate the nature of the representation. The raw current data were low pass filtered with a three hour low pass (3HRLP) Lanczos filter to reduce surface wave noise, and then subsampled hourly. The current data were then low pass filtered by convolution with a Lanczos data window to separate the inertial, semi-diurnal, and diurnal fluctuations from longer period motions. The energy response envelope of the 40-hour low pass (40HRLP) filter is shown in Figure 10. The filter attenuation is everywhere at least as great as that shown by the envelope. The 40HRLP time series were decimated to provide a sampling interval of 6 hours.

Start times, stop times, and record lengths of the original and filtered time series for both the summer and fall experiments are shown in Table 3.

Meteorological Data. Three-hourly values of surface wind speed, wind direction, atmospheric pressure, and temperature were obtained from NOAA, Environmental Data Service, Asheville, North Carolina. Wind vector and wind stress vector components were computed for the rotated coordinate system, with the positive vector sense in the direction toward which the wind blows. The wind stress vector components were computed from the wind vector components using a quadratic drag law with the drag coefficient $C_D = 1.5 \times 10^{-3}$. Two low pass filters were used for the meteorological data. A 48 hour low pass (2DLP) Lanczos filter was used, with subsequent decimation to a 9 hour interval and linear interpolation to an 8 hour interval, for initial examination of the meteorological data. Figure 11 shows the filter energy response envelope. Later, a 40HRLP filter equivalent to the one used for the current data was used to facilate comparisons between the data sets.

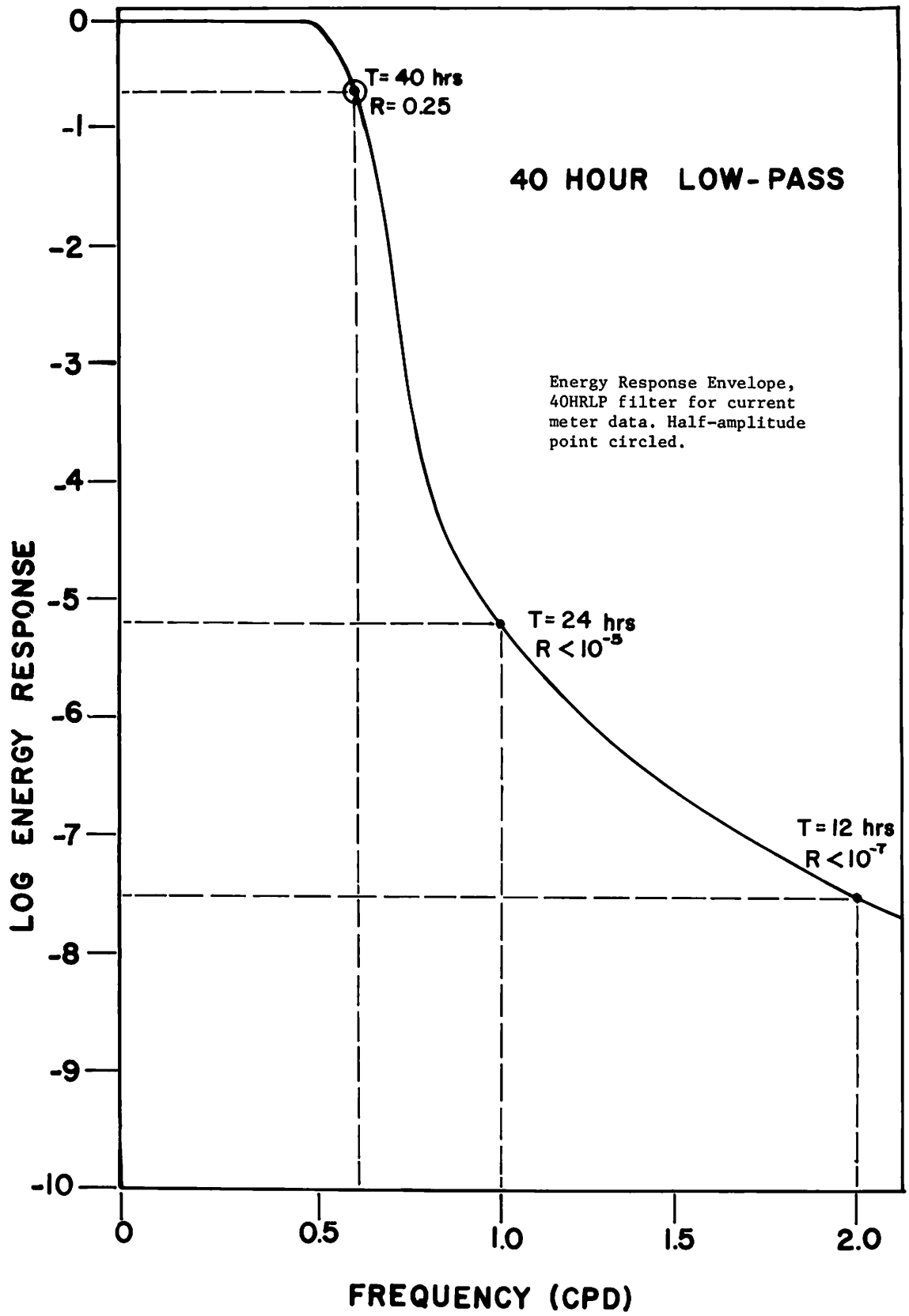

Figure 10 Filter energy response envelope for 40HRLP

TABLE 3

Instrument #	Original Data	40HRLP	3HRLP
(318 & 317) Al_{top} & Al_{bot}			
Start Time (EST)	6 Aug. '75 1000 hrs.	10 Aug. '75 1800 hrs.	6 Aug. '75 1800 hrs.
Stop Time (EST)	26 Sept. '75 0630 hrs.	21 Sept. '75 1800 hrs.	25 Sept. '75 2300 hrs.
# of Points	2442	169	1205
Interval	0.5 hrs.	6 hrs.	1 hr.
(247) Bl_{bot}			
Start Time (EST)	7 Aug. '75 1100 hrs.	11 Aug. '75 1900 hrs.	7 Aug. '75 1900 hrs.
Stop Time (EST)	25 Sept. '75 1700 hrs.	21 Sept. '75 0700 hrs.	25 Sept. '75 1000 hrs.
# of Points	2365	163	1167
Interval	0.5 hrs.	6 hrs.	1 hr.
(316 & 247) $A2_{top}$ & $A2_{bot}$			
Start Time (EST)	14 Oct. '75 0930 hrs.	18 Oct. '75 1730 hrs.	14 Oct. '75 1730 hrs.
Stop Time (EST)	9 Dec. '75 1230 hrs.	4 Dec. '75 2330 hrs.	9 Dec. '75 0500 hrs.
# of Points	2696	190	1332
Interval	0.5 hrs.	6 hrs.	1 hr.

Sea Level. Hourly sea level heights from coastal tide gauges were obtained in punched card form from NOAA, National Ocean Survey, Rockville, Maryland. The long period sea level fluctuations were separated from the semidiurnal and diurnal tidal fluctuations with a 2DLP filter; the time series were then decimated to provide a sampling interval of 8 hours. The filter energy response envelope is shown in Figure 11.

Frequency Domain Presentations. Spectral representations of data in this report are given in two formats:

a) Graphs of variance (spectrum density times frequency) versus the logarithm of frequency. These are "quick look" calculations based on the fast Fourier transform (FFT). The FFT's of original data were smoothed by block averaging over five adjacent estimates, yielding about ten degrees of freedom for each averaged estimate. The FFT's of low passed data were not smoothed, yielding two degrees of freedom for each estimate.

b) Auto and cross spectra, phase and coherence squared computed for paired input time series. The spectral calculations were performed by Fourier transforming correlation functions. The maximum correlation lag, spectral bandwidth, degrees of freedom, and input time series names are shown on each figure. The first named time series corresponds to "spectrum x". Additionally, positive phase values indicate series y leading series x.

Figure Formats. The current meter information in figures 12-51 is shown in six different basic formats. For the low passed records, the following quantities are displayed: time series of current components u and v, vector stick diagrams, FFT's, and spectra. For the raw (unfiltered) records, the following quantities are displayed: time series of current components u and v, progressive vector diagrams (PVD's) of original (unfiltered) data and FFT's. 3HRLP records were used for spectra (u vs. v for same meter) and hodograph parameters. The current meter naming convention used in this report is

$$A(B)\ 1(2)_{top\ (bottom)},$$

where A(B) and 1(2) respectively identify the mooring location and date, as shown in Table 1, and the top (bottom) subscript identifies the location of the instrument on the mooring string. For example, the notation $A1_{top}$ refers to the uppermost instrument on mooring A during the summer experiment. First-order statistics for the unfiltered current data are given in Table 4.

Intermooring and intramooring spectra for the low passed currents are shown in Figures 52-83. Figures 52-67 are in the

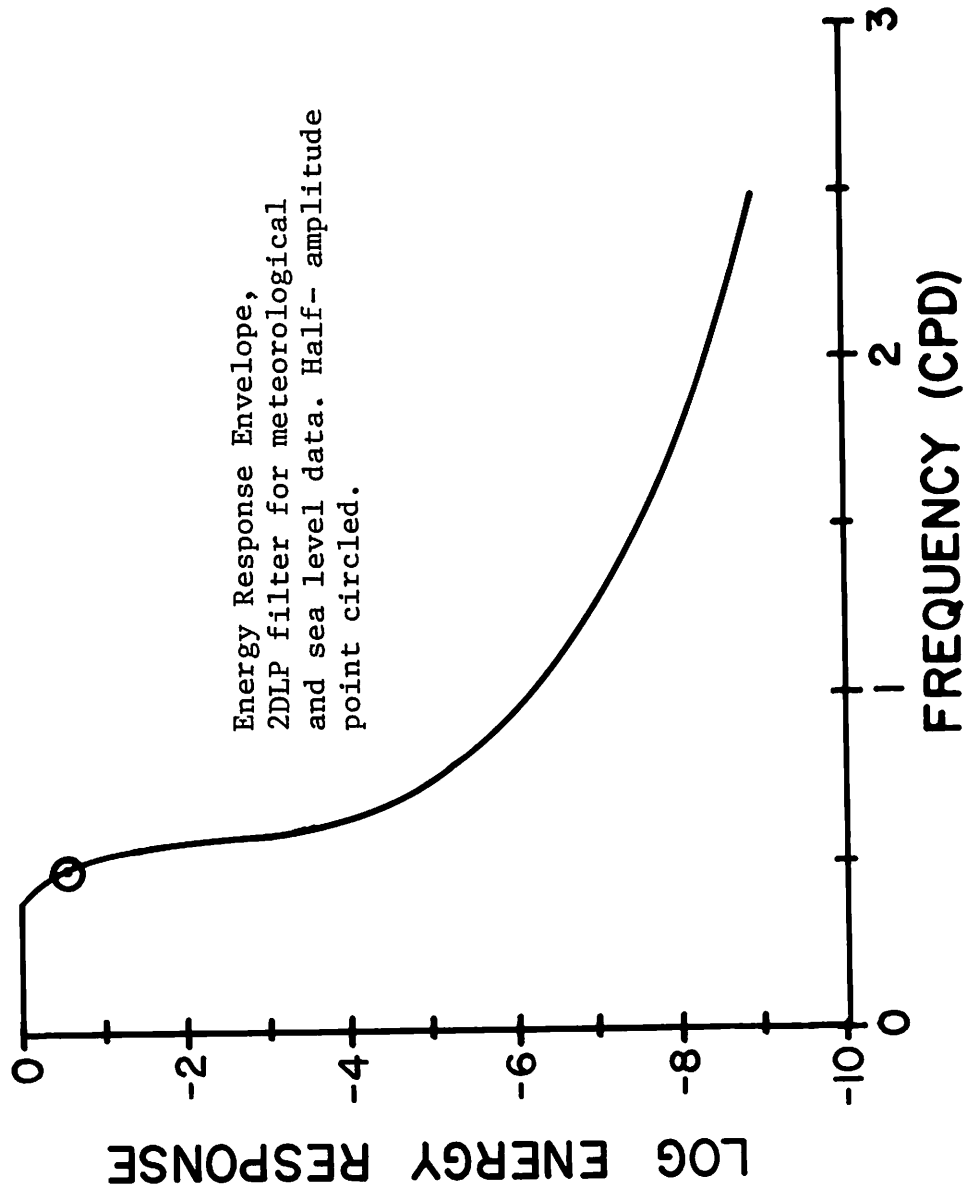

Figure 11 Filter energy response envelope for 2DLP

Table 4

First Order Statistics

Meter	Meter Depth(m)	Min.	Max.	Avg.	S.D.	Parameter (cm/sec)
$A1_{top}$(318)	10	-34.0	42.0	2.78	13.40	u
		-27.0	43.0	5.29	10.85	v
$A1_{bot}$(317)	25	-20.0	21.0	0.18	7.47	u
		-21.0	26.0	1.95	7.29	v
$B1_{bot}$(247)	25	-26.0	21.0	-1.53	8.45	u
		-23.0	19.0	-0.32	5.68	v
$A2_{top}$(316)	10	-41.0	35.0	-2.72	13.55	u
		-33.0	48.0	2.43	11.34	v
$A2_{bot}$(247)	23	-28.0	24.0	1.89	9.15	u
		-32.0	26.0	2.44	7.59	v

topographic coordinate system ($R \tilde{=} 56^{o}$) while Figures 68-83 are in the principal axis coordinate system computed for each meter. Time series and FFT's of low passed and unfiltered meteorological data from Cape Hatteras and Wilmington are shown in Figures 84-115. Time series comparisons between current and wind stress vectors are shown in Figures 116-117, and cross spectra between currents and meteorological variables are shown in Figures 118-177. Figures 138-177 is a special case series. Here the wind stress is maintained in the topographic coordinate system and the currents are seen in the principal axis coordinate system which is computed for each meter. Figures 138-157 have no detrending while Figures 158-177 are detrended. Time series of low passed sea level at Wilmington, N. C. and Charleston, S. C. are shown in Figures 178-179.

Additionally, a time series of temperature data, collected at 15 minute intervals at mooring B (top) during the August-September experiment , is presented, unfiltered, in Figure 180 and, 40 HRLP filtered, in Figure 181. A case study of bottom intrusion is presented in Figure 182. Figure 183 is a graphic presentation comparing wind and current averaged vectors.

V. Preliminary Conclusions

These data are the first reasonably "long term", i.e., 2 - 4 month period of observations, and allow for some interesting initial finds as concerns Gulf Stream intrusions, effluent transport and shelf flushing. Before speculating on any relationships between atmospheric forcing, Gulf Stream influences and continental shelf responses, it is of use to consider what we know to date, given these data sets. Reports to follow will elucidate further on the state-of-the-art knowledge as it develops from the Department of Energy and the National Oceanographic and Atmospheric Administration and University of North Carolina Sea Grant College Program funded studies.

Additionally, the Very-High-Resolution Radiometer on the NOAA-2 (National Oceanic and Atmospheric Administration) satellite has recently obtained imagery in the visible channel over a major portion of the coastal waters off the eastern seaboard of the United States. Strong and DeRycke (1973) indicated an abrupt change in surface roughness at the shoreward edge of the Gulf Stream Current from Florida to Cape Hatteras that could result from the opposition of waves propagating against the flow of the Gulf Stream. Herein, DeRycke and Rao (1973) pointed out an apparent relationship between the occurrence of eddies along the western side of the Gulf Stream and strong westerly winds.

Satellite images (Legeckis, 1975; Stumpf and Rao, 1975) suggest that the eddies evolve from growing instabilities (Florida Current meander), which may initially be wind induced. They manifest themselves as warm, southward-oriented, tongue-

like extrusions of Florida Current water onto the shelf, similar to the shingle structure observed by Von Arx, Bumpus and Richardson (1955). In the Florida Straits they are confined by the narrow shelf coastal boundary and observed diameters range from 10 to 30 km. Eddy vertical extent is approximately 200m. Lee (1975) concludes that spin-off eddies are a dominant mechanism for shelf water mass exchange off southeast Florida and estimates the shelf residence time as 1 week due to eddy water renewal. Atkinson, et. al. (1977) and Blanton and Pietrafesa (1978) have essentially concluded that the similar flushing mechanism is at work throughout the whole of the South Atlantic Bight. Satellite imagery show that eddy-like excursions are a consistent feature along the shelf break of the SAB and appear to grow to much larger proportions.

Near the shelf break (50 to 75 m isobaths) Gulf Stream frontal instability processes, such as wave-like meanders and spin-off eddies become a significant contributor to current variability and water mass exchange. The Gulf Stream surface front may meander about 10 to 25 km in the east-west direction with a wave length of 100 to 200 km. These meanders are known to grow at times into the tongue-like disturbances (shingles, sausages or eddies). The cyclonic circulation in the eddies transports shelf water offshore in the southern region of the vorticity, which provides a mechanism for rapid water exchange. It is thus appreciated that eddy like events displace large volumes of shelf water with onshore flows of Gulf Stream waters at the surface and bottom and offshore shelf water displacement and subsequent entrainment into the slope waters.

Flushing frequency is thought to tie directly to the frequency with which meanders and eddy events occur. Conventional wisdom is that meanders and eddy events occur at frequencies between 0.1 and 0.2 cycles per day; figures which embrace the pioneering study by Webster (1961), as well as studies of sea level by Mysak and Hamon (1969), and present current studies. We should point out that studies have yet to unambigously link onshore/offshore flow cycles on the North Carolina Shelf with meanders or accelerations of the Gulf Stream. From the Pietrafesa data sets, it is obvious that large amplitude current fluctuations with periods ranging from several days to several weeks are common features on the continental shelfs off North Carolina. These current meter data indicate that cycles in onshore/offshore flow often precede local wind events occurring more or less simultaneously at Cape Hatteras and Wilmington, North Carolina (separating-distance about 120 km). Perturbations in the Gulf Stream represent a mechanism which could be causing those flow cycles in mid-shelf that seem poorly correlated with local winds.

Considering the data covering 42 days collected during August-September, 1975 by Pietrafesa and shown in this report: over this period, eight cycles of onshore/offshore flow ocurred, about one cycle each 5 days. The most dramatic onshore/offshore

event occurred at the SW mooring from 10-22 August 1975 (Fig.182). The other seven cycles in the SW had durations from 4 to 5 days long. The onshore flow in all but one cycle lasted 2 to 4 times longer than the following offshore flow, indicating that that flow was predominantly onshore in the SW corner near bottom. Onshore/offshore flow cycles near bottom in the NE were weak and poorly coherent with near bottom flow in the SW. The average flow from the smoothed record is shown in Figure 183 where averages were computed for the entire 42-day record. The near bottom flow in the SW is clearly stronger than that observed in the NE. The strong average northeastward flow near surface in the northeast is closely aligned with the prevailing northeastward wind stress during the summer season in a conventional Ekman barotropic geostrophic sense. Onslow Bay responds to discrete wind events from the SW (prevailing) and the NE (after frontal passages). A selected five days of the 42-day record to demonstrate this response is shown in Figure 183 . Three illustrations cover northeastward wind stress whose daily average varied from less than 1 dyne/cm^2 to almost 3 dynes/cm^2. Under these conditions, only the surface flow in the northeast increases with increasing wind stress. The onshore flow in the SW averaged 10-15 cm/sec during the day under the three different stress magnitudes. Two other illustrations cover episodes of southwestward wind stress. The first daily average stress was about 1 dyne/cm^2; the second was almost 3 dynes/cm^2. Bottom flow tended to follow the trend of the isobaths. It was not clearly proportional to the wind's strength. Neither was the surface flow.

Hydrographic data obtained at the time the two moorings were set showed Onslow Bay to be highly stratified in the vertical with a well mixed surface layer of about 27.5°C and salinites less than 35.5°/oo over a well mixed bottom layer whose temperature ranged from 25.5°C less than 20 km offshore to less than 22.5°C near the shelf break. Salinities were everywhere greater than 36°/oo in the lower layer. The bottom meters were within this bottom layer. Temperature and salinity (Atkinson, et.al., 1976) confirm that the onshore/offshore flow cycles in this bottom layer transported water of Gulf Stream origin.

Onslow Bay seems to respond in a discrete manner to different directions of the alongshelf wind stress. Northeastward stress induces offshore flow near the surface almost 45° to the right of the wind. This is really no support of Ekman drift since the Cape Lookout Shoals in the NE corner undoubtedly deflect, i.e. steer the flow to some degree. The occasional insensitivity of the bottom flow to wind stress magnitude implies another driving source which we will discuss below. Southwestward wind stress reverses the sense of the near surface flow and bottom flow is more clearly aligned with the isobaths. There was strong onshore bottom flow observed in the SW between 10-18 August. The along shelf component was very small. Bottom topography in this region is quite complex, and it is entirely

possible that this strong onshore component is following the local topography. Nevertheless, water is clearly being carried toward the inner portion of the embayment. Three points can be stressed here. First, strong bottom flow began at least two days before strong northeastward winds. Secondly, the maximum current speeds occurred 2 to 3 days before the strongest winds. Thirdly, the currents diminished and reversed while the winds still blew hard toward the northeast. In fact, the strongest observed winds occurred on 18 August. The effect of this strong onshore flow in the SW can be seen in the temperature at this point was approximately 26°C for the entire 42 day record except between 14 and 16 August. At this time, the temperature dropped on 14 August to 22°C. The low temperature occurred simultaneously with the strongest bottom flow in the SW which had been acting for the previous 3 days at only slightly lesser speed. These facts suggest that the dramatic onshore/offshore event was triggered by a large-scale disturbance, probably originating in the Gulf Stream and enhanced by the upwelling favorable, subsequent winds. The onshore flow carried relatively cold temperature water of Gulf Stream origin (Atkinson, et.al., 1976) to the inner portions of the embayment where vertical mixing in the shallow water cooled the entire water column to around 22°C. This water was returned offshore in the upper portions of the water column where it passed by the NE mooring on 14 August.

The other seven cycles in the 42-day record had much less effect on the inner portions of Onslow Bay because they were not as strong nor did they persist as long. Nevertheless, these cycles represent processes that remove or flush water from the embayment. Our data seem to indicate that such cycles occur about once every 5 days.

The Cape Fear i.e. Frying Pan, and Cape Lookout shoals bounding the southern and northern parts respectively of Onslow Bay appear to exert a degree of topographic control on the circulation. The response of Onslow Bay to onshore flow events indicate that water tends to cross the embayment predominantly in the southern portion. We assumed therefore, that the onshore flow occurs over one-half the along shelf length or L - 50 km. The average thickness of this flow was estimated from extensive hydrographic data taken over several years. The sharp thermocline that separates the surface shelf water from the more saline and colder bottom water (Blanton, 1971) averages roughly 10 meters off of the bottom. This onshore flow is typically about 10 meters thick. Average onshore speeds are about 7 to 10 cm/sec at the SW mooring which last on the average of about 3 days. Using the above values, we calculate the volume flux of onshore flow across a half length of the embayment to be about 1.3×10^{16} cm^3 over a 3-day duration. The embayment's total volume (100 km x 50 km x 30 m) is about 1.5×10^{17} cm^3. Thus 12 onshore events are required to remove the total volume of Onslow Bay. If these events occur each 5 days, a replacement rate = 12 events x 5 day/events = 60 days. Thus about 2 months are required to flush Onslow Bay by these onshore flow cycles.

This flushing rate of 2 months can be compared with other calculations for the shelf south of Cape Hatteras. Atkinson, Blanton and Haines (1977) calculated an overall flushing rate of 2.7 months based on the freshwater distribution and input to the Georgia Bight area. In that paper, it was shown that this rate was remarkedly constant from season to season, and a Gulf Stream entrainment model was proposed to account for the rate at which freshwater could be removed from the Continental Shelf. Using typical freshwater filament dimensions and salinities observed by satellite and hydrographic cruises and assuming that the stream entrains one of these filaments each five days, it is speculated that about 2 to 3 months are required to remove the freshwater observed on the Continental Shelf in the South Atlantic Bight.

VI. Current Meter Data

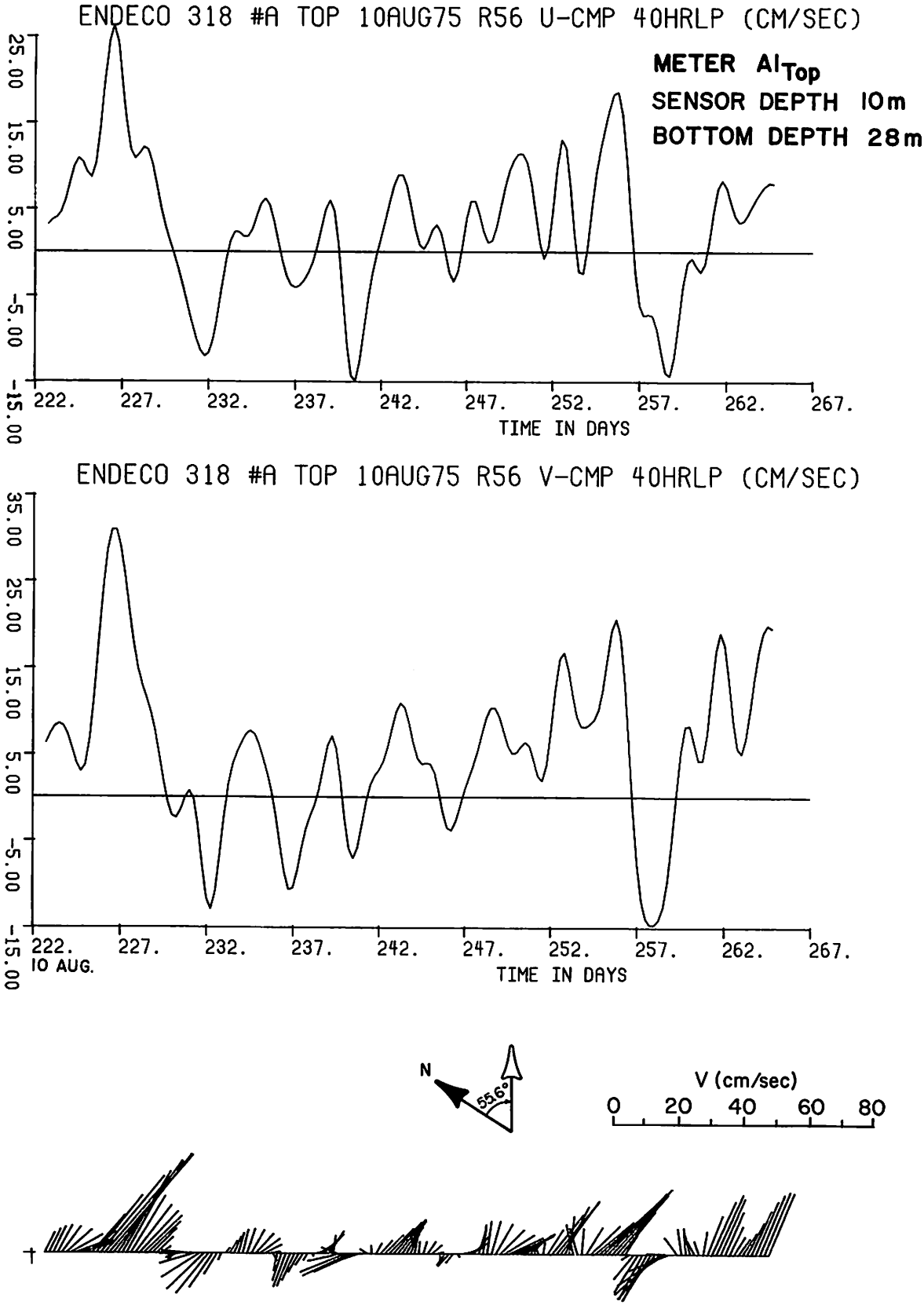

Figure 12 Low pass current velocity components and vectors from meter Al_{top}

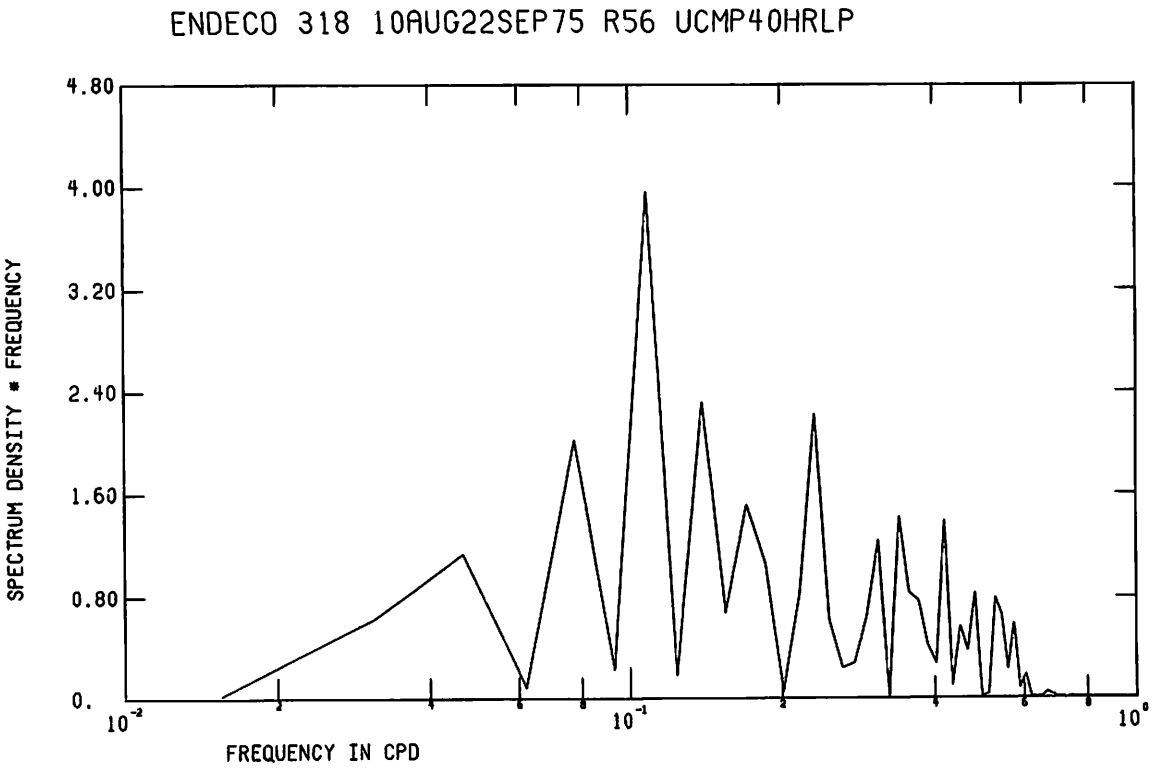

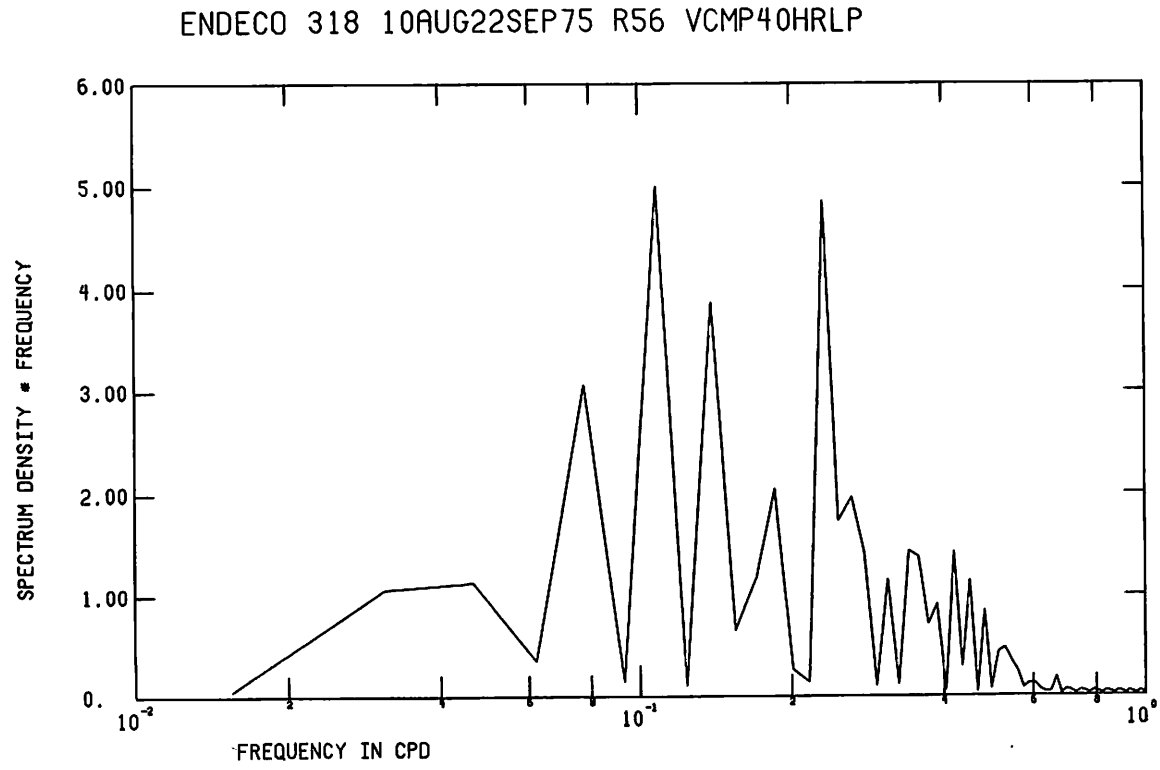

Figure 13 FFT of low pass current velocity components from meter Al_{top}

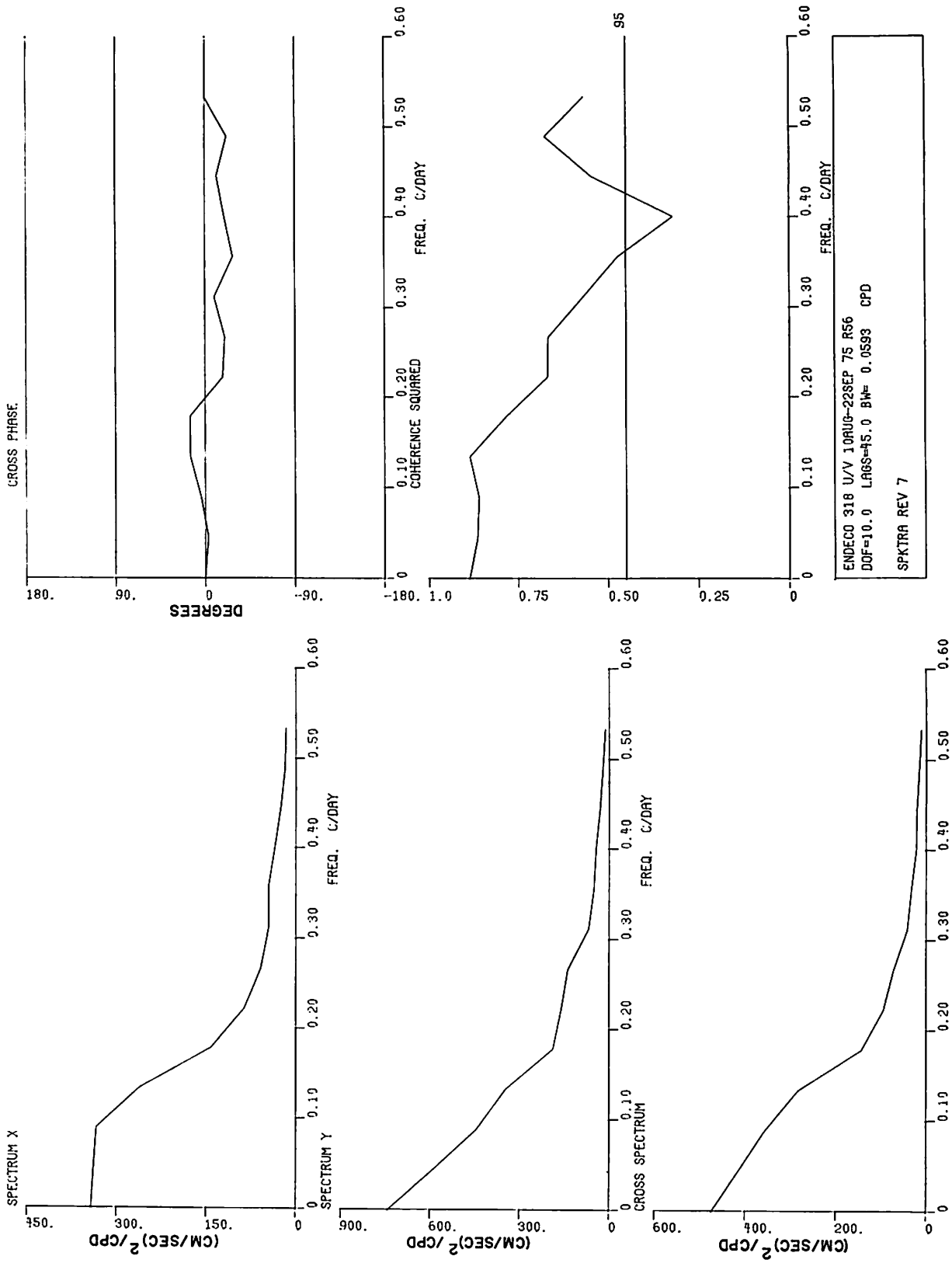

Figure 14 Spectra of low pass current velocity components from meter $A1_{top}$

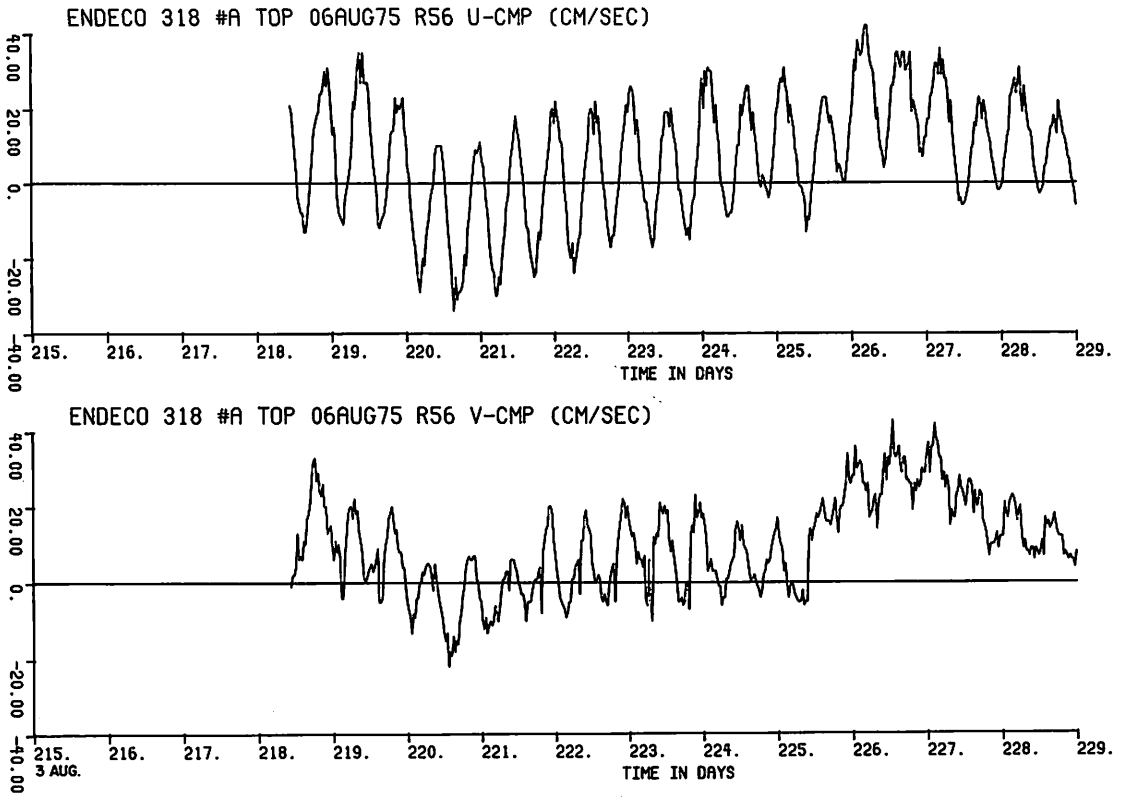

Figure 15a

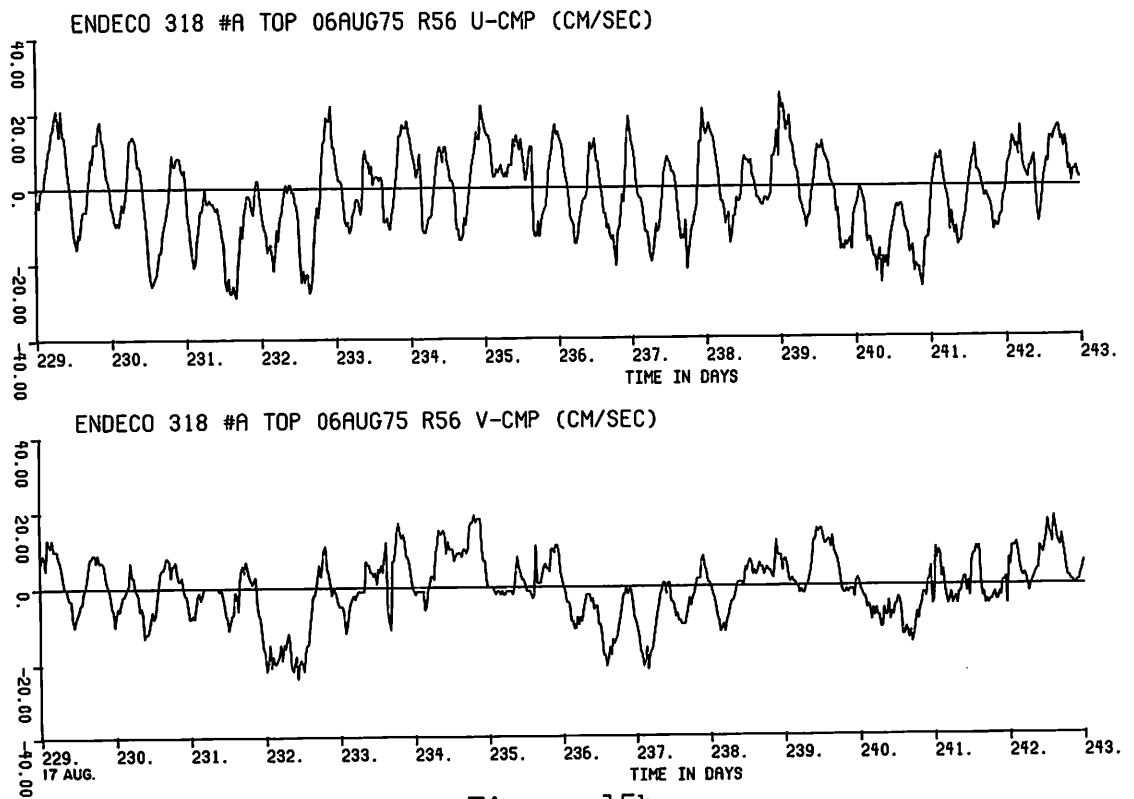

Figure 15b

Figure 15 (a,b,c,d) Unfiltered current velocity components from meter Al_{top}

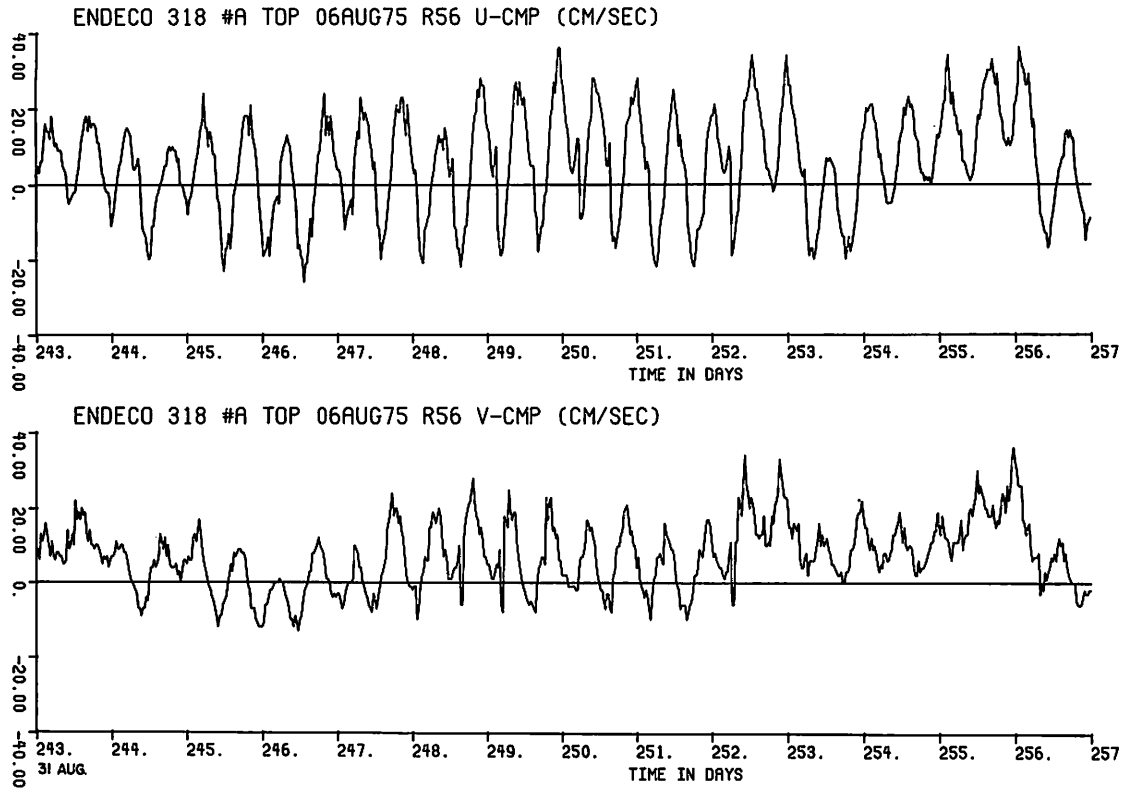

Figure 15c

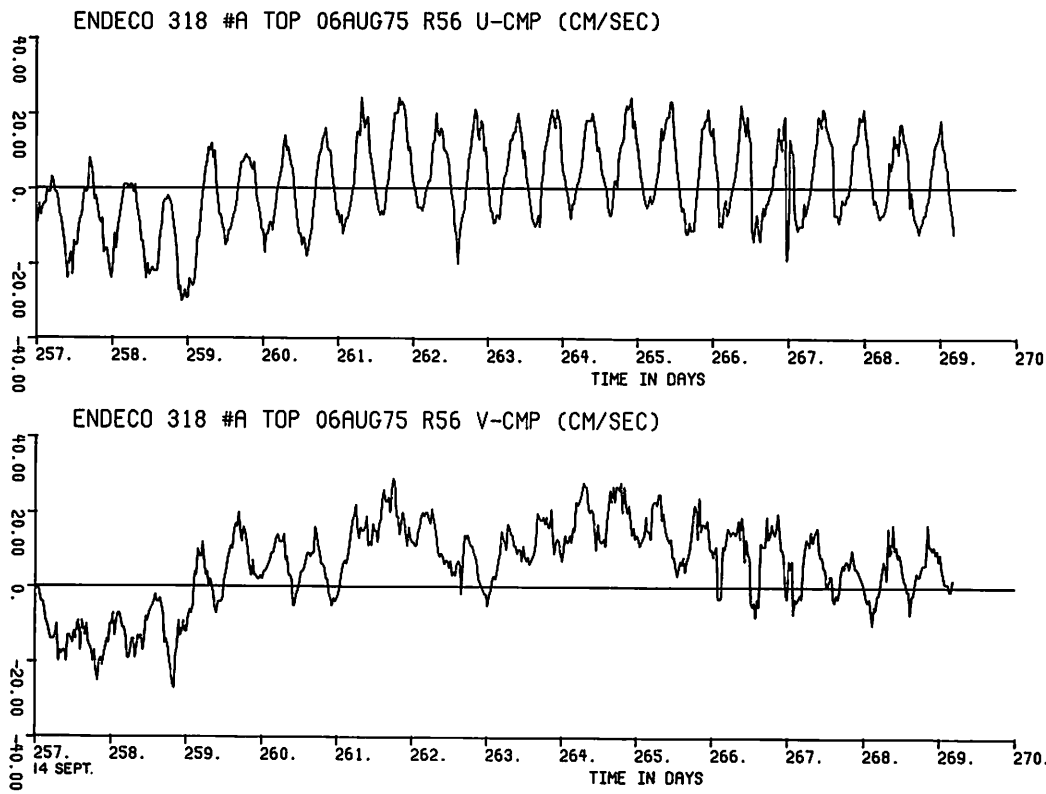

Figure 15d

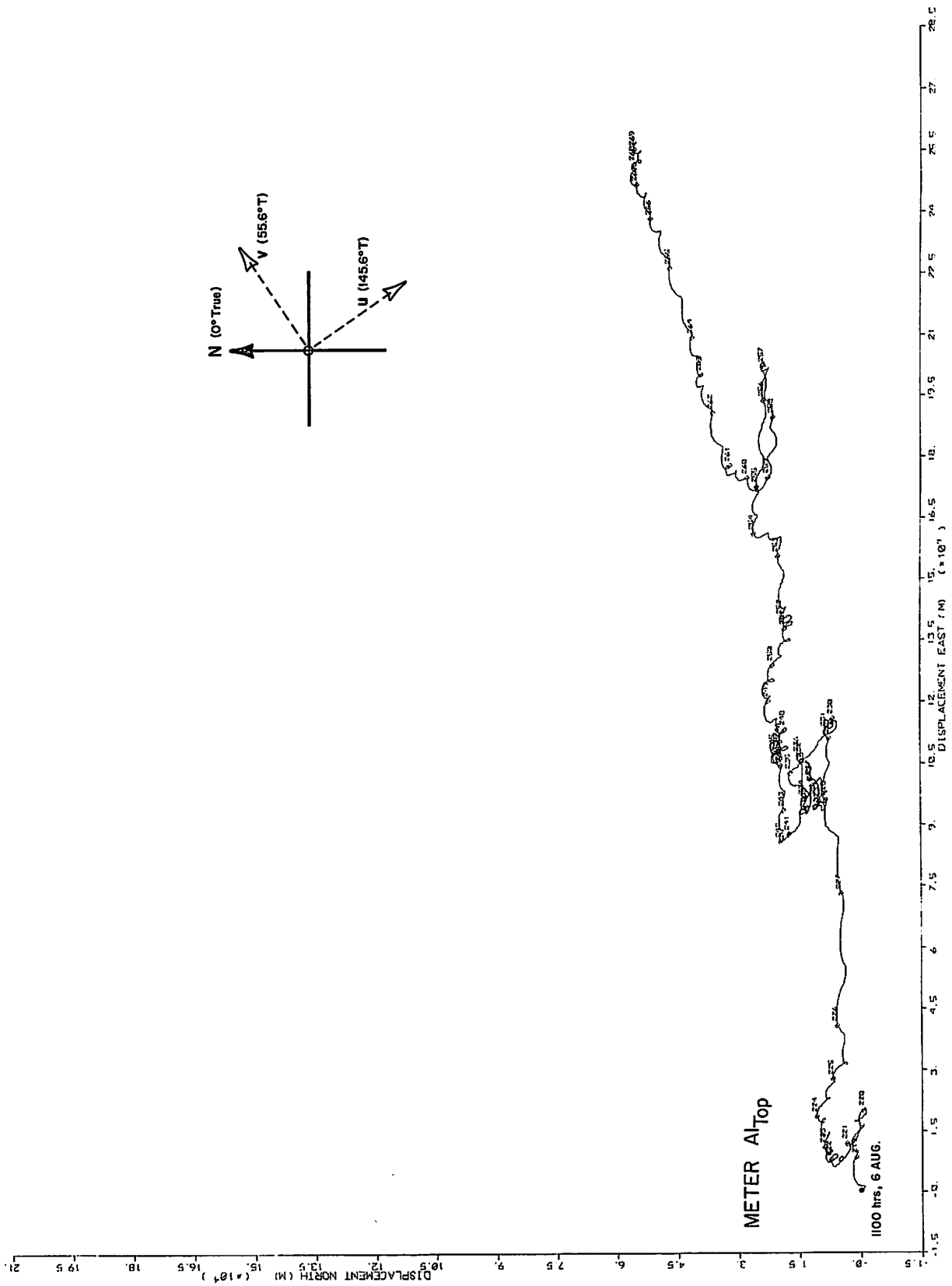

Figure 16 Progressive vector diagram of unfiltered current velocity from meter Al_{top}

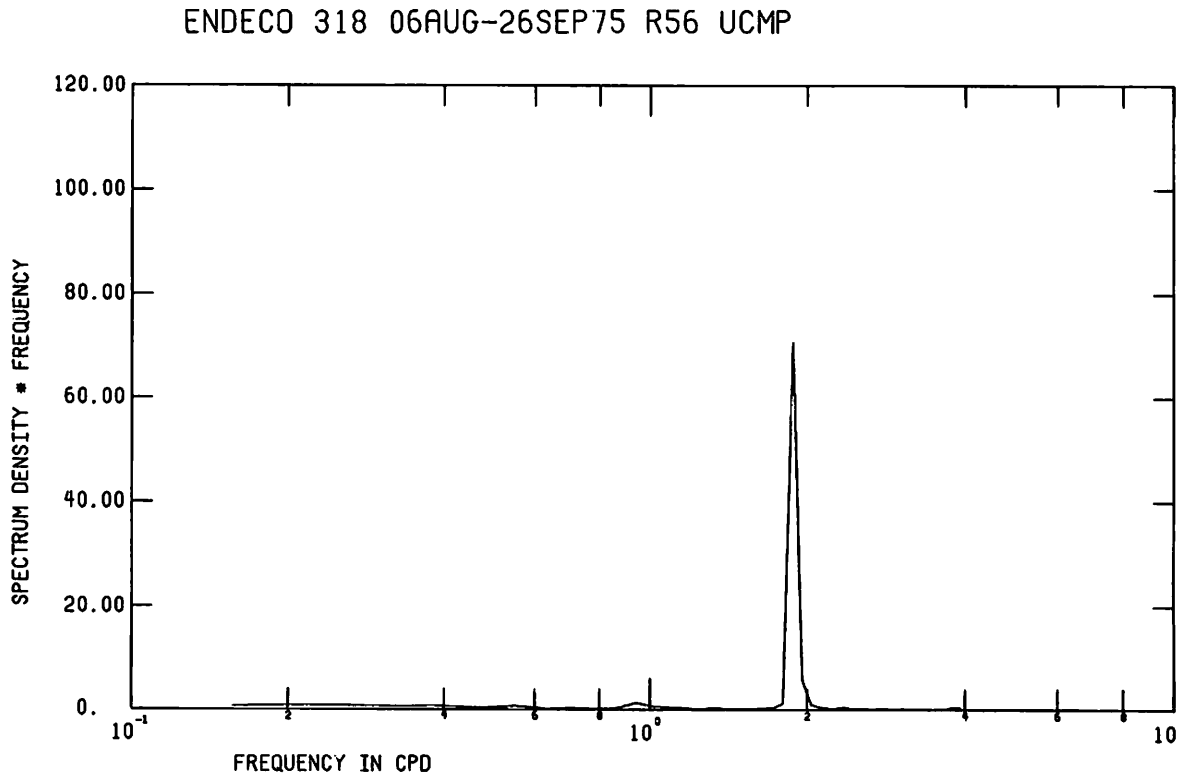

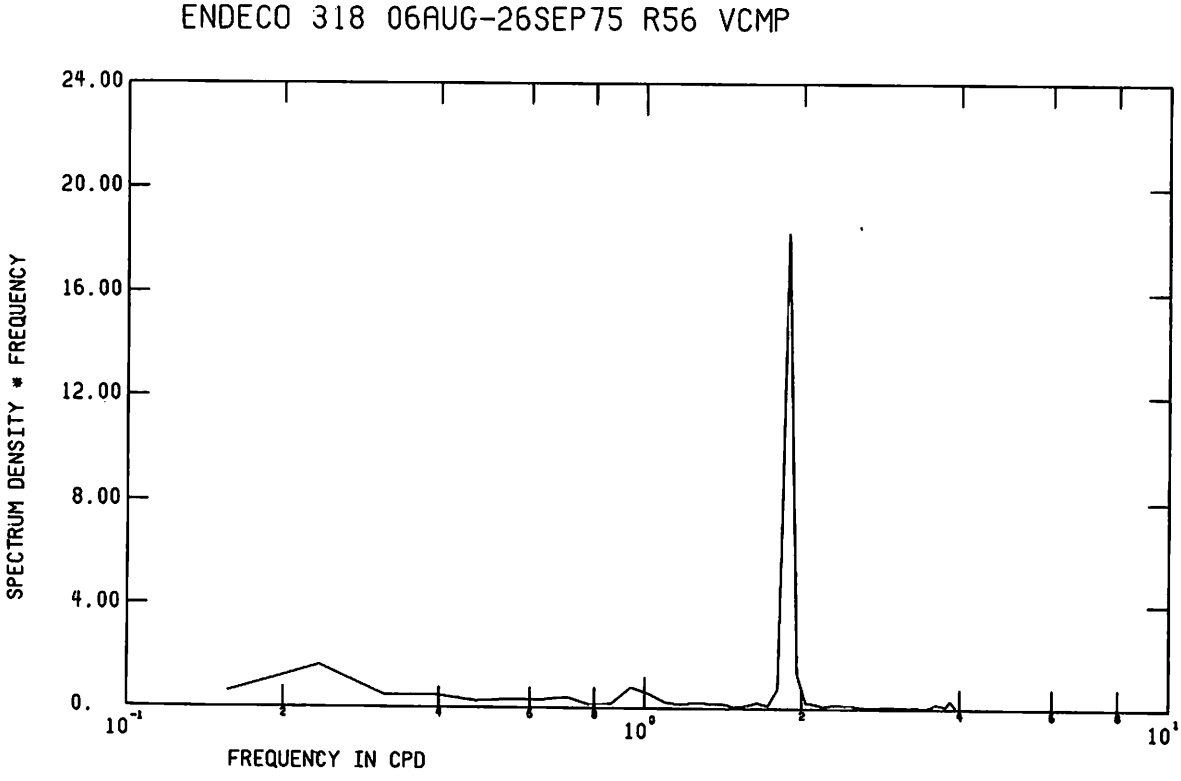

Figure 17 FFT of unfiltered current velocity components from meter Al_{top}

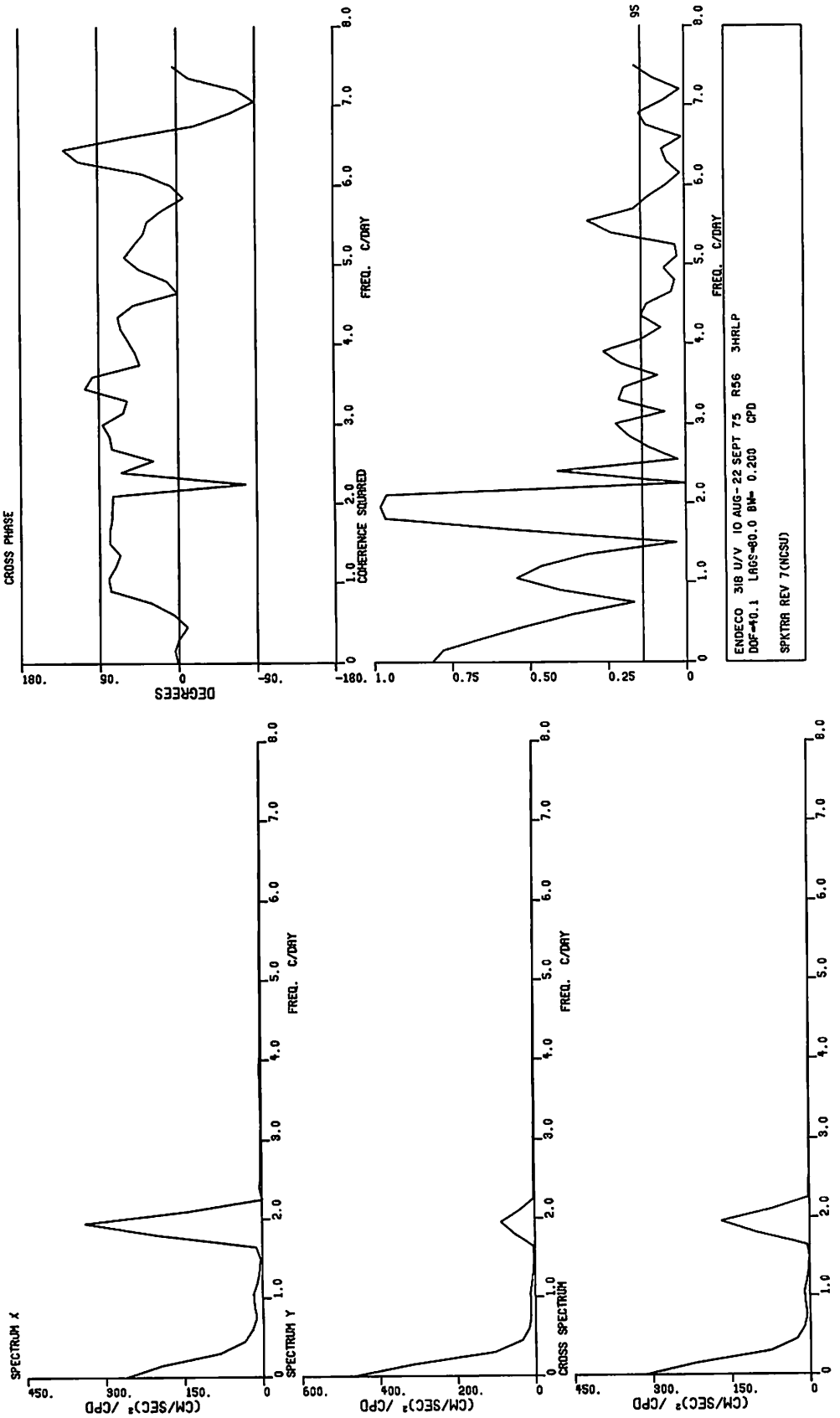

Figure 18 Spectra of 3HRLP current velocity components from meter $A1_{top}$

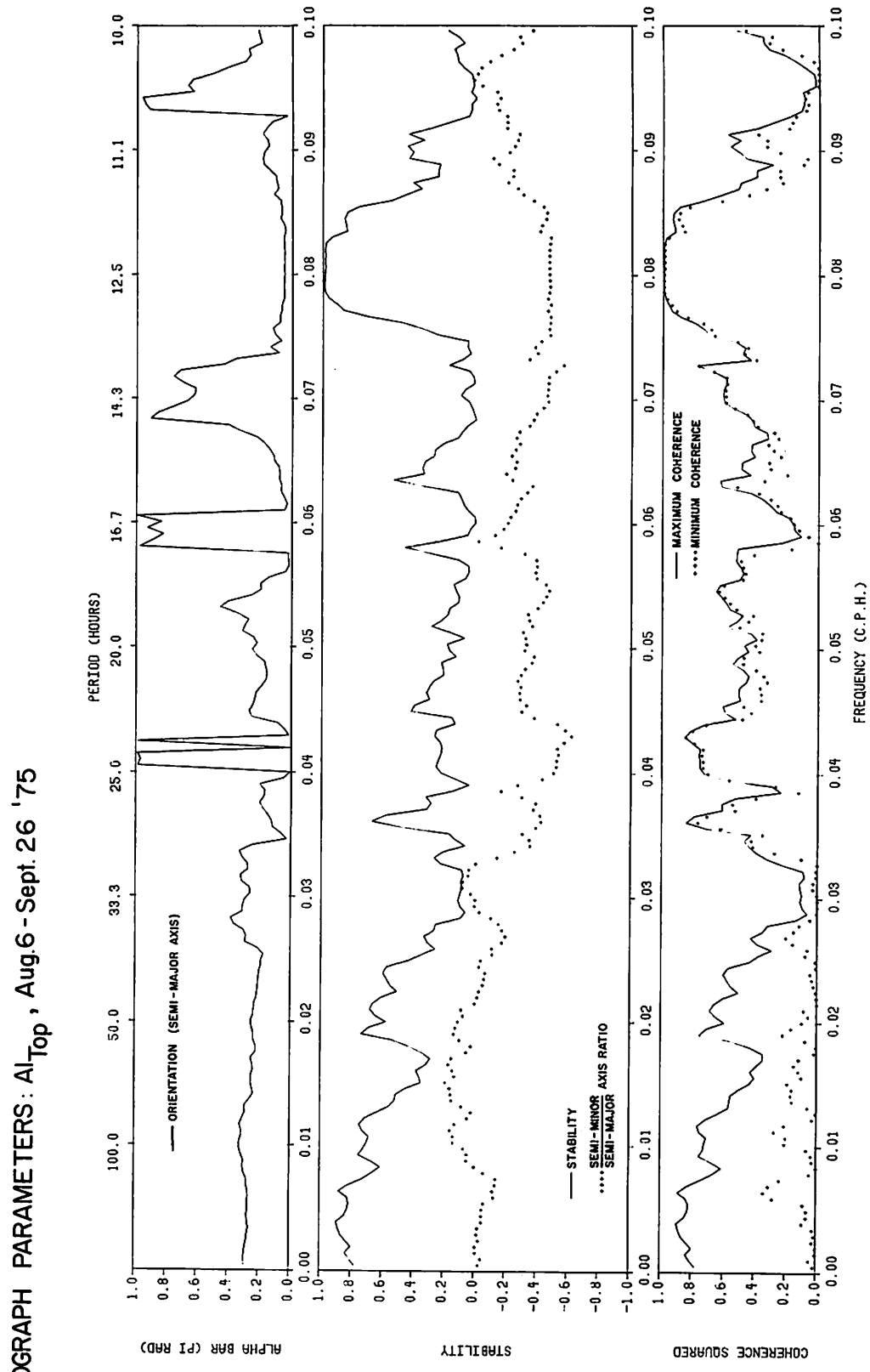

Figure 19 Hodograph parameters of 3HRLP current velocity from meter Al_{top}

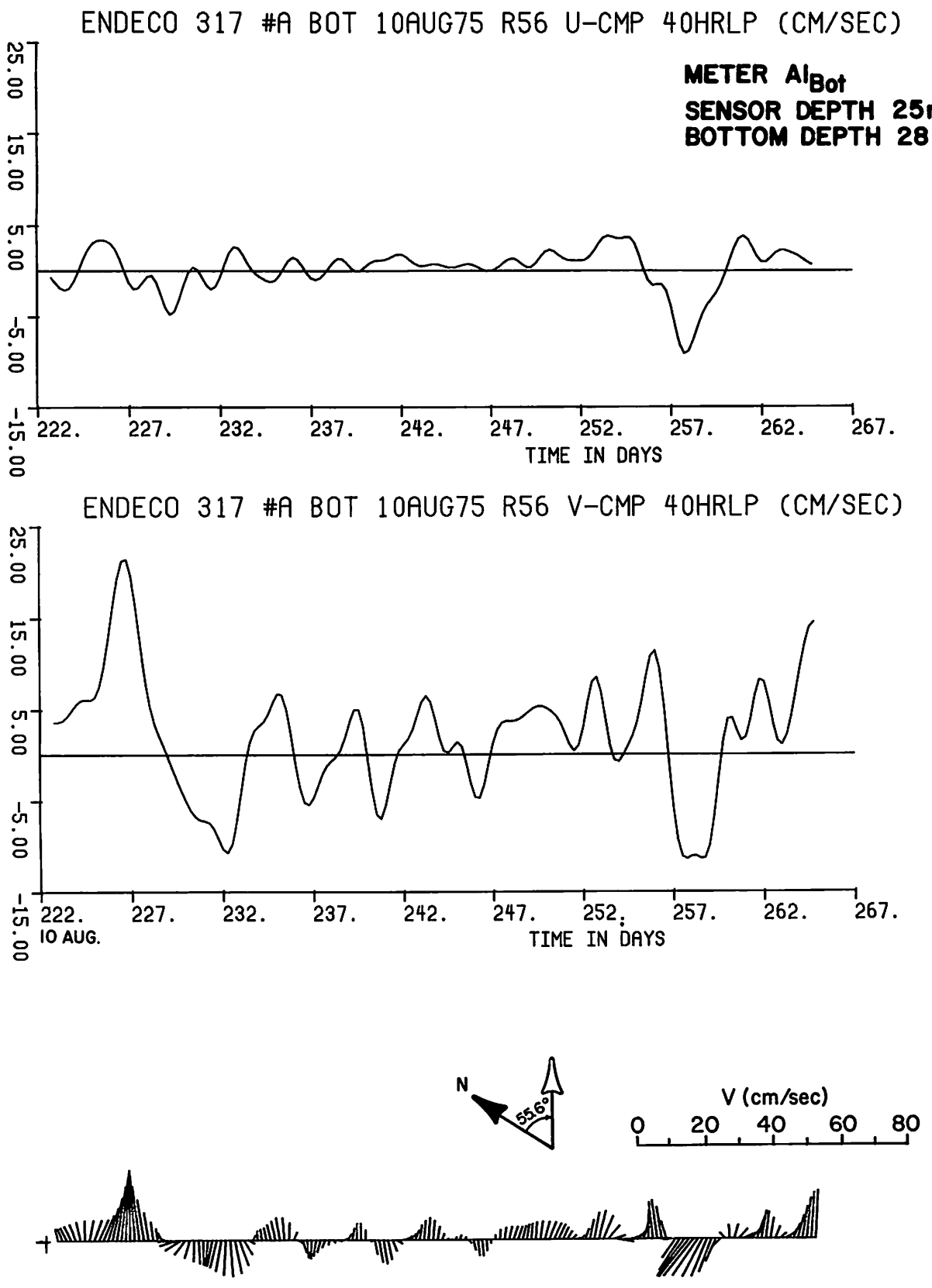

Figure 20 Low pass current velocity components and vectors from meter Al_{bot}

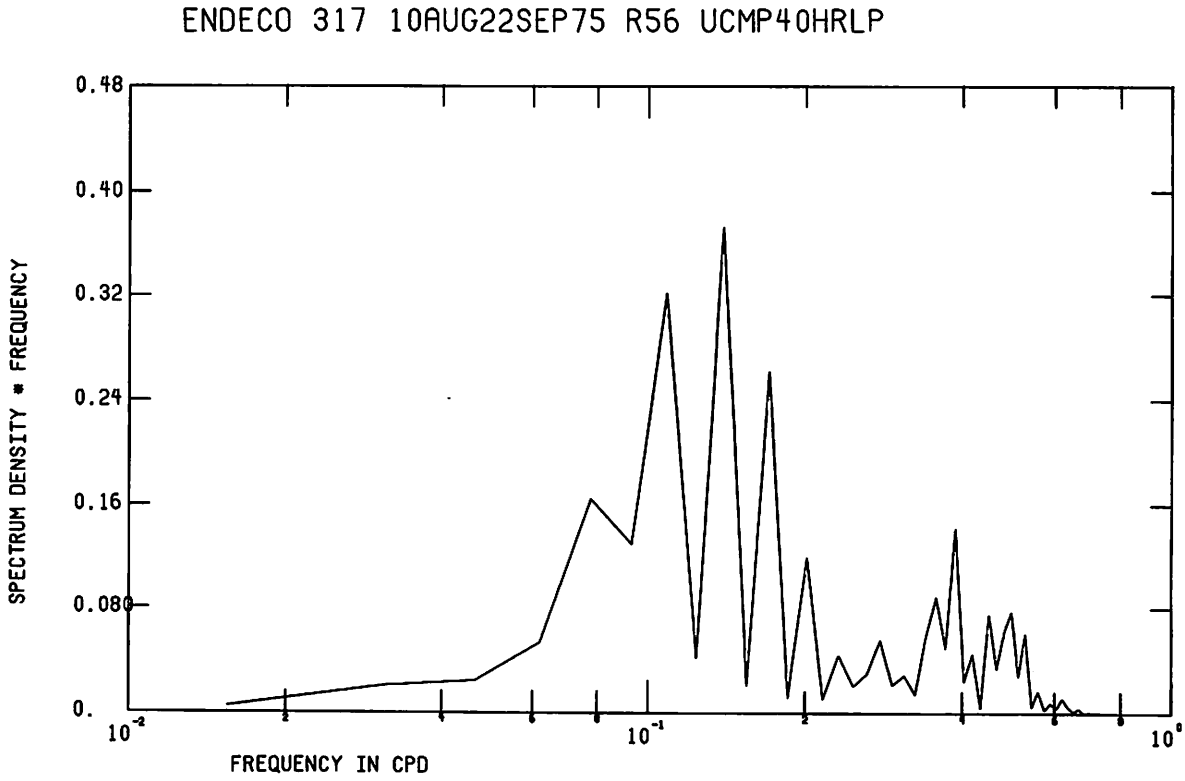

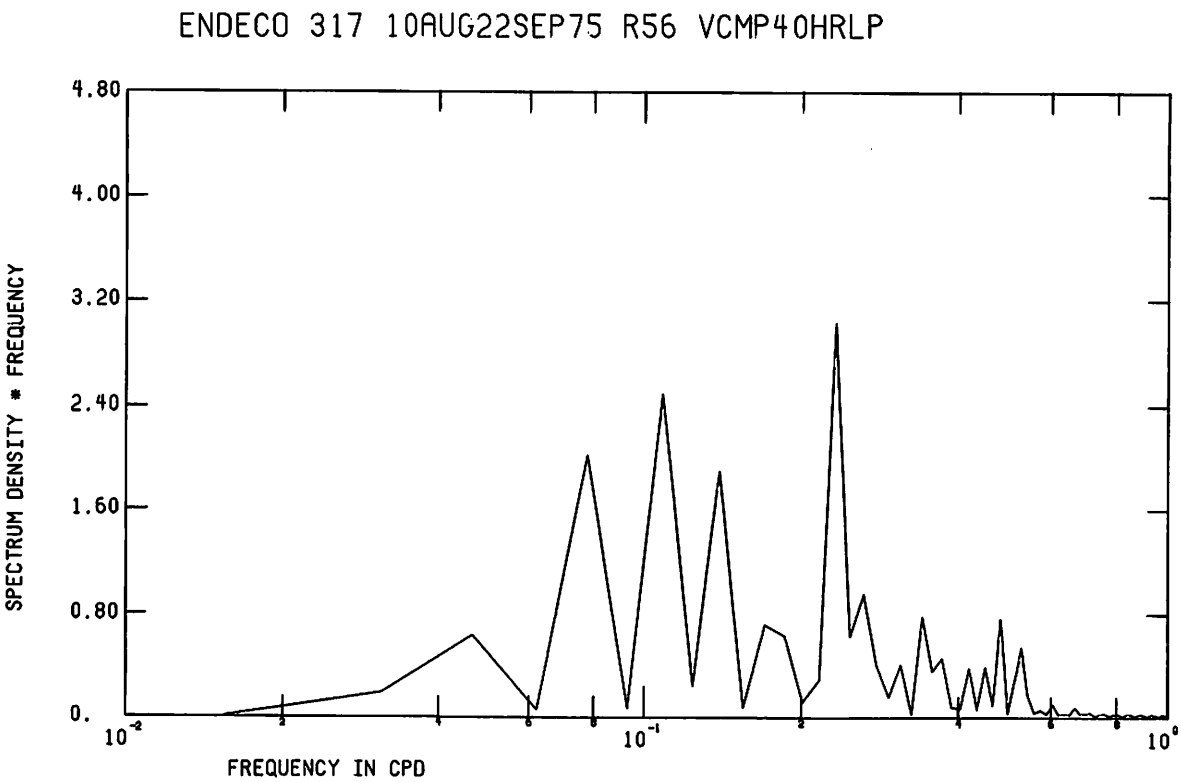

Figure 21 FFT of low pass current velocity components from meter $A1_{bot}$

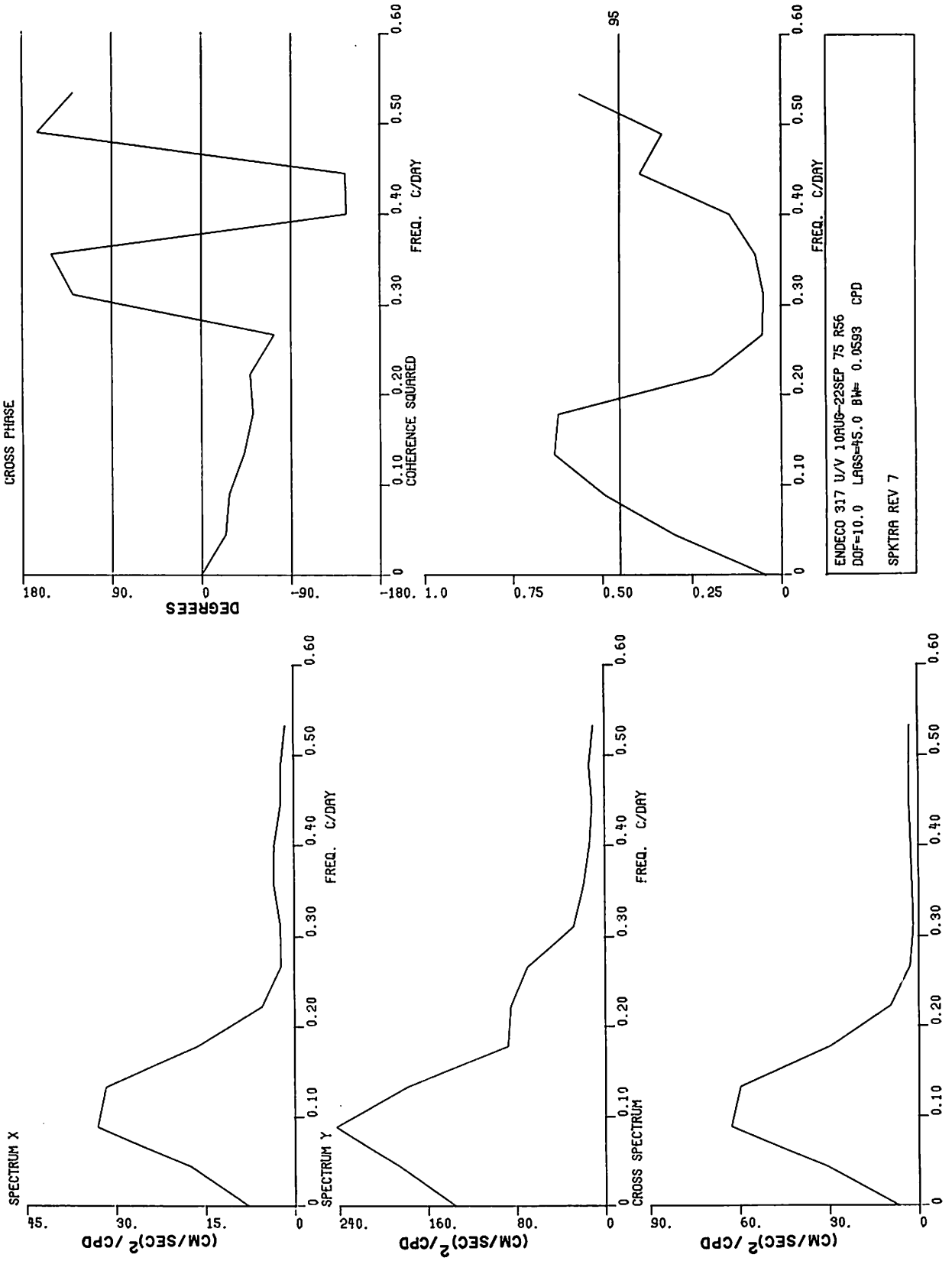

Figure 22 Spectra of low pass current velocity components from meter Al_{bot}

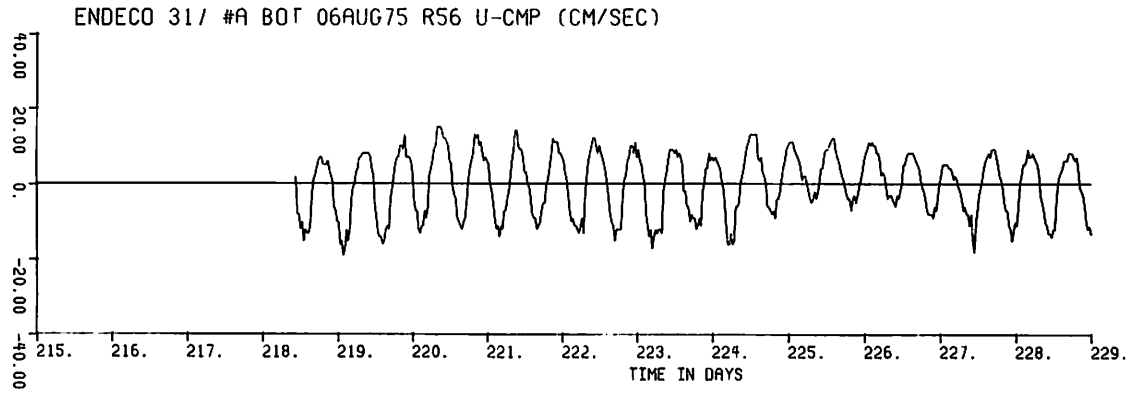

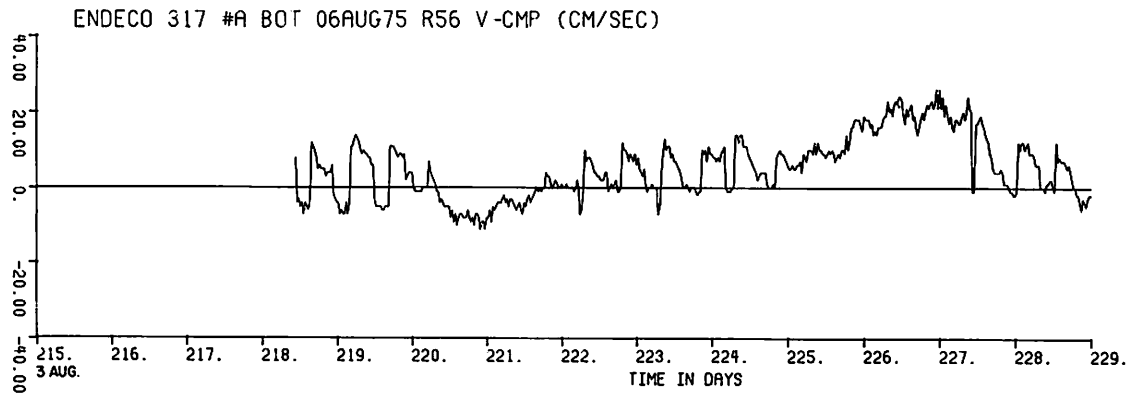

Figure 23a

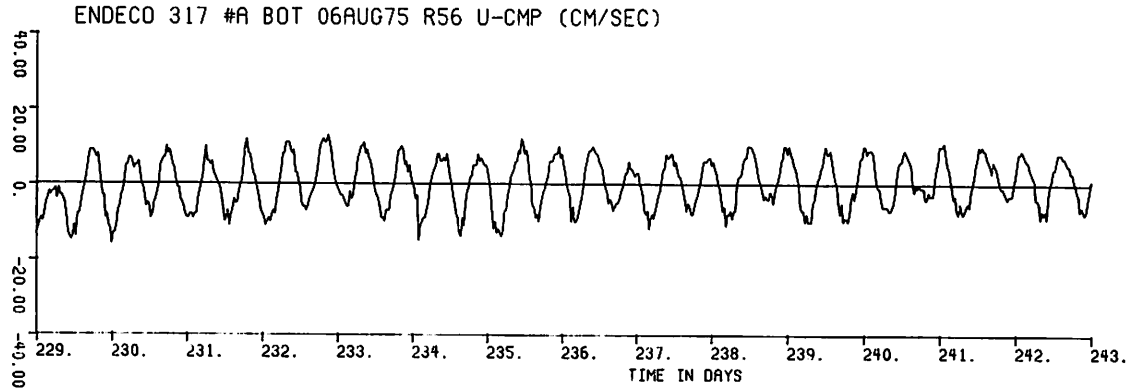

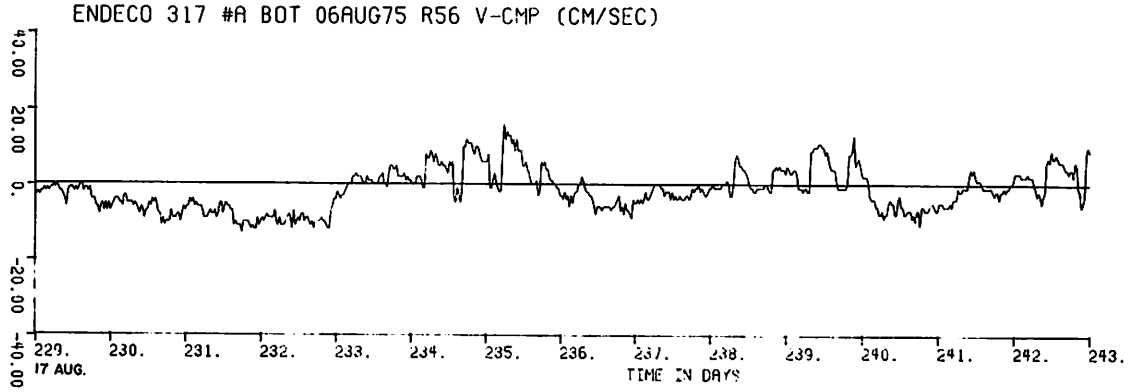

Figure 23b

Figure 23 (a,b,c,d) Unfiltered current velocity components from meter $A1_{bot}$

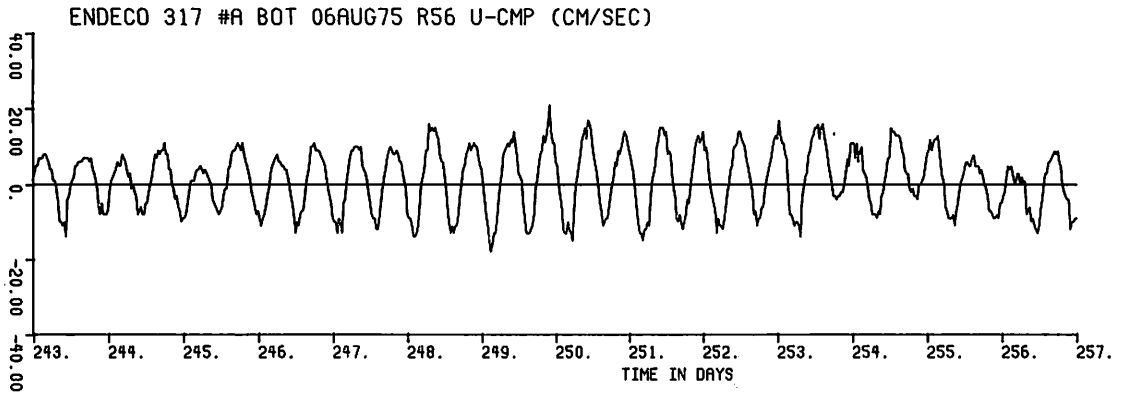

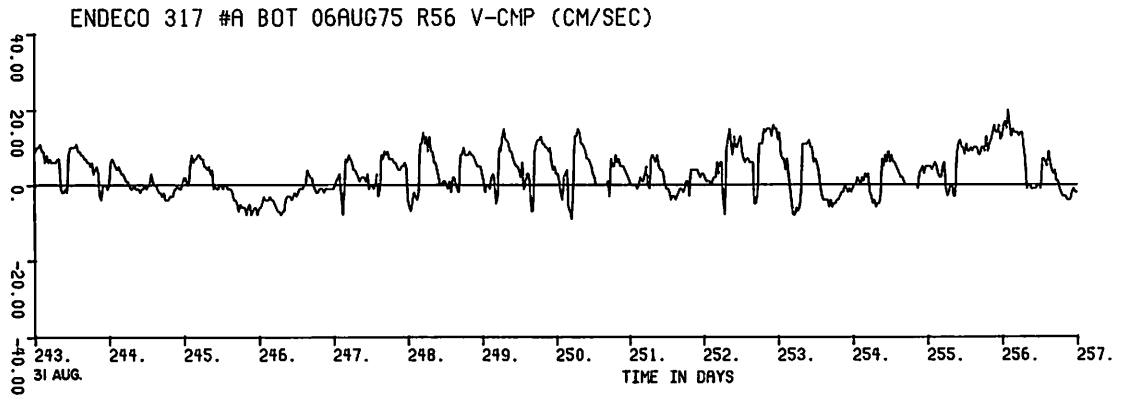

Figure 23c

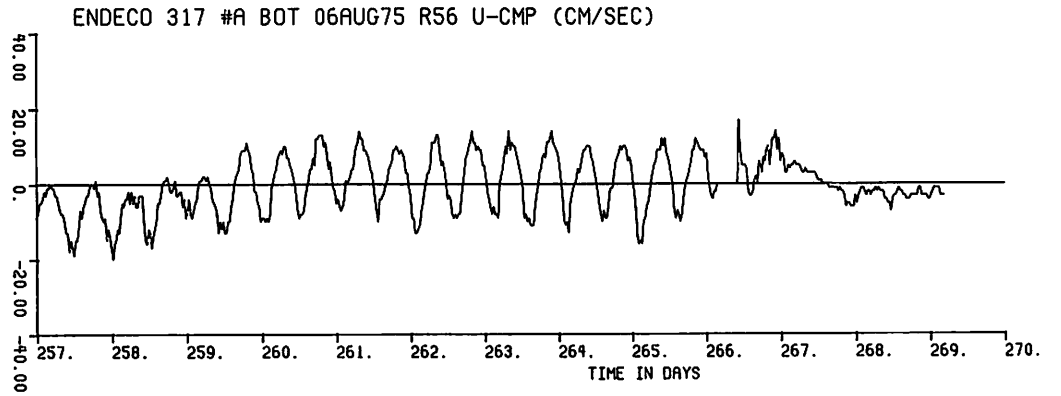

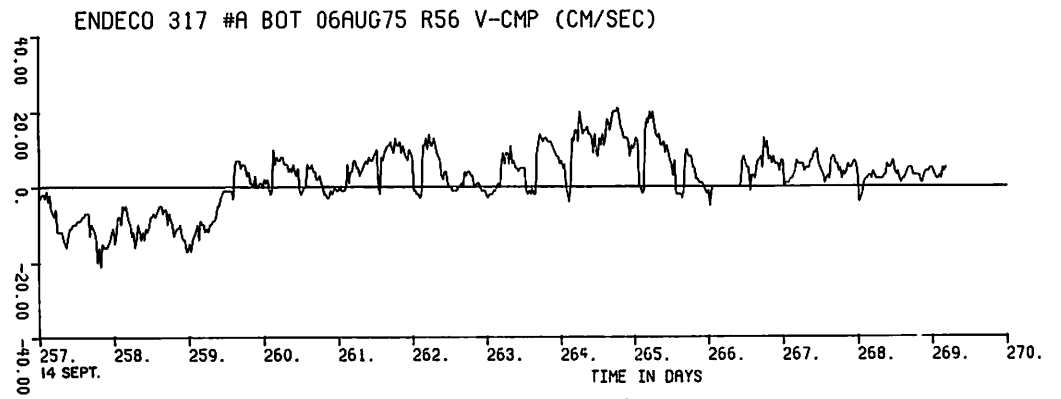

Figure 23d

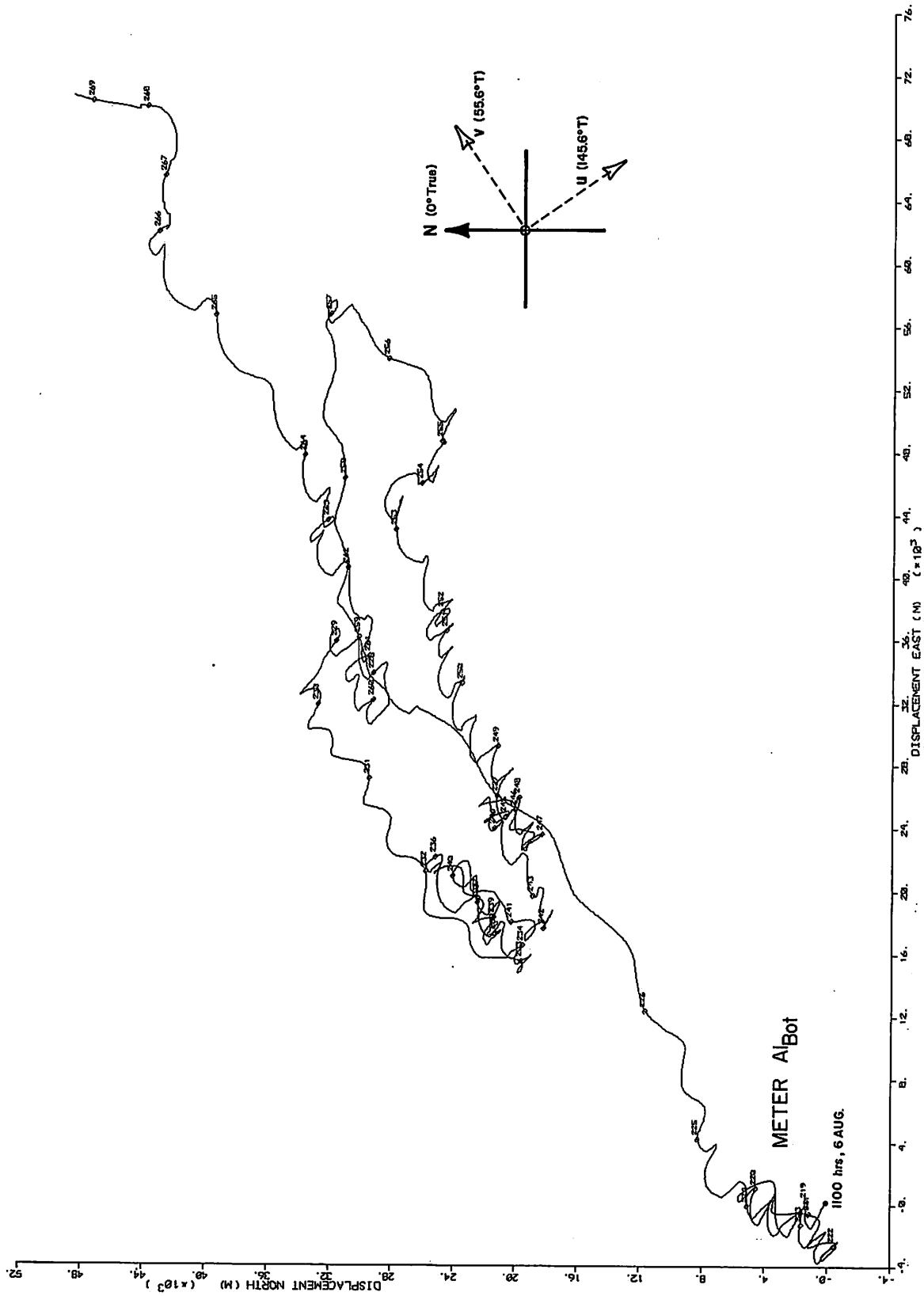

Figure 24 Progressive vector diagram of unfiltered current velocity from meter Al_{bot}

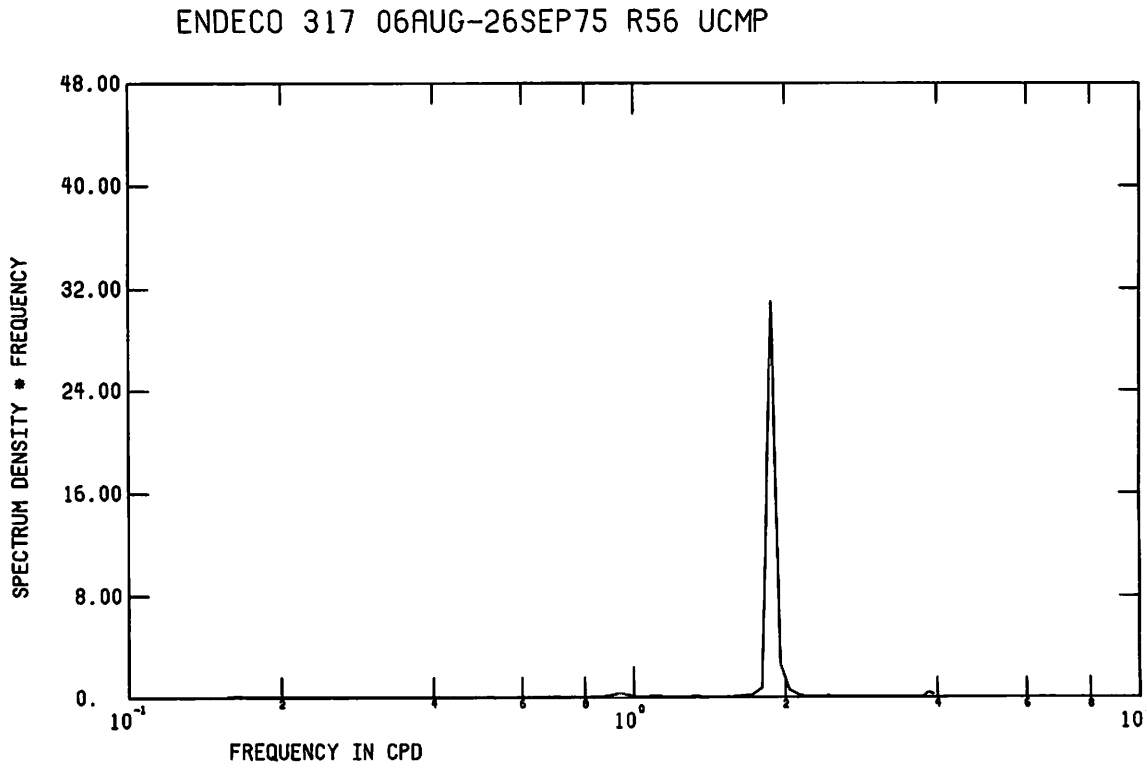

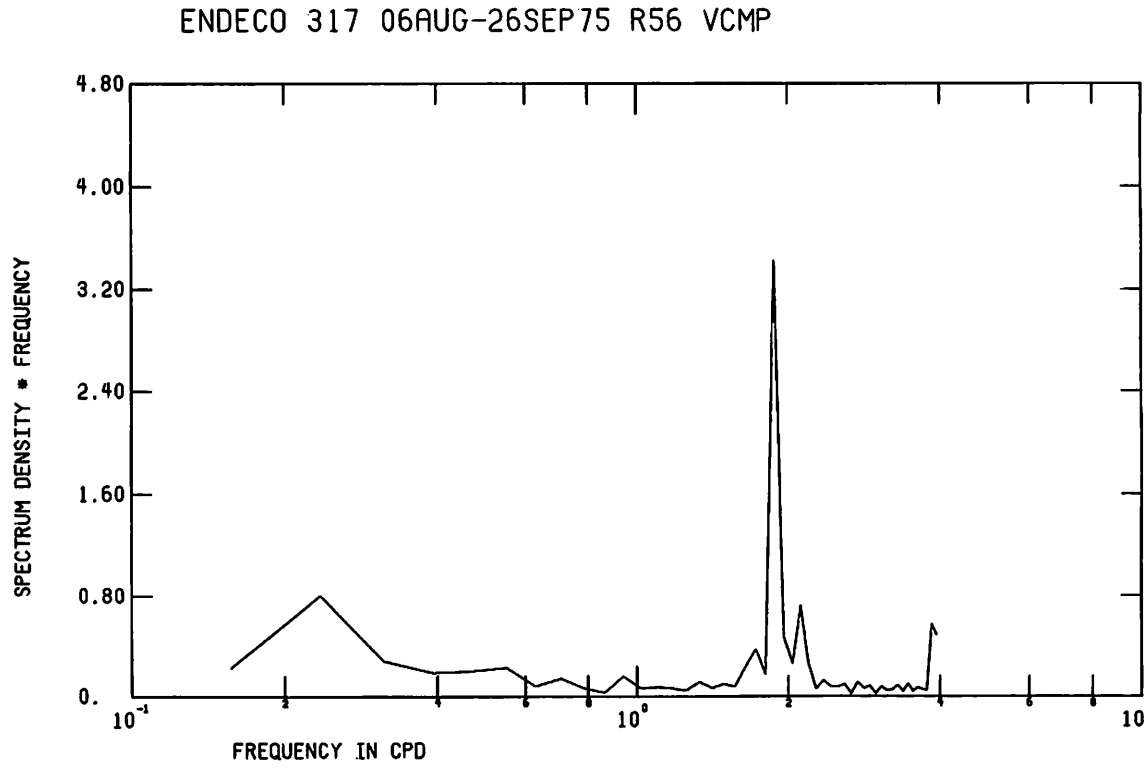

Figure 25 FFT of unfiltered current velocity components from meter $A1_{bot}$

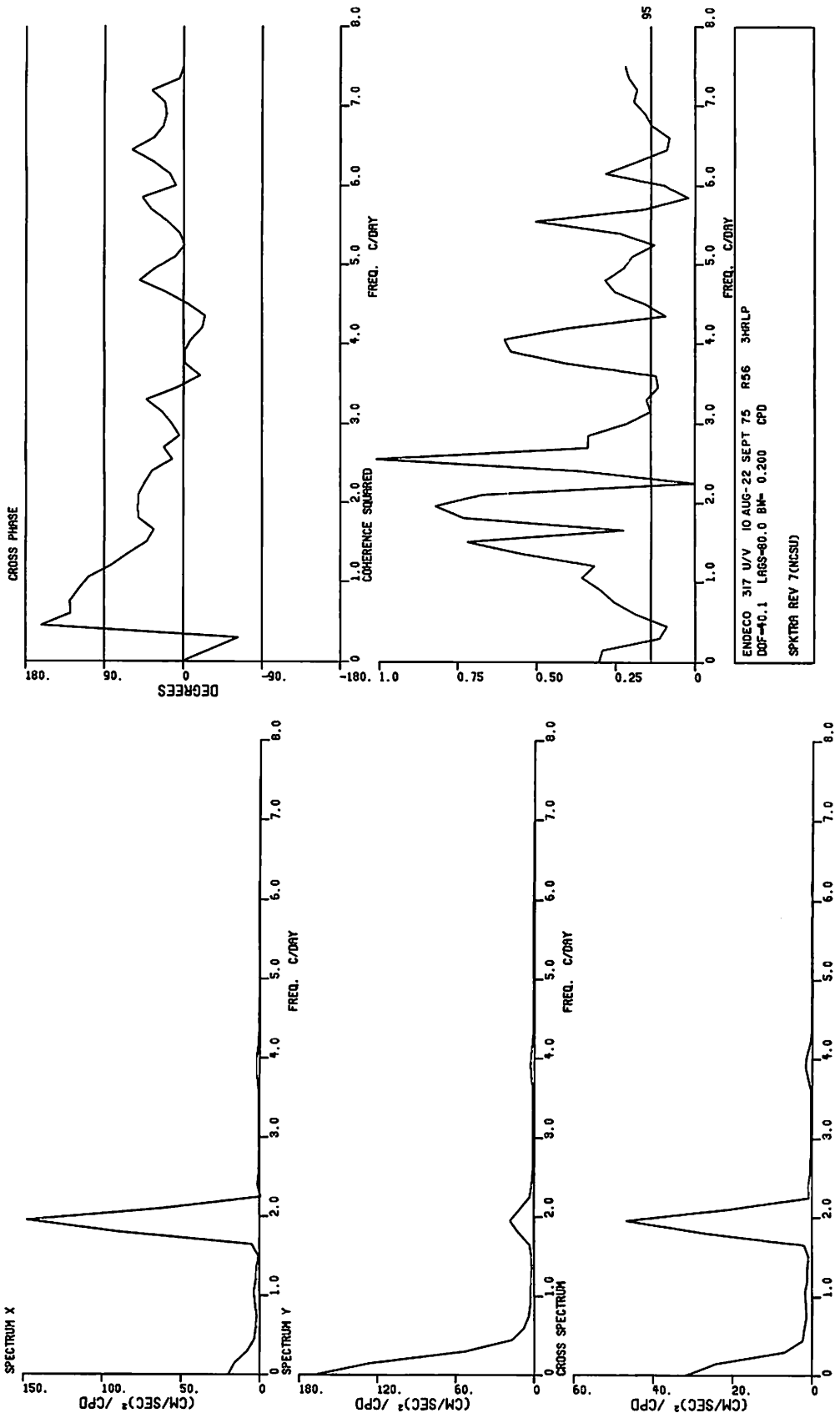

Figure 26 Spectra of 3HRLP current velocity components from meter Al_{bot}

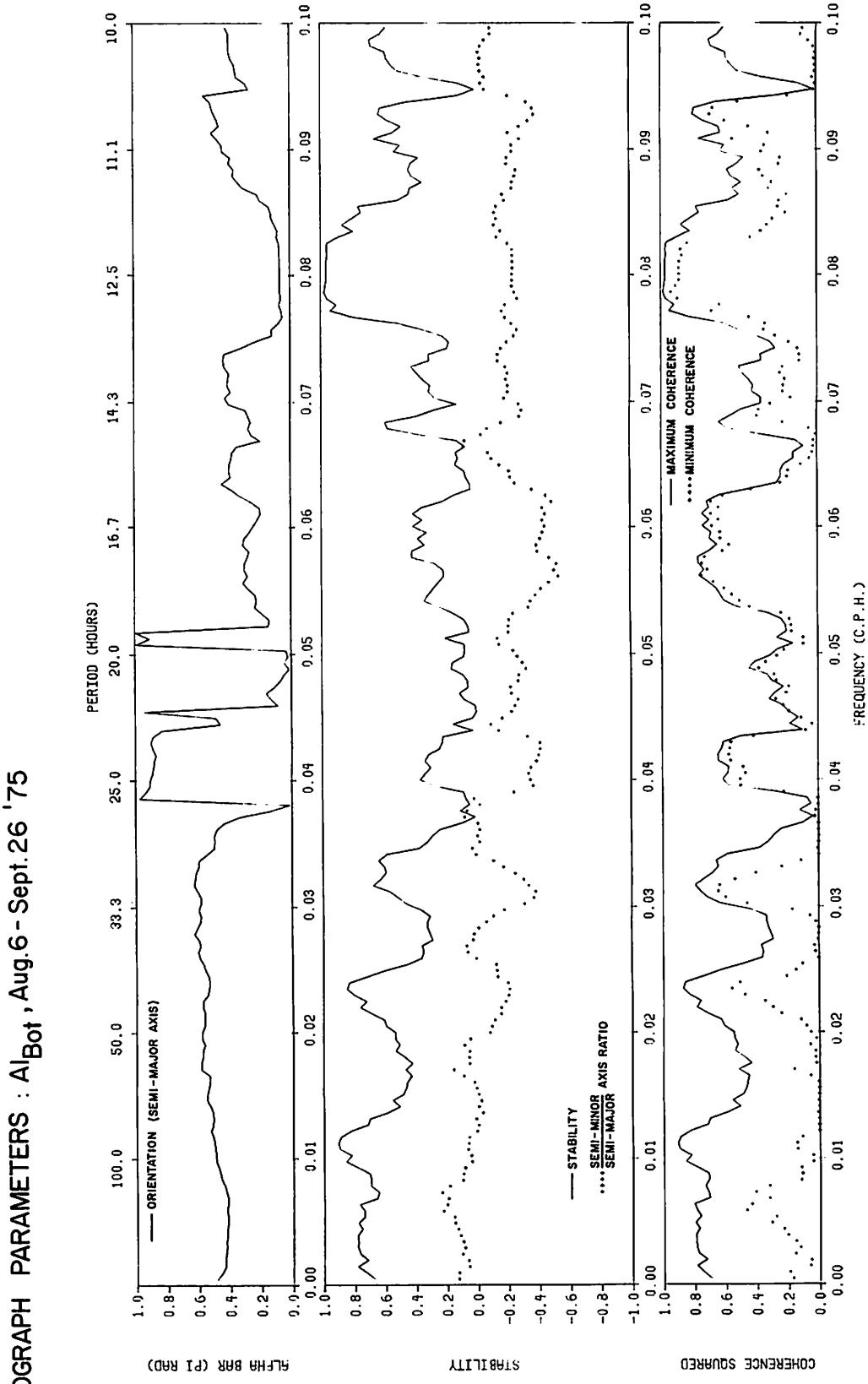

Figure 27 Hodograph parameters of 3HRLP current velocity from meter Al_{bot}

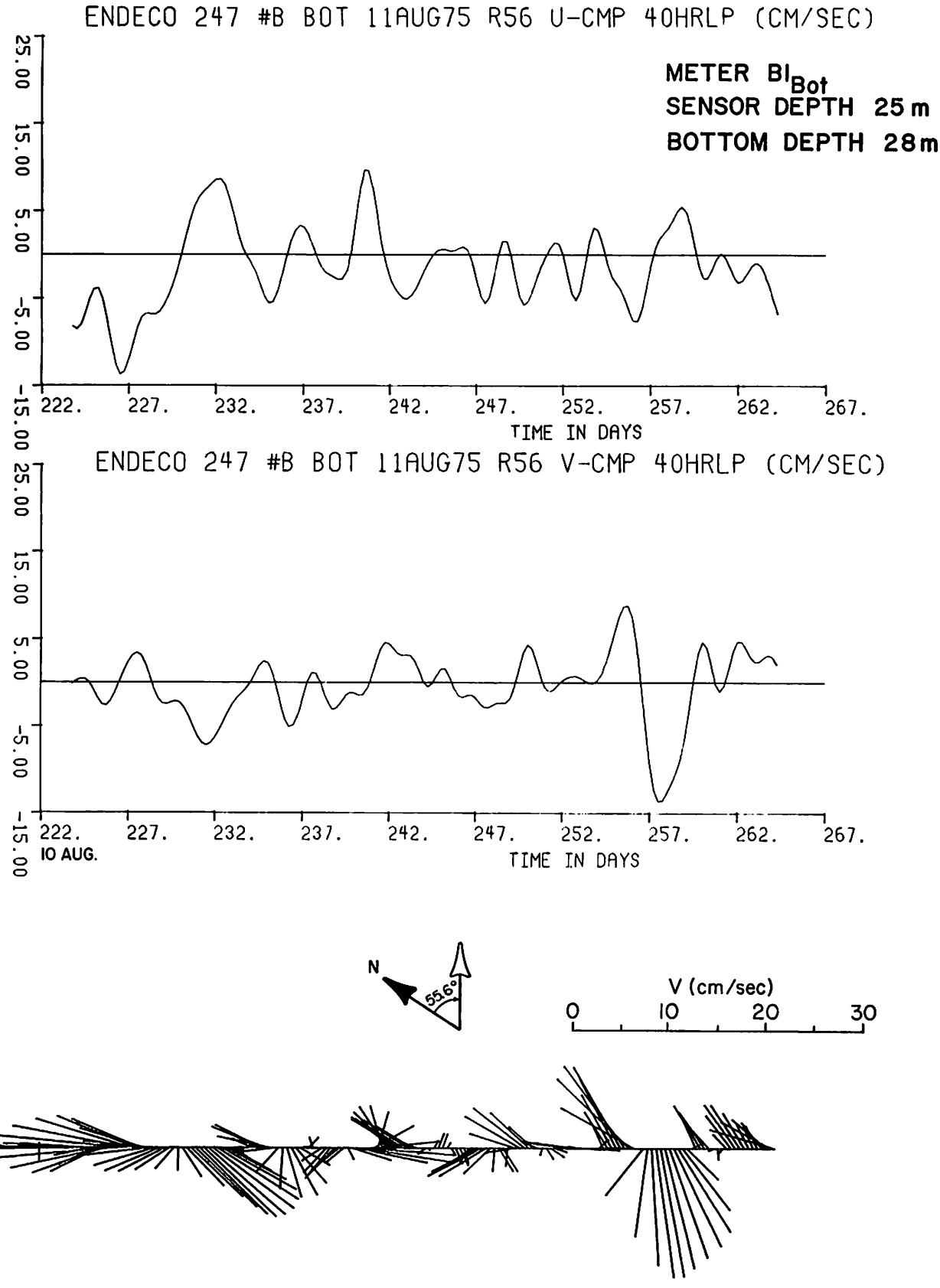

Figure 28 Low pass current velocity components and vectors from meter Bl_{bot}

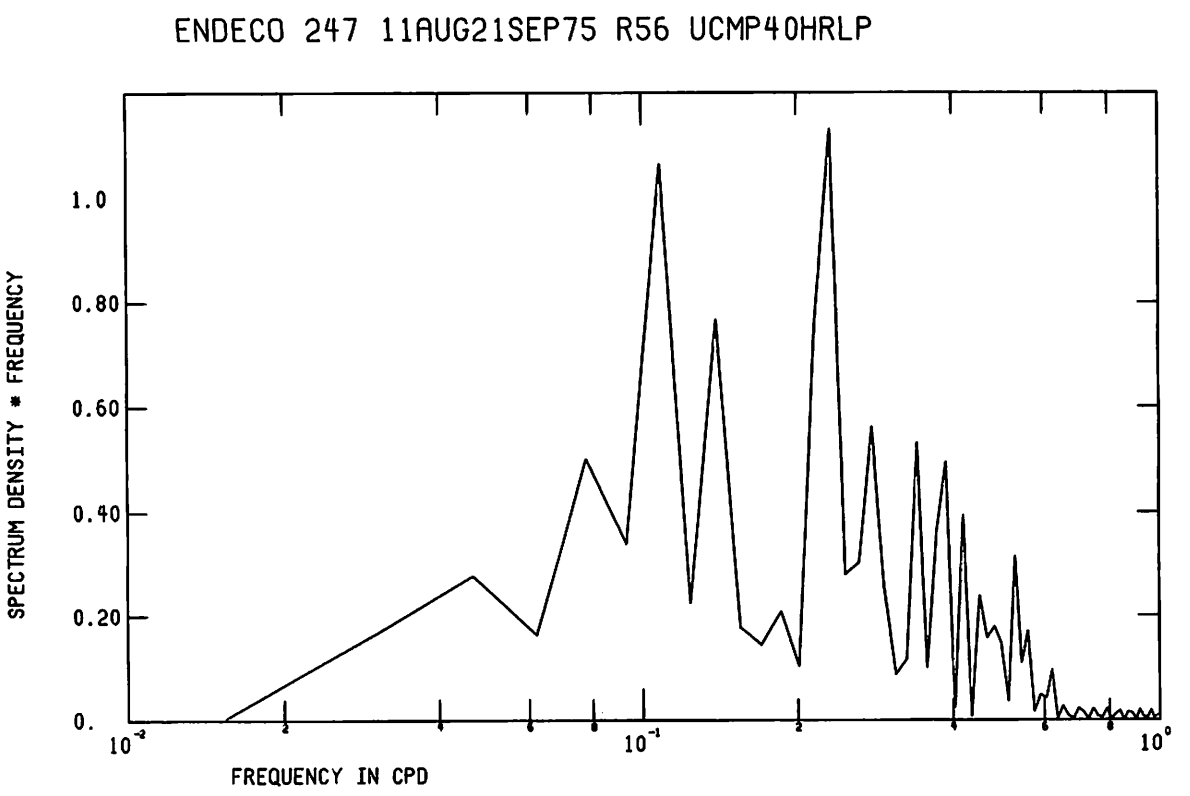

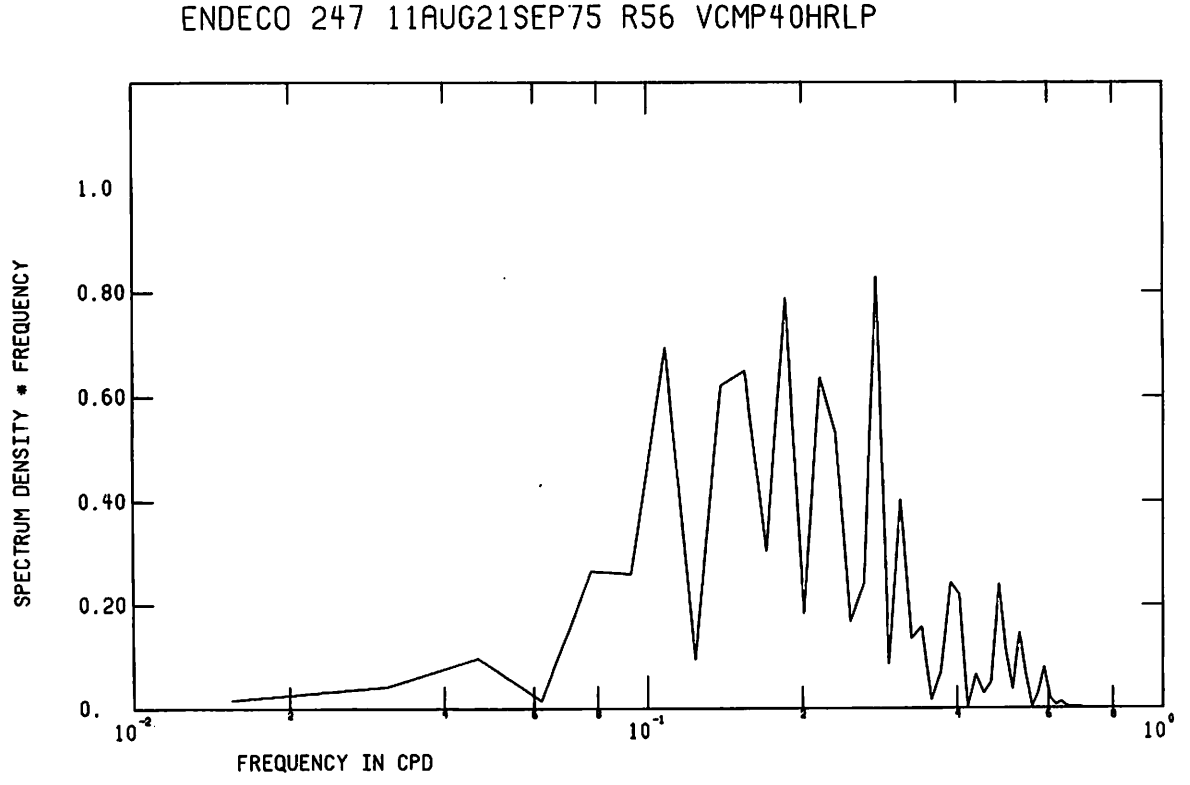

Figure 29 FFT of low pass current velocity components from meter Bl_{bot}

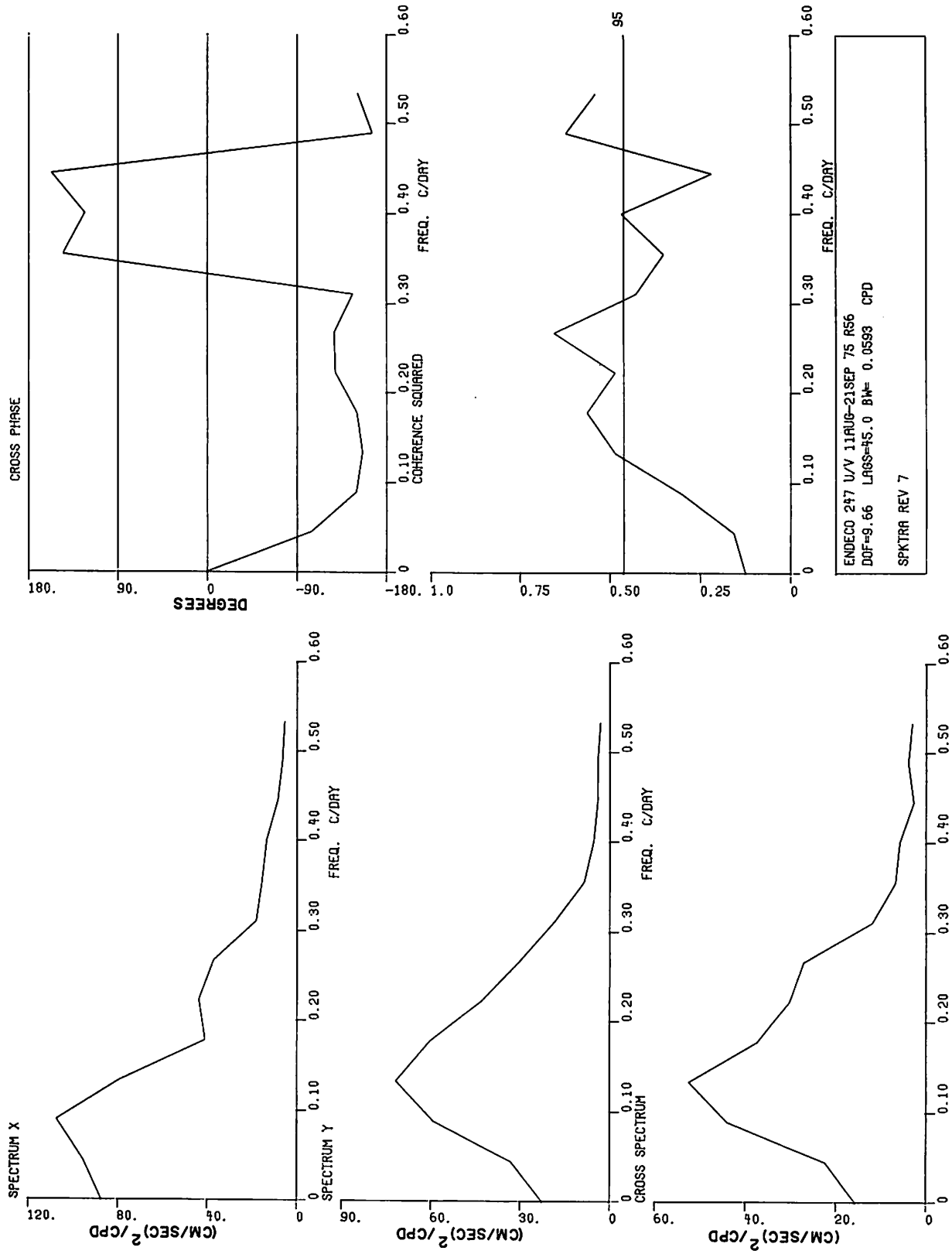

Figure 30 Spectra of low pass current velocity components from meter Bl_{bot}

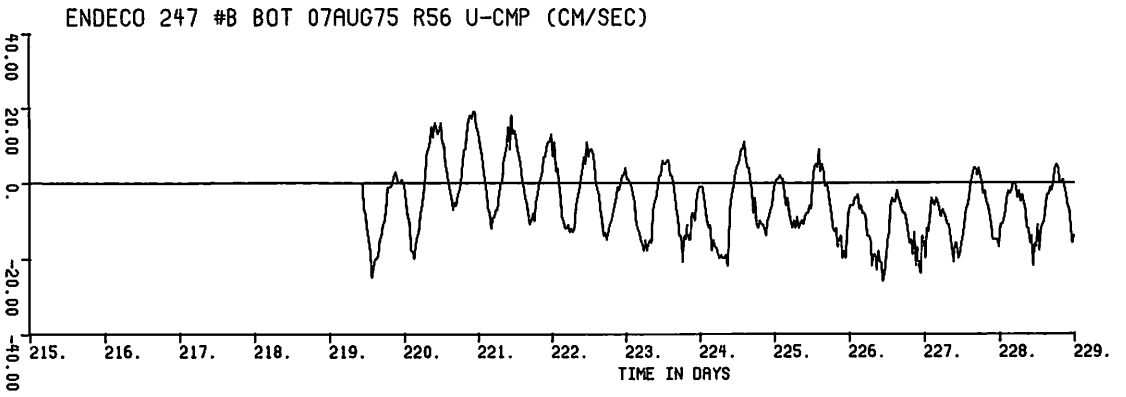

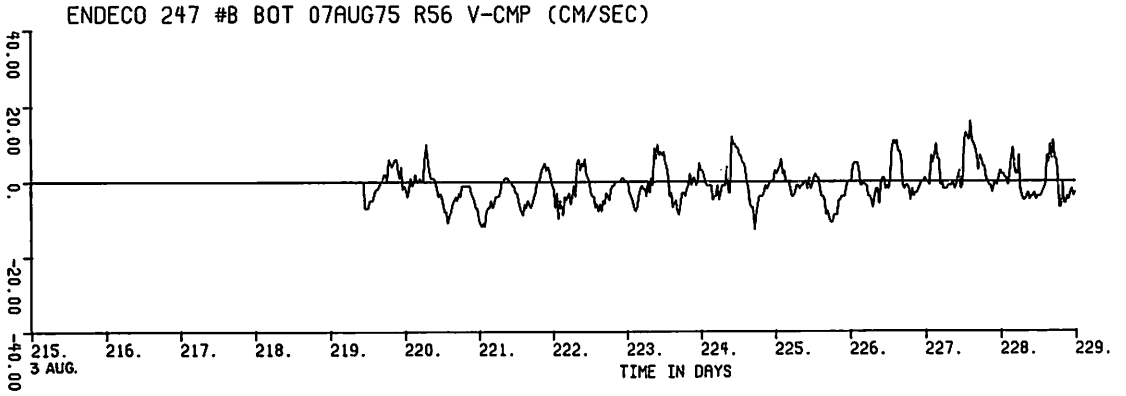

Figure 31a

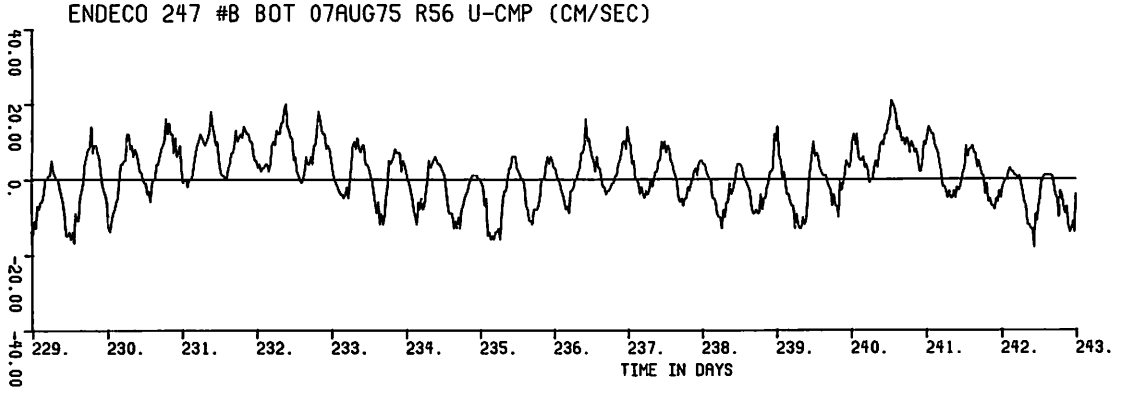

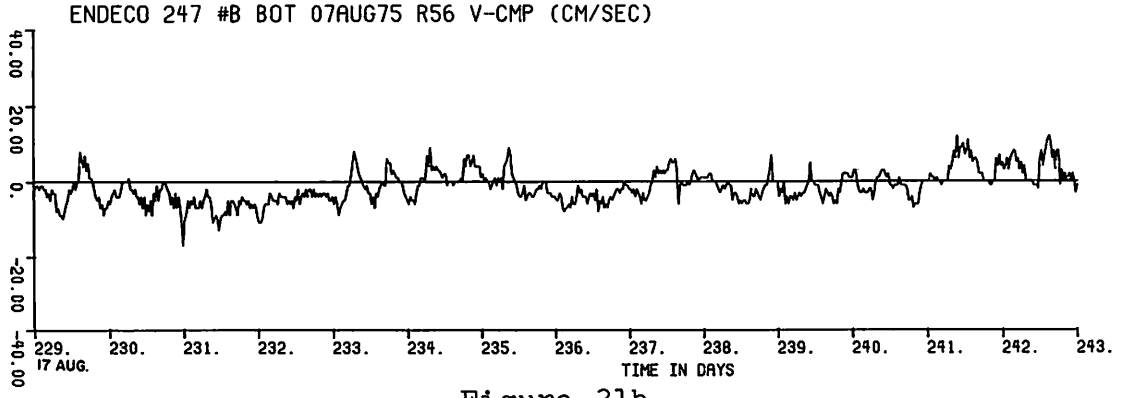

Figure 31b

Figure 31 Unfiltered current velocity components (a,b,c,d) from meter Bl_{bot}

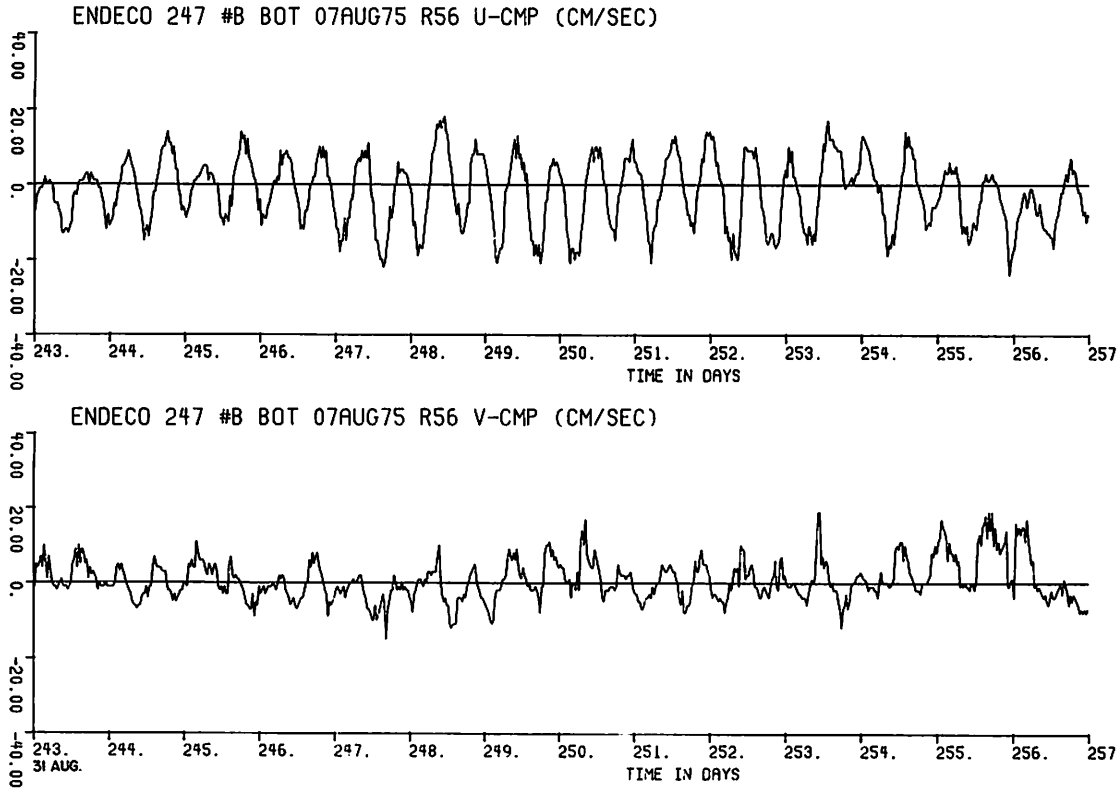

Figure 31c

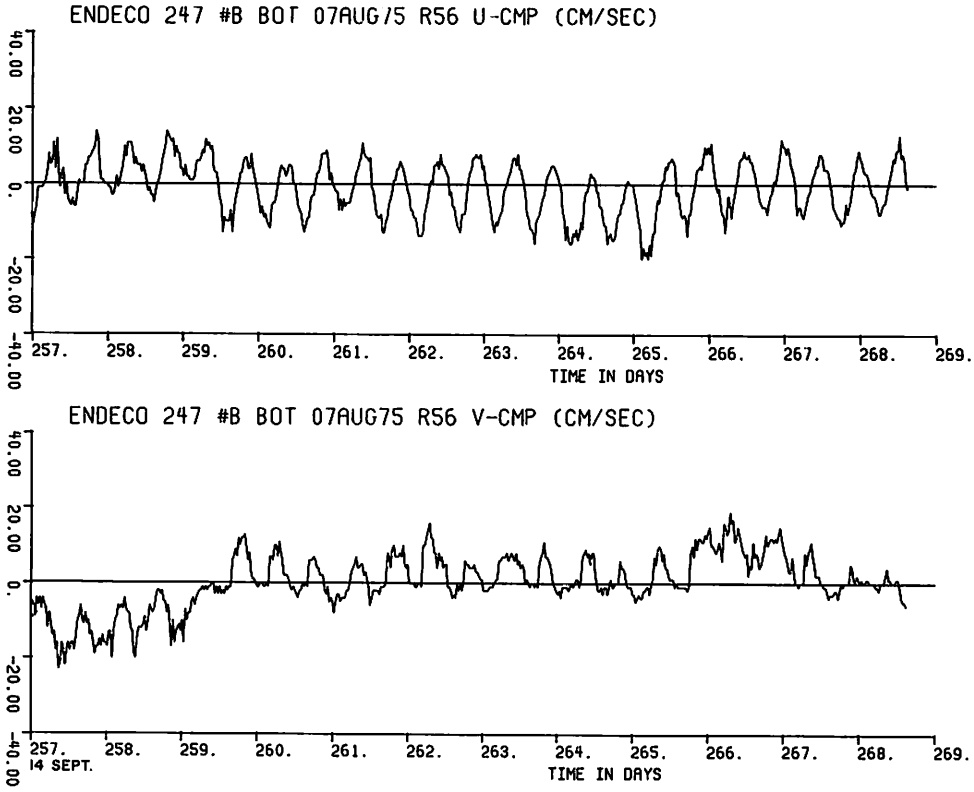

Figure 31d

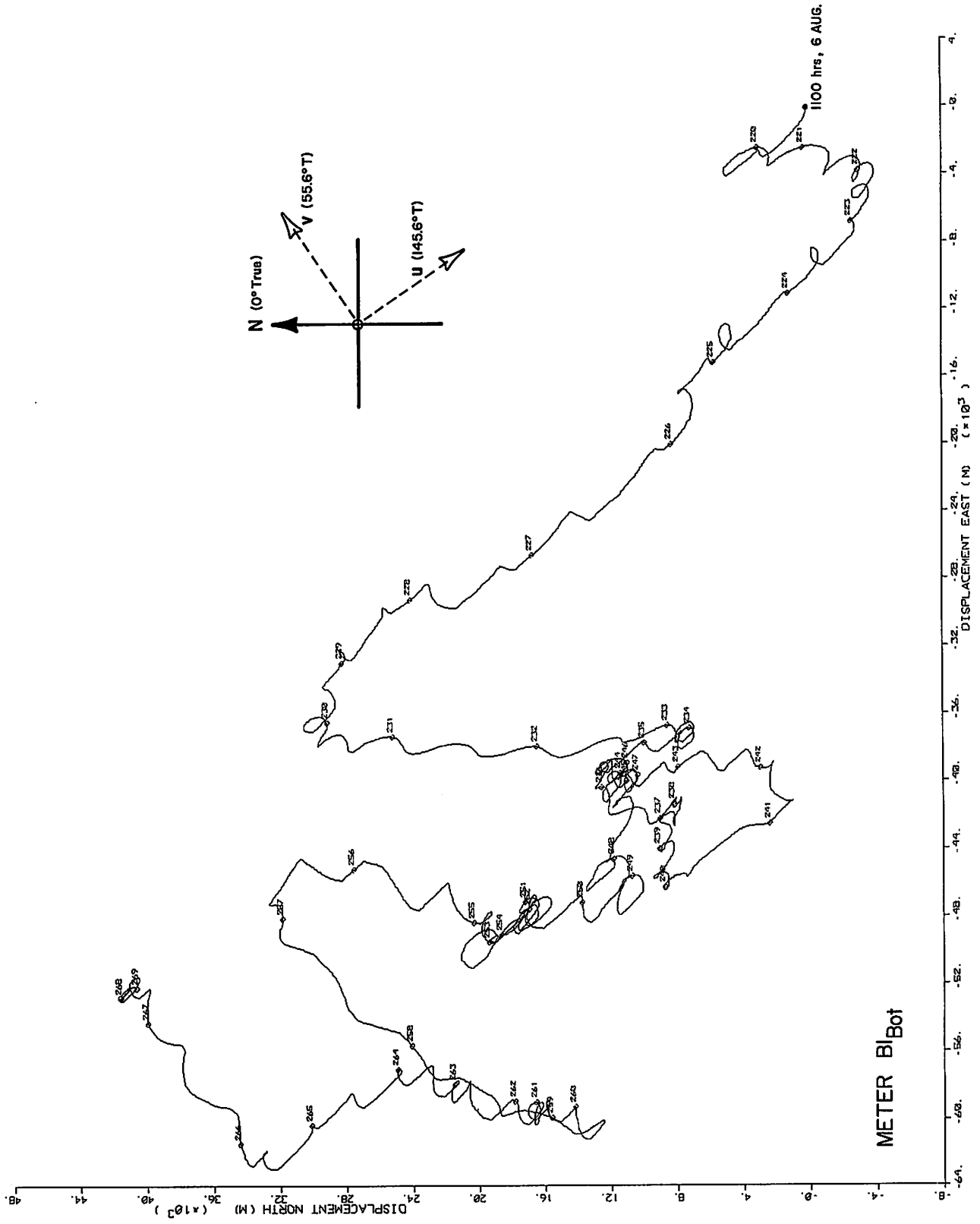

Figure 32 Progressive vector diagram of unfiltered current velocity from meter Bl_{bot}

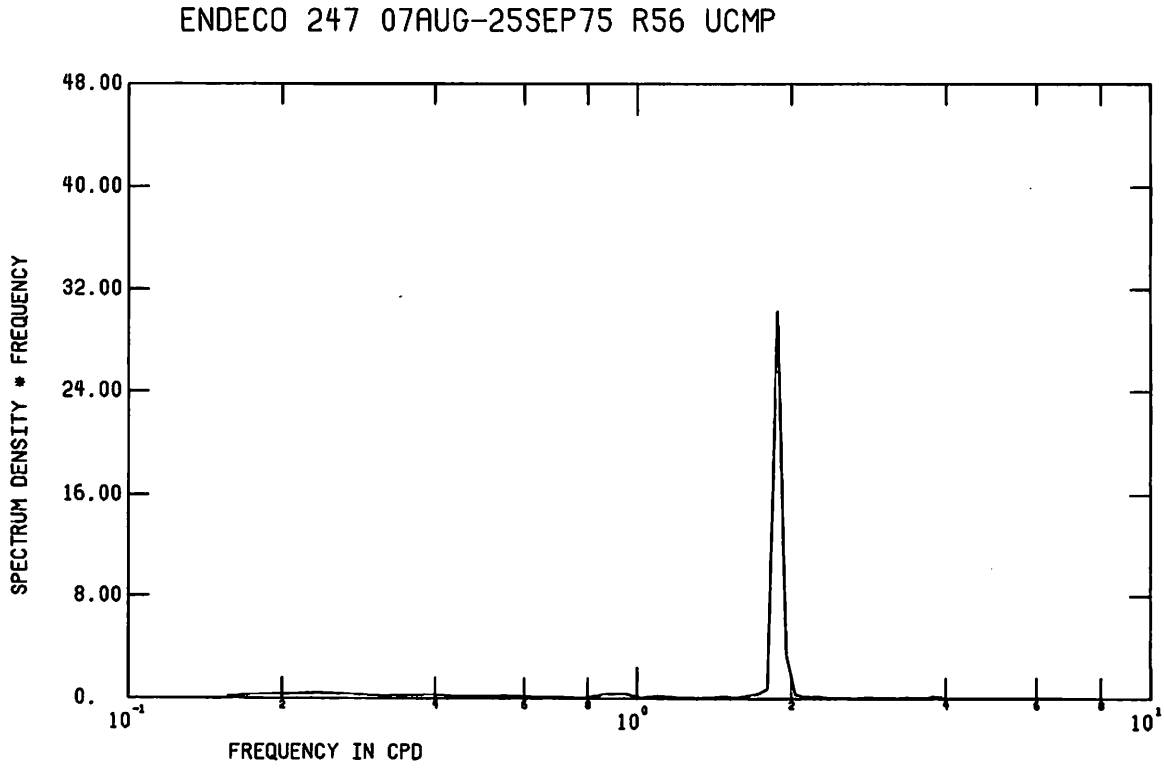

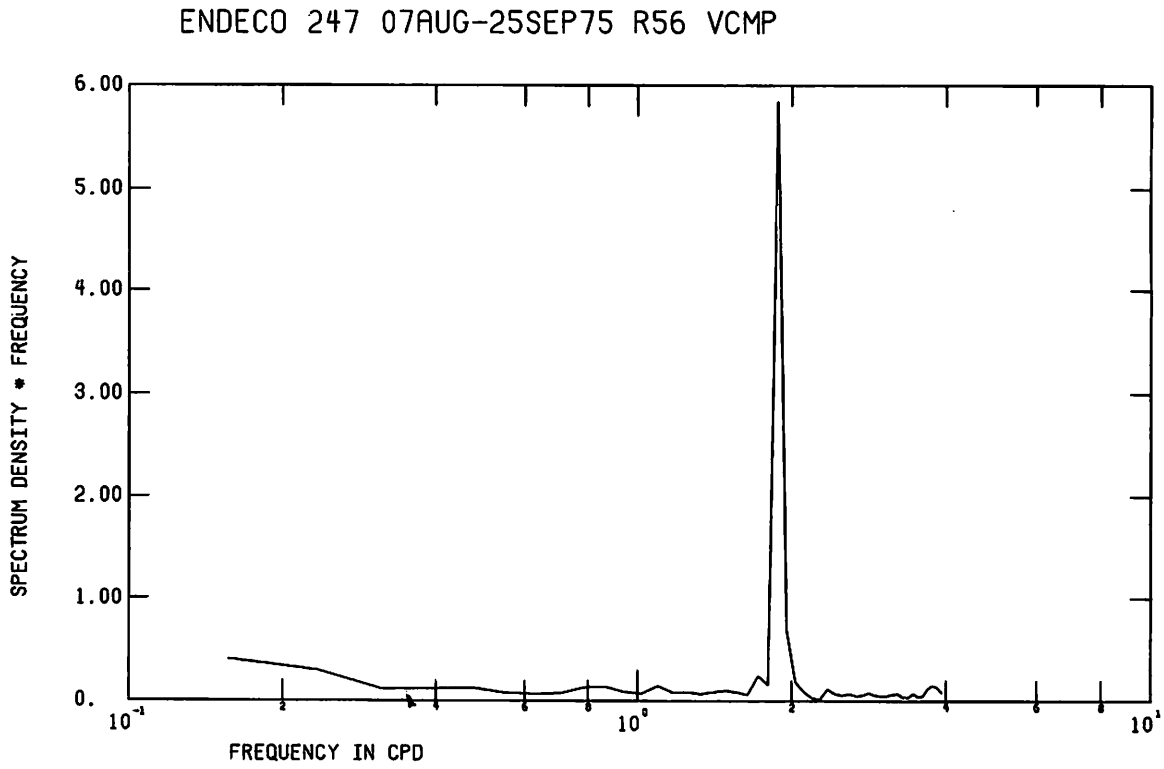

Figure 33 FFT of unfiltered current velocity components from meter Bl_{bot}

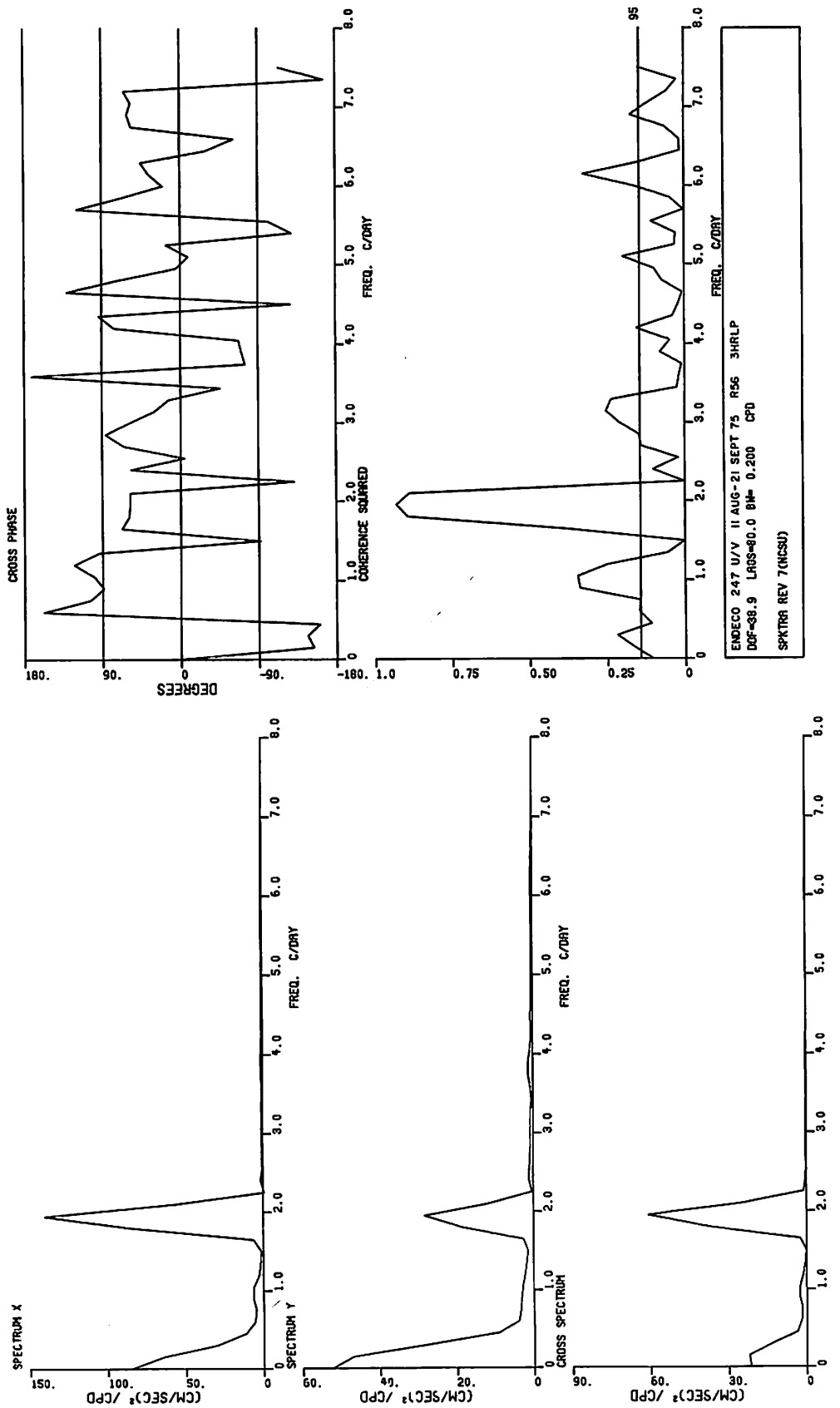

Figure 34 Spectra of 3HRLP current velocity components from meter Bl_{bot}

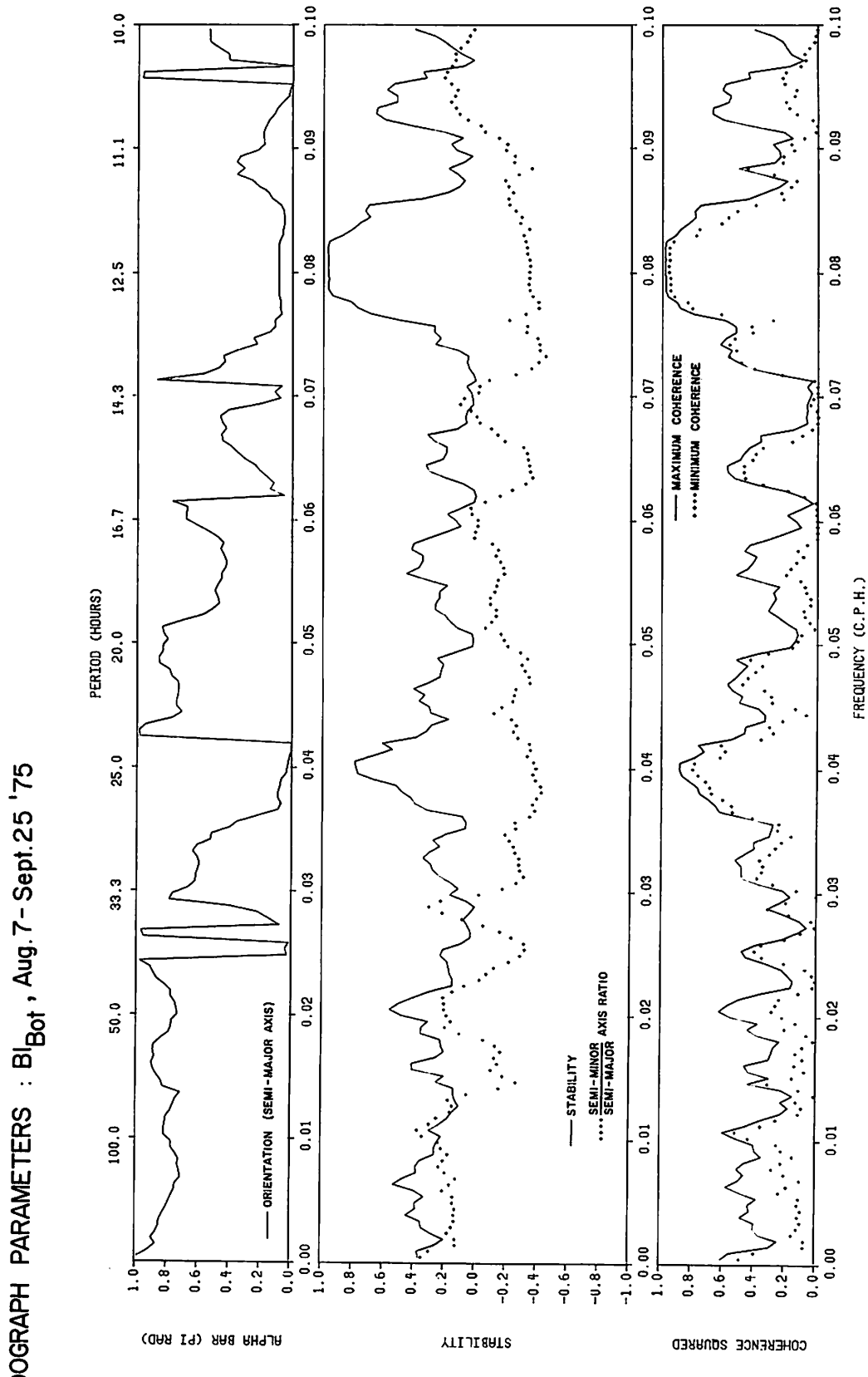

Figure 35 Hodograph parameters of 3HRLP current velocity from meter Bl_{bot}

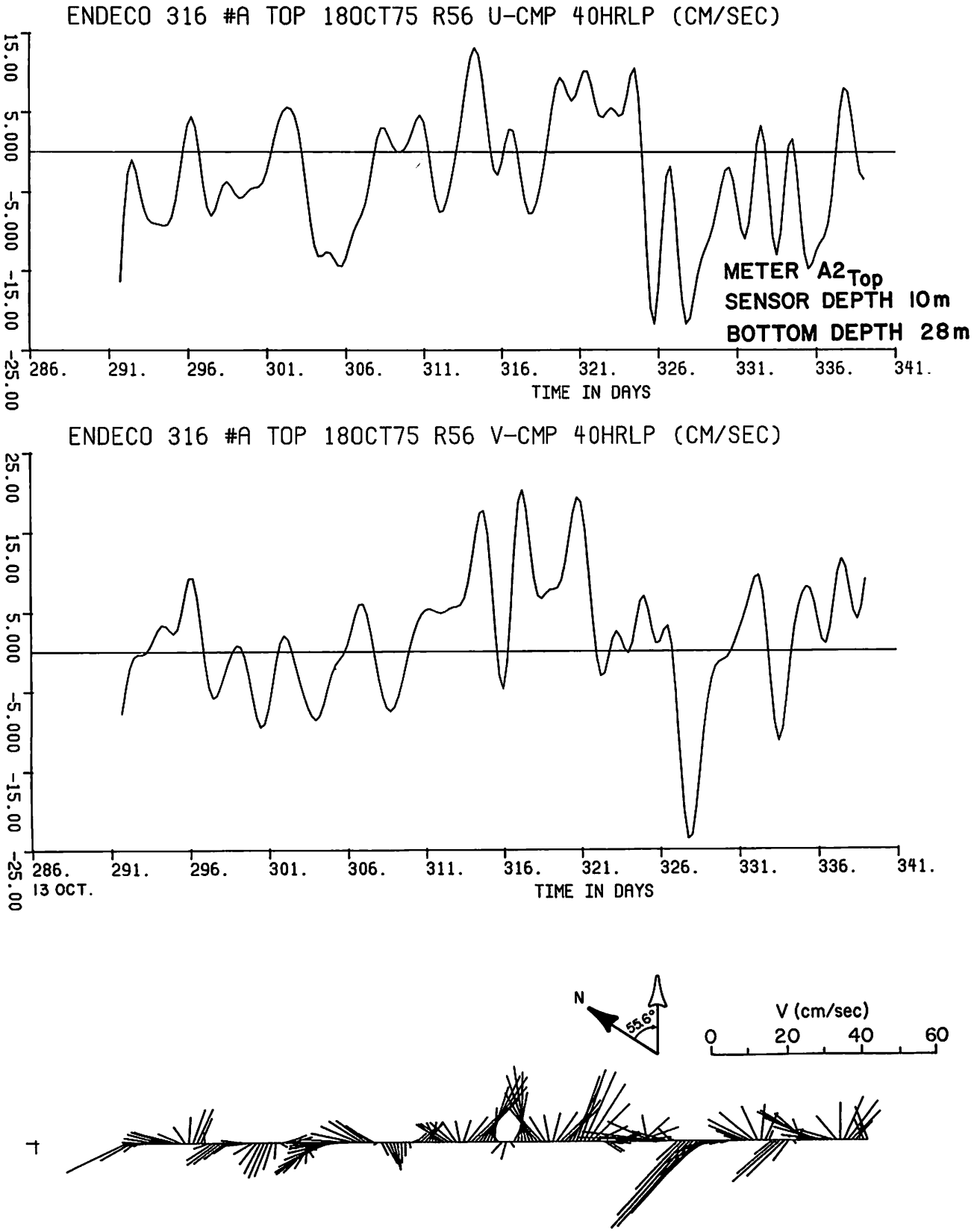

Figure 36 Low pass current velocity components and vectors from meter $A2_{top}$

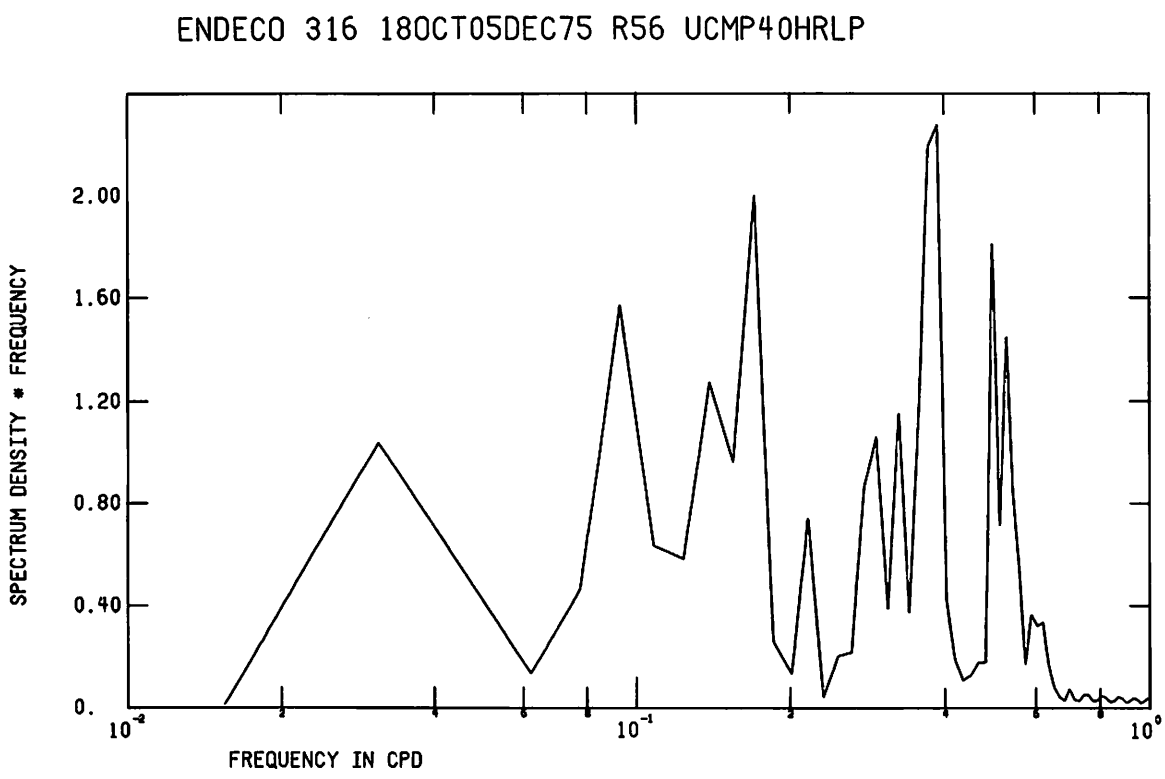

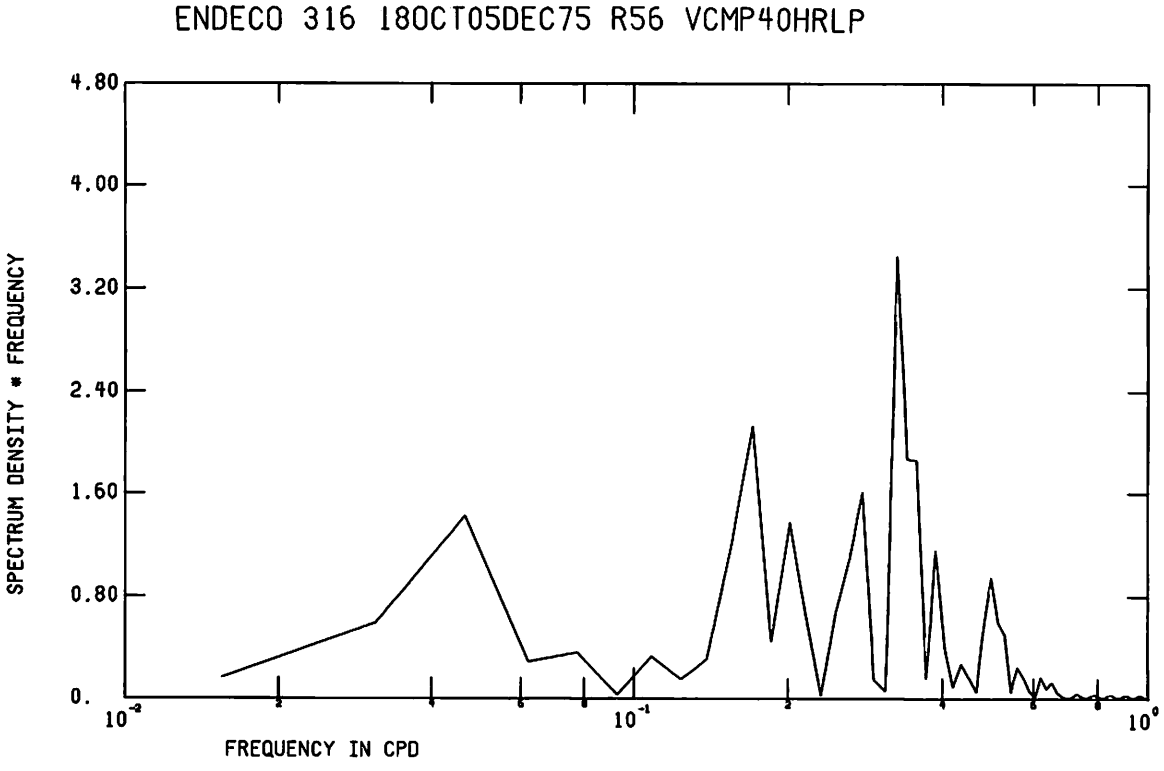

Figure 37 FFT of low pass current velocity components from meter $A2_{top}$

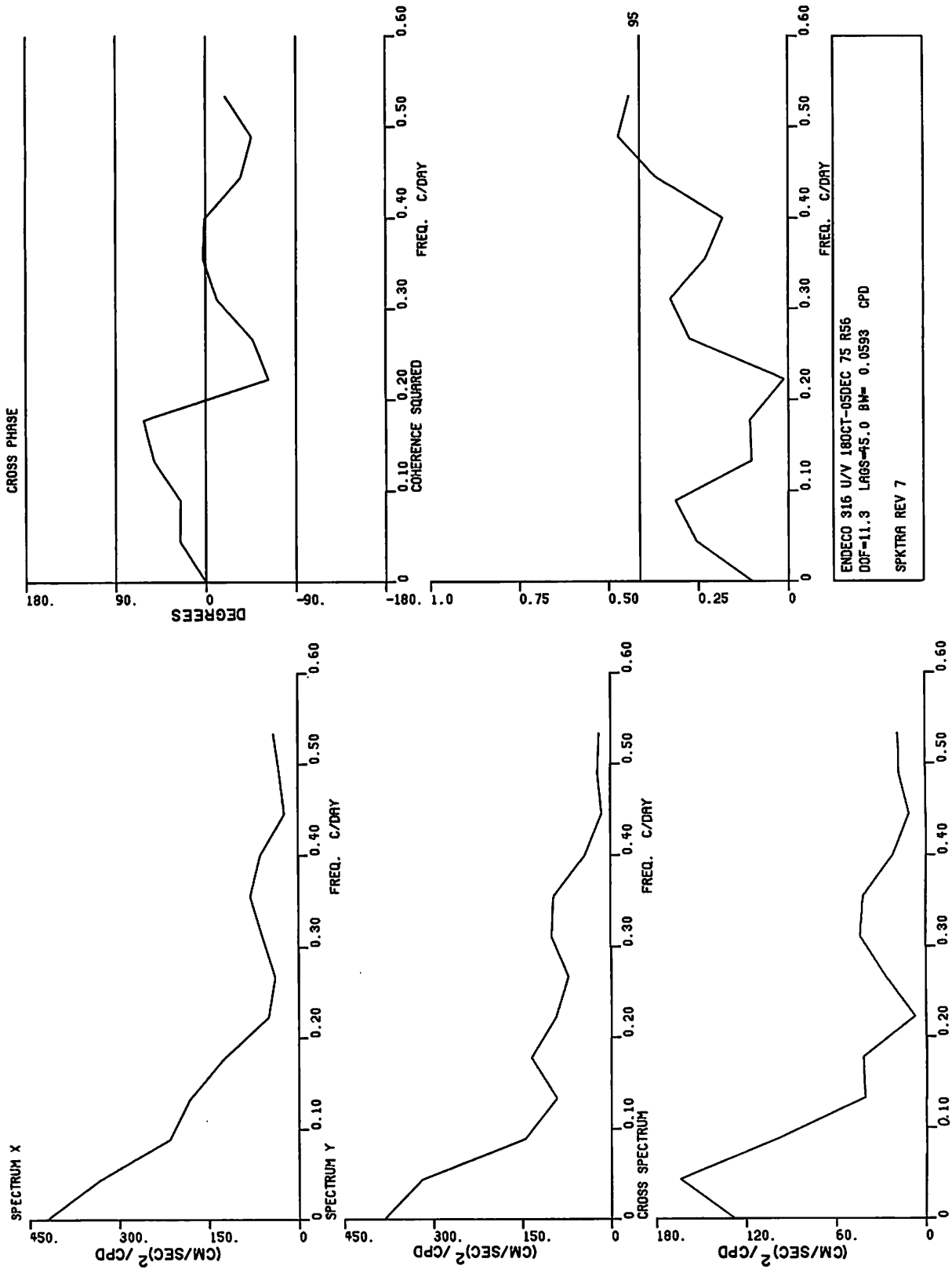

Figure 38 Spectra of low pass current velocity components from meter $A2_{top}$

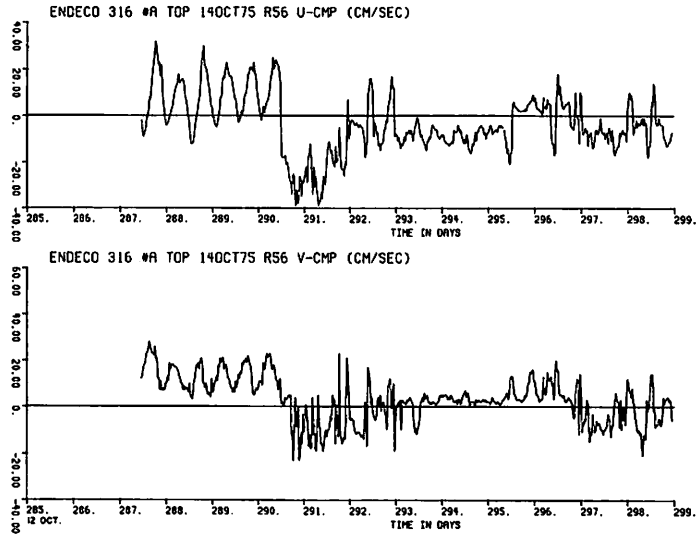

Figure 39a

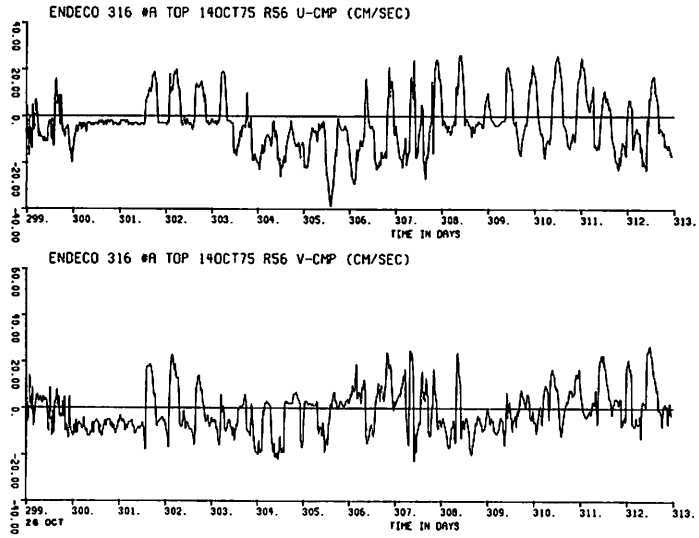

Figure 39b

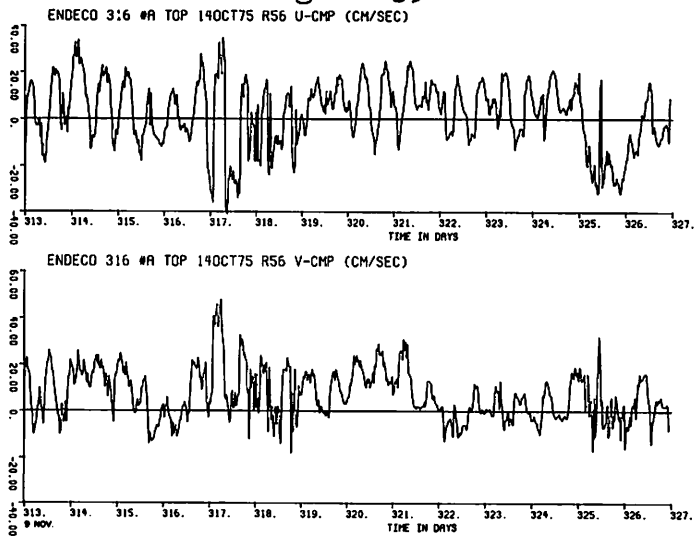

Figure 39c

Figure 39 Unfiltered current velocity components (a,b,c,d,e) from meter $A2_{top}$

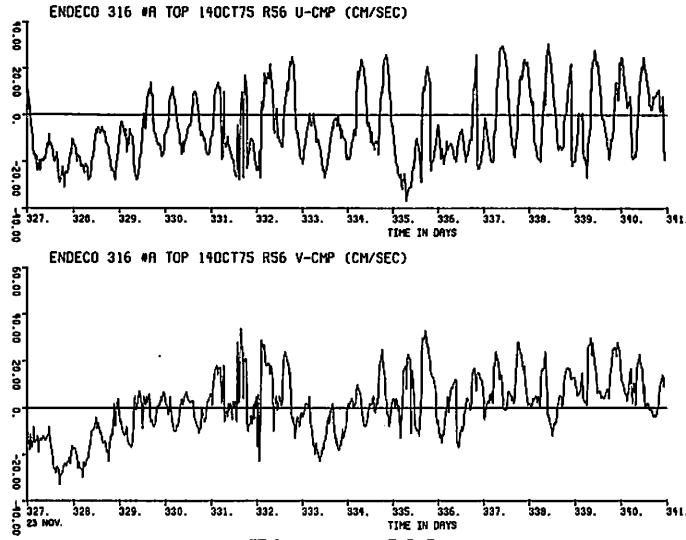

Figure 39d

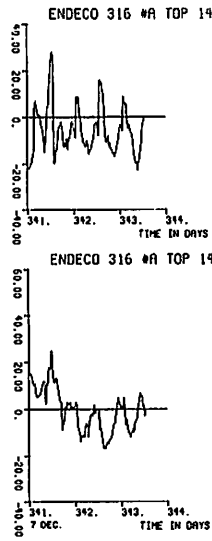

Figure 39e

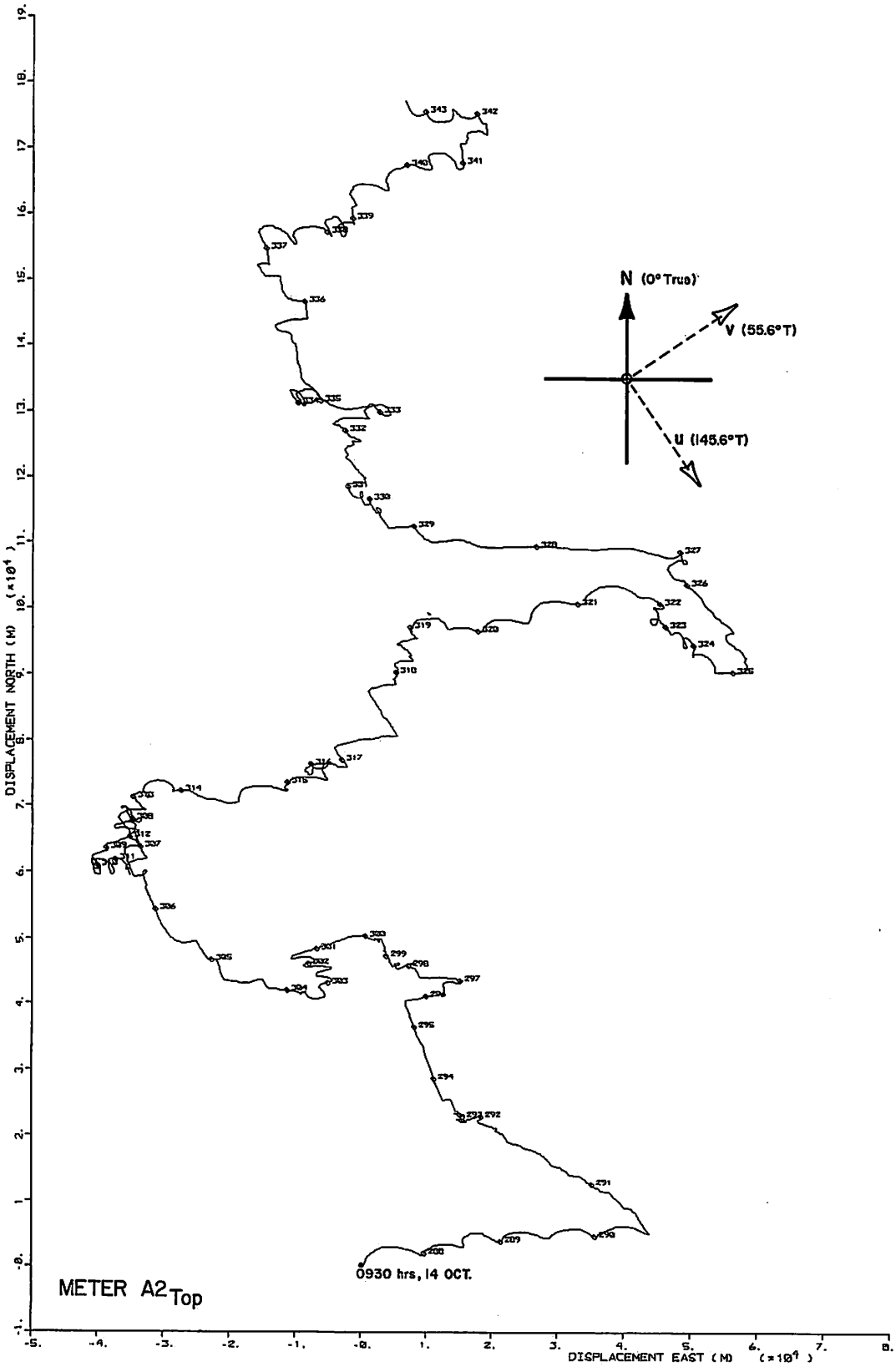

Figure 40 Progressive vector diagram of unfiltered current velocity from meter $A2_{top}$

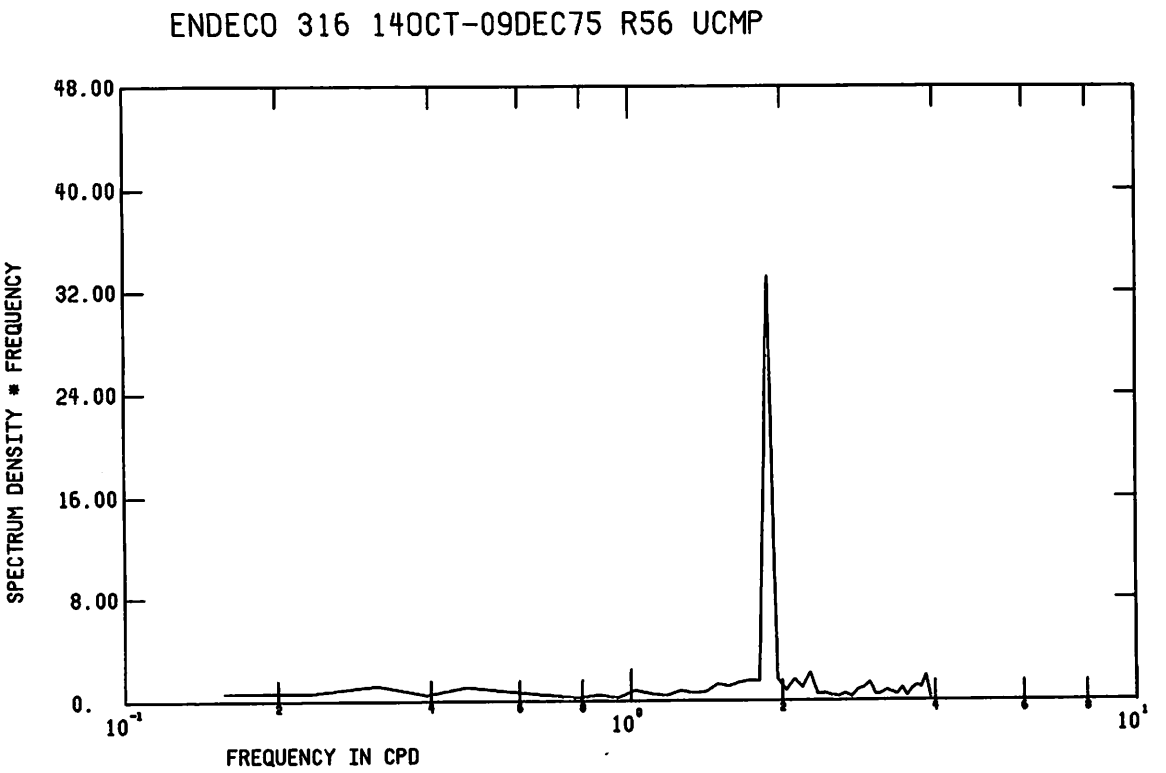

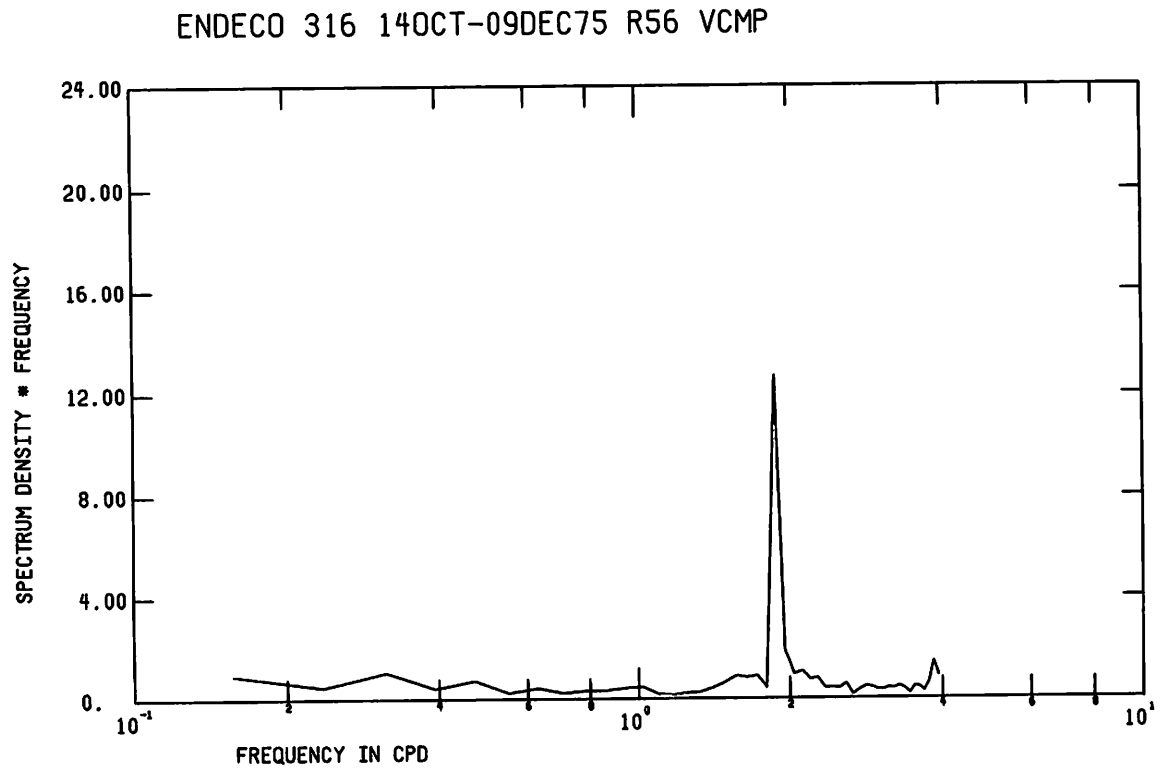

Figure 41 FFT of unfiltered current velocity components from meter $A2_{top}$

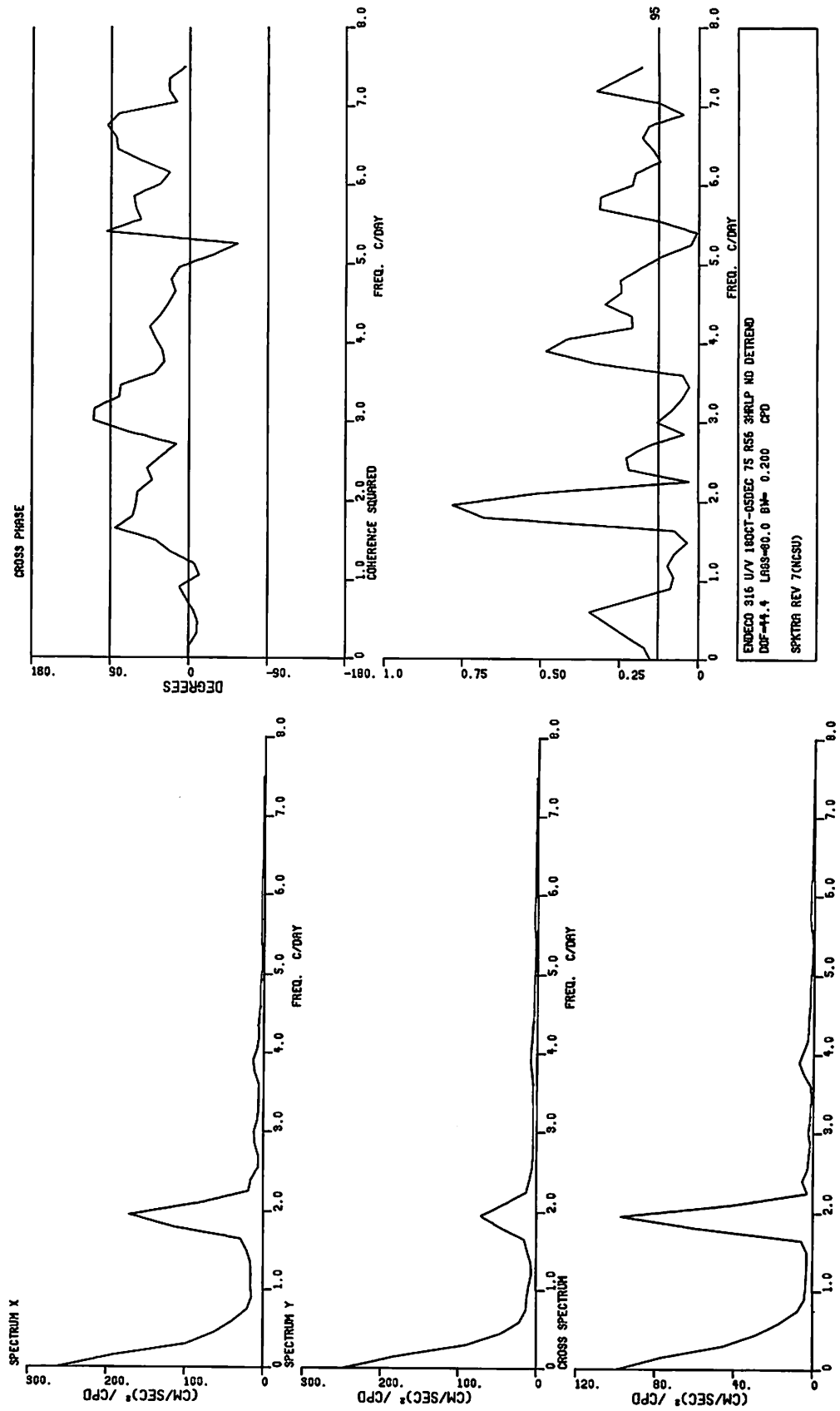

Figure 42 Spectra of 3HRLP current velocity components from meter $A2_{top}$

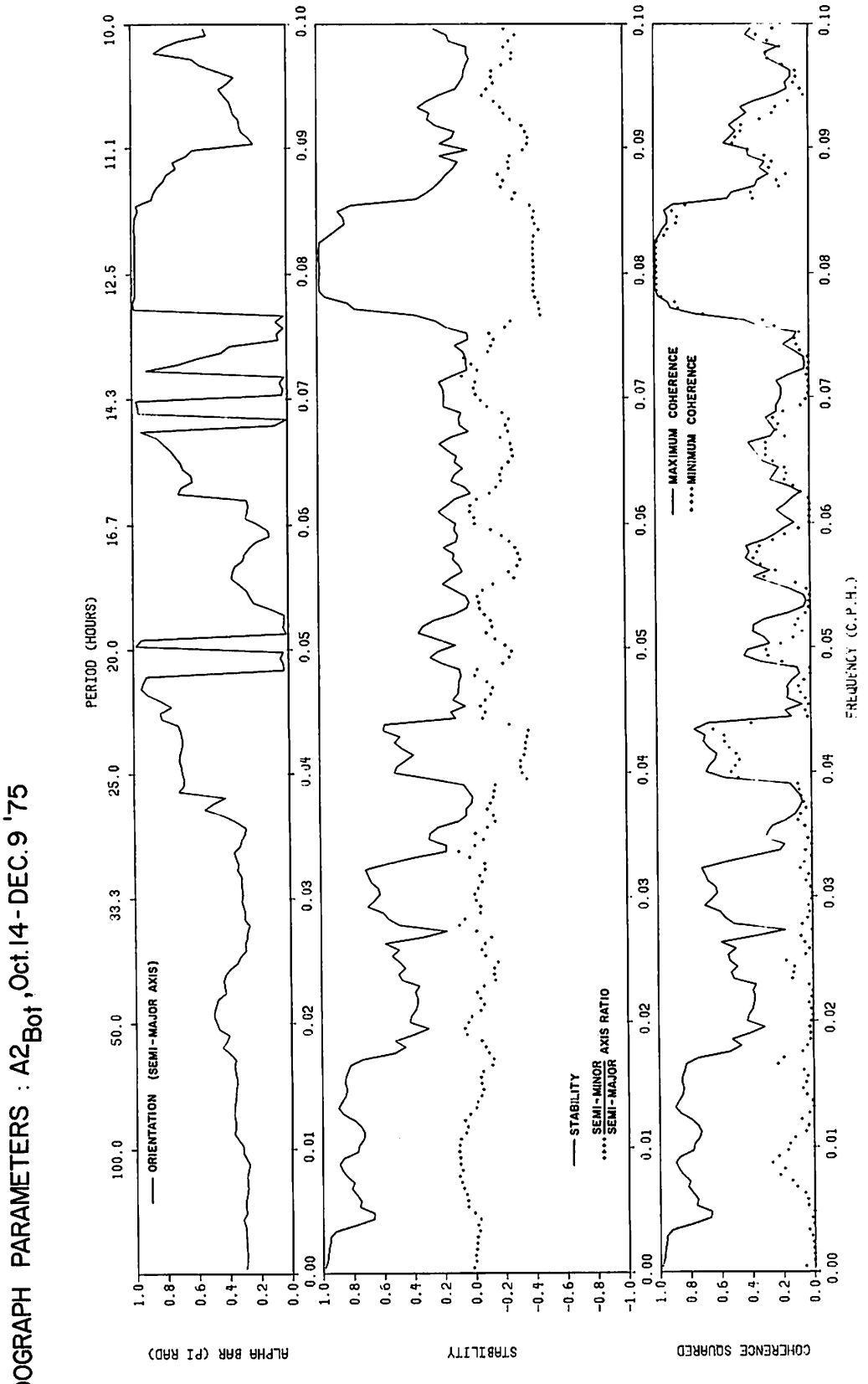

Figure 43 Hodograph parameters of 3HRLP current velocity from meter $A2_{top}$

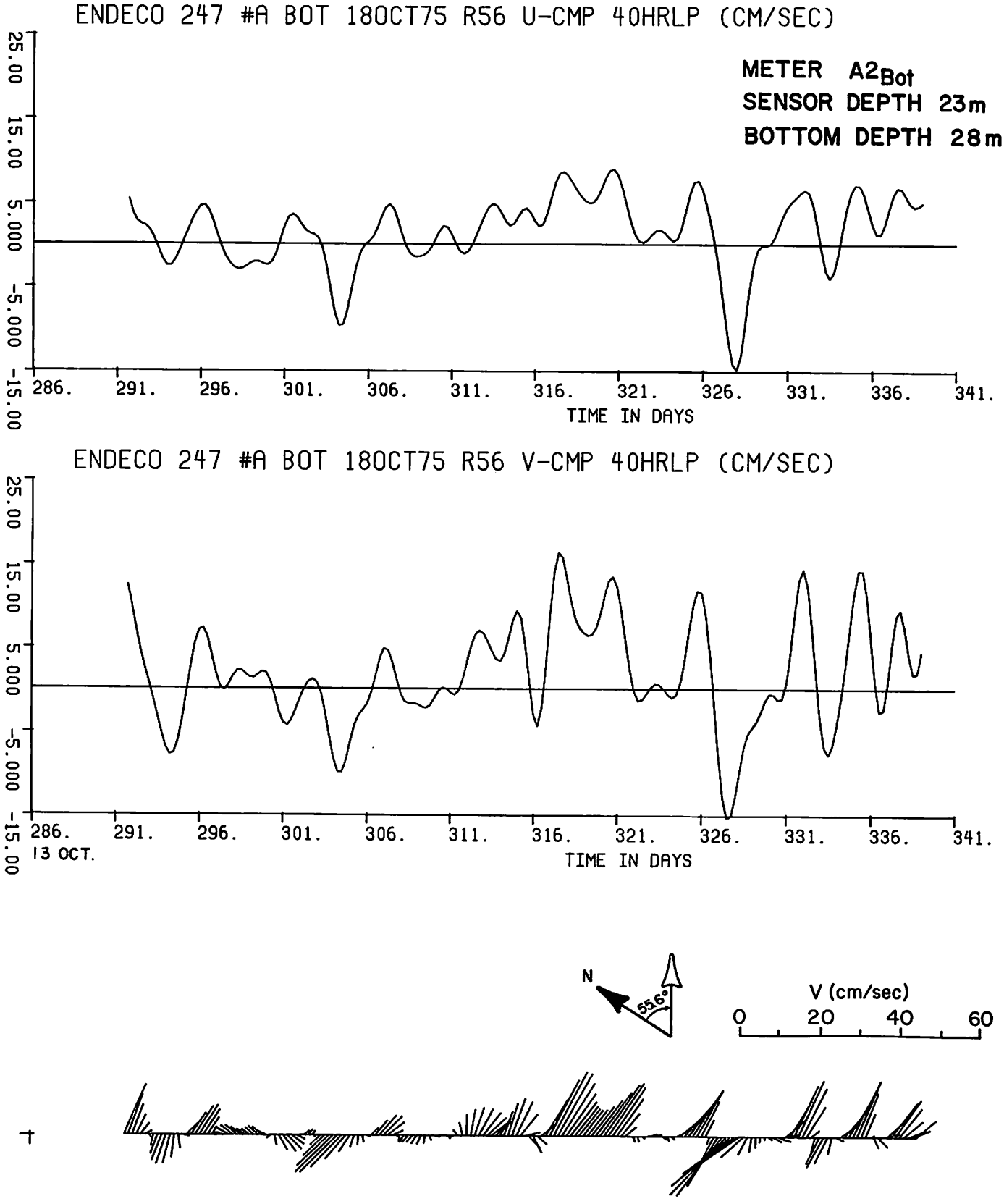

Figure 44 Low pass current velocity components and vectors from meter $A2_{bot}$

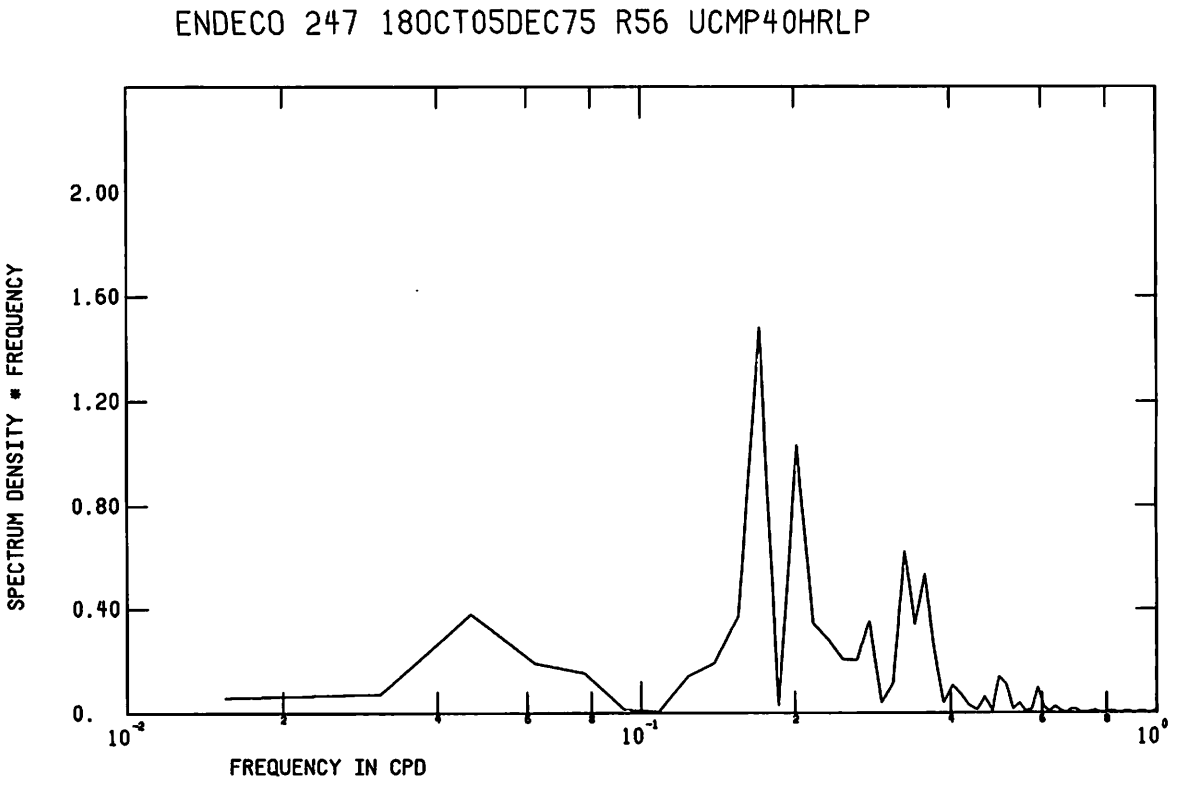

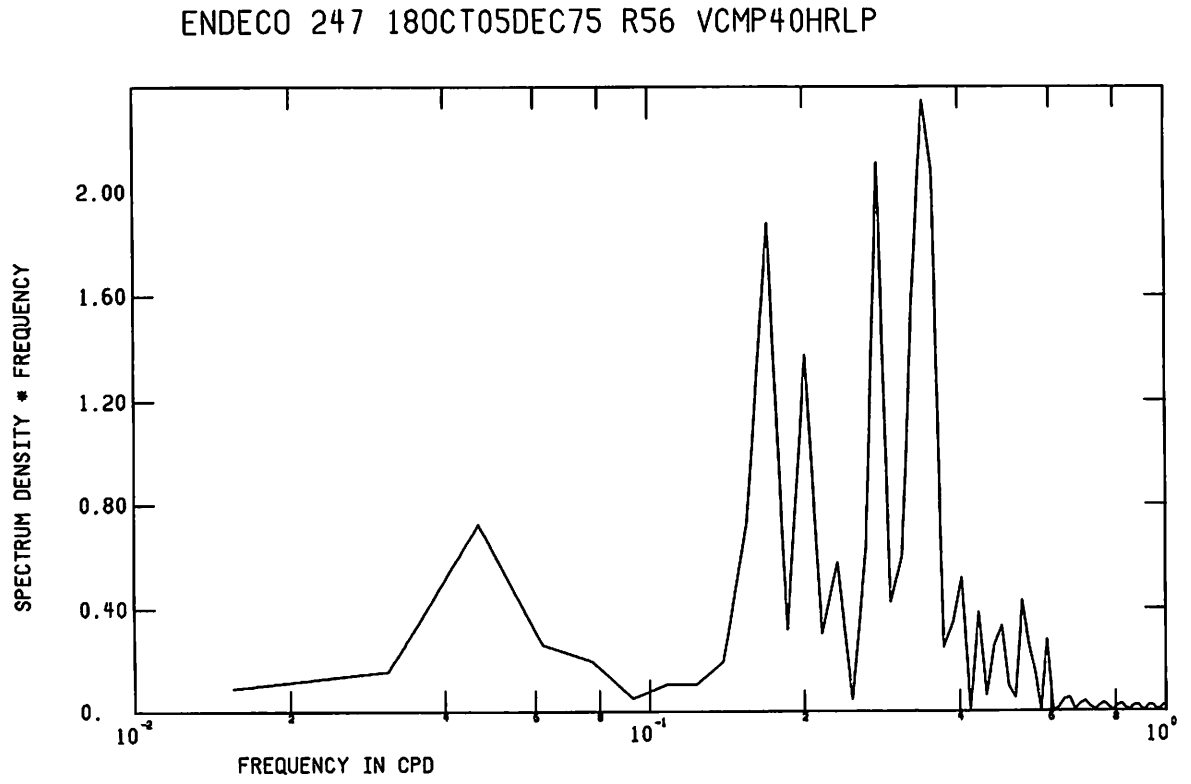

Figure 45 FFT of low pass current velocity components from meter $A2_{bot}$

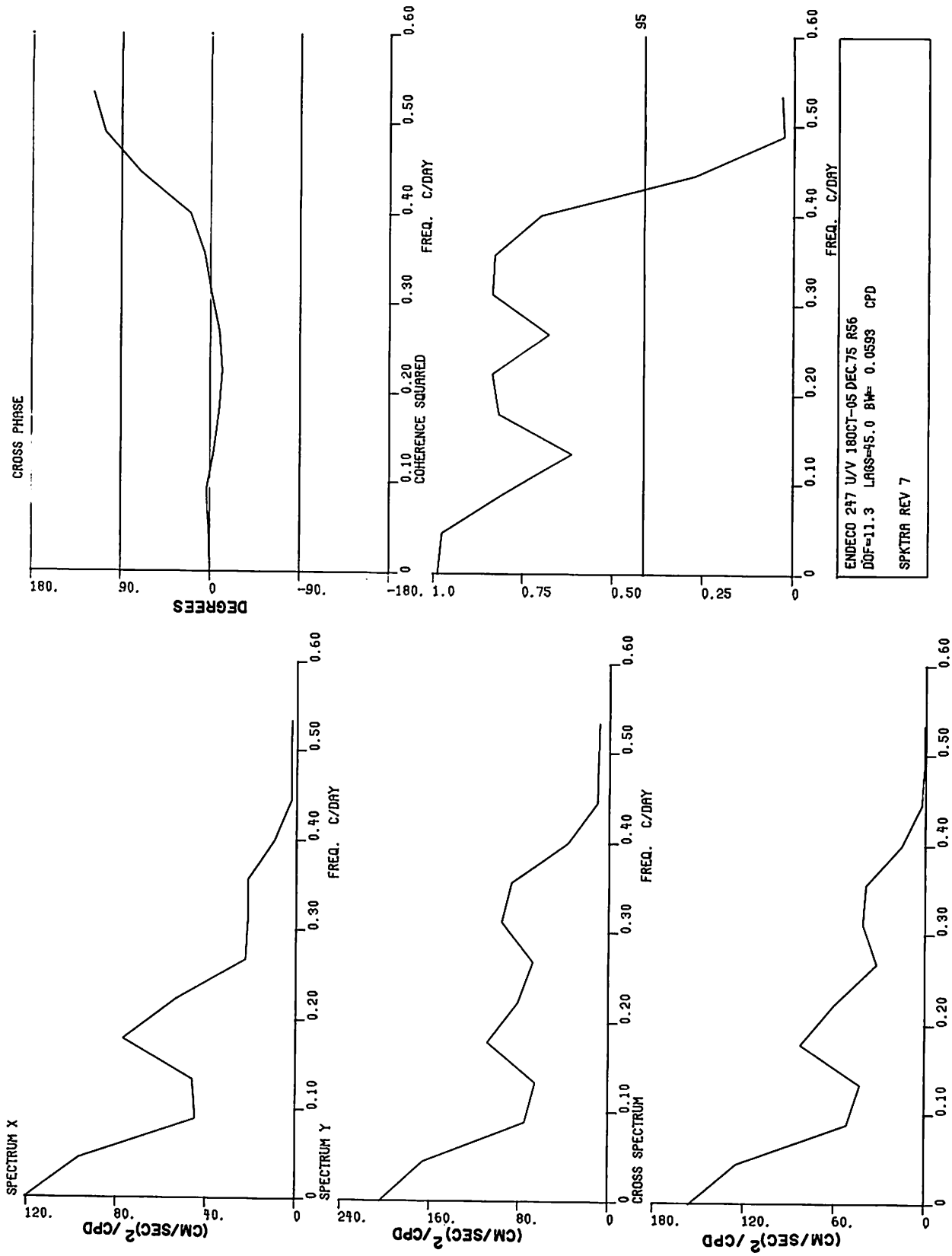

Figure 46 Spectra of low pass current velocity components from meter $A2_{bot}$

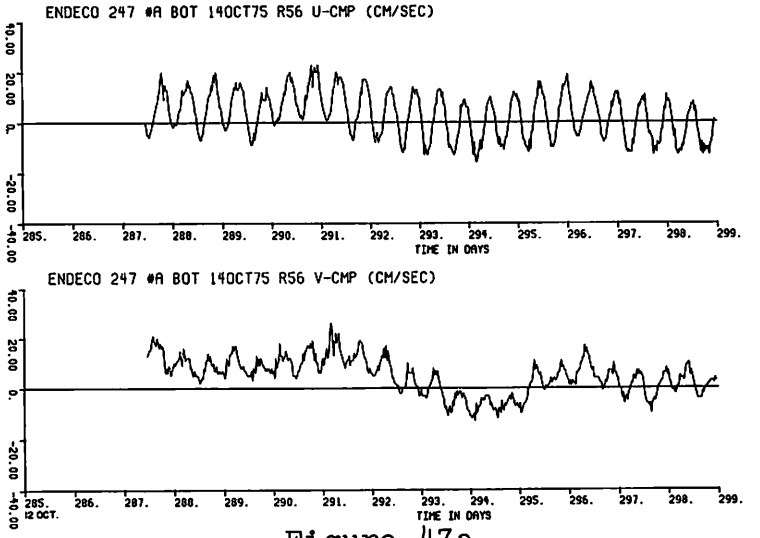

Figure 47a

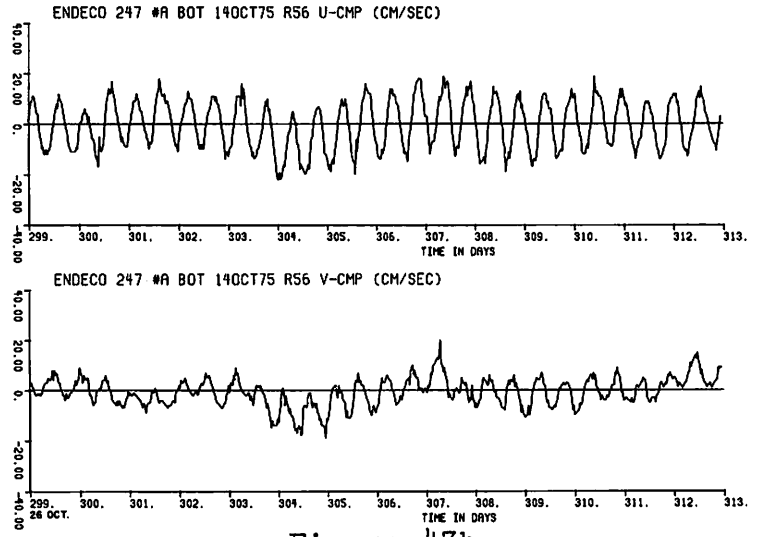

Figure 47b

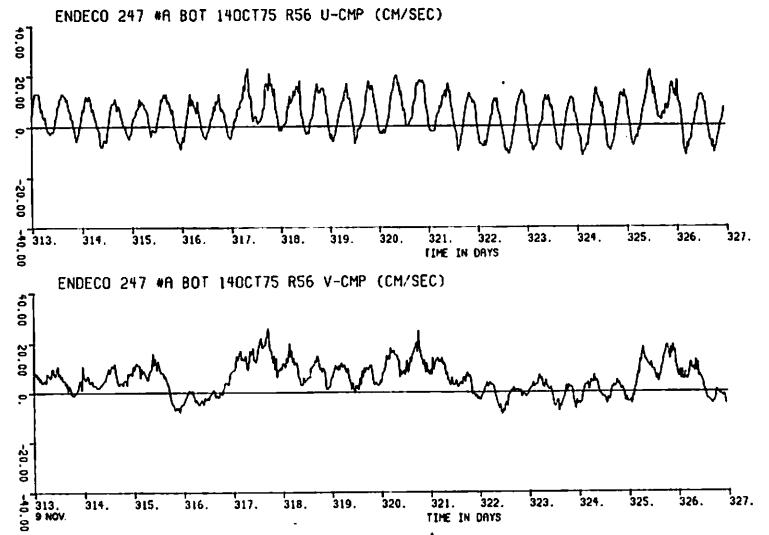

Figure 47c

Figure 47 Unfiltered current velocity components (a,b,c,d,e) from meter $A2_{bot}$

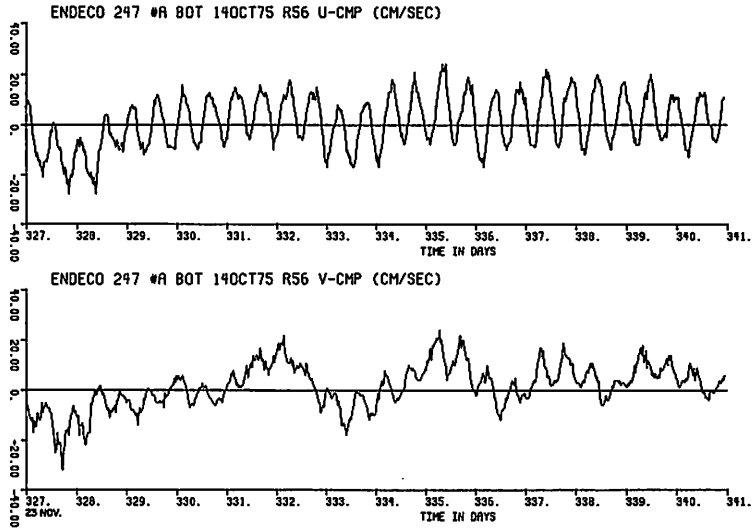

Figure 47d

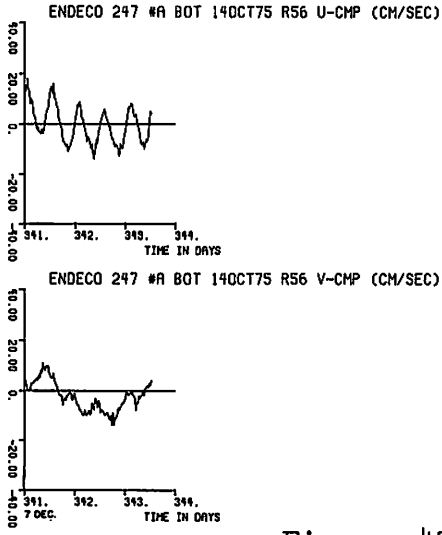

Figure 47e

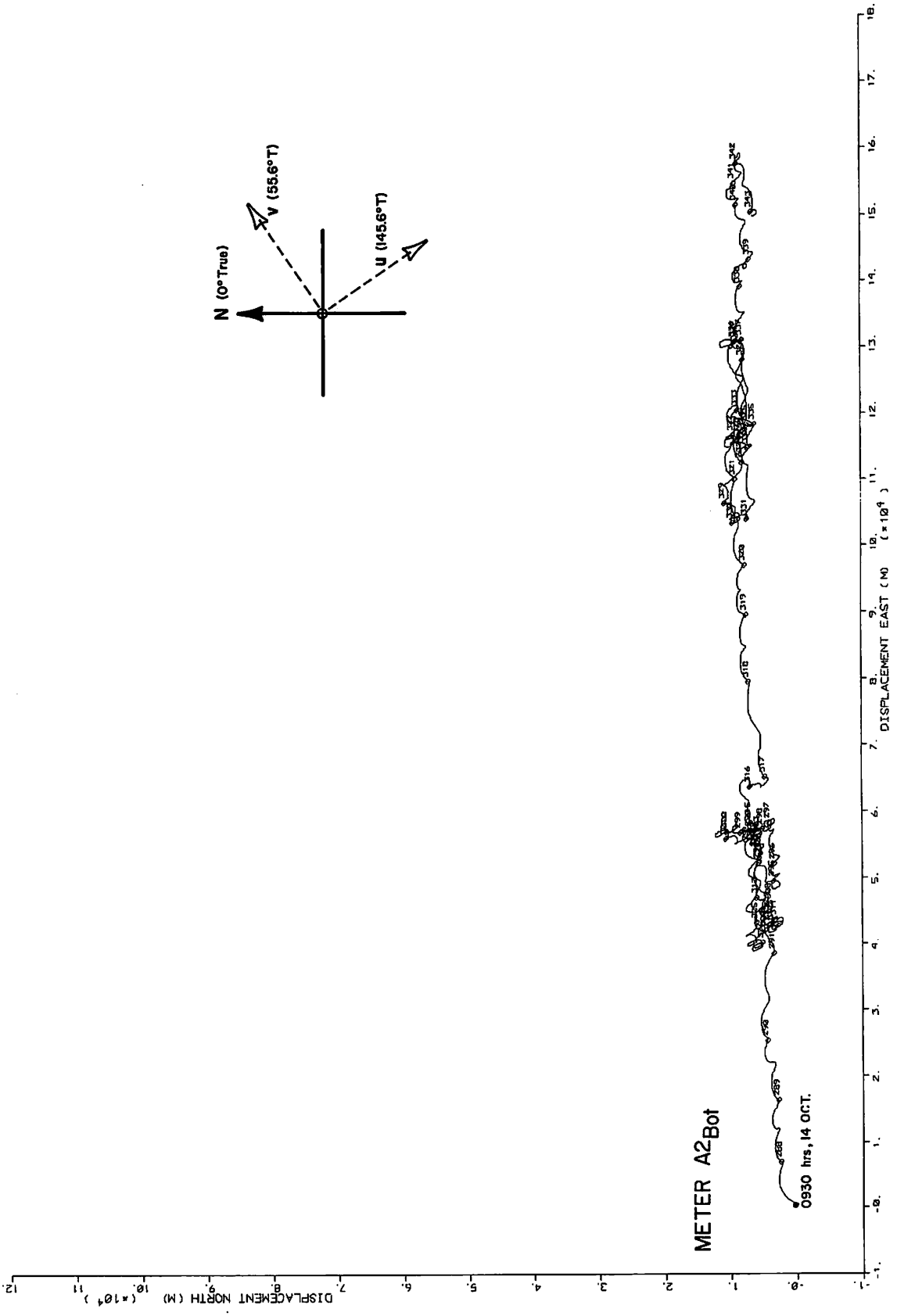

Figure 48 Progressive vector diagram of unfiltered current velocity from meter $A2_{bot}$

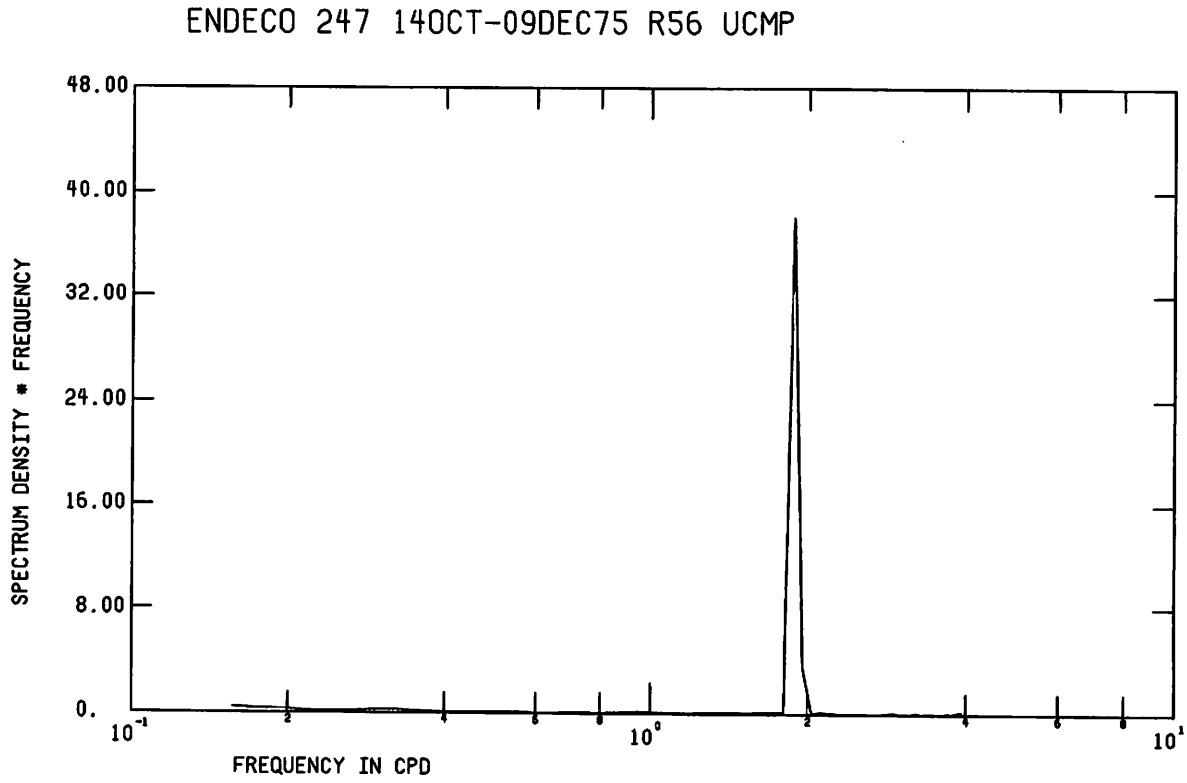

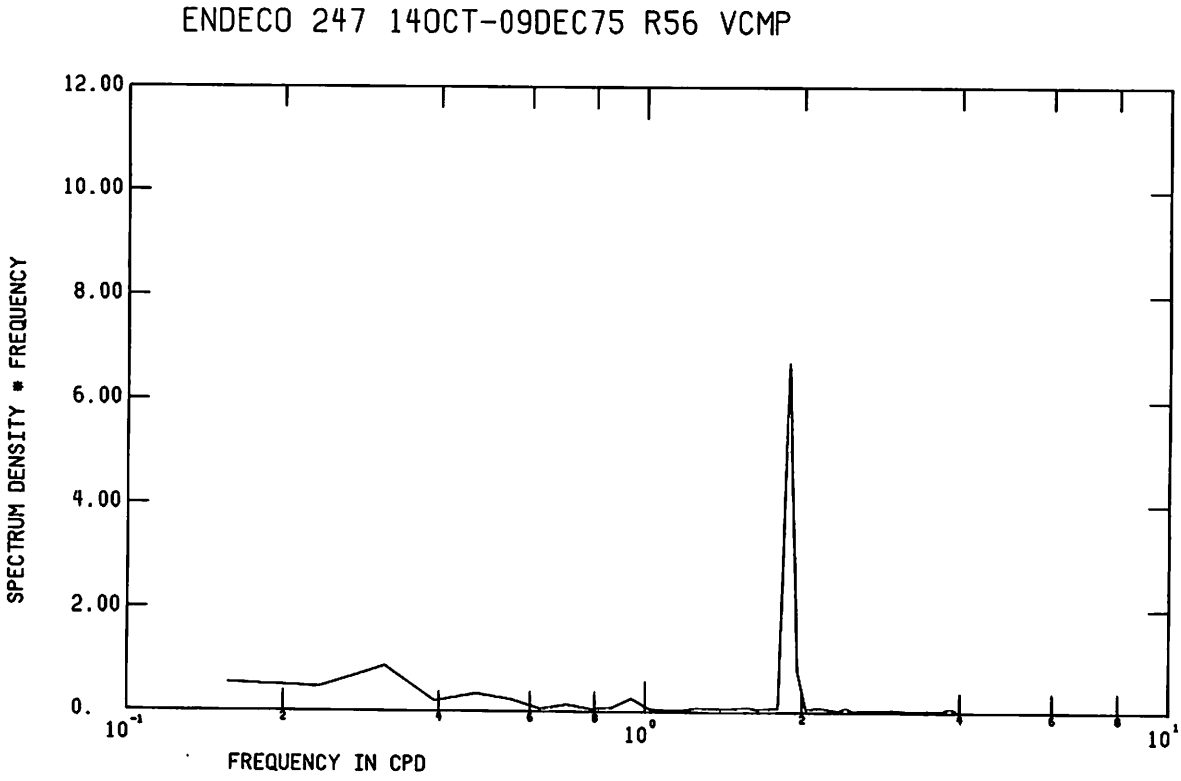

Figure 49 FFT of unfiltered current velocity components from meter $A2_{bot}$

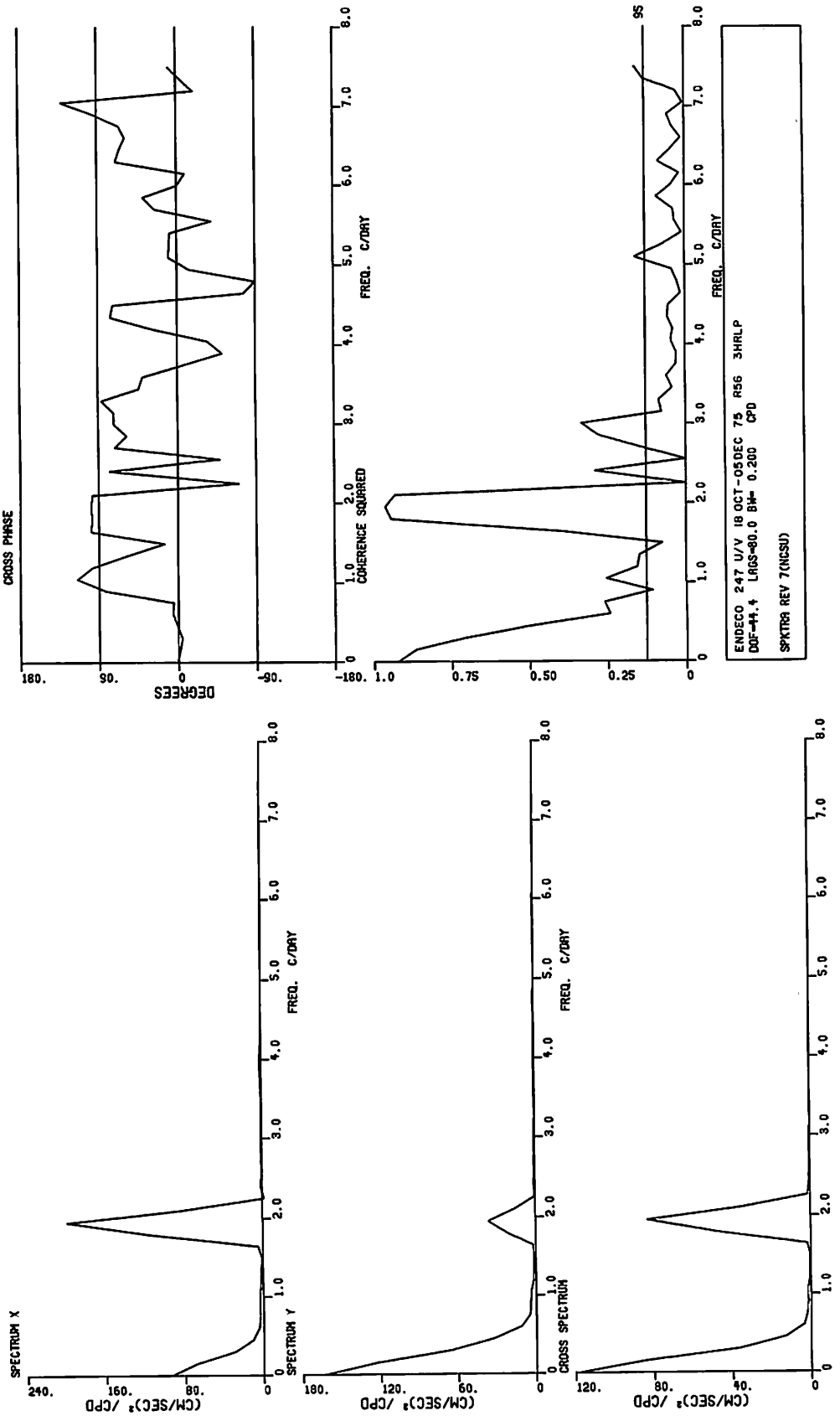

Figure 50 Spectra of 3HRLP current velocity components from meter $A2_{bot}$

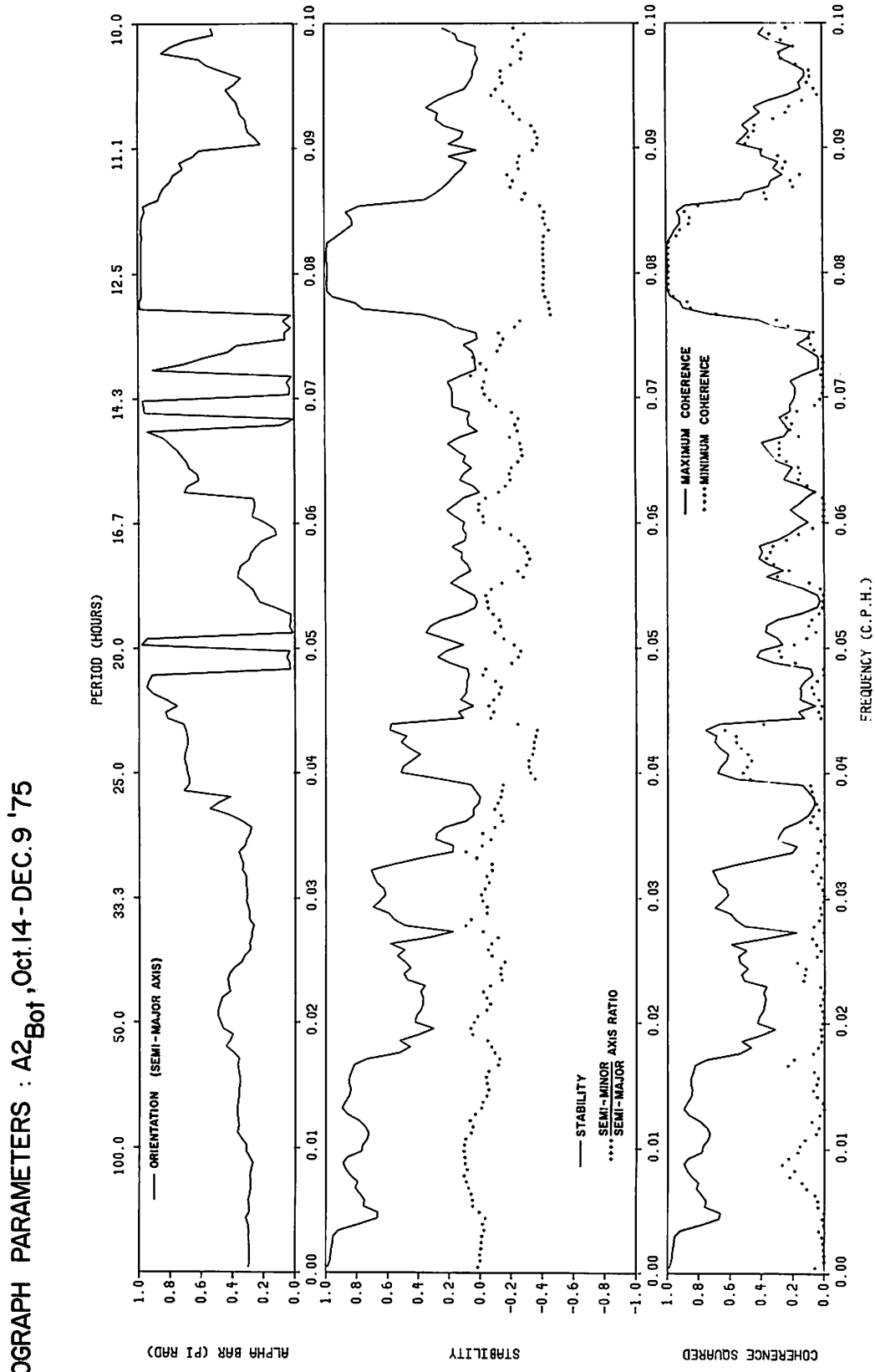

Figure 51 Hodograph parameters of 3HRLP current velocity from meter $A2_{bot}$

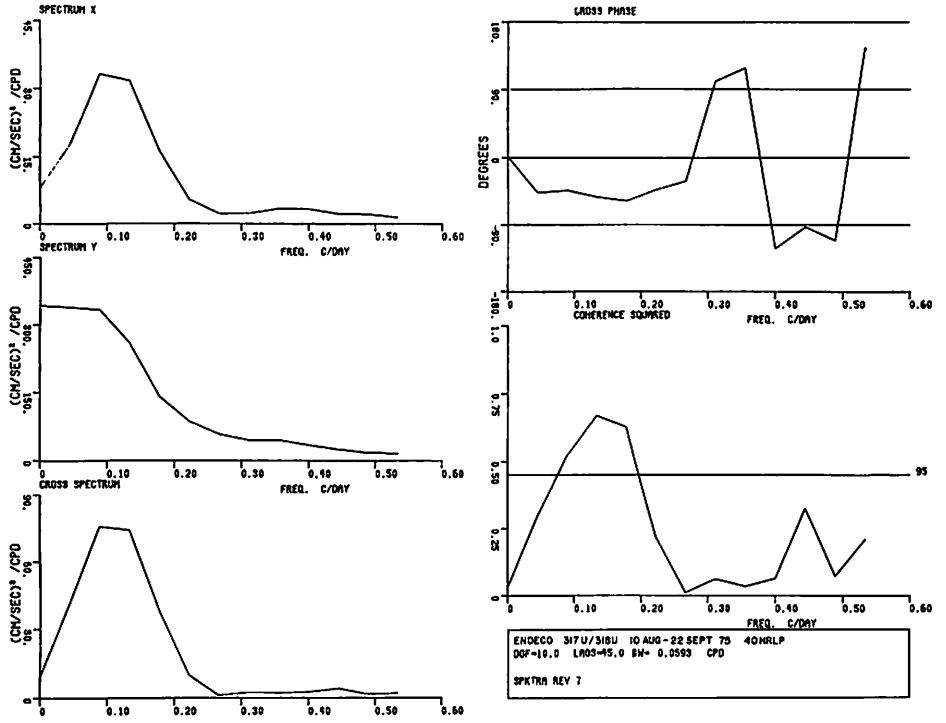

Figure 52 Spectra of low pass current velocity components from meter Al_{bot} (u component) and meter Al_{top} (u component)

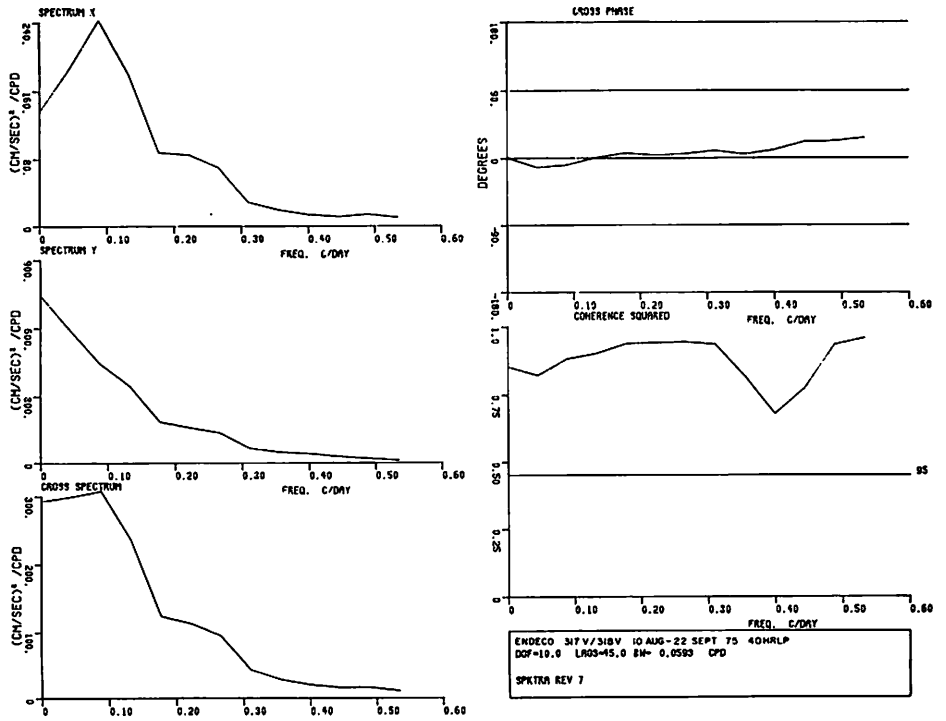

Figure 53 Spectra of low pass current velocity components from meter Al_{bot} (v component) and meter Al_{top} (v component)

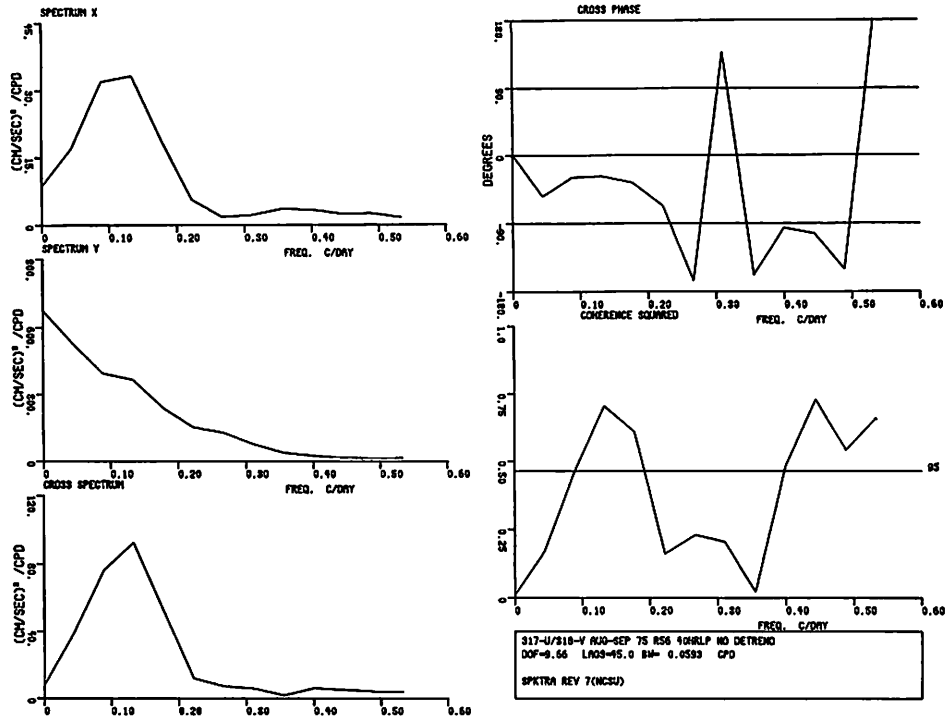

Figure 54 Spectra of low pass current velocity components from meter Al_{bot} (u component) and meter Al_{top} (v component)

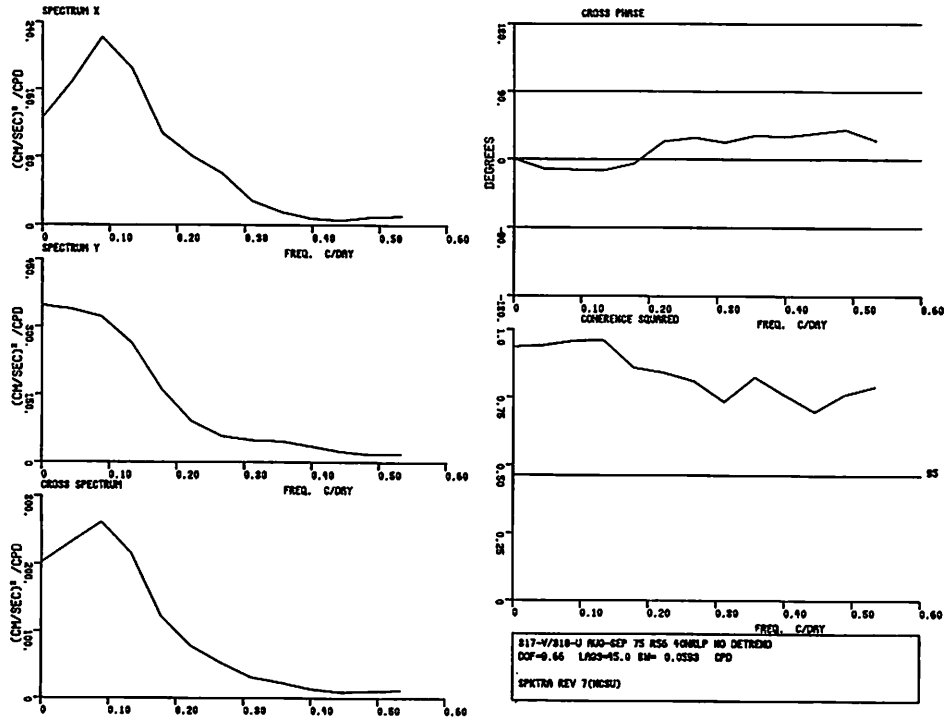

Figure 55 Spectra of low pass current velocity components from meter Al_{bot} (v component) and meter Al_{top} (u component)

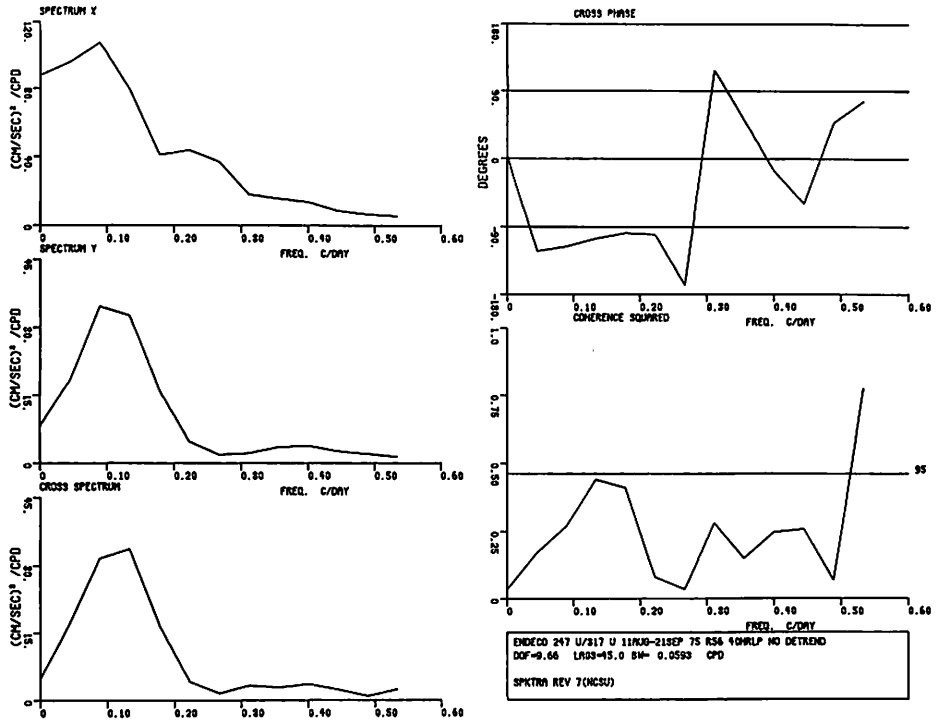

Figure 56 Spectra of low pass current velocity components from meter Bl_{bot} (u component) and meter Al_{bot} (u component)

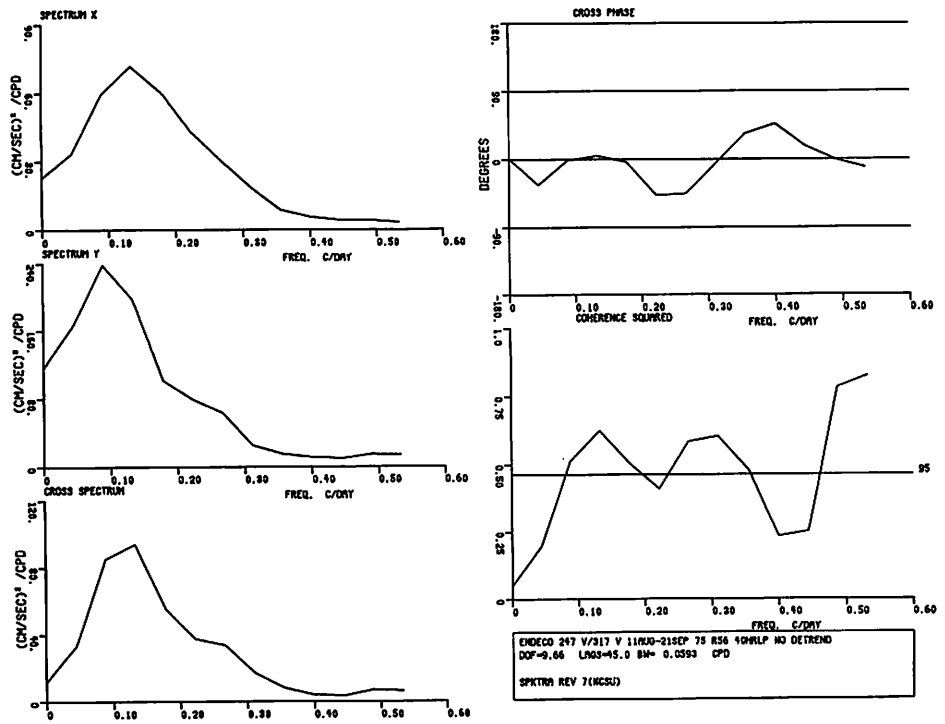

Figure 57 Spectra of low pass current velocity components from meter Bl_{bot} (v component) and meter Al_{bot} (v component)

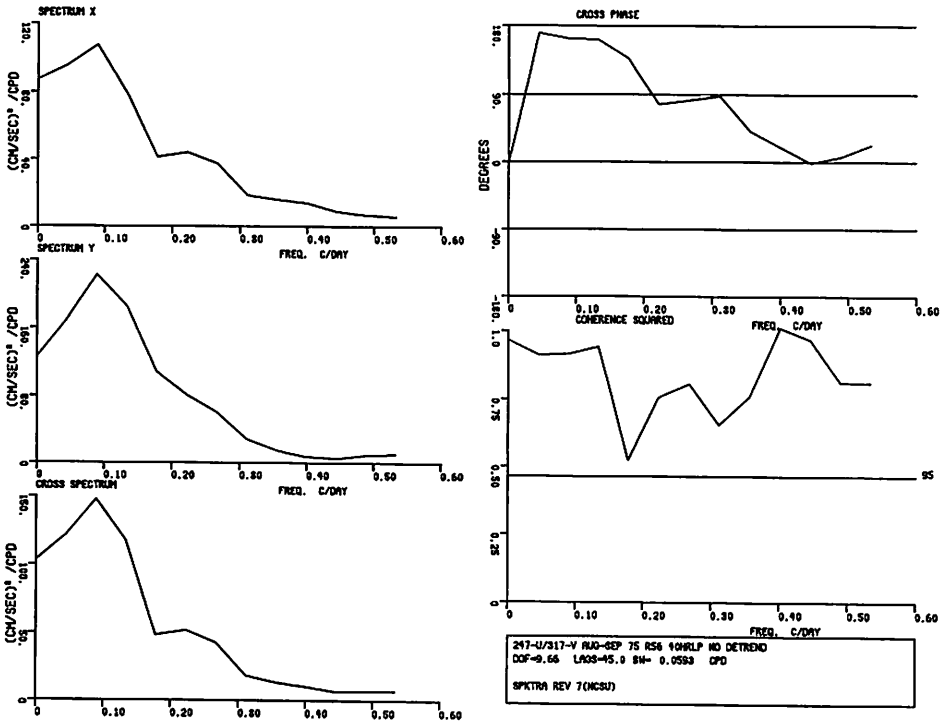

Figure 58 Spectra of low pass current velocity components from meter Bl_{bot} (u component) and meter Al_{bot} (v component)

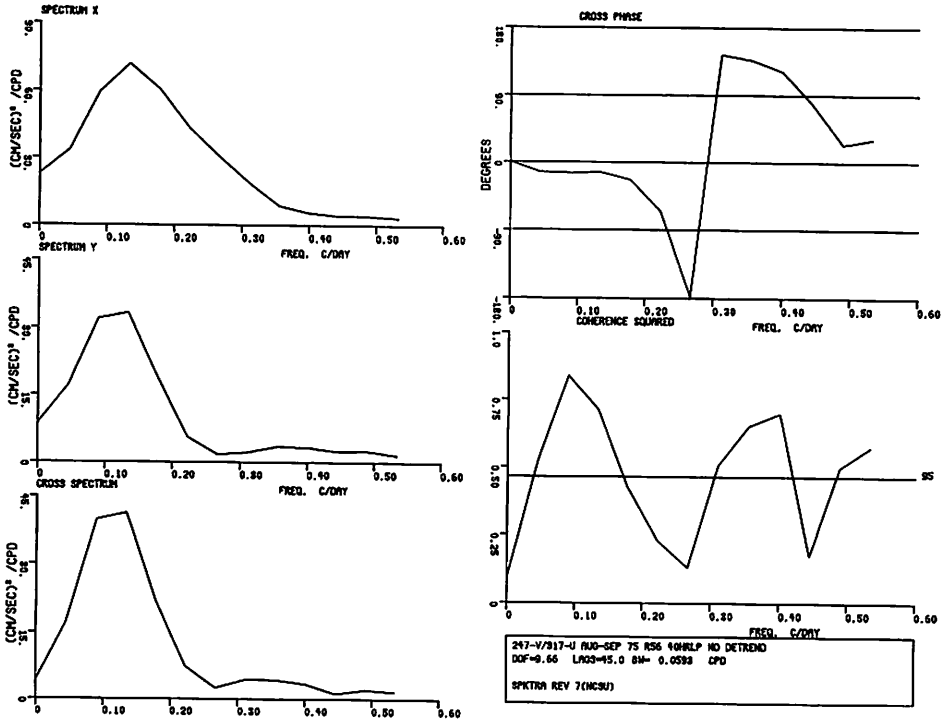

Figure 59 Spectra of low pass current velocity components from meter Bl_{bot} (v component) and meter Al_{bot} (u component)

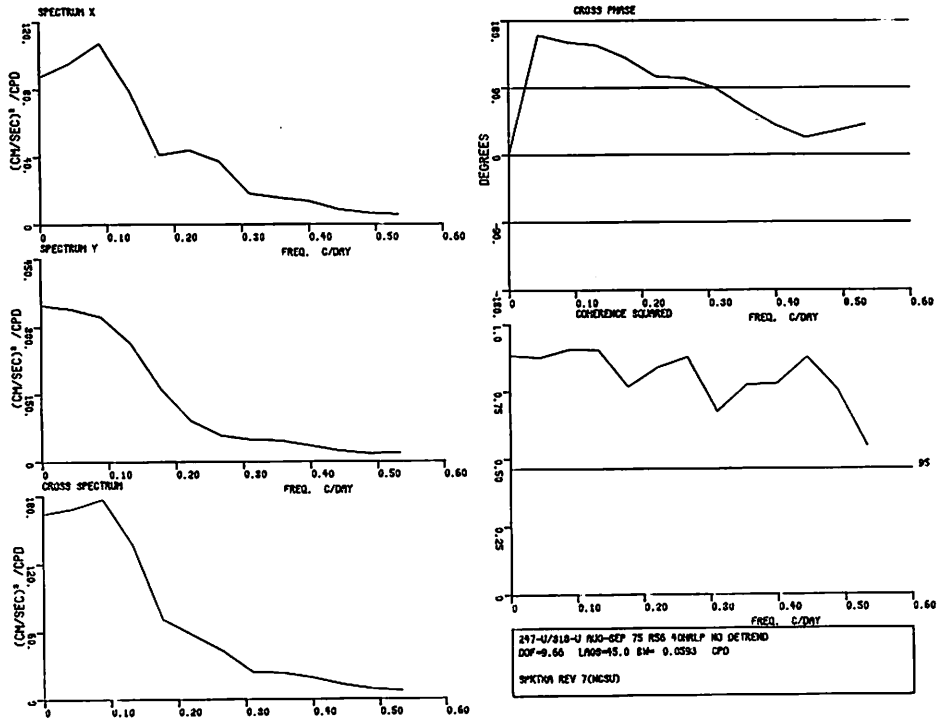

Figure 60 Spectra of low pass current velocity components from meter Bl_{bot} (u component) and meter Al_{top} (u component)

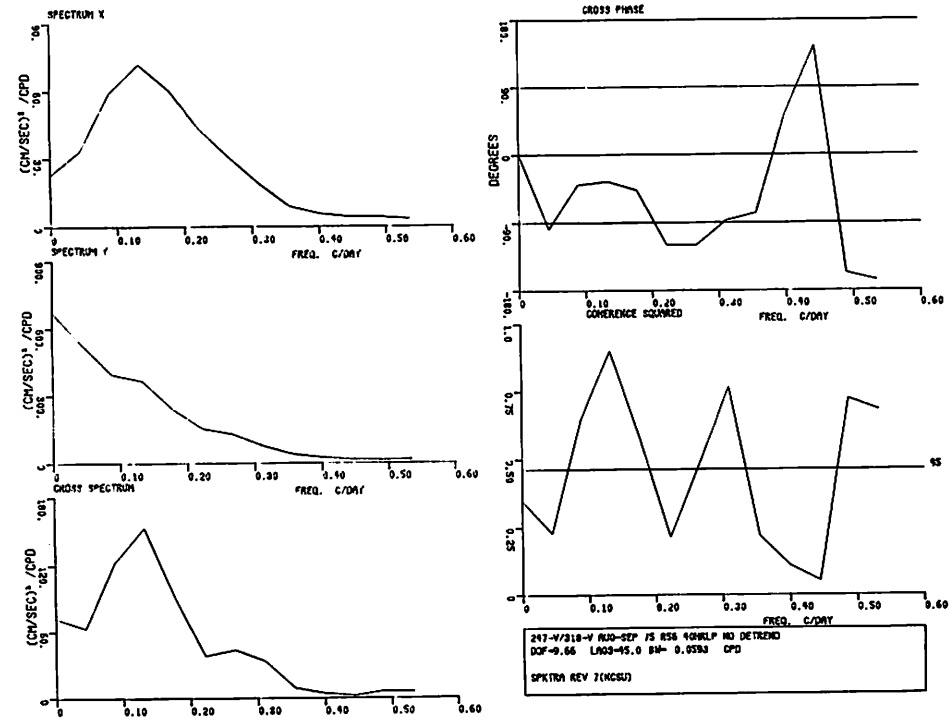

Figure 61 Spectra of low pass current velocity components from meter Bl_{bot} (v component and meter Al_{top} (v component)

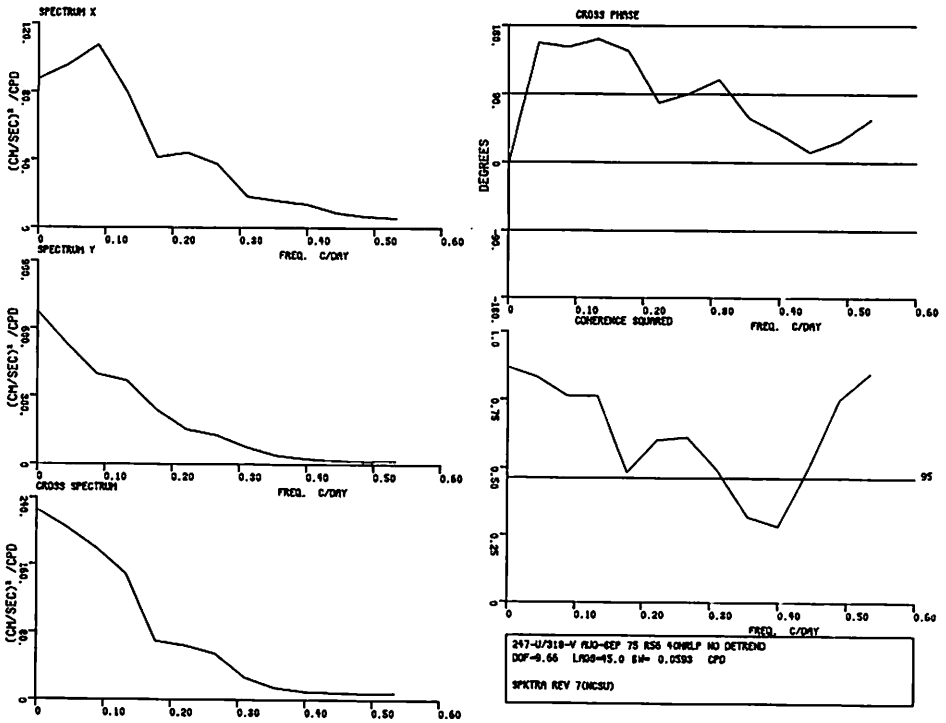

Figure 62 Spectra of low pass current velocity components from meter Bl_{bot} (u component) and meter Al_{top} (v component)

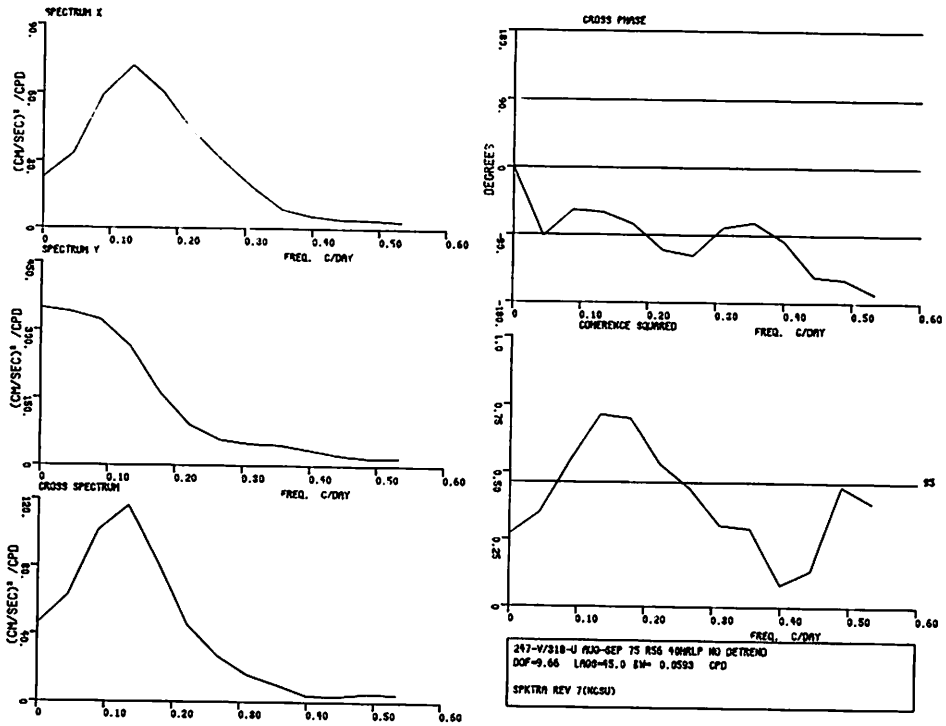

Figure 63 Spectra of low pass current velocity components from meter Bl_{bot} (v component) and meter Al_{top} (u component)

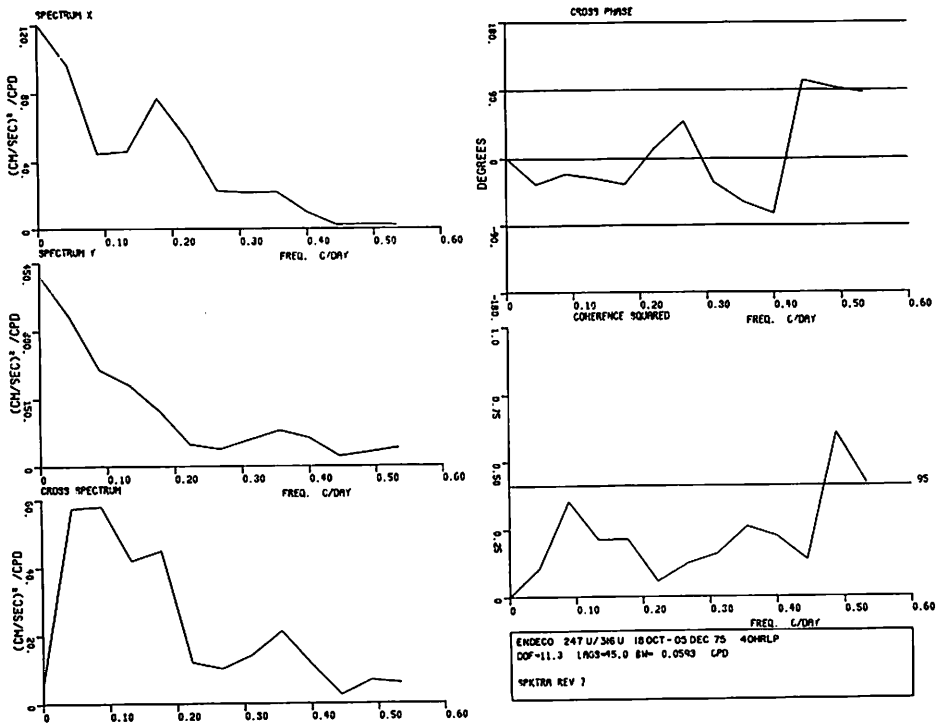

Figure 64 Spectra of low pass current velocity components from meter $A2_{bot}$ (u component) and meter $A2_{top}$ (u component)

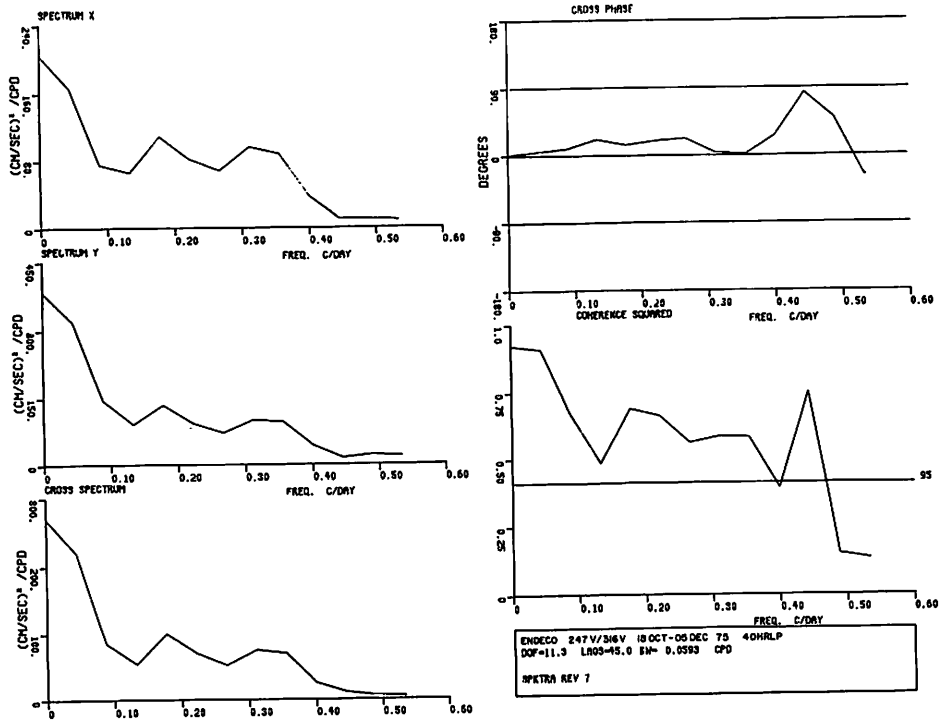

Figure 65 Spectra of low pass current velocity components from meter $A2_{bot}$ (v component) and meter $A2_{top}$ (v component)

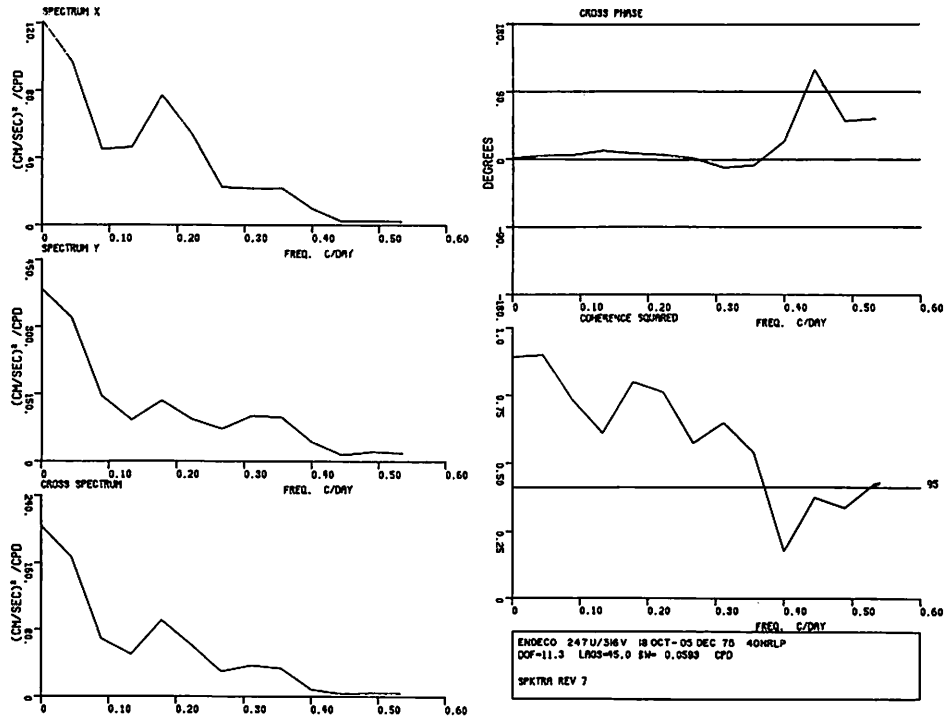

Figure 66 Spectra of low pass current velocity components from meter $A2_{bot}$ (u component) meter $A2_{top}$ (v component)

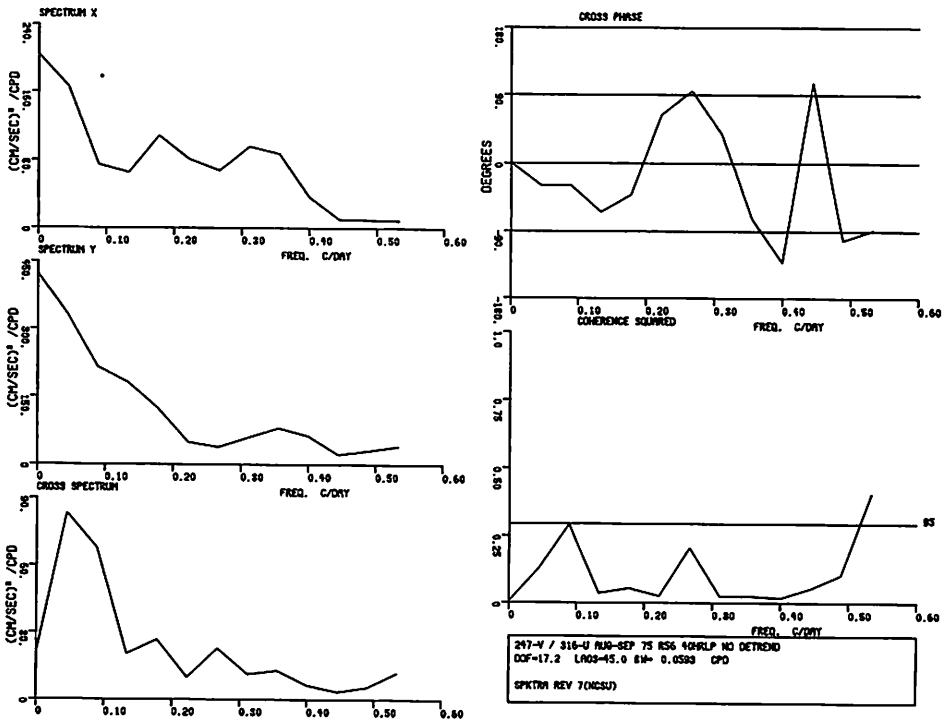

Figure 67 Spectra of low pass current velocity components from meter $A2_{bot}$ (v component) meter $A2_{top}$ (u component)

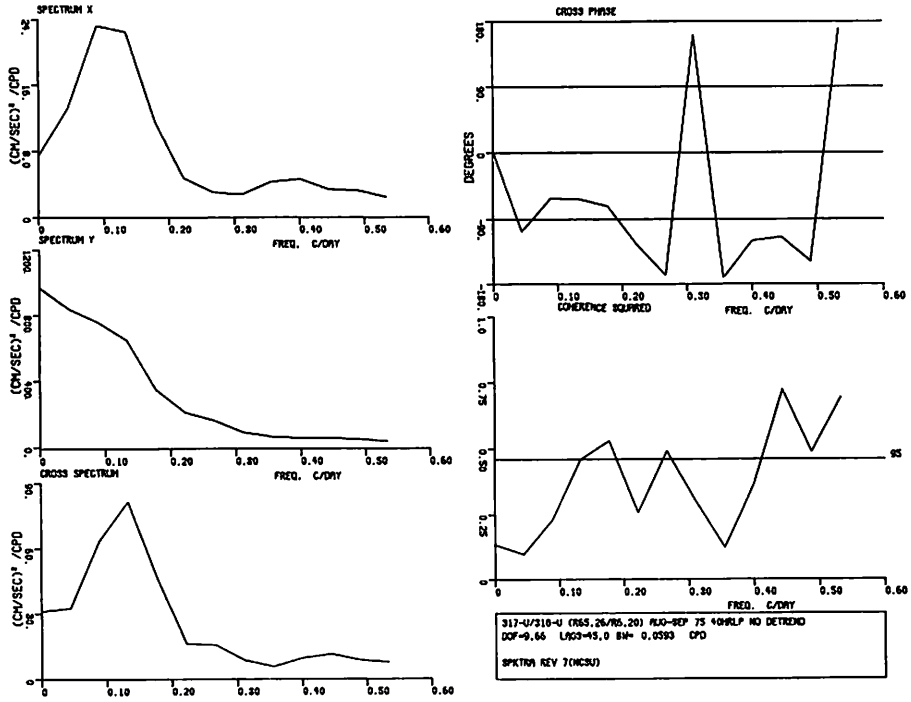

Figure 68 Spectra of low pass current velocity components from meter Al_{bot} (u component, Principal Axis = 65.26°) and meter Al_{top} (u component, Principal Axis = 6.20°)

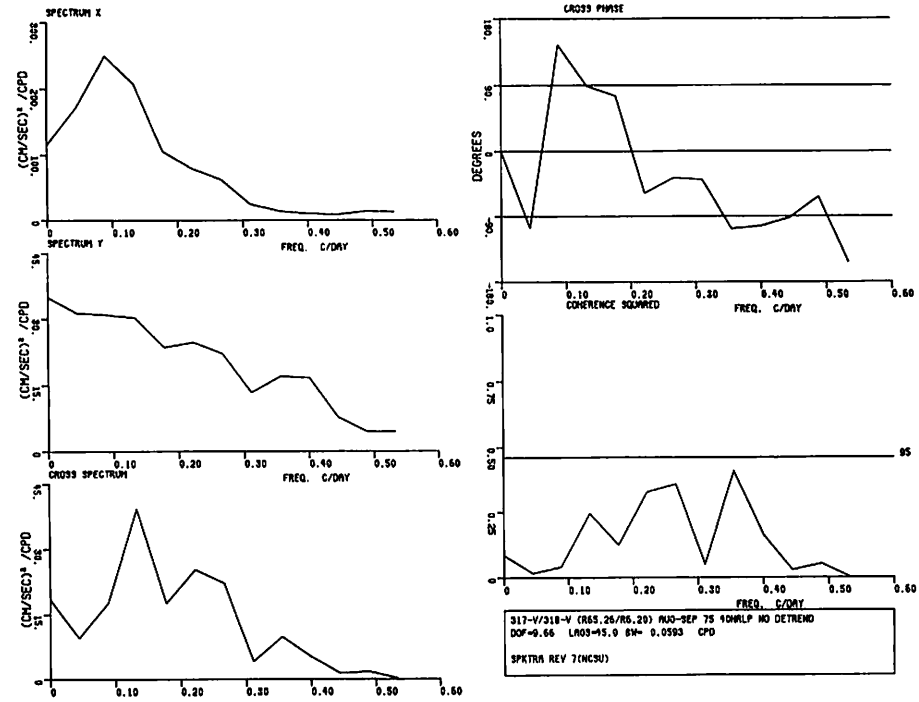

Figure 69 Apectra of low pass current velocity components from meter Al_{bot} (v component), Principal Axis = 65.26°) and meter Al_{top} (v component, Principal Axis = 6.20°)

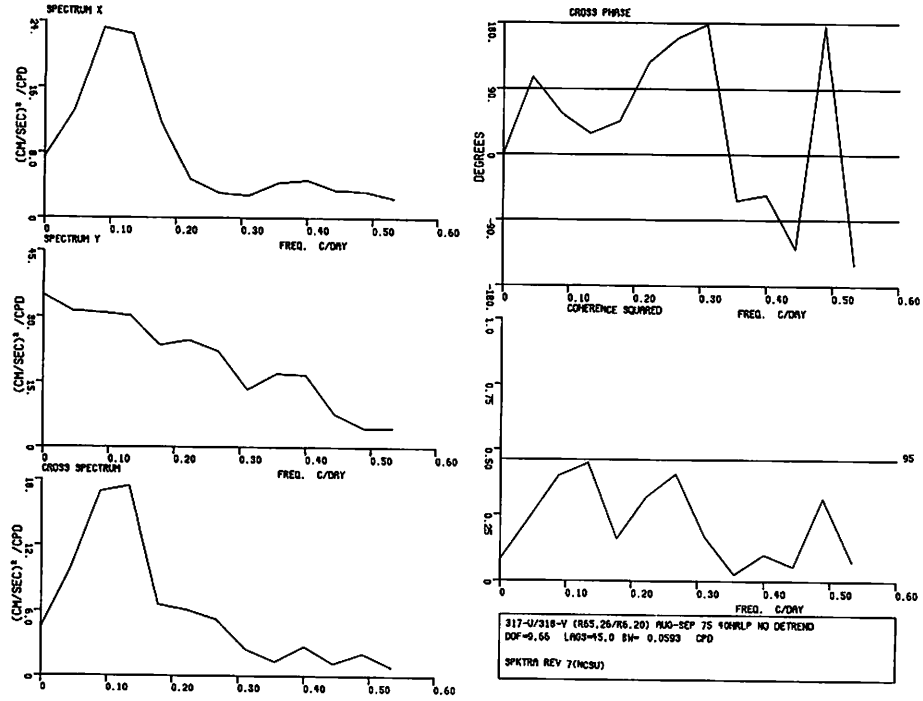

Figure 70 Spectra of low pass current velocity components from meter Al_{bot} (u component, Principal Axis = 65.26°) and meter Al_{top} (v component, Principal Axis = 6.20°)

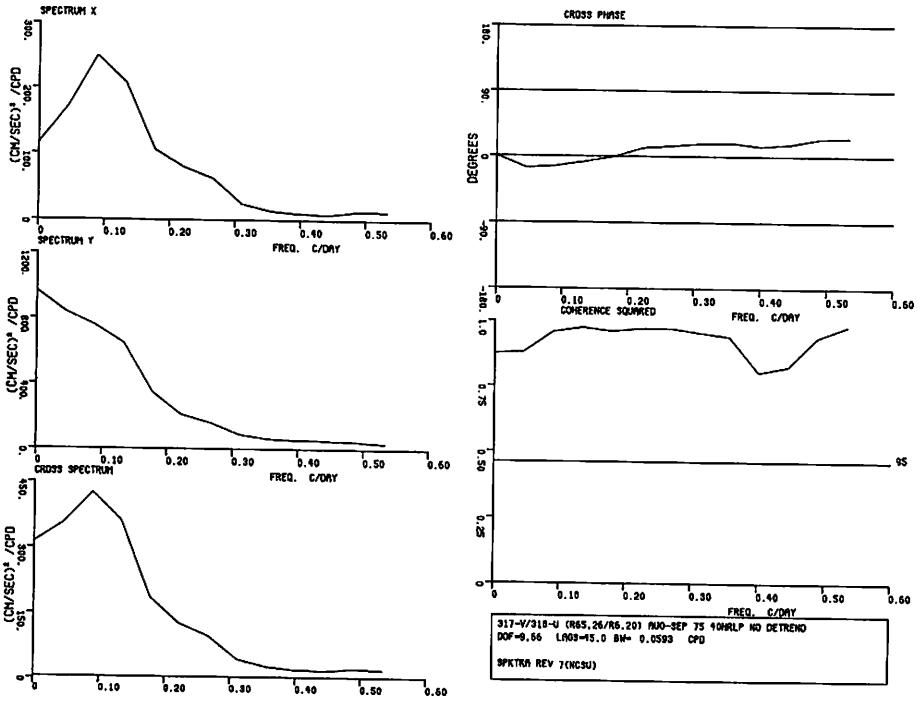

Figure 71 Spectra of low pass current velocity components from meter Al_{bot} (v component, Principal Axis = 65.26°) and meter Al_{top} (u component, Principal Axis = 6.20°)

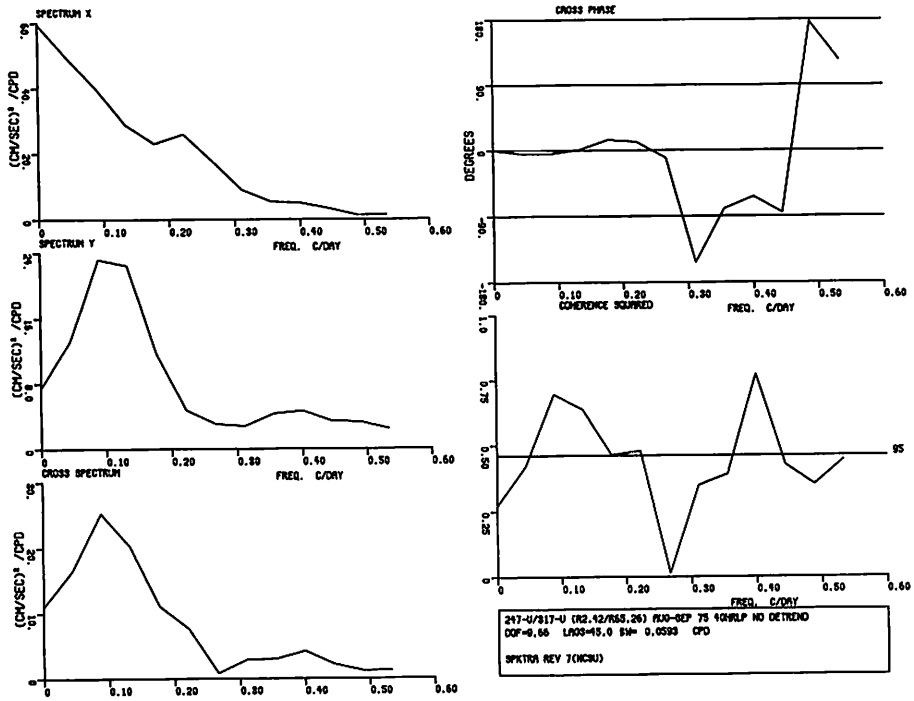

Figure 72 Spectra of low pass current velocity components from meter Bl_{bot} (u component, Principal Axis = 2.42°) and meter Al_{bot} (u component, Principal Axis = 65.26°)

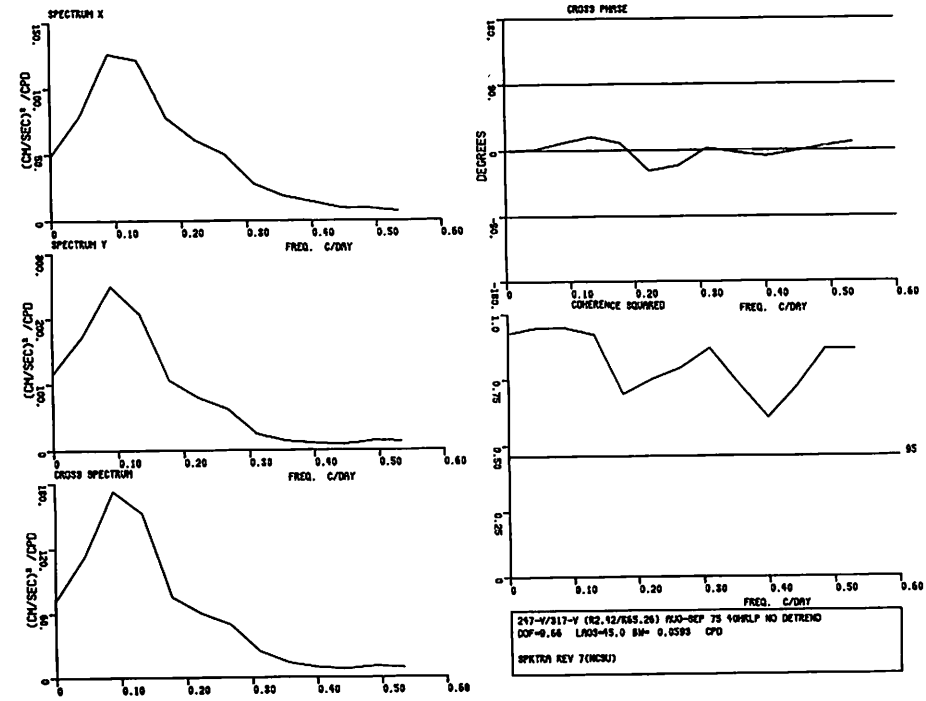

Figure 73 Spectra of low pass current velocity components from meter Bl_{bot} (v component, Principal Axis = 2.42°) and meter Al_{bot} (v component, Principal Axis = 65.26°)

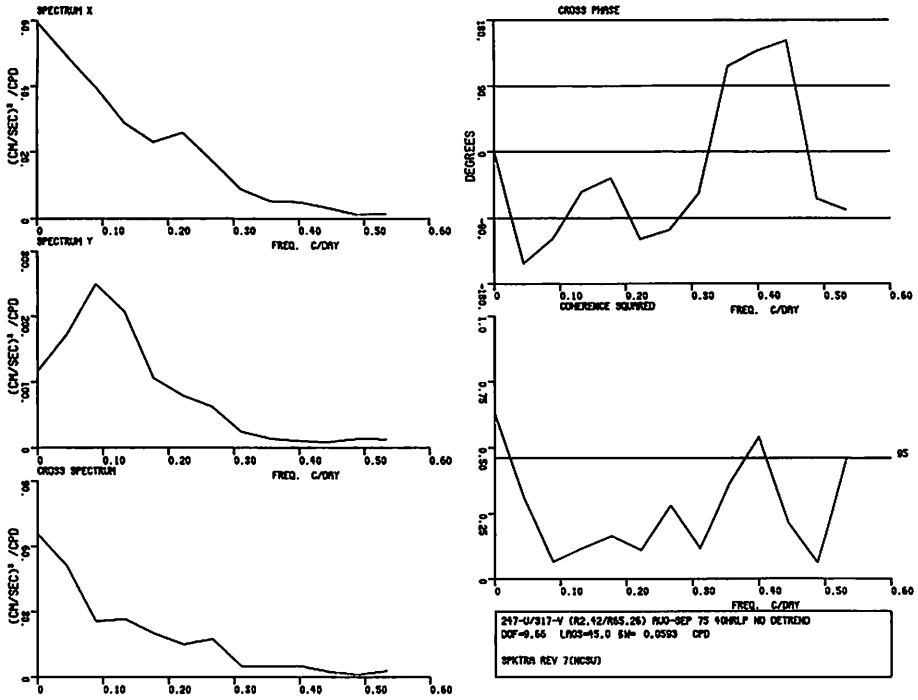

Figure 74 Spectra of low pass current velocity components from meter Bl_{bot} (u component, Principal Axis = 2.42°) and meter Al_{bot} (v component, Principal Axis = 65.26°)

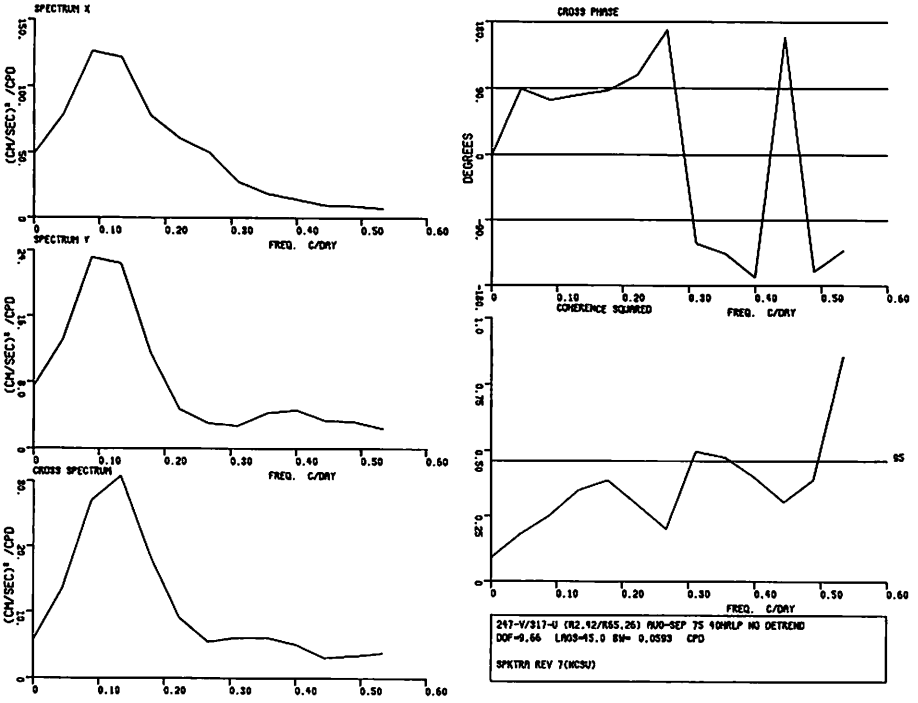

Figure 75 Spectra of low pass current velocity components from meter Bl_{bot} (v component, Principal Axis = 2.42°) and meter Al_{bot} (u component, Principal Axis = 65.26°)

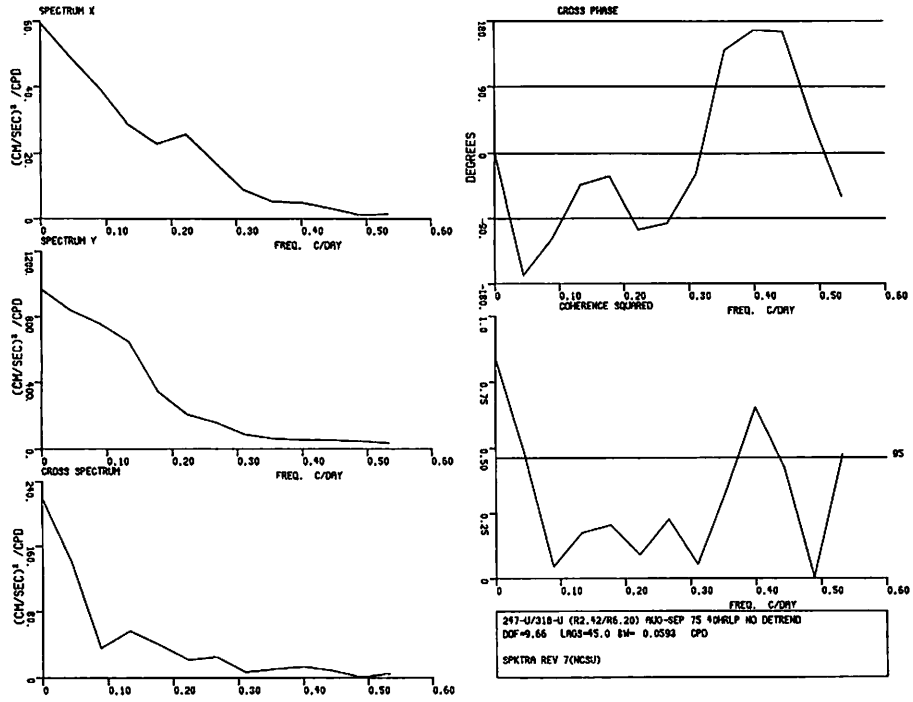

Figure 76 Spectra of low pass current velocity components from meter Bl_{bot} (u component, Principal Axis = 2.42°) and meter Al_{top} (u component, Principal Axis = 6.20°)

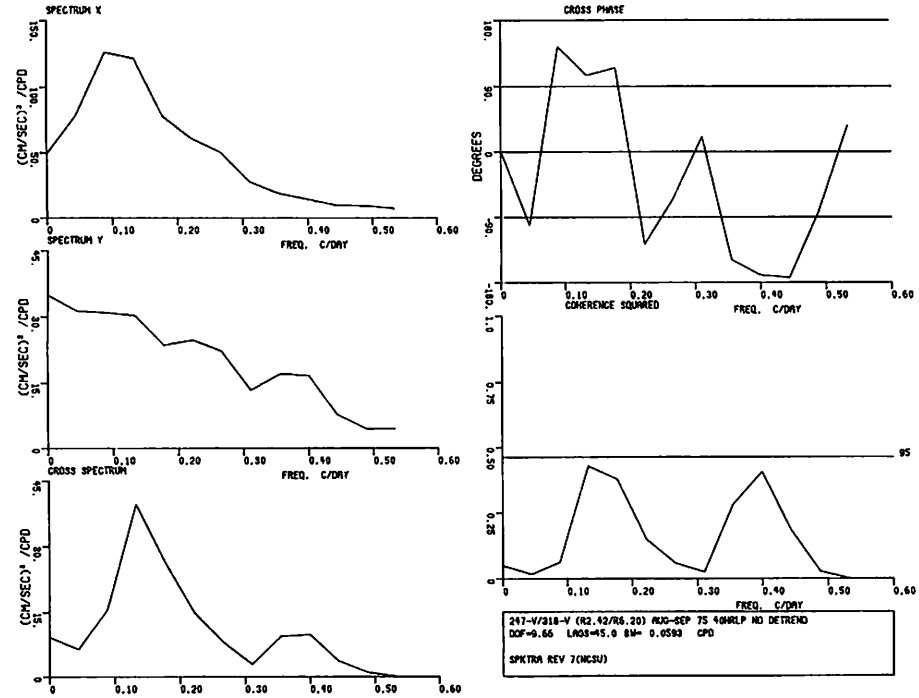

Figure 77 Spectra of low pass current velocity components from meter Bl_{bot} (v component, Principal Axis = 2.42°) and meter Al_{top} (v component, Principal Axis = 6.20°)

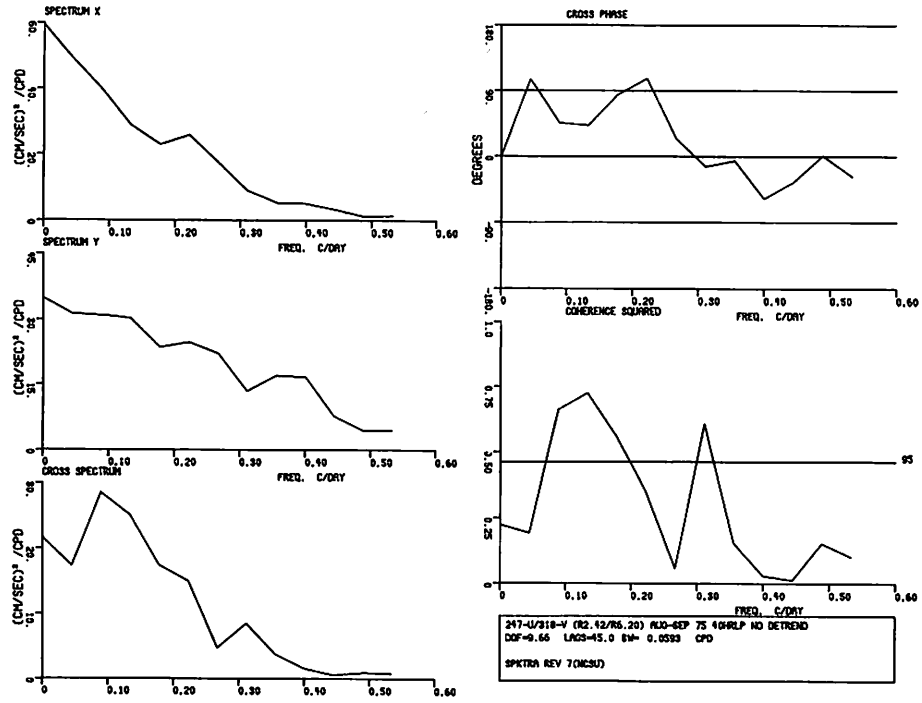

Figure 78 Spectra of low pass current velocity components from meter Bl_{bot} (u component, Principal Axis = 2.42°) and meter Al_{top} (v component, Principal Axis = 6.20°)

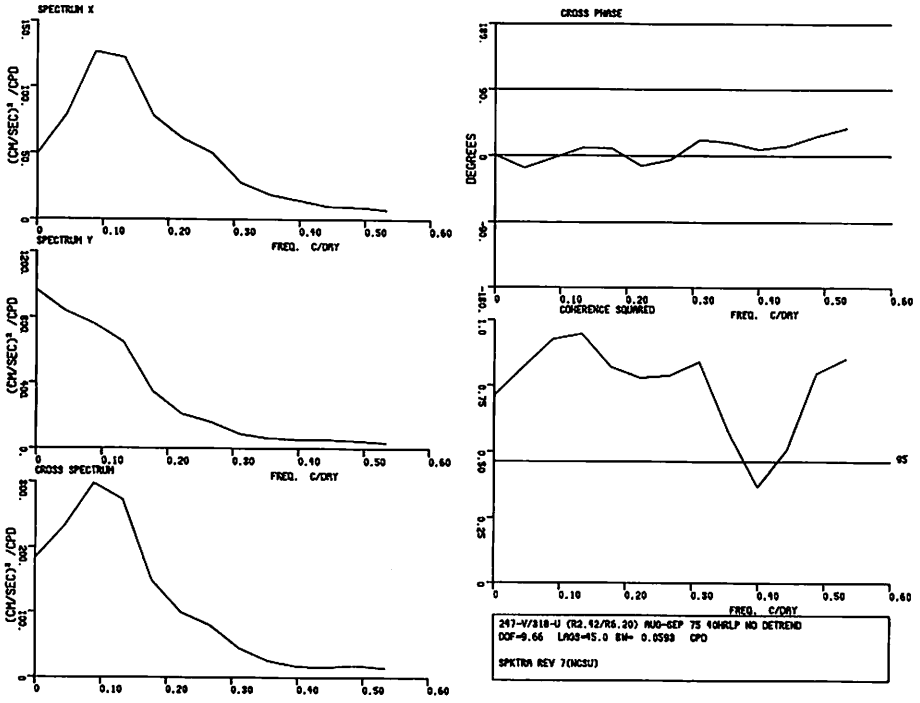

Figure 79 Spectra of low pass current velocity components from meter Bl_{bot} (v component, Principal Axis = 2.42°) and meter Al_{top} (u component, Principal Axis = 6.20°)

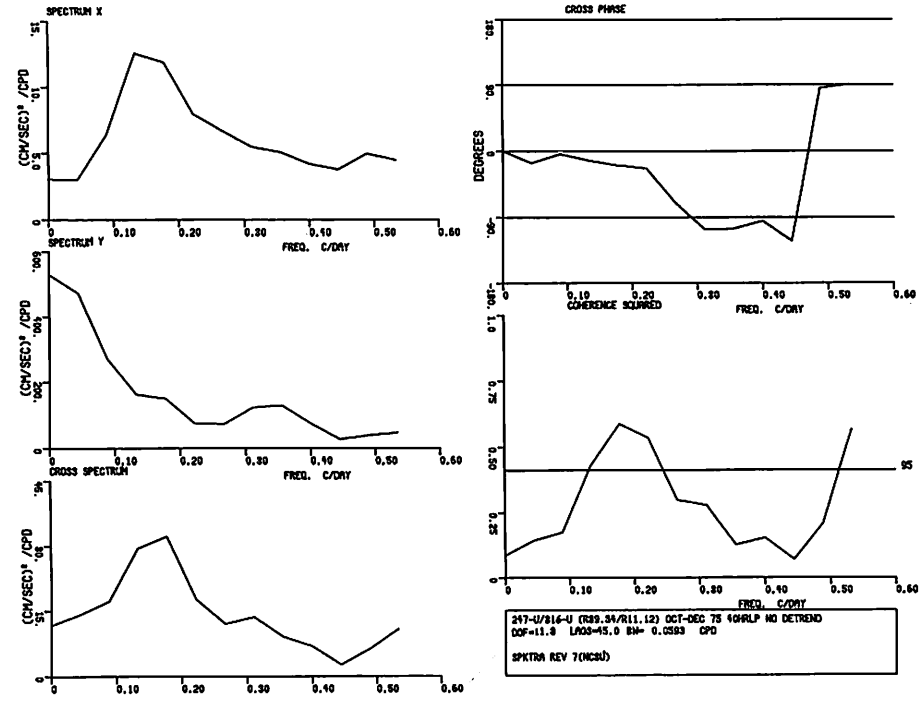

Figure 80 Spectra of low pass current velocity components from meter $A2_{bot}$ (u component, Principal Axis = 89.34°) and meter $A2_{top}$ (u component, Principal Axis = 11.12°)

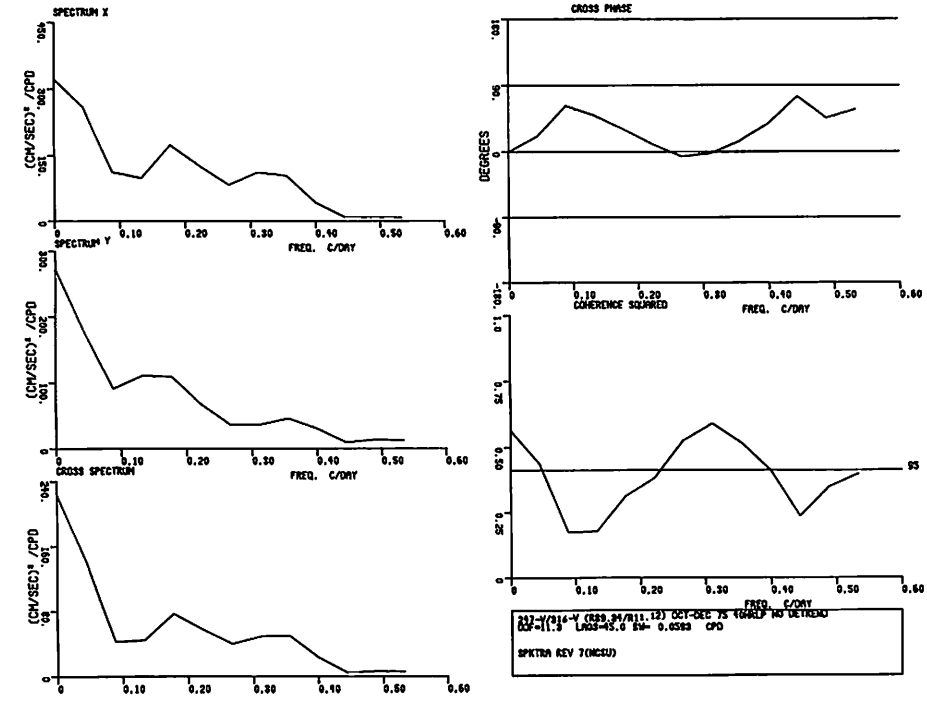

Figure 81 Spectra of low pass current velocity components from meter $A2_{bot}$ (v component, Principal Axis = 89.34°) and meter $A2_{top}$ (v component, Principal Axis = 11.12°)

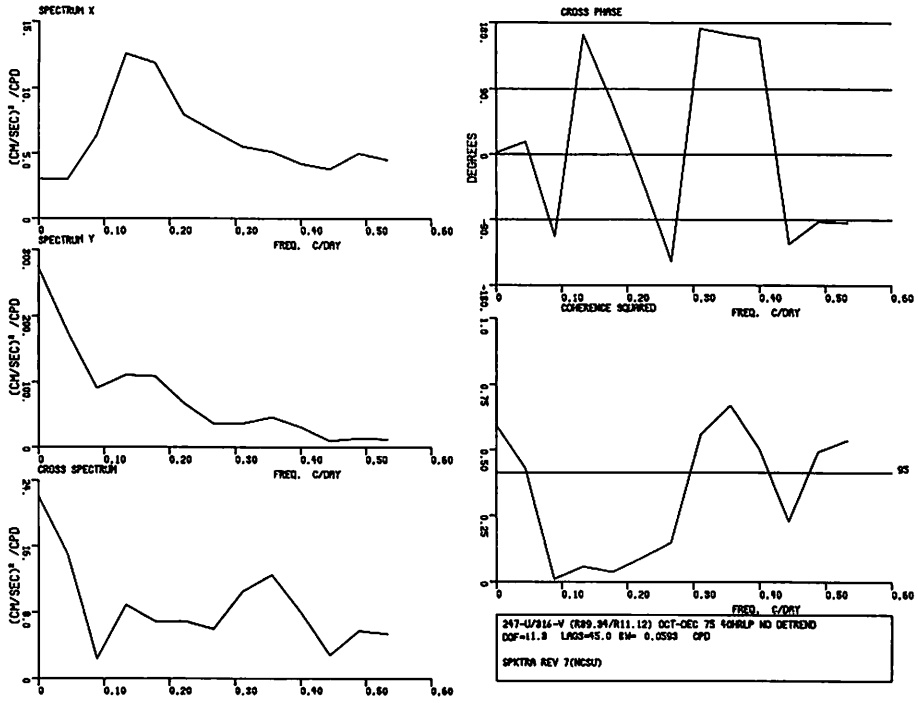

Figure 82 Spectra of low pass current velocity components from meter $A2_{bot}$ (u component, Principal Axis = 89.34°) and meter $A2_{top}$ (v component, Principal Axis = 11.12°)

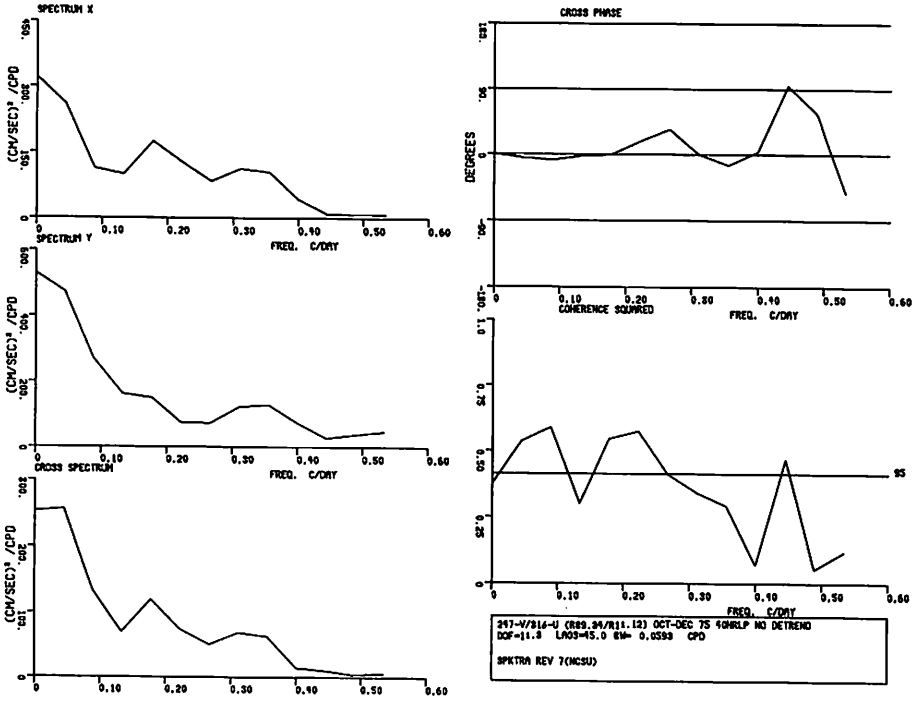

Figure 83 Spectra of low pass current velocity components from meter $A2_{bot}$ (v component, Principal Axis = 89.34°) and meter $A2_{top}$ (u component, Principal Axis = 11.12°)

VII. Meteorological Data

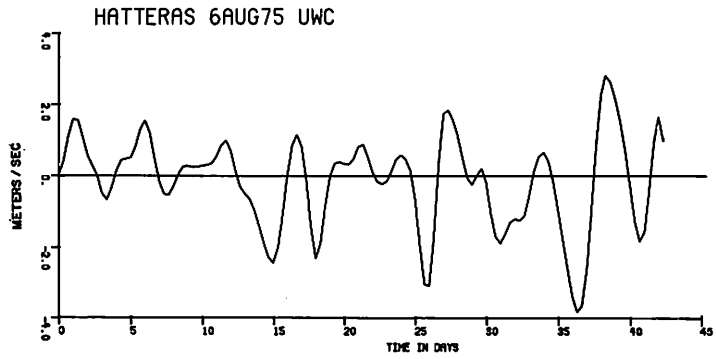

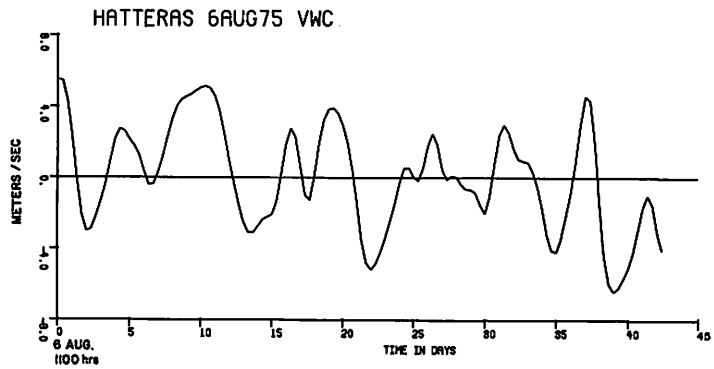

Figure 84 Low pass wind velocity components at Cape Hatteras, Aug-Sept 1975

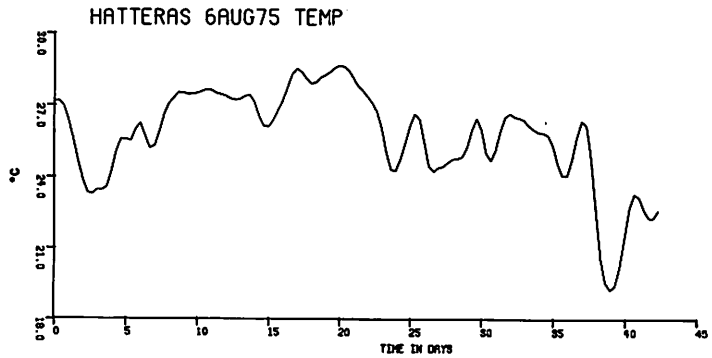

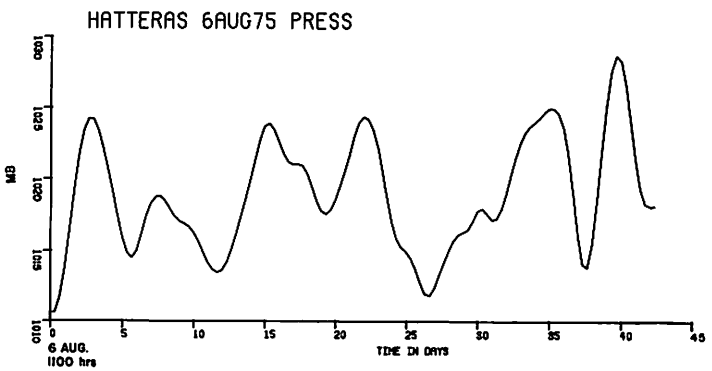

Figure 85 Low pass temperature and pressure at Cape Hatteras, Aug-Sept 1975

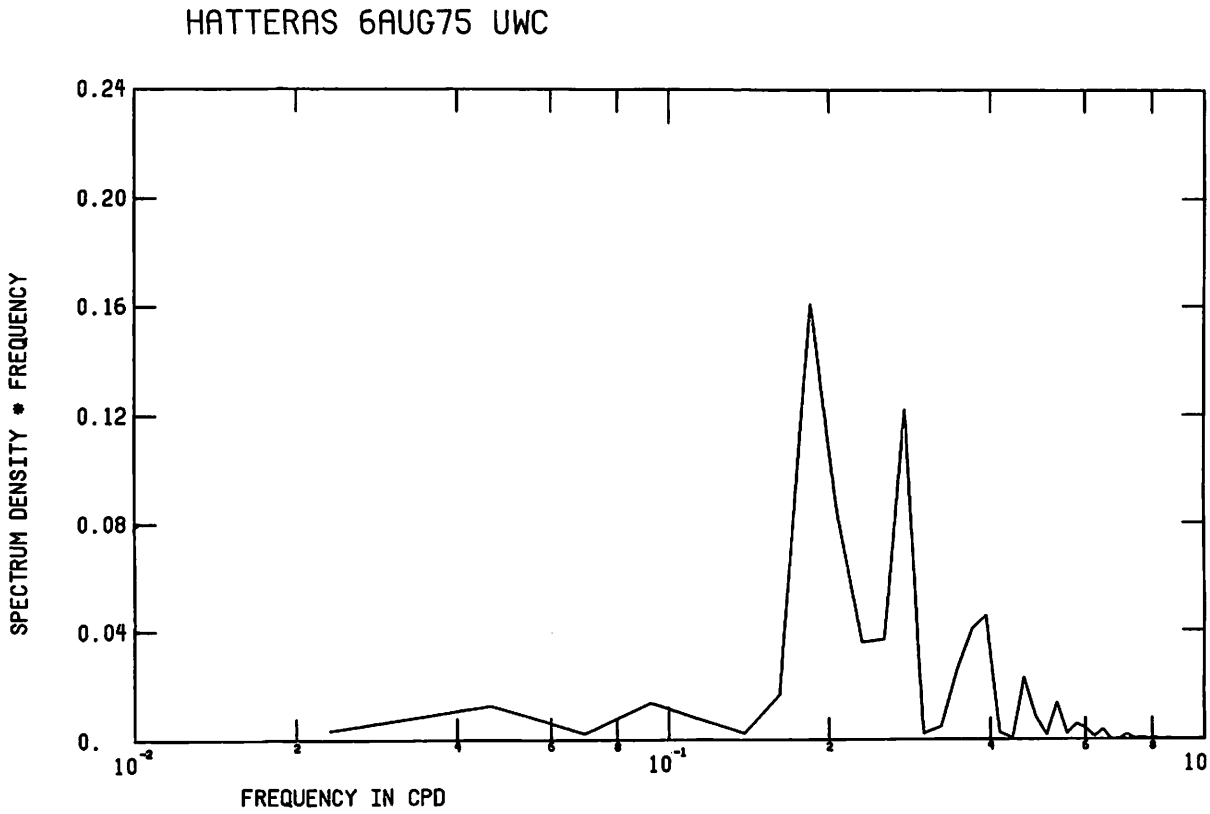

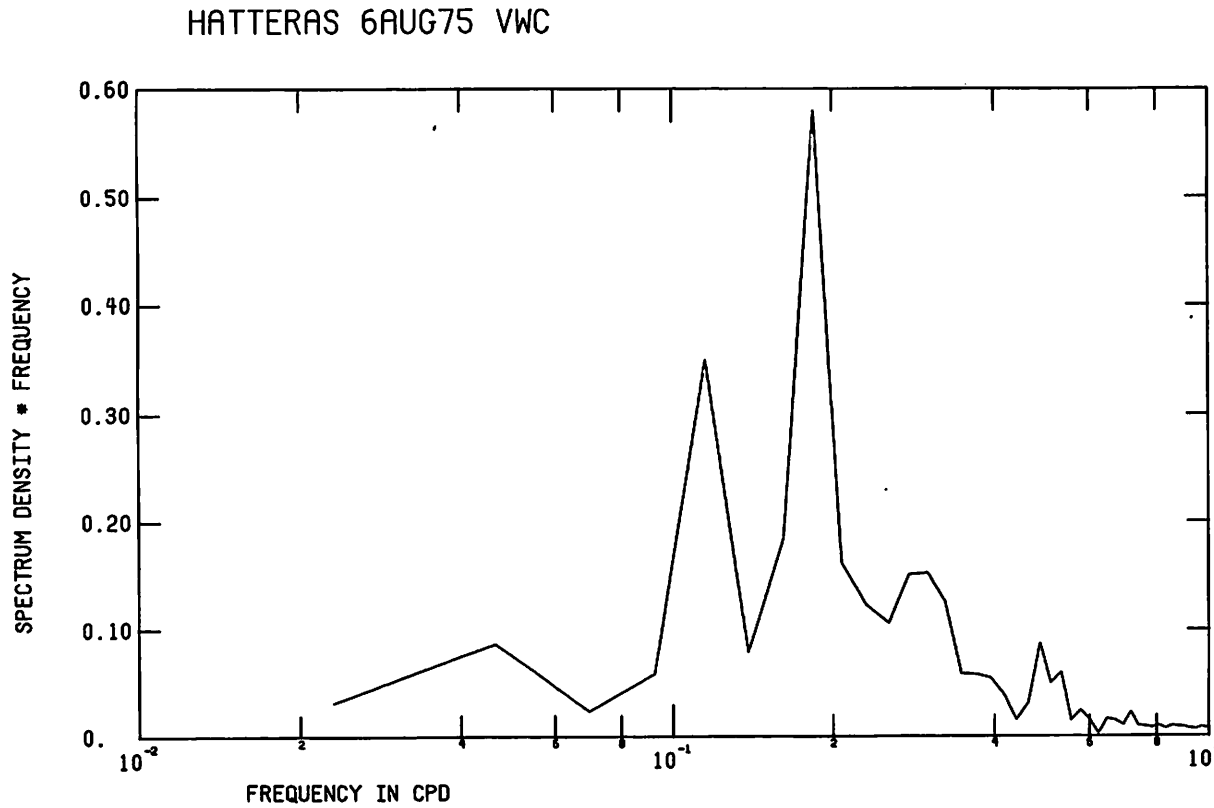

Figure 86 FFT of low pass wind velocity components at Cape Hatteras, Aug-Sept 1975

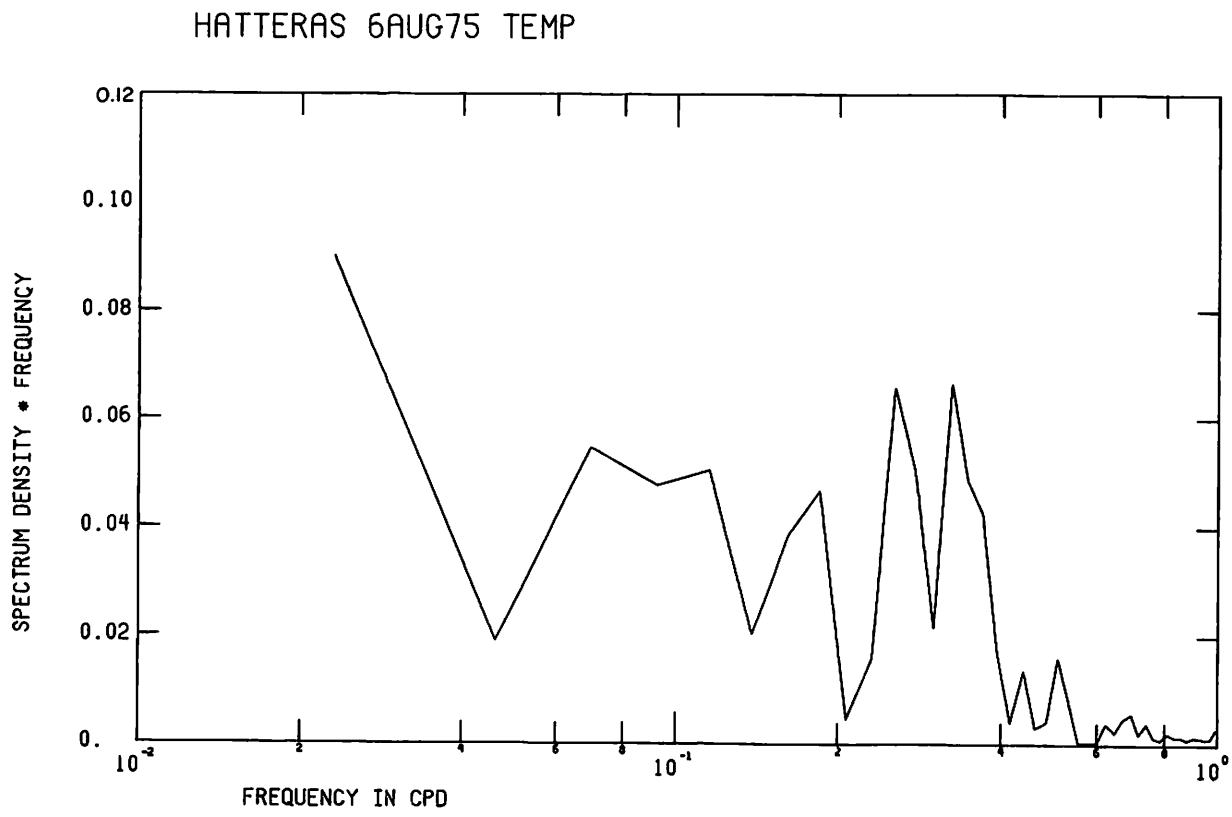

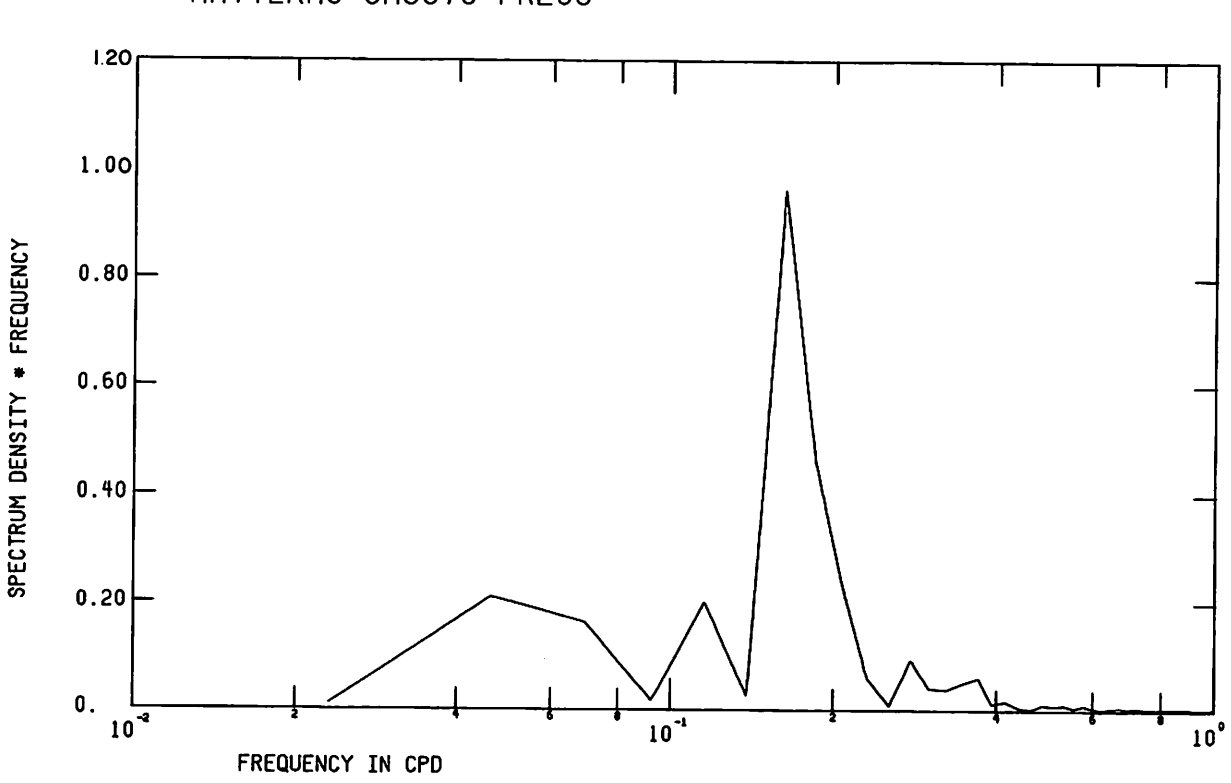

Figure 87 FFT of low pass temperature and pressure at Cape Hatteras, Aug-Sept 1975

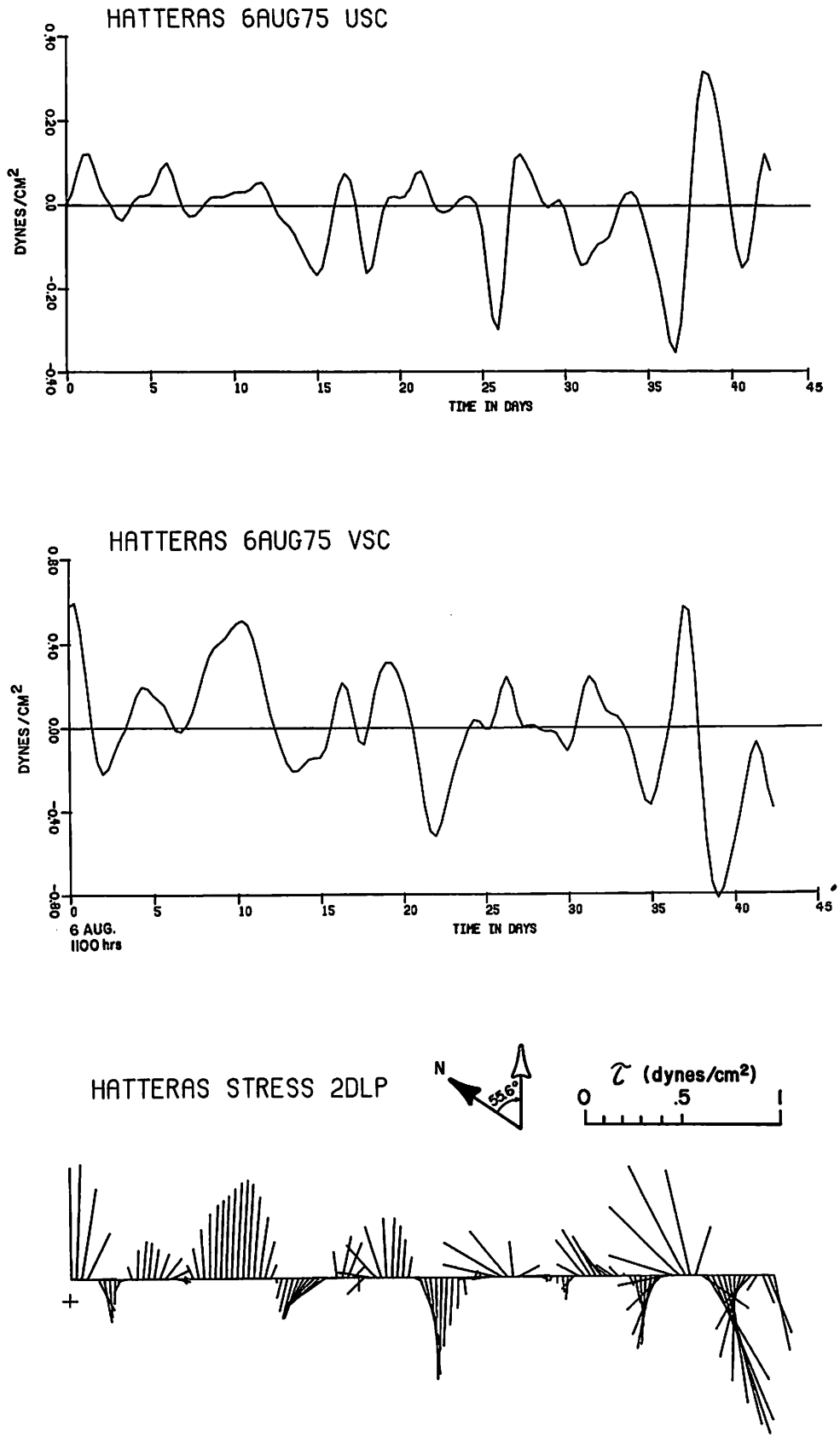

Figure 88 Low pass wind stress components and vectors at Cape Hatteras, Aug-Sept 1975

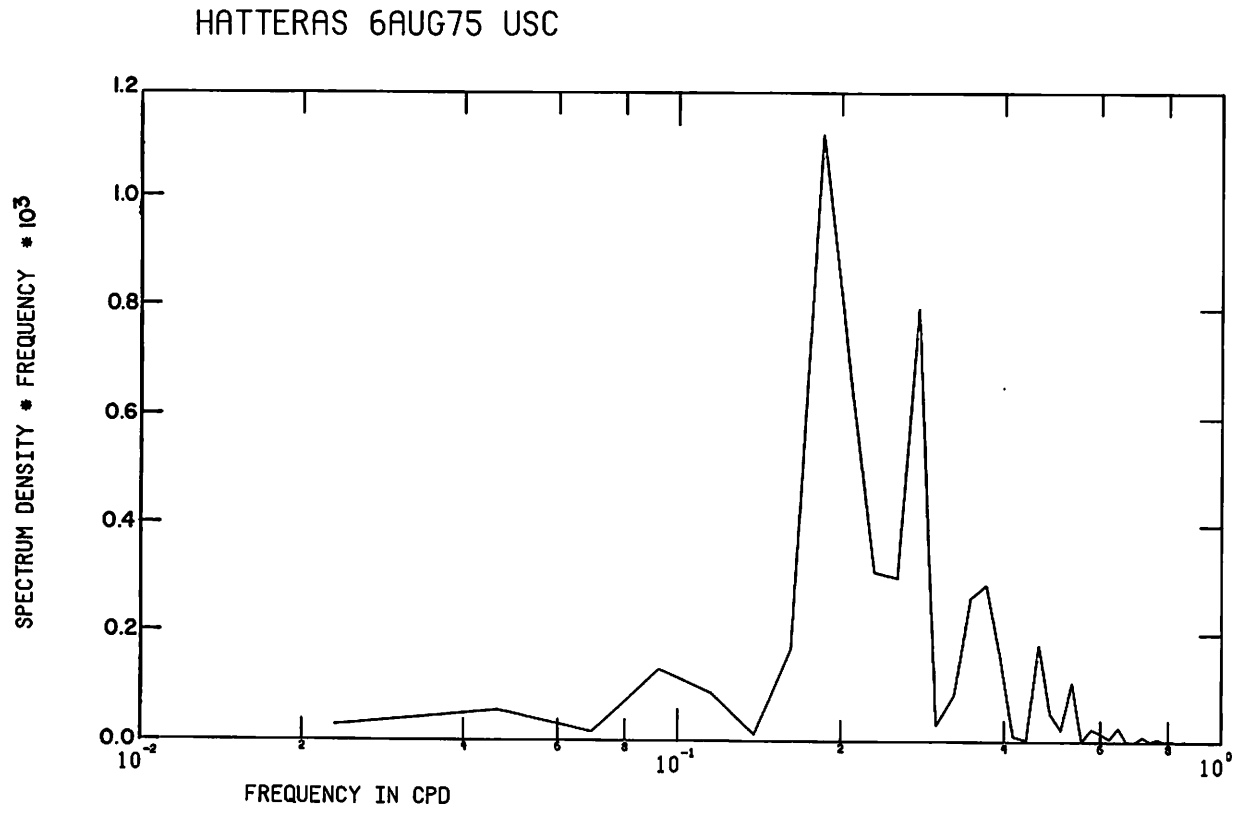

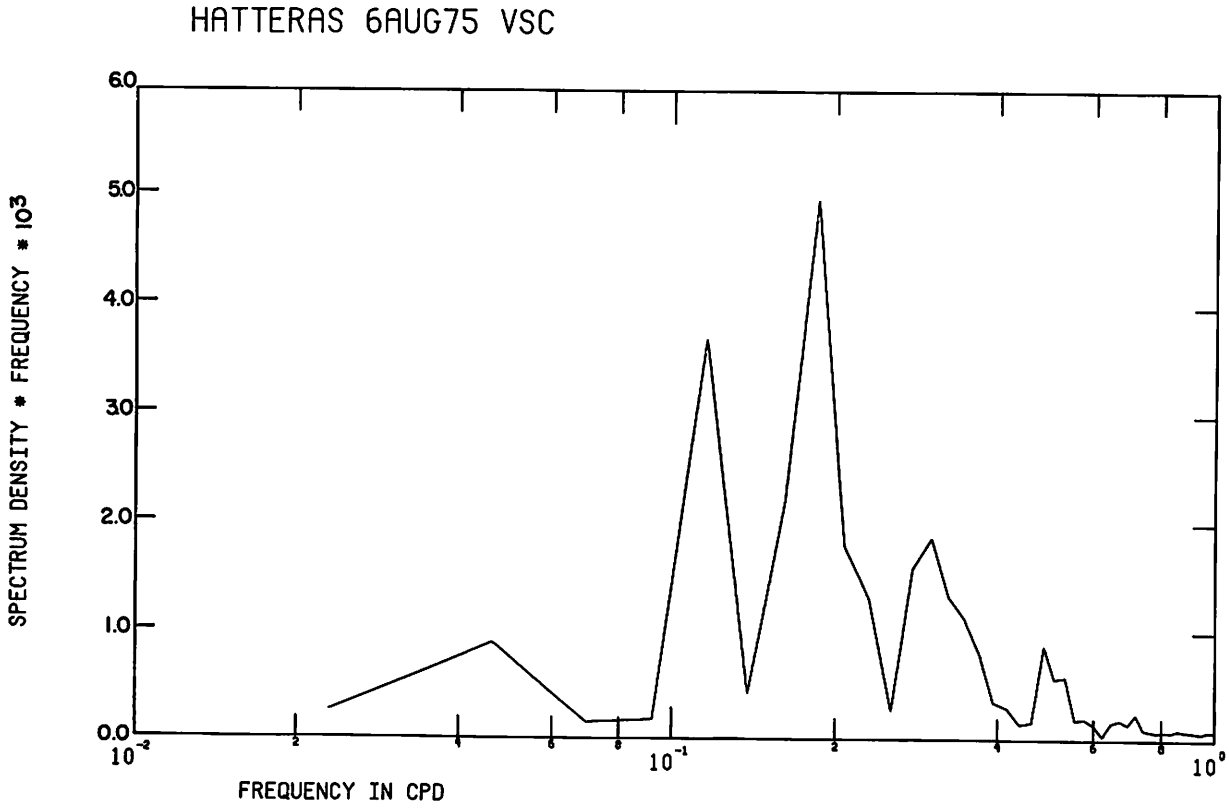

Figure 89 FFT of low pass wind stress components at Cape Hatteras, Aug-Sept 1975

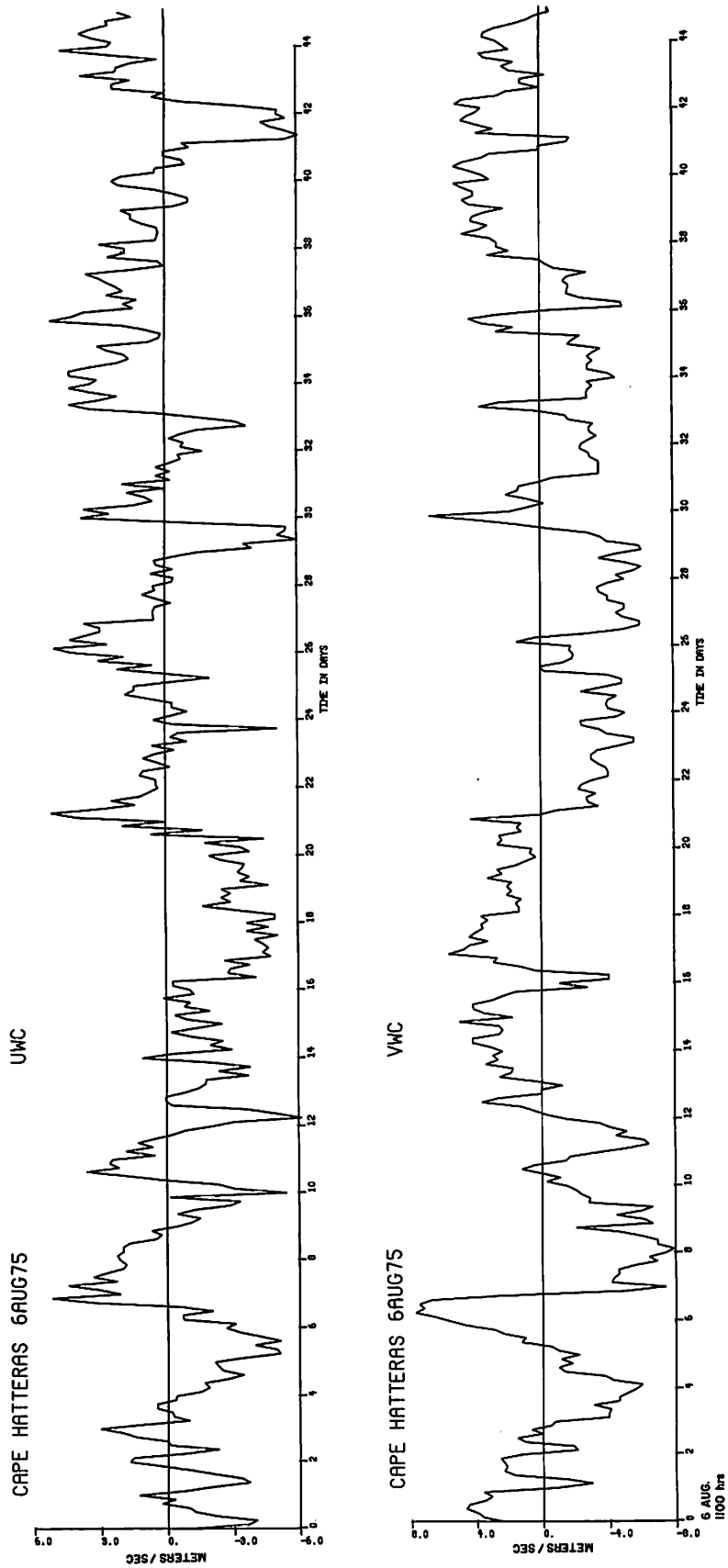

Figure 90 Unfiltered wind velocity components at Cape Hatteras, Aug-Sept 1975

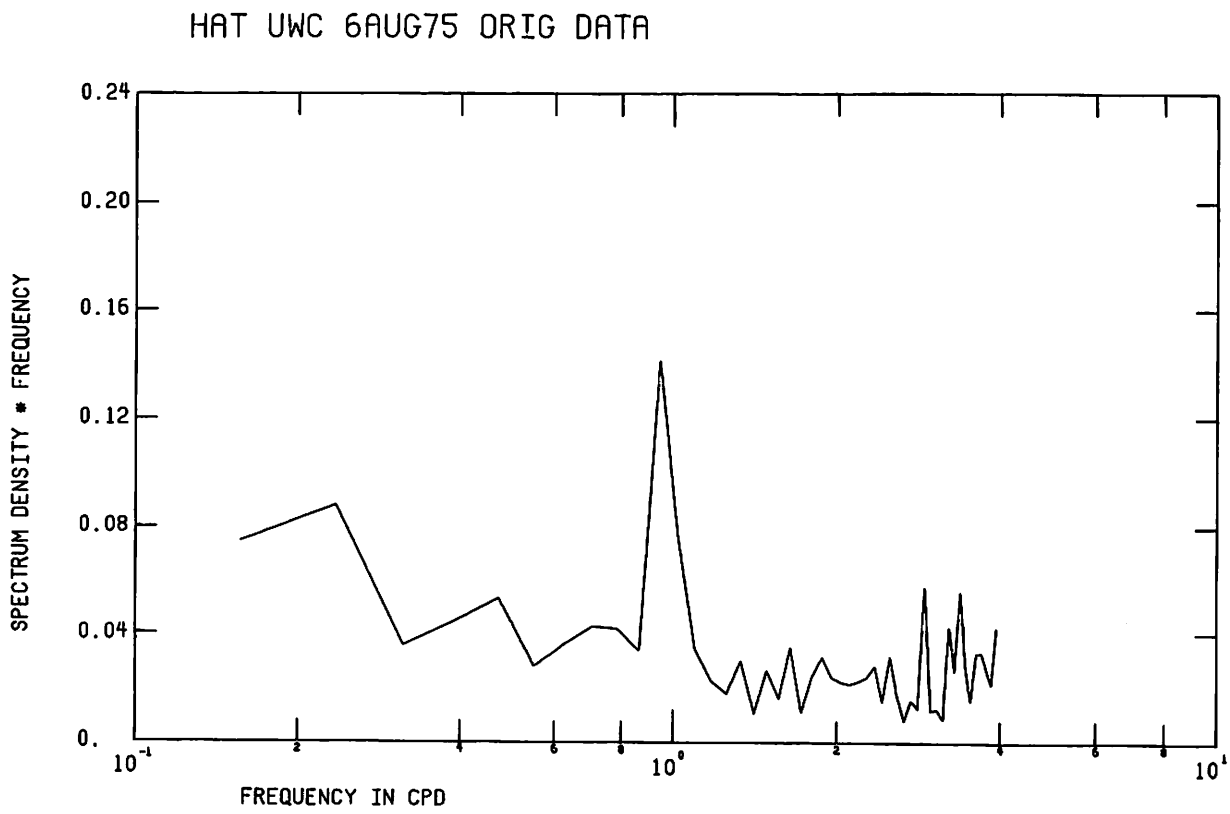

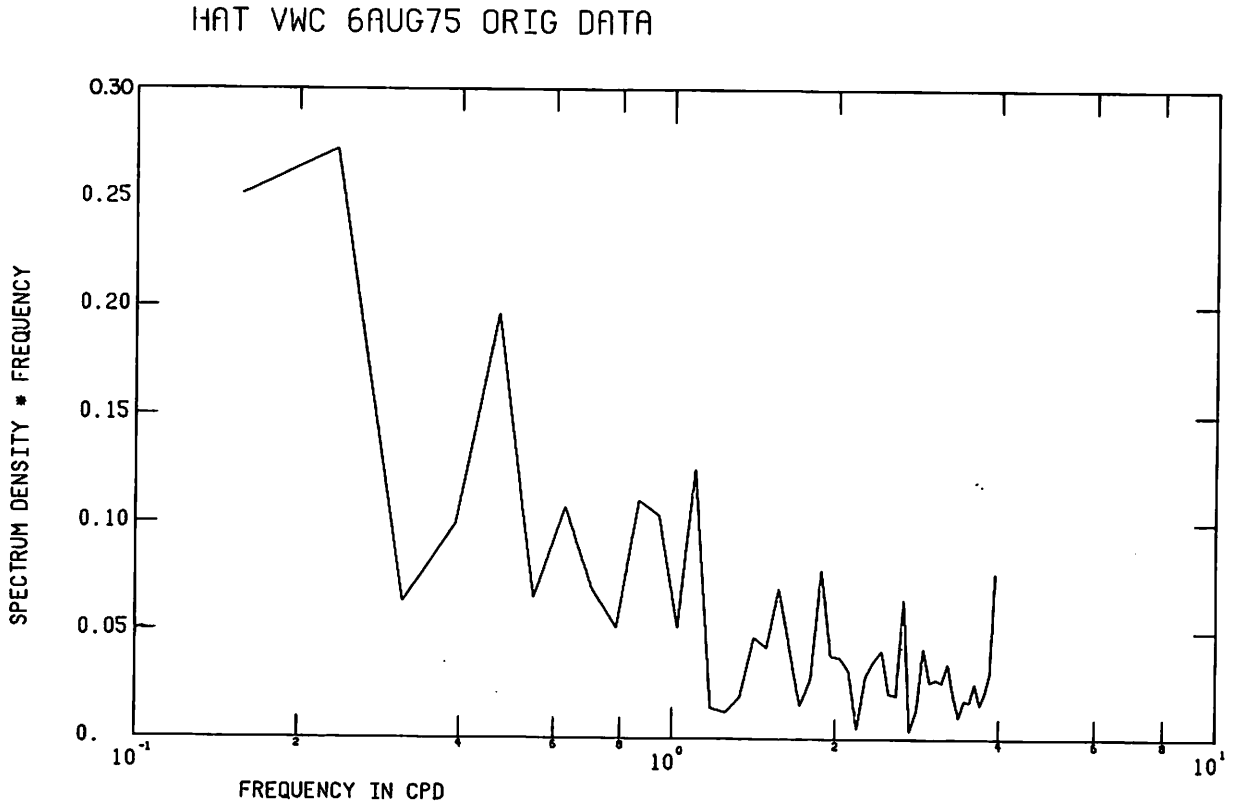

Figure 91 FFT of unfiltered wind velocity components at Cape Hatteras, Aug-Sept 1975

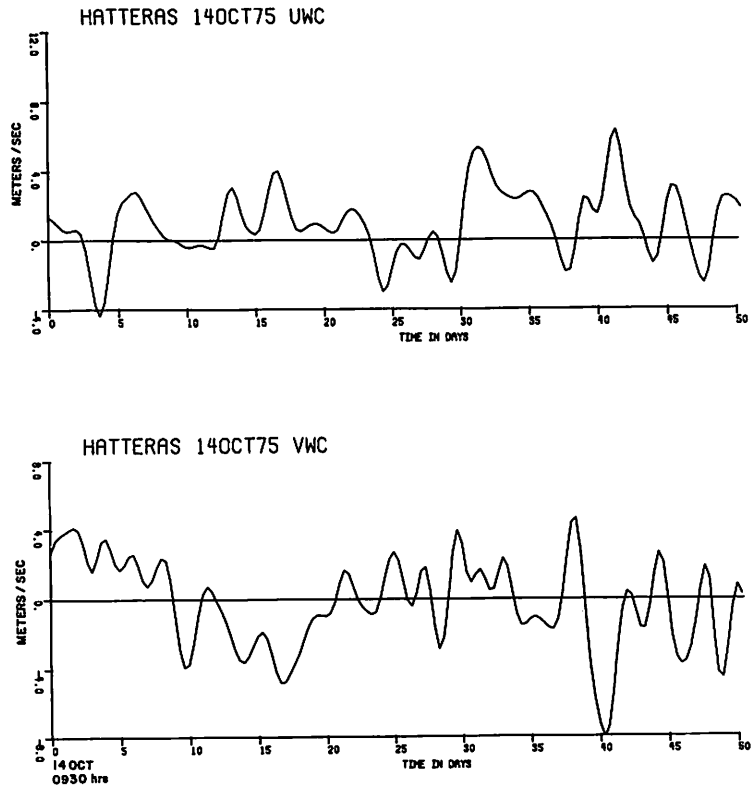

Figure 92 Low pass wind velocity components at Cape Hatteras, Oct-Dec 1975

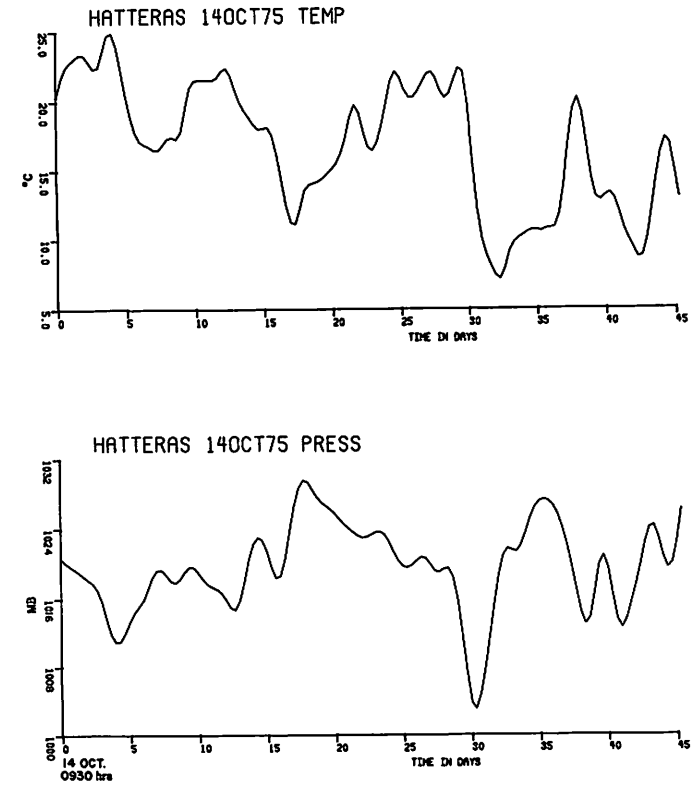

Figure 93 Low pass temperature and pressure at Cape Hatteras, Oct-Dec 1975

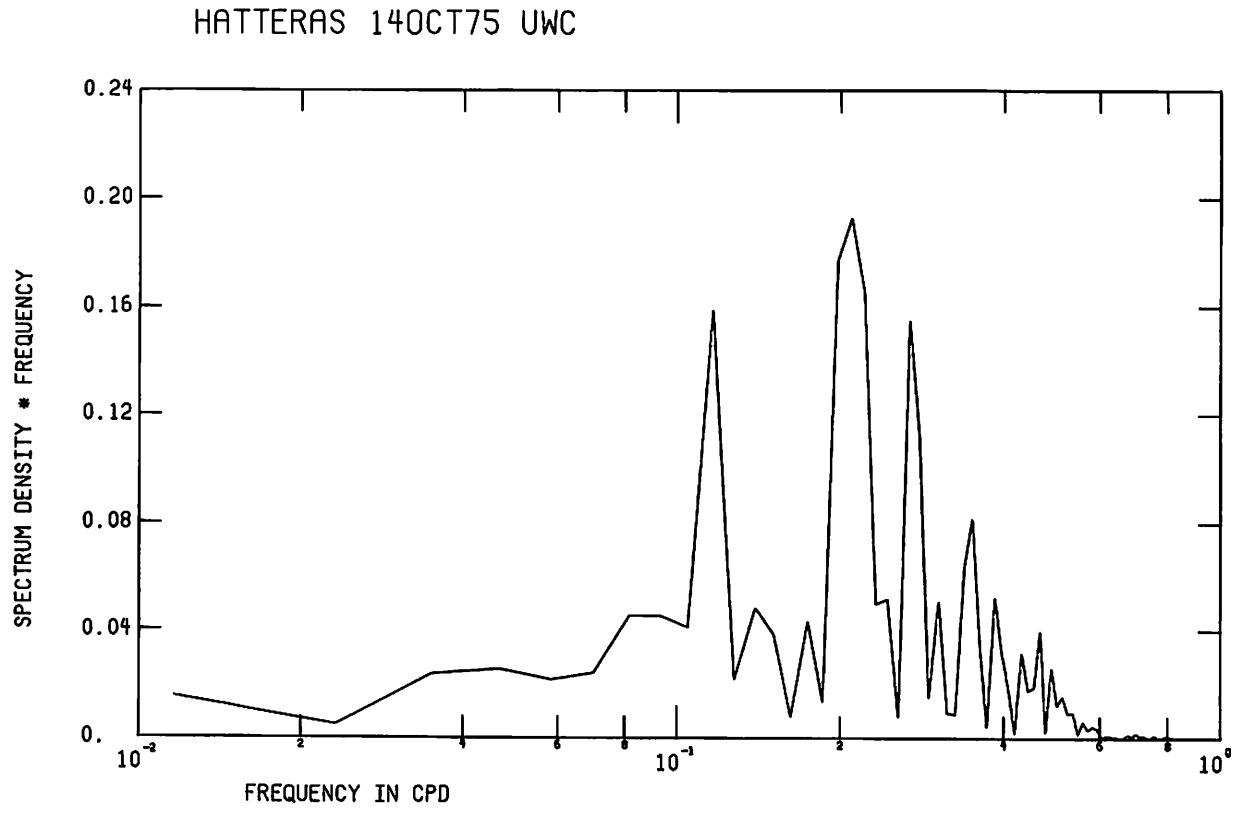

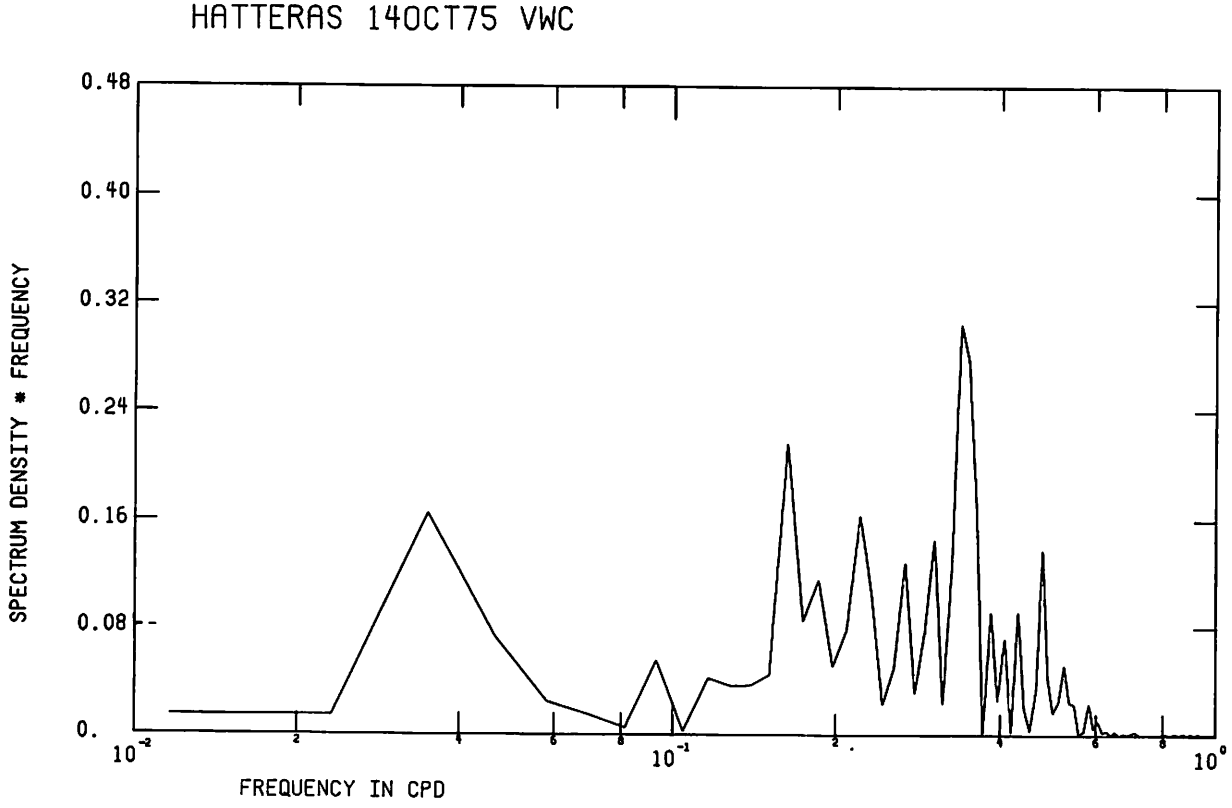

Figure 94 FFT of low pass wind velocity components at Cape Hatteras, Oct-Dec 1975

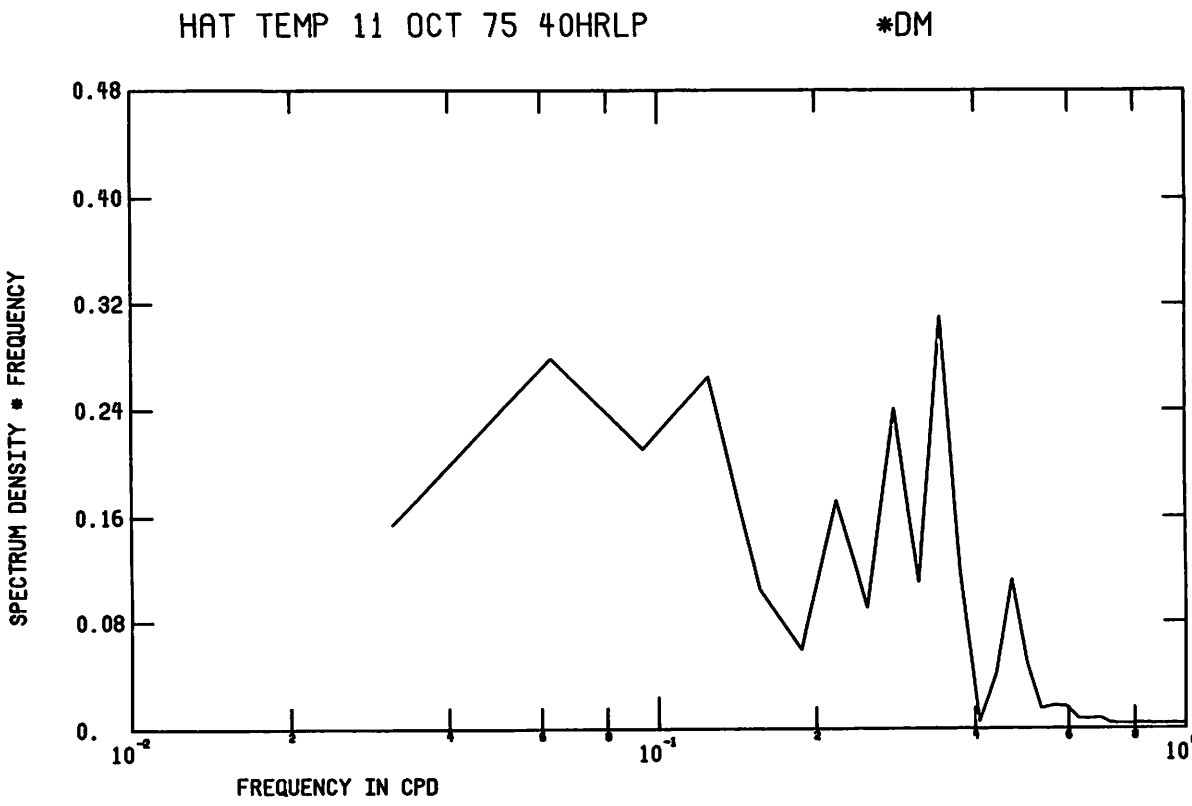

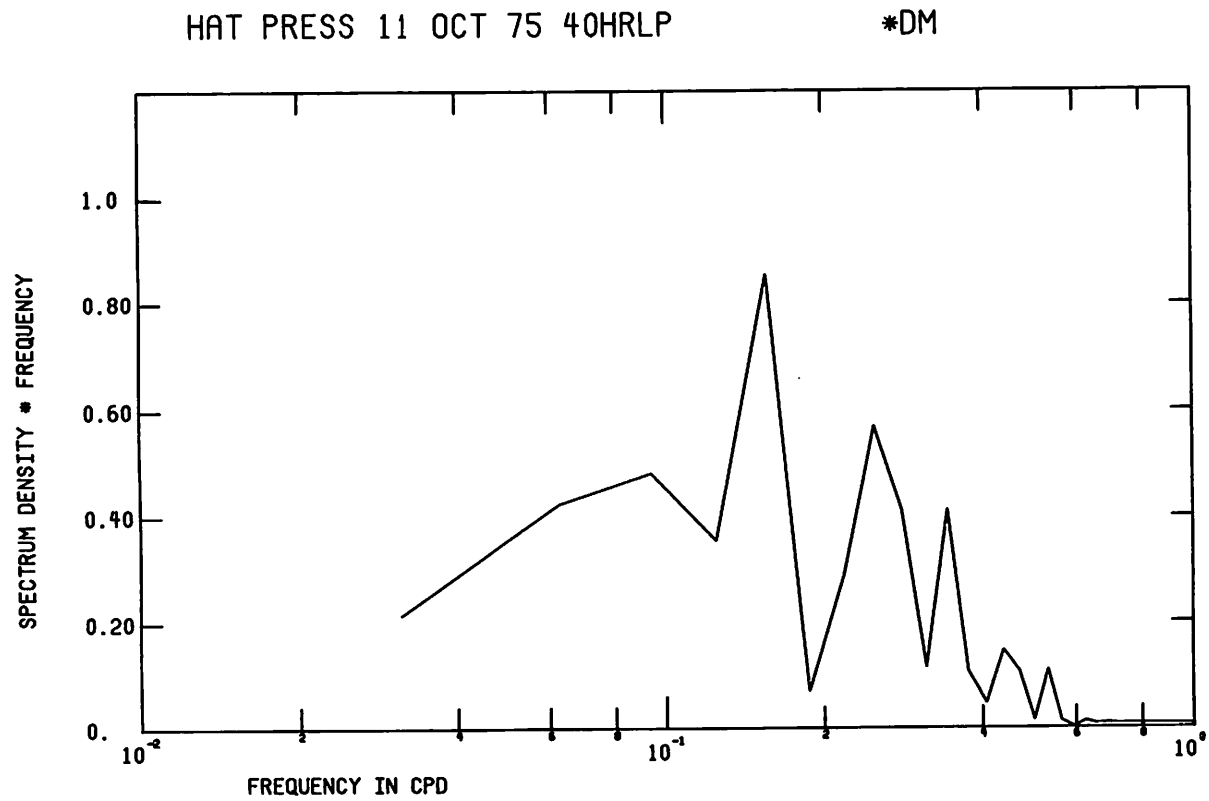

Figure 95 FFT of low pass temperature and pressure at Cape Hatteras, Oct-Dec 1975

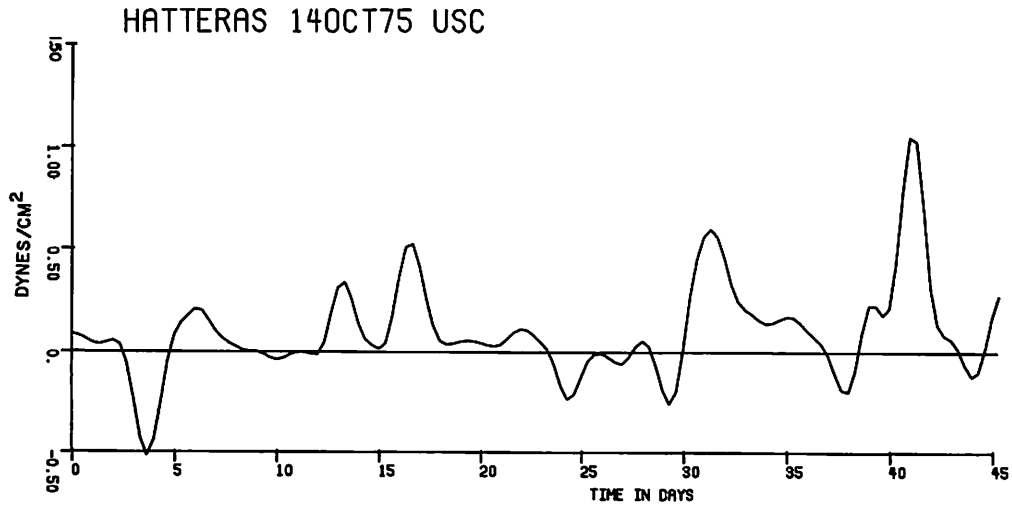

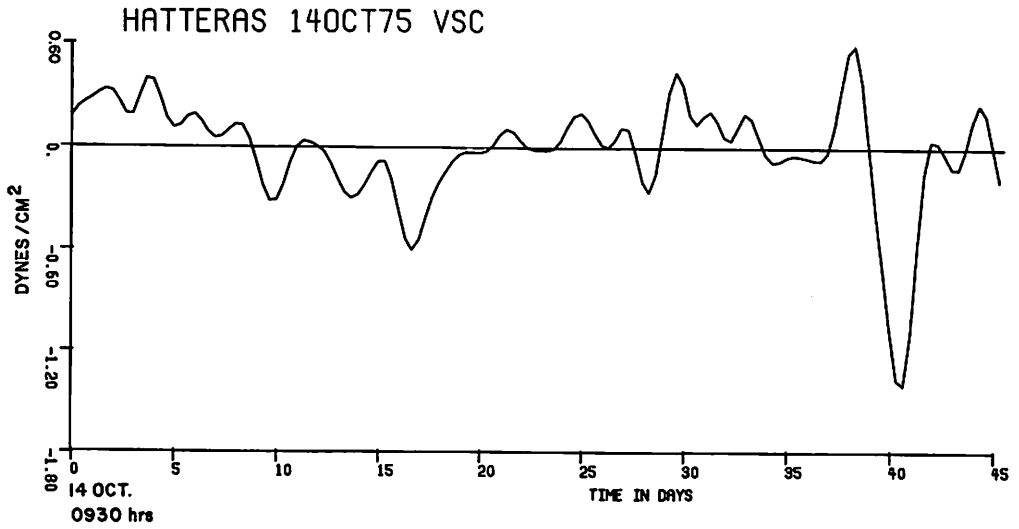

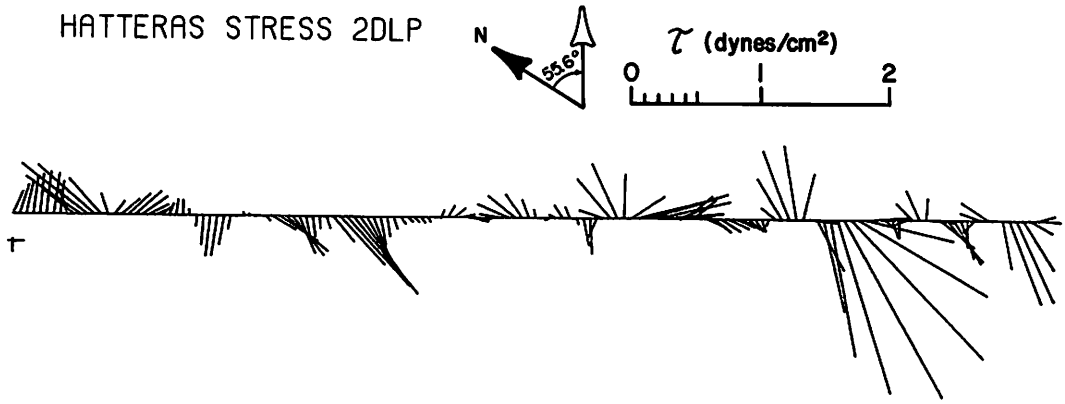

Figure 96 Low pass wind stress components and vectors at Cape Hatteras, Oct-Dec 1975

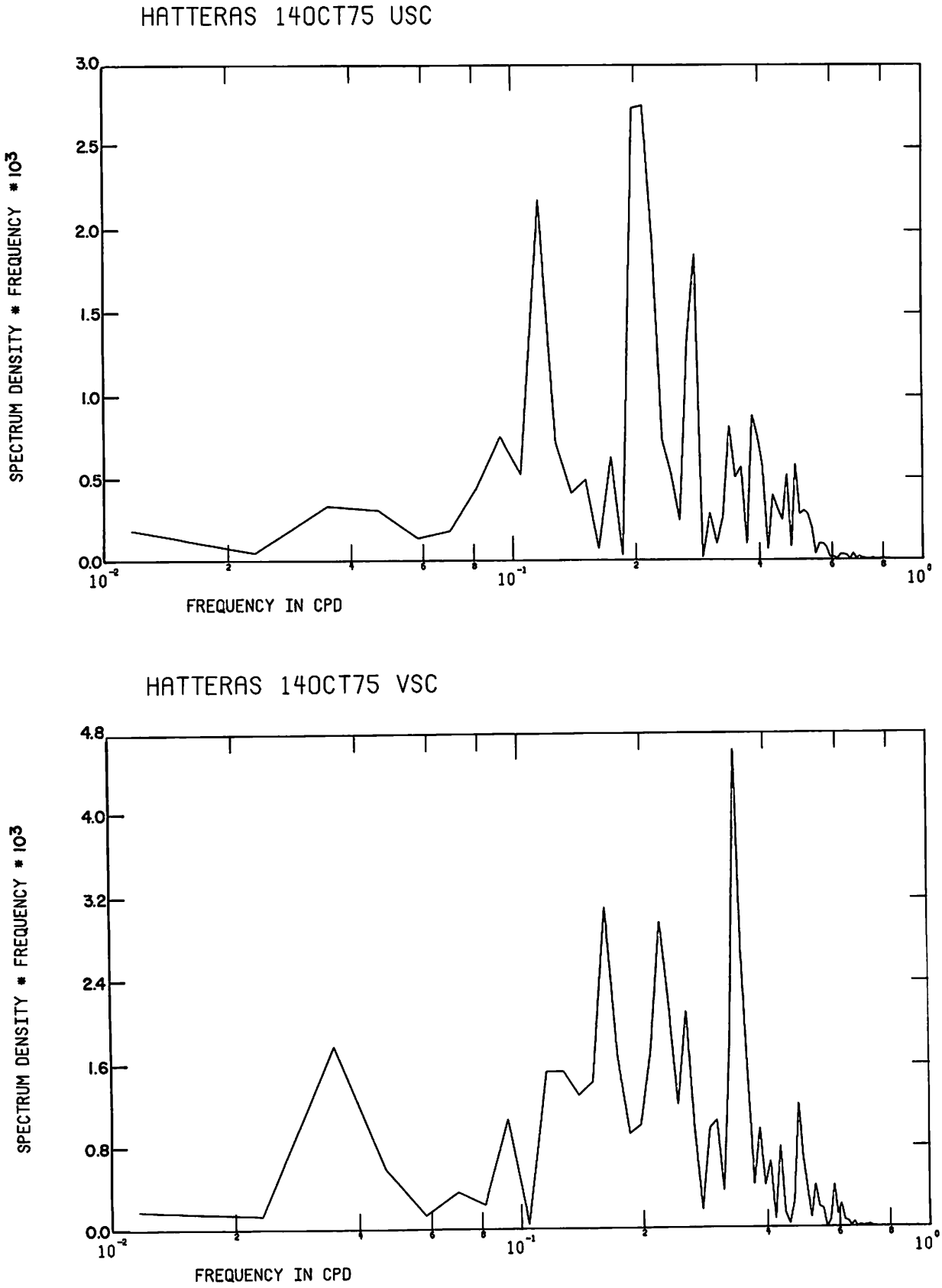

Figure 97 FFT of low pass wind stress components at Cape Hatteras, Oct-Dec 1975

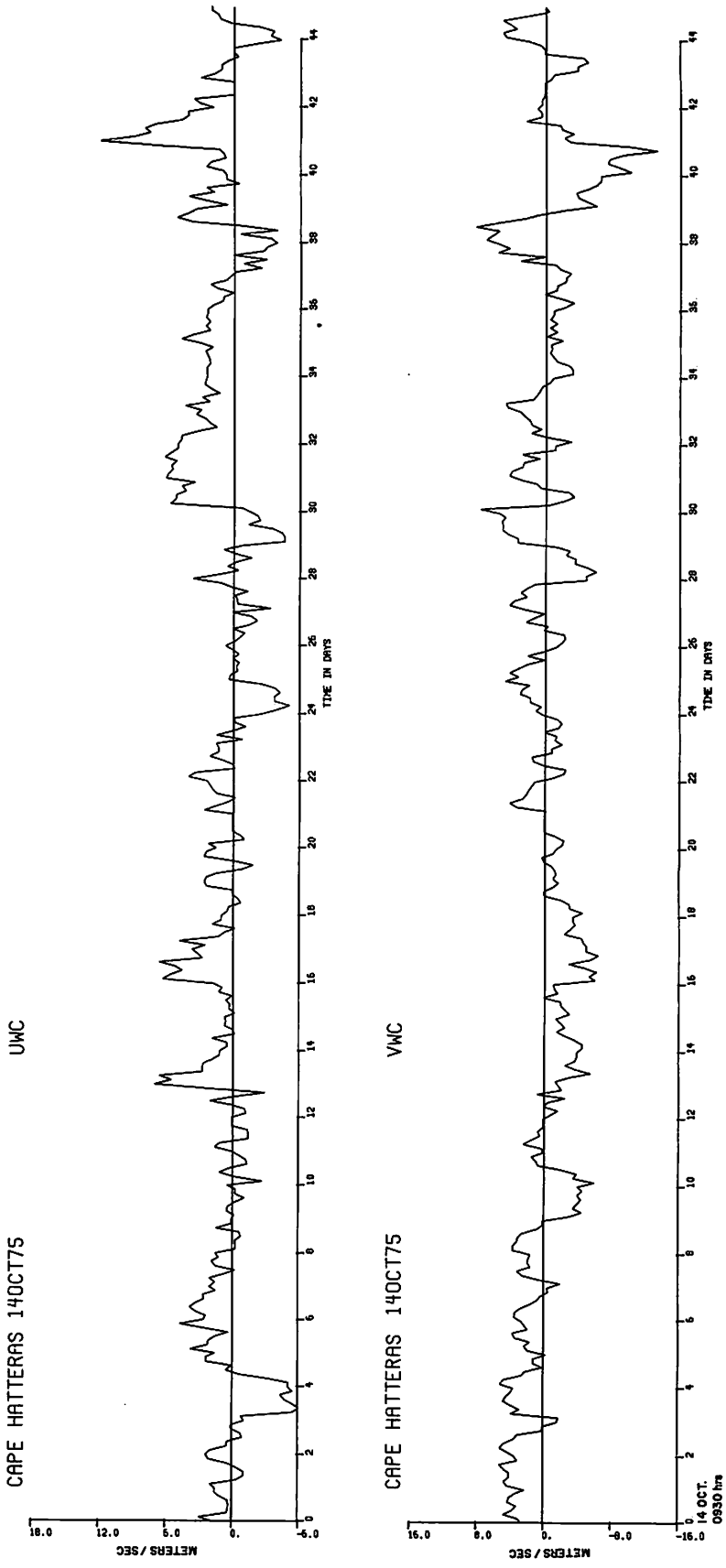

Figure 98 Unfiltered wind velocity components at Cape Hatteras, Oct-Dec 1975

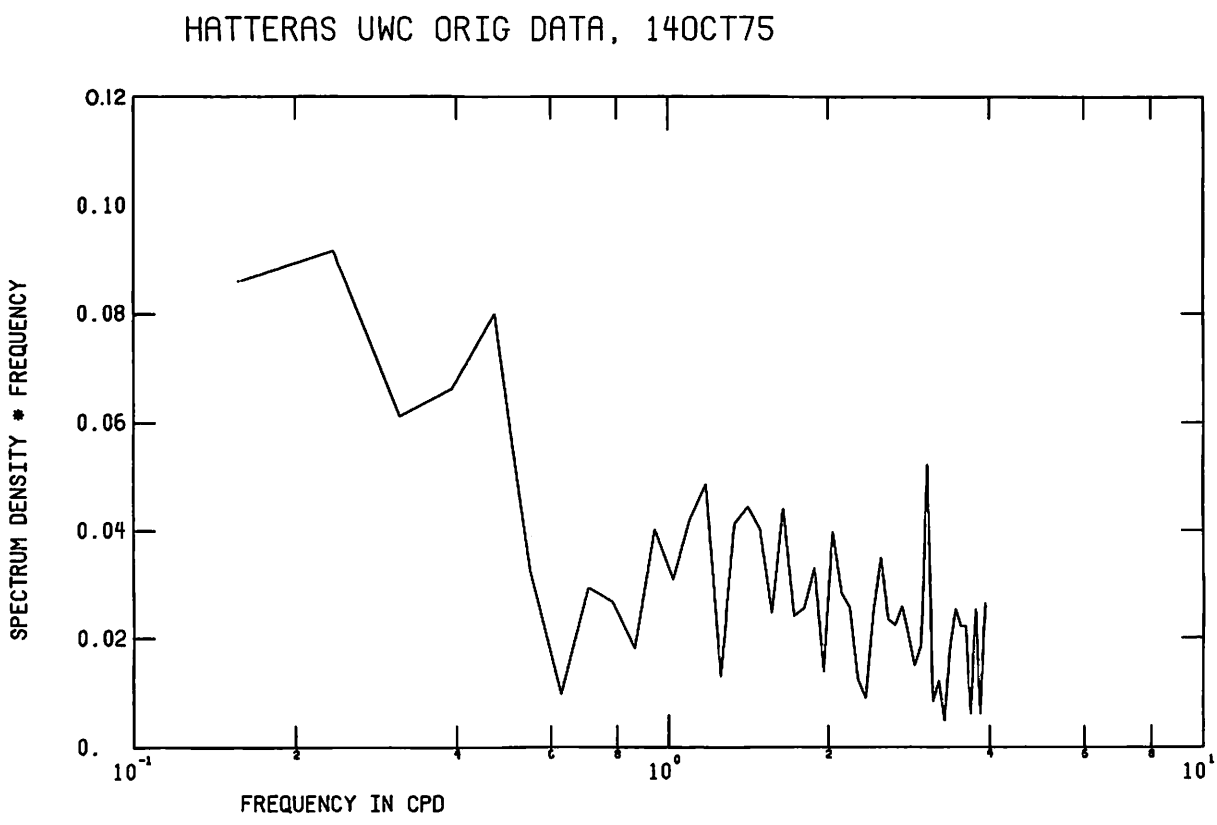

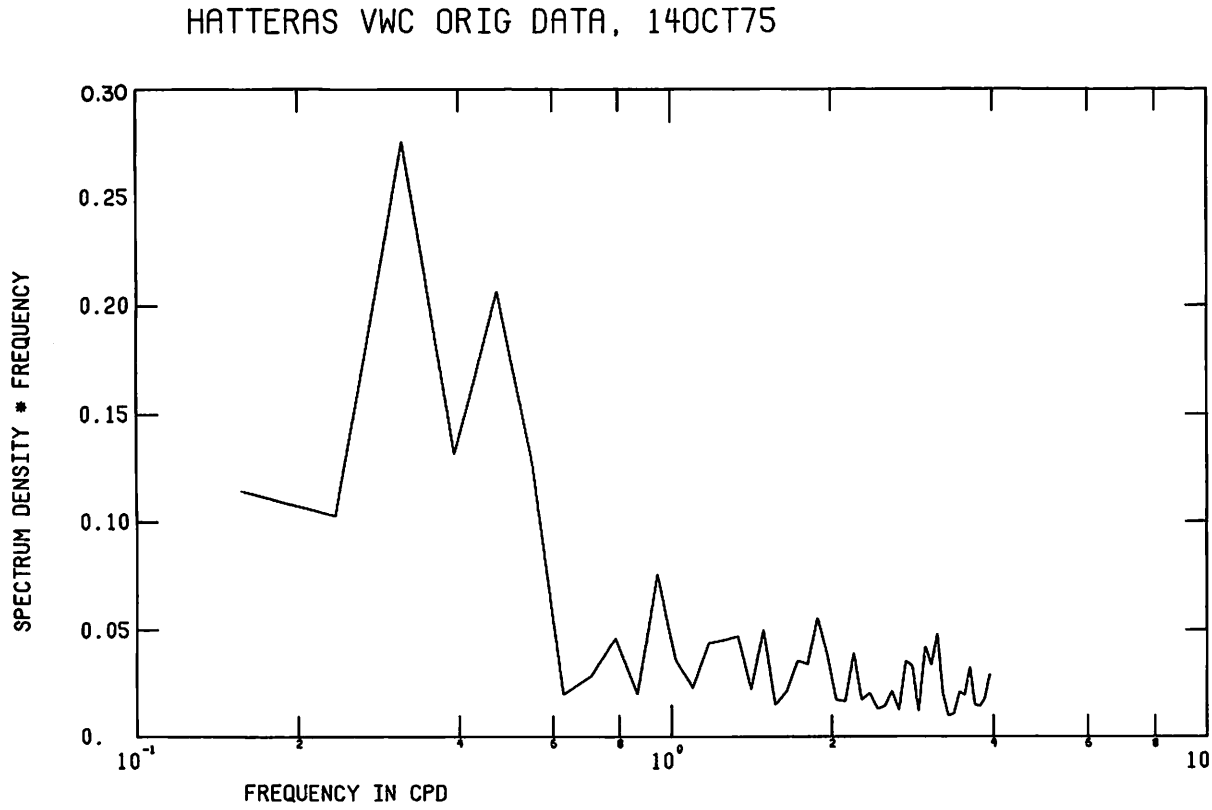

Figure 99 FFT of unfiltered wind velocity components at Cape Hatteras, Oct-Dec 1975

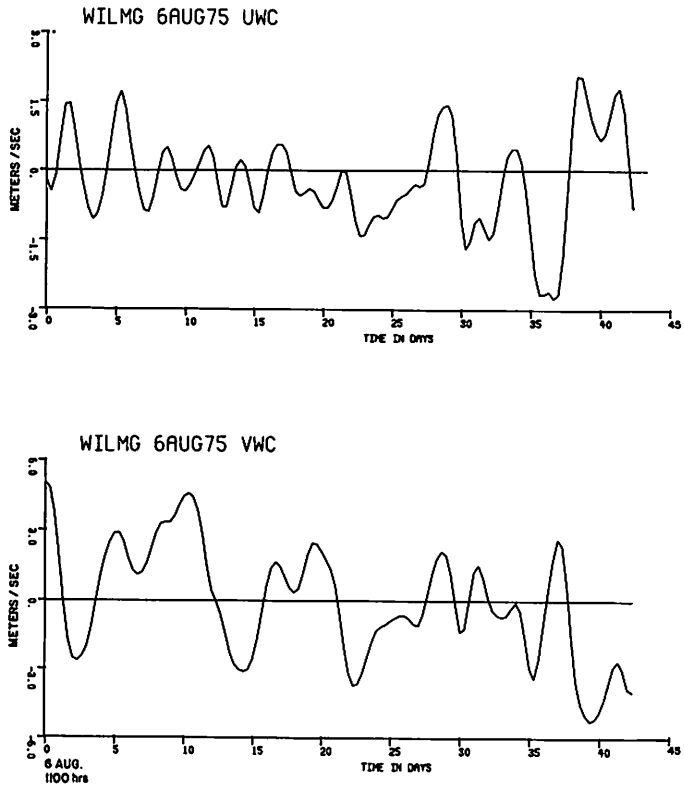

Figure 100 Low pass wind velocity components at Wilmington, Aug-Sept 1975

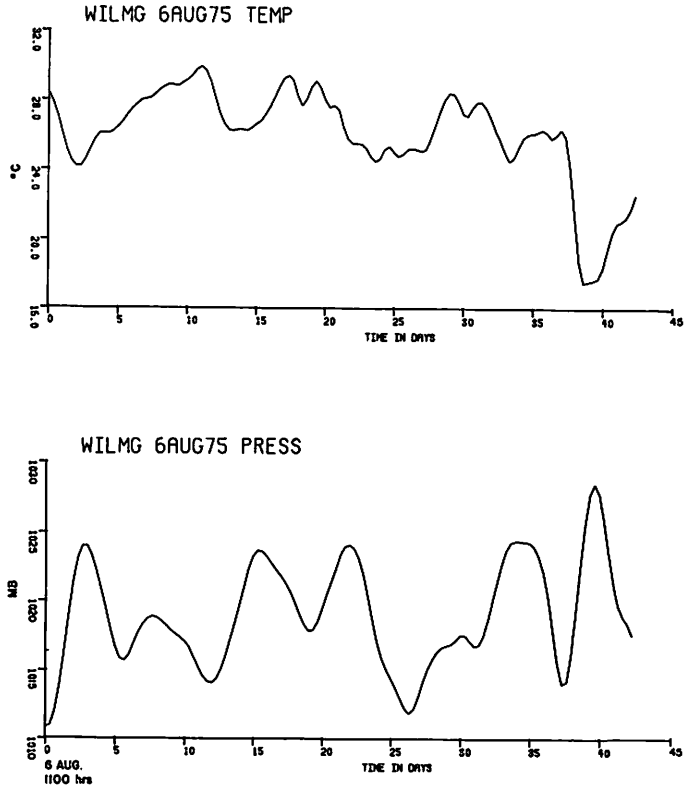

Figure 101 Low pass temperature and pressure at Wilmington, Aug-Sept 1975

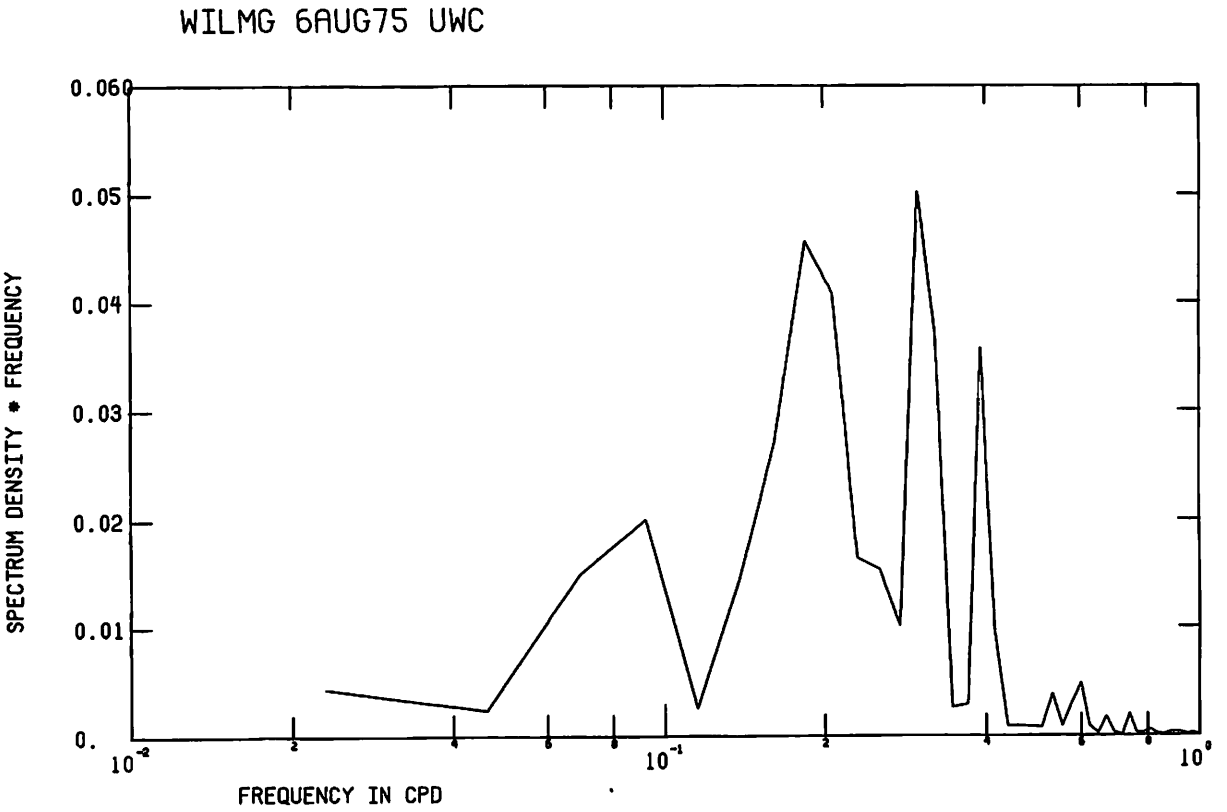

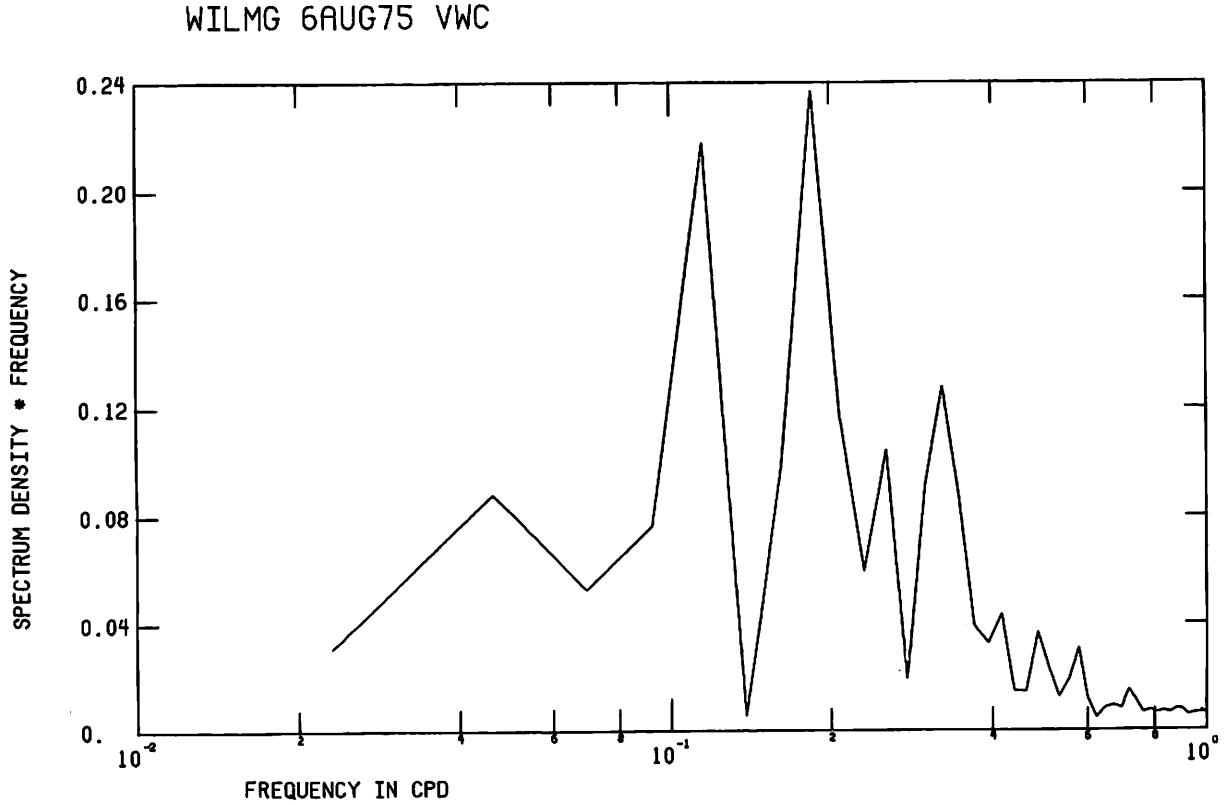

Figure 102 FFT of low pass wind velocity components at Wilmington, Aug-Sept 1975

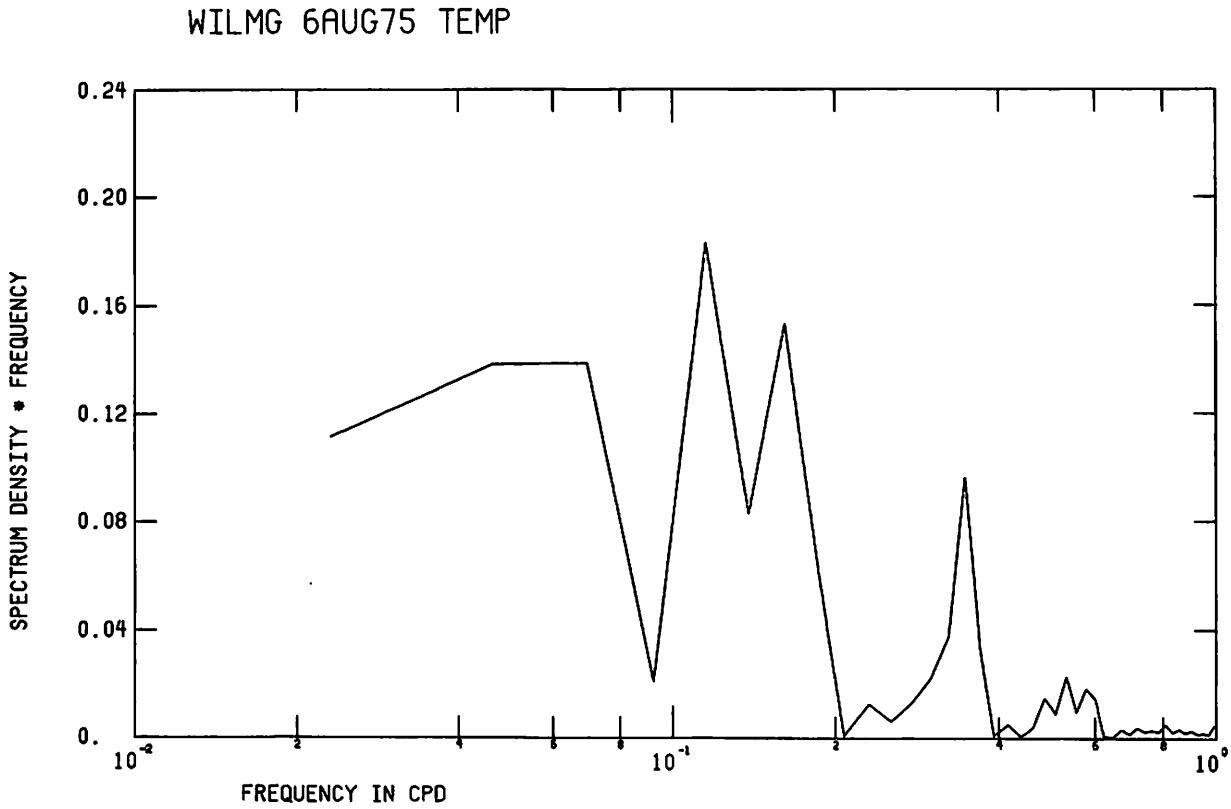

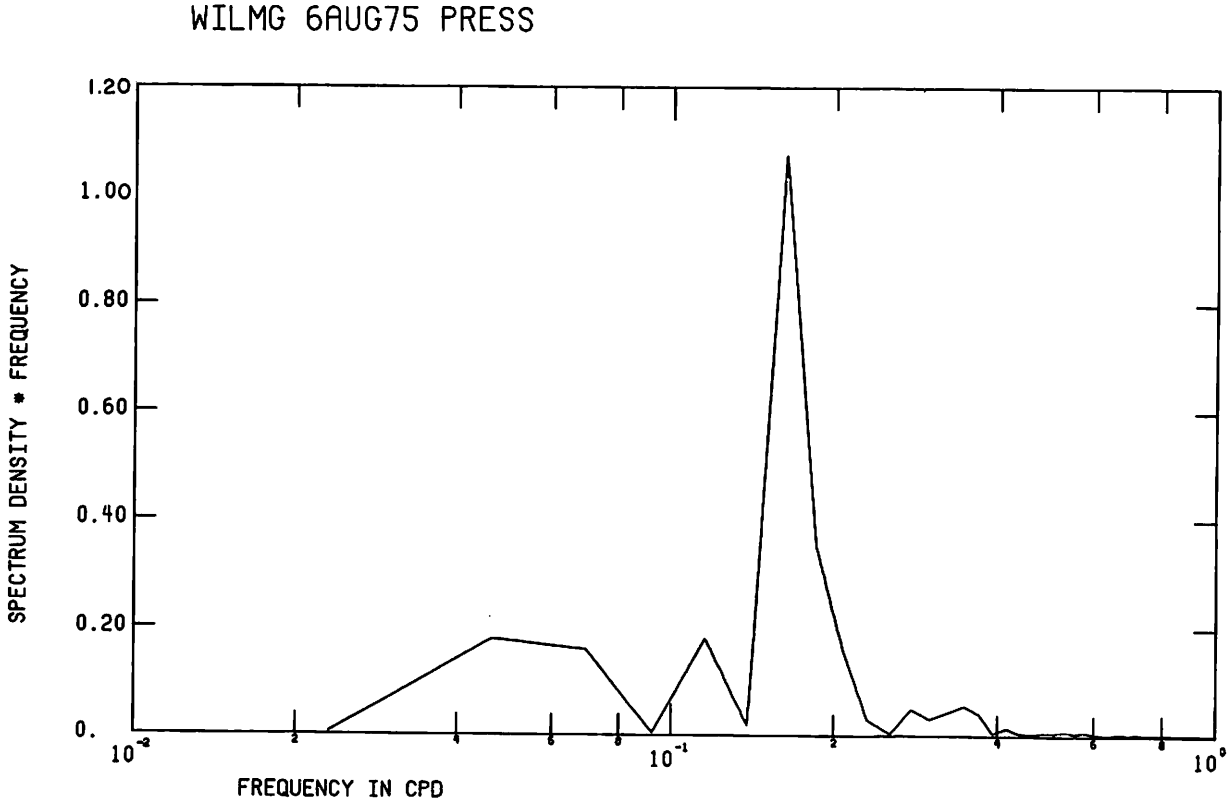

Figure 103 FFT of low pass temperature and pressure at Wilmington, Aug-Sept 1975

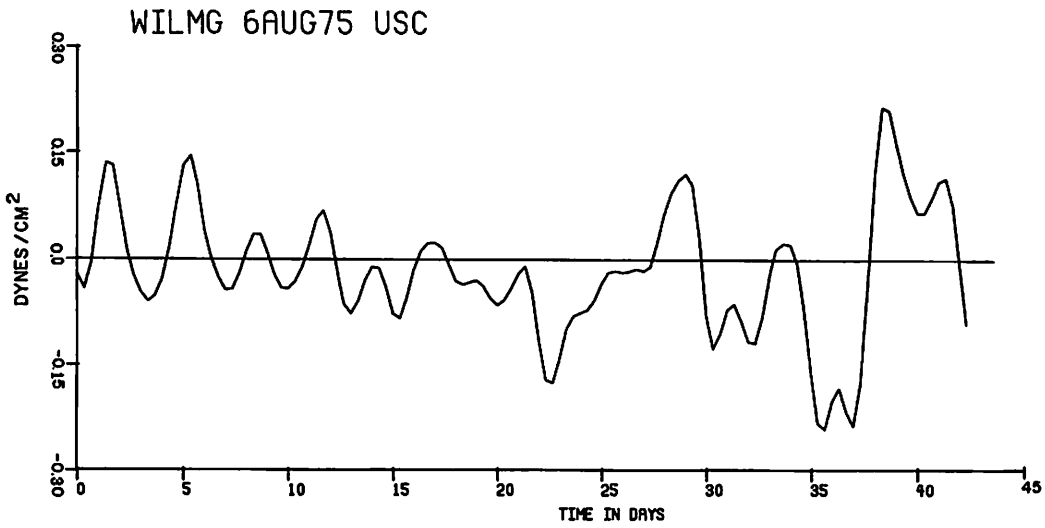

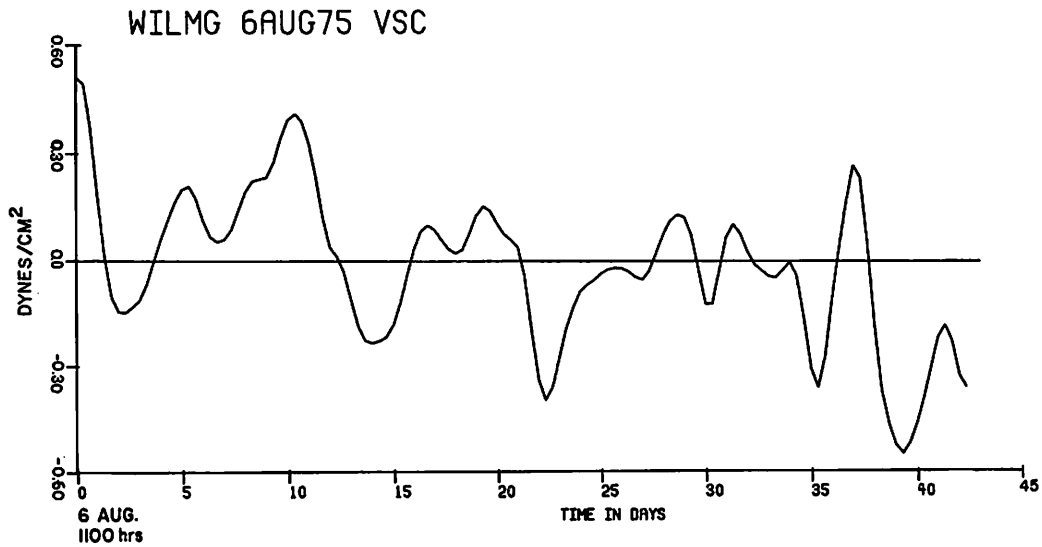

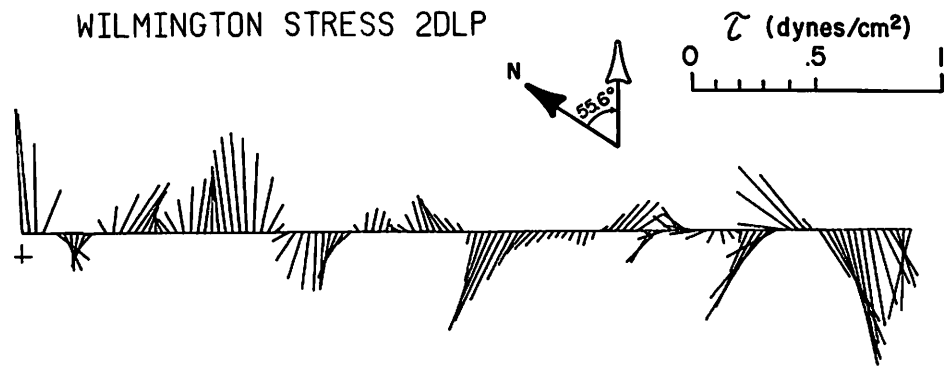

Figure 104 Low pass wind stress components and vectors at Wilmington, Aug-Sept 1975

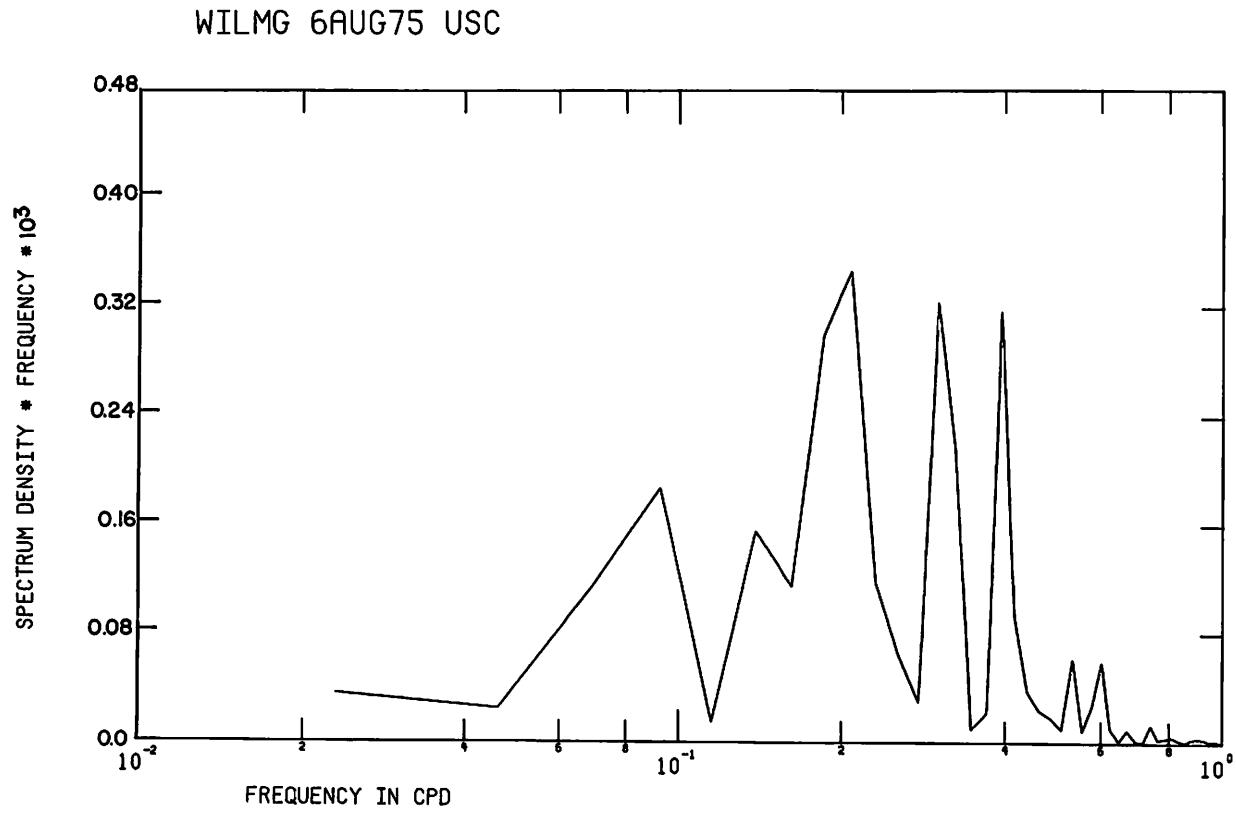

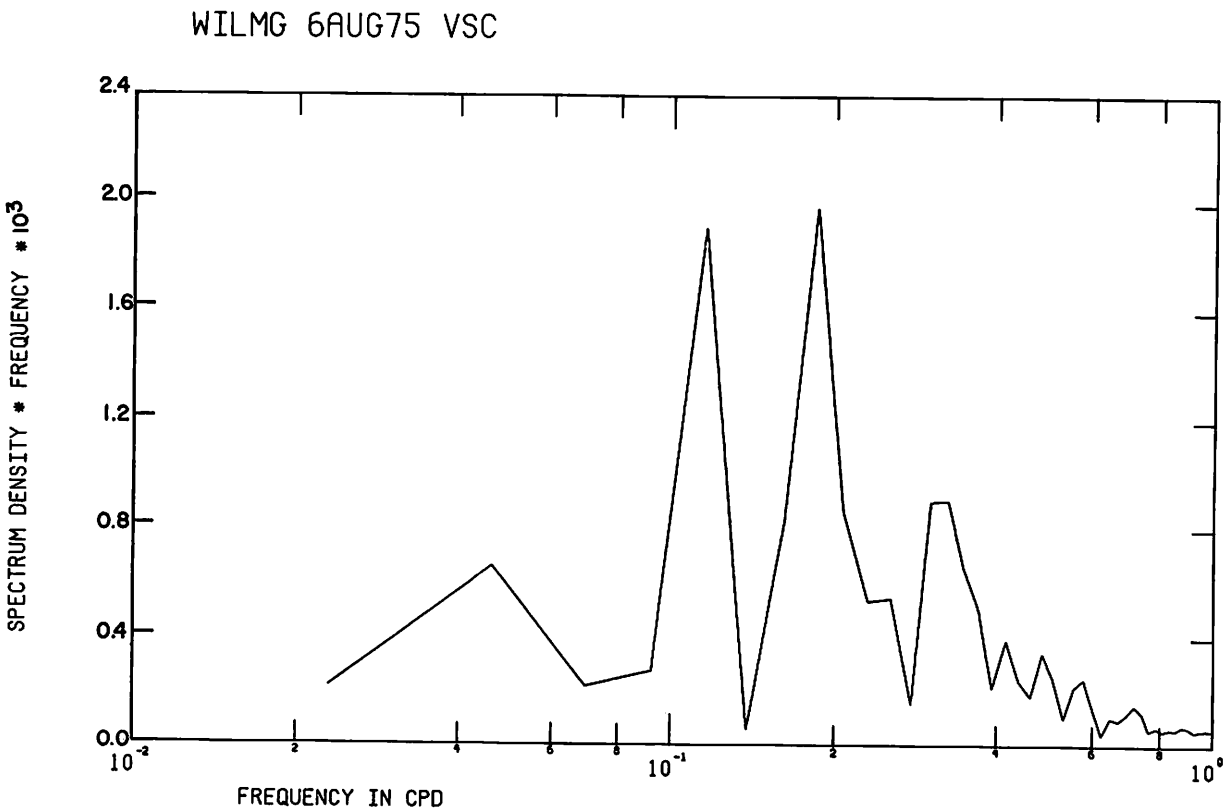

Figure 105 FFT of low pass wind stress components at Wilmington, Aug-Sept 1975

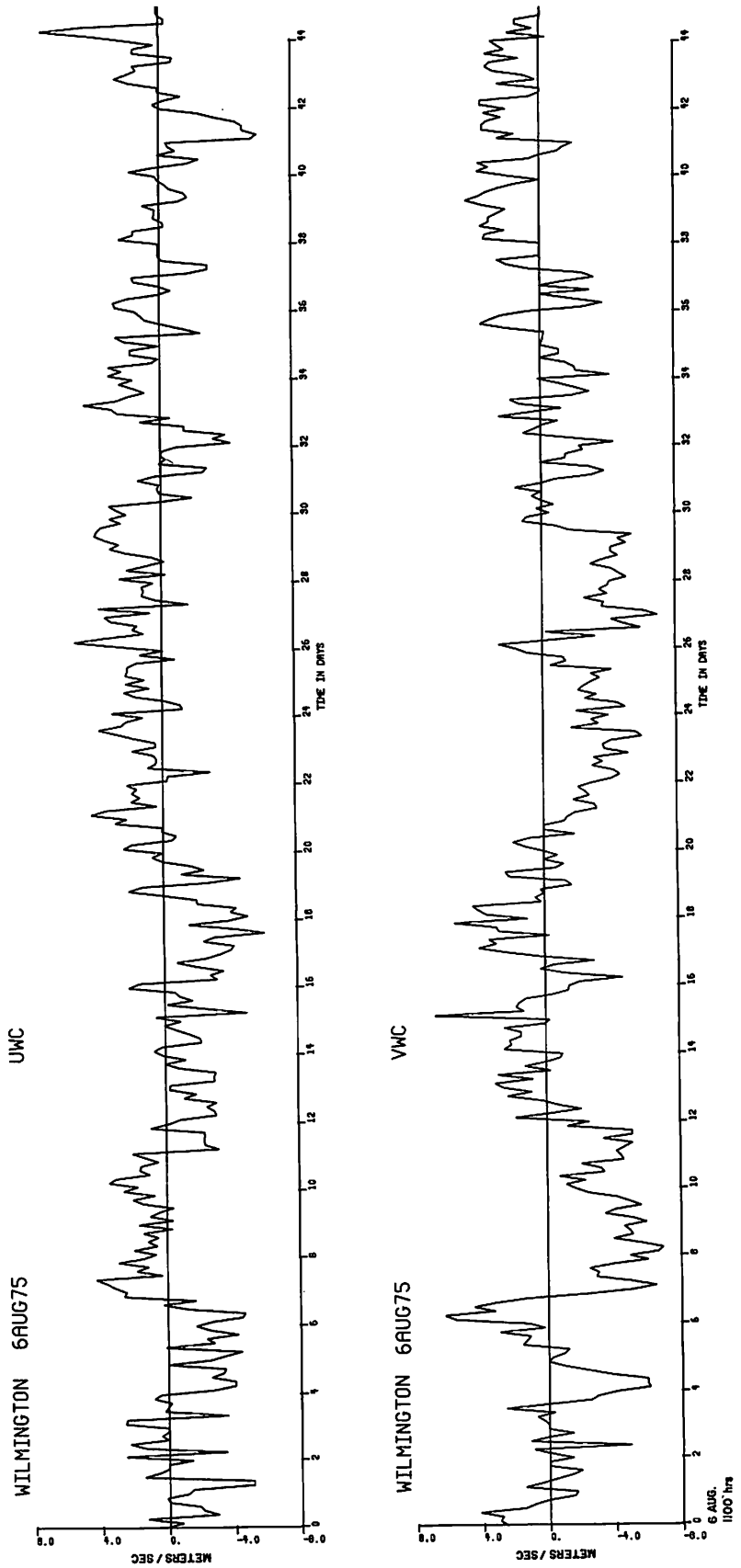

Figure 106 Unfiltered wind velocity components at Wilmington, Aug-Sept 1975

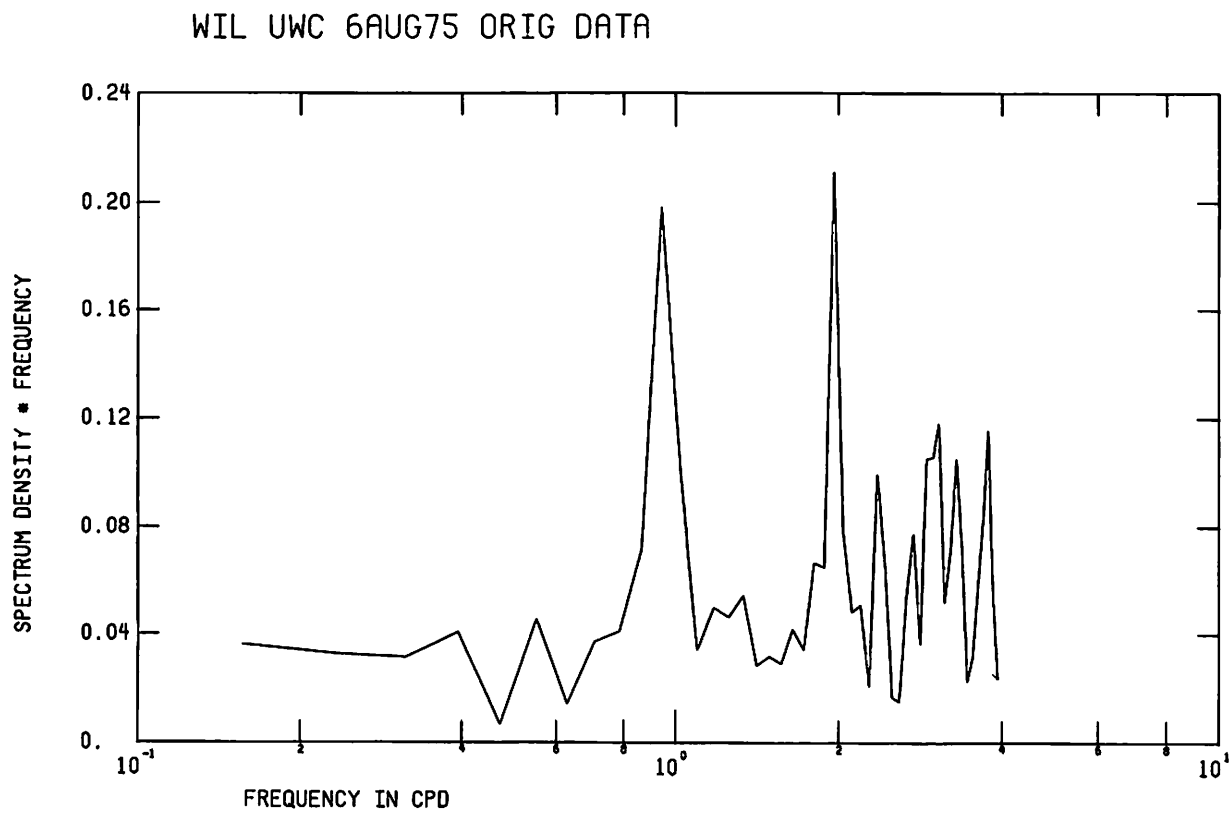

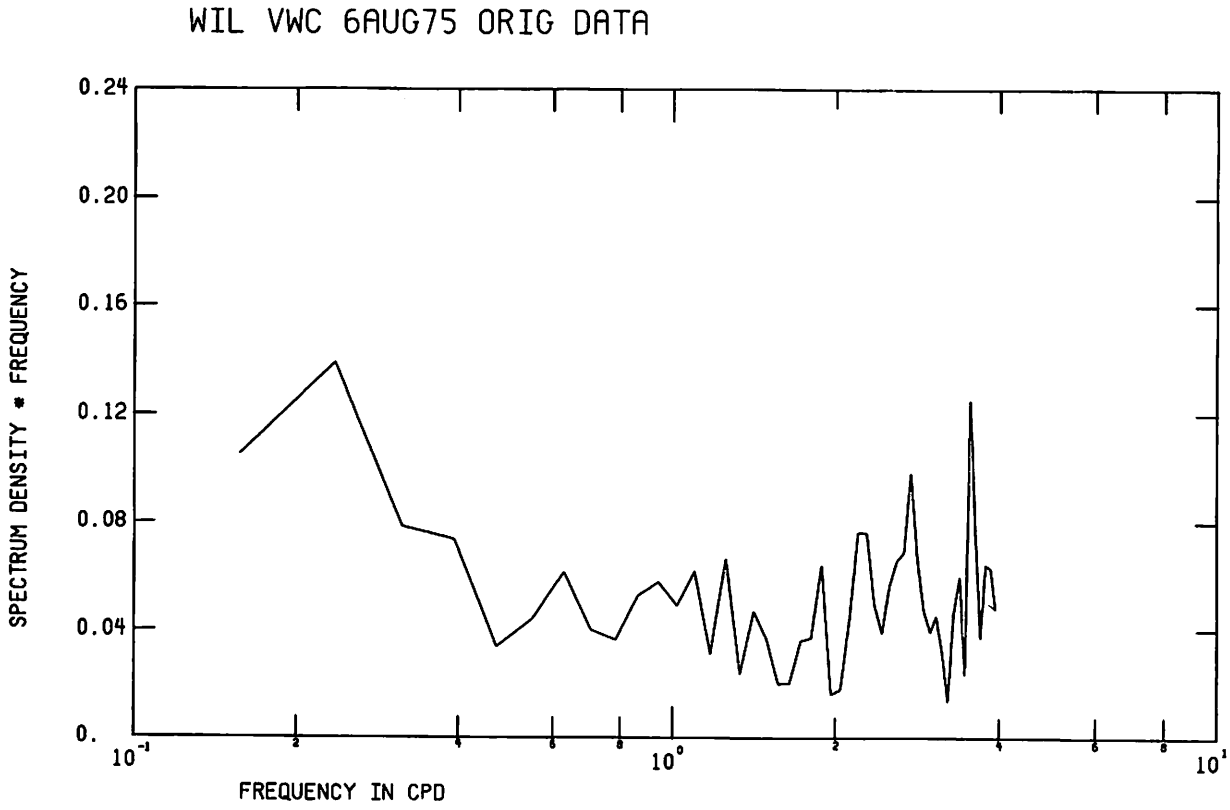

Figure 107 FFT of unfiltered wind velocity components at Wilmington, Aug-Sept 1975

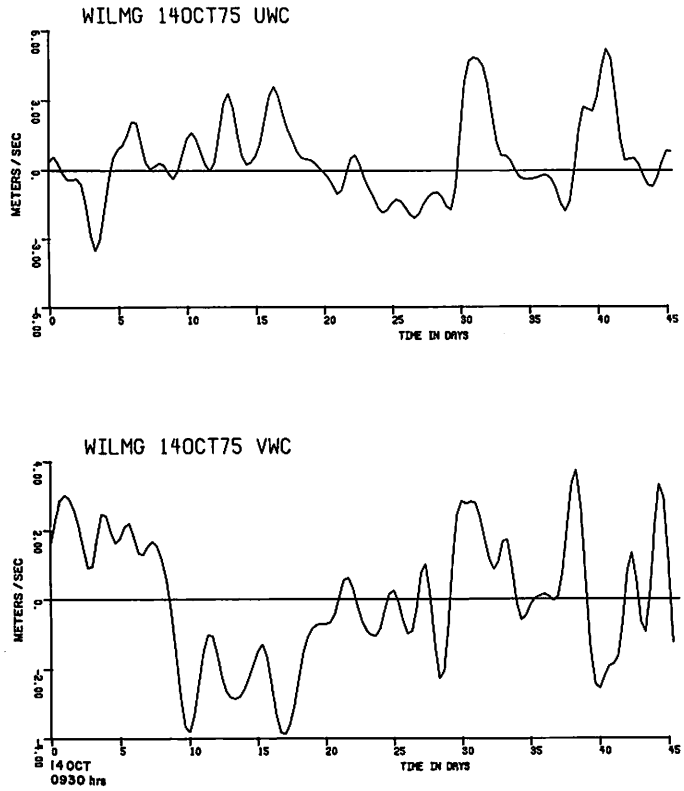

Figure 108 Low pass wind velocity components at Wilmington, Oct-Dec 1975

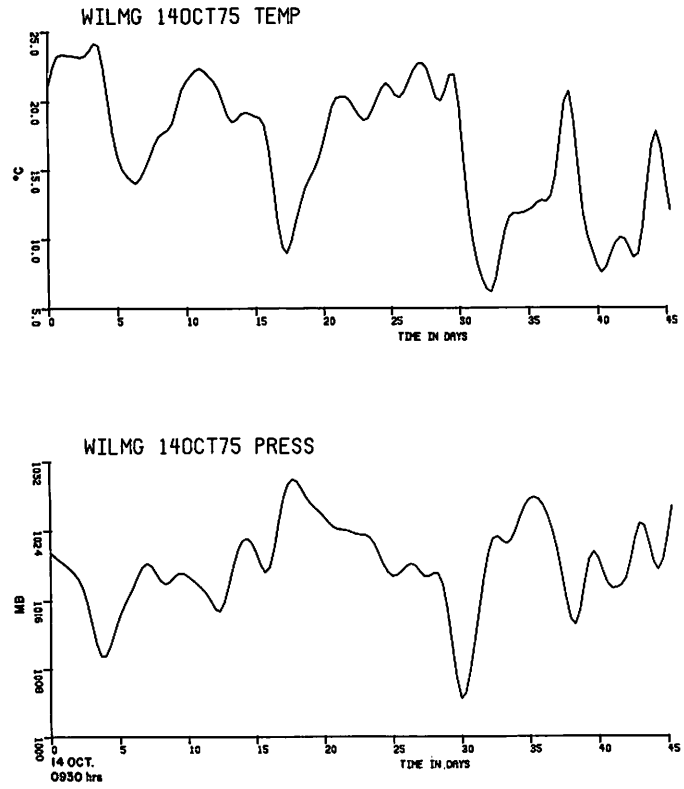

Figure 109 Low pass temperature and pressure at Wilmington, Oct-Dec 1975

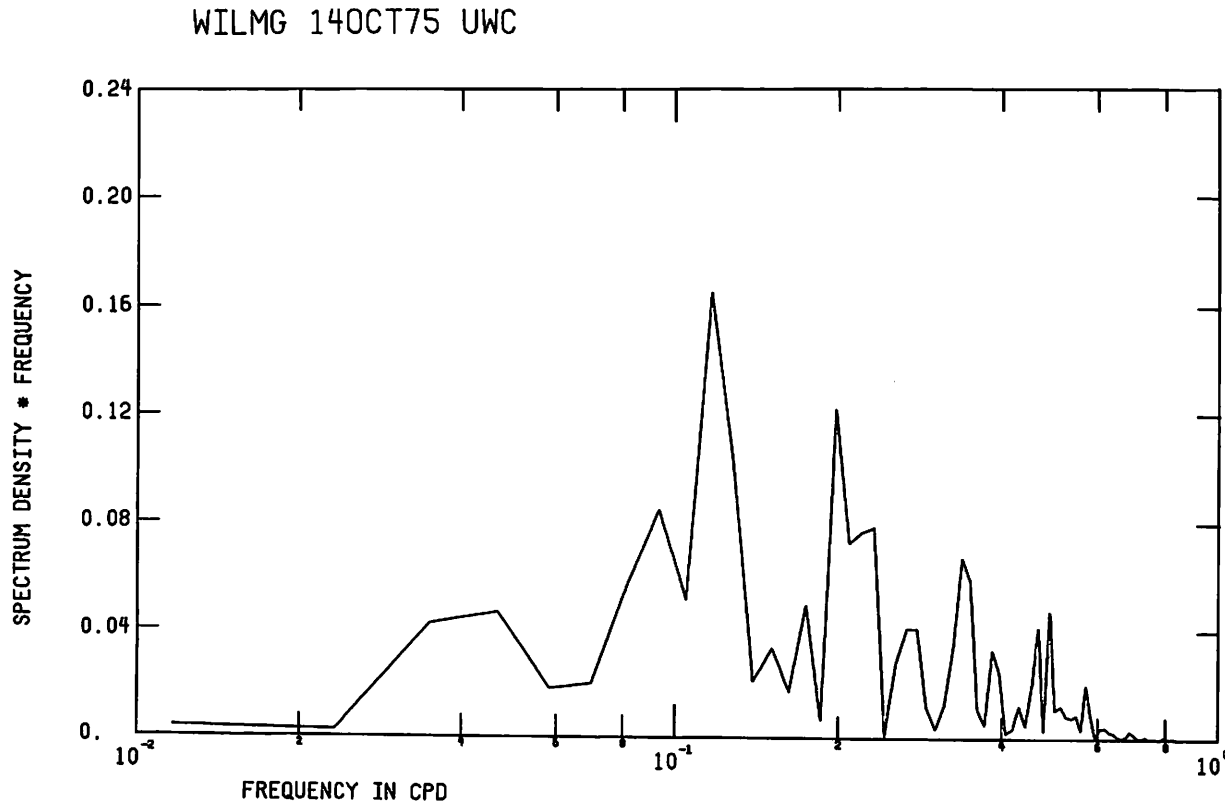

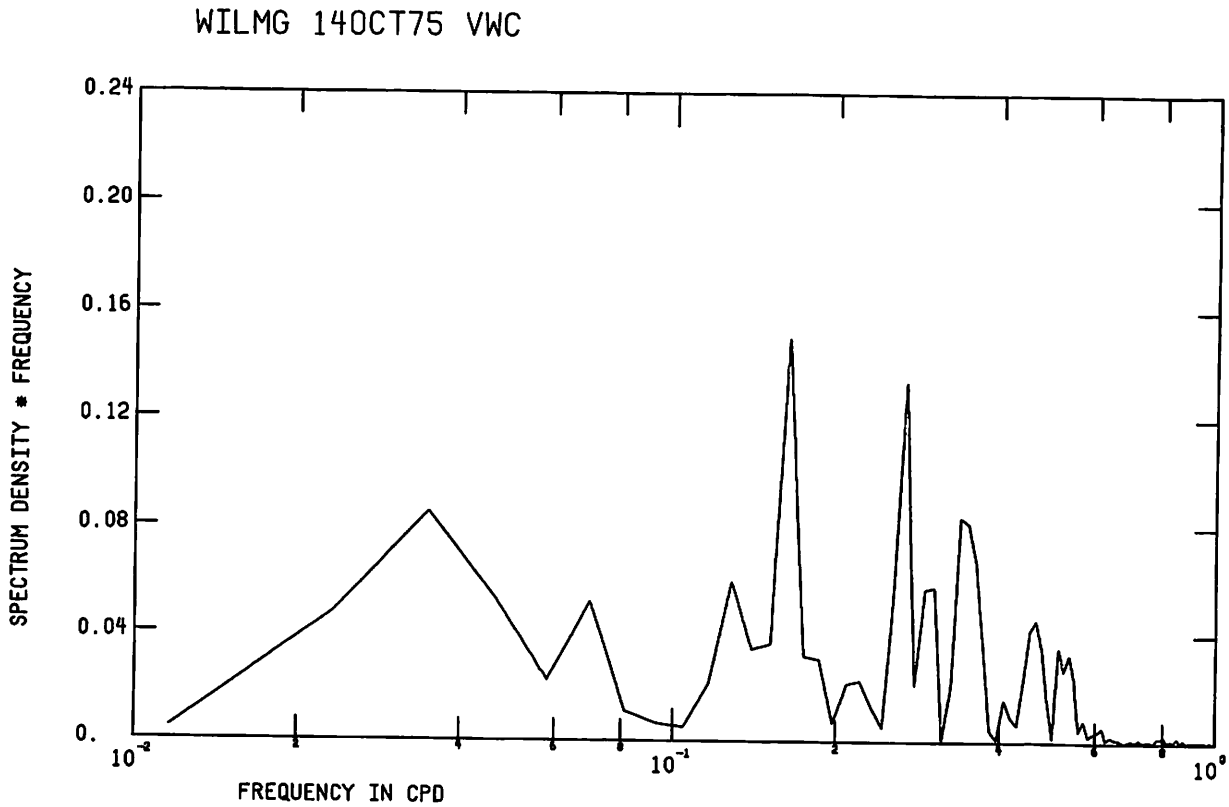

Figure 110 FFT of low pass wind velocity components at Wilmington, Oct-Dec 1975

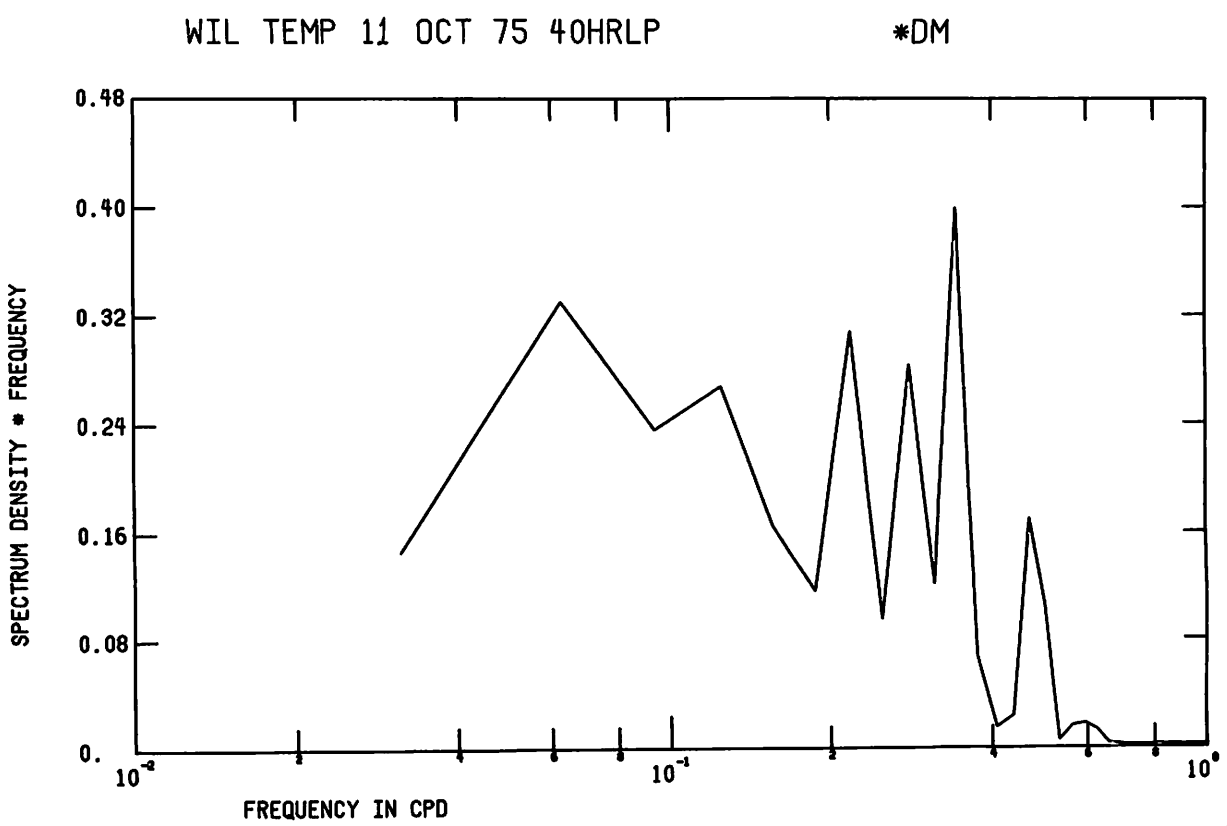

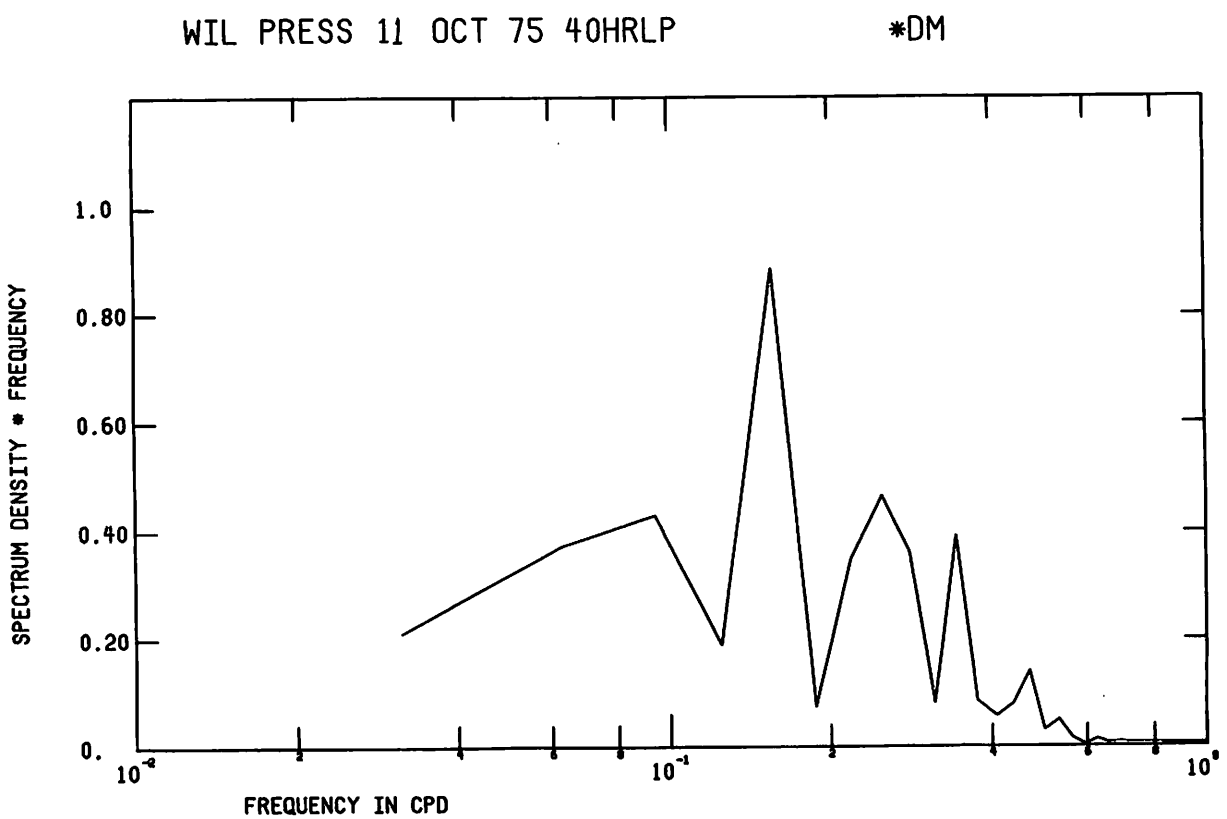

Figure 111 FFT of low pass temperature and pressure at Wilmington, Oct-Dec 1975

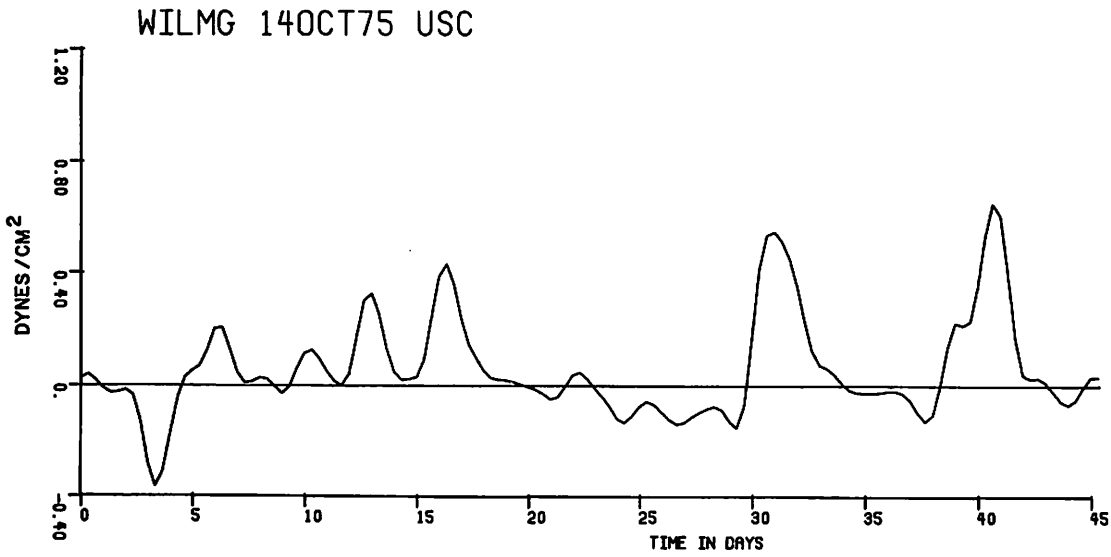

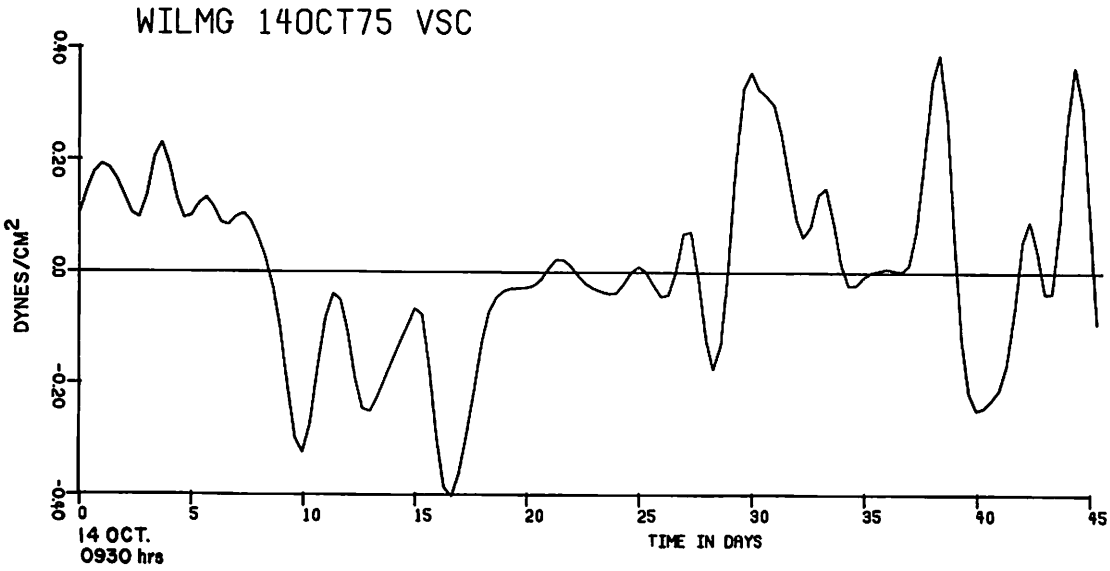

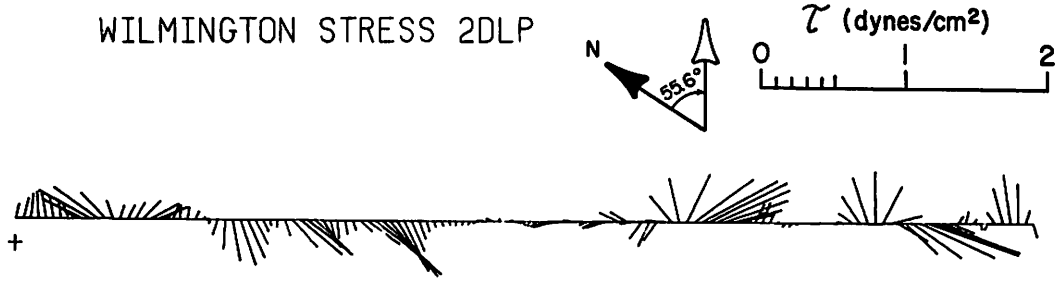

Figure 112 Los pass wind stress components and vectors at Wilmington, Oct-Dec 1975

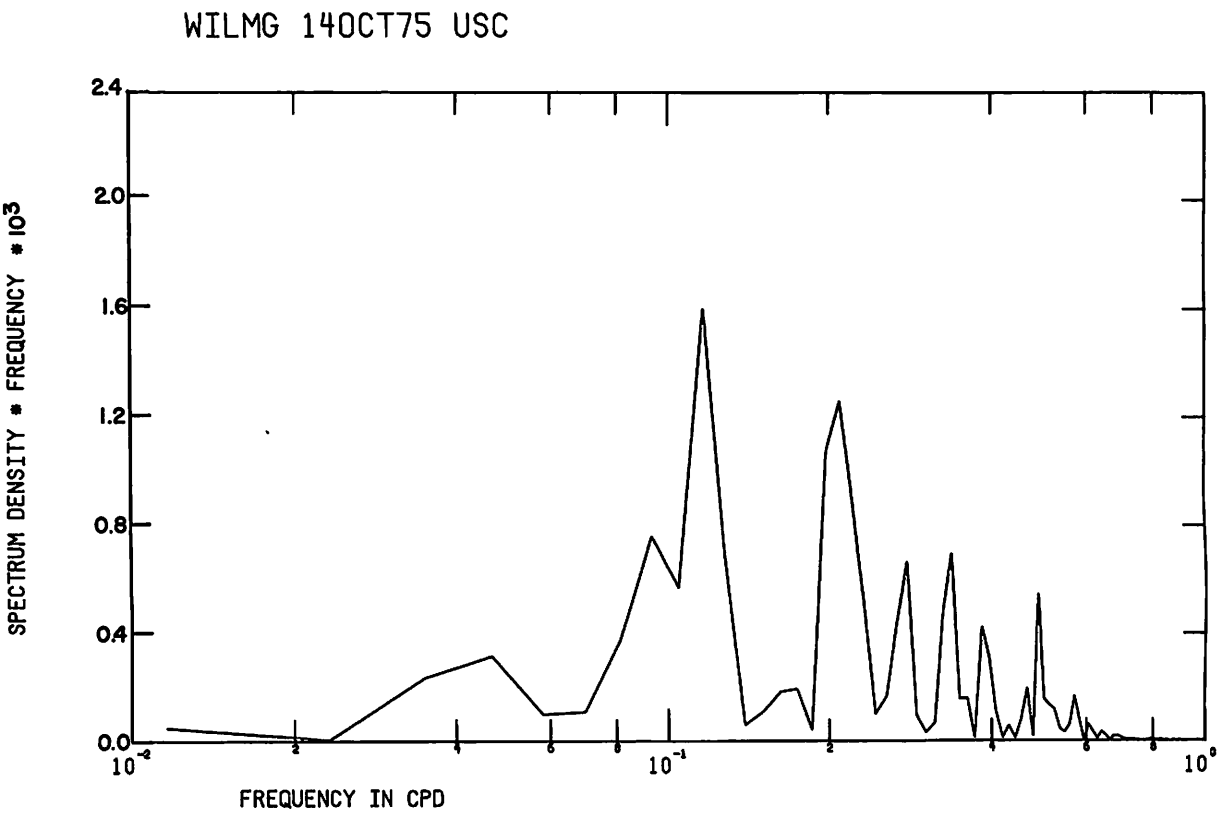

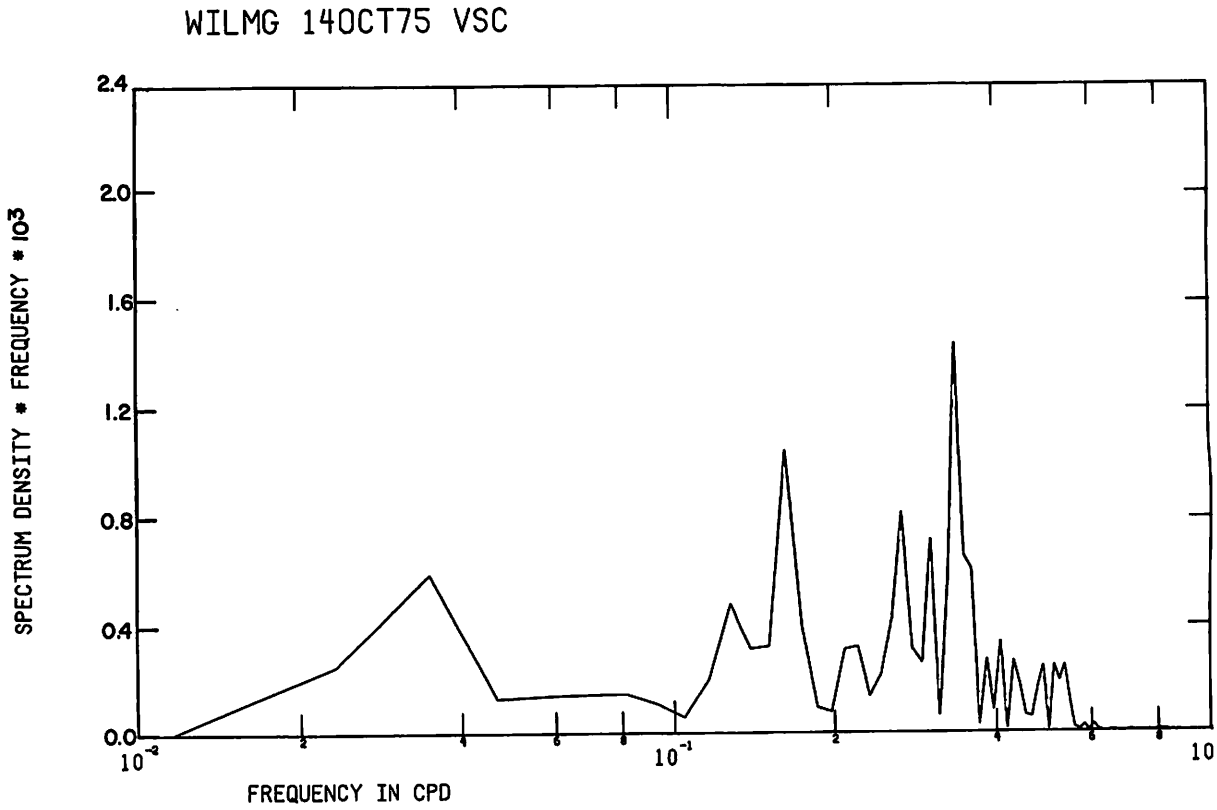

Figure 113 FFT of low pass wind stress components at Wilmington, Oct-Dec 1975

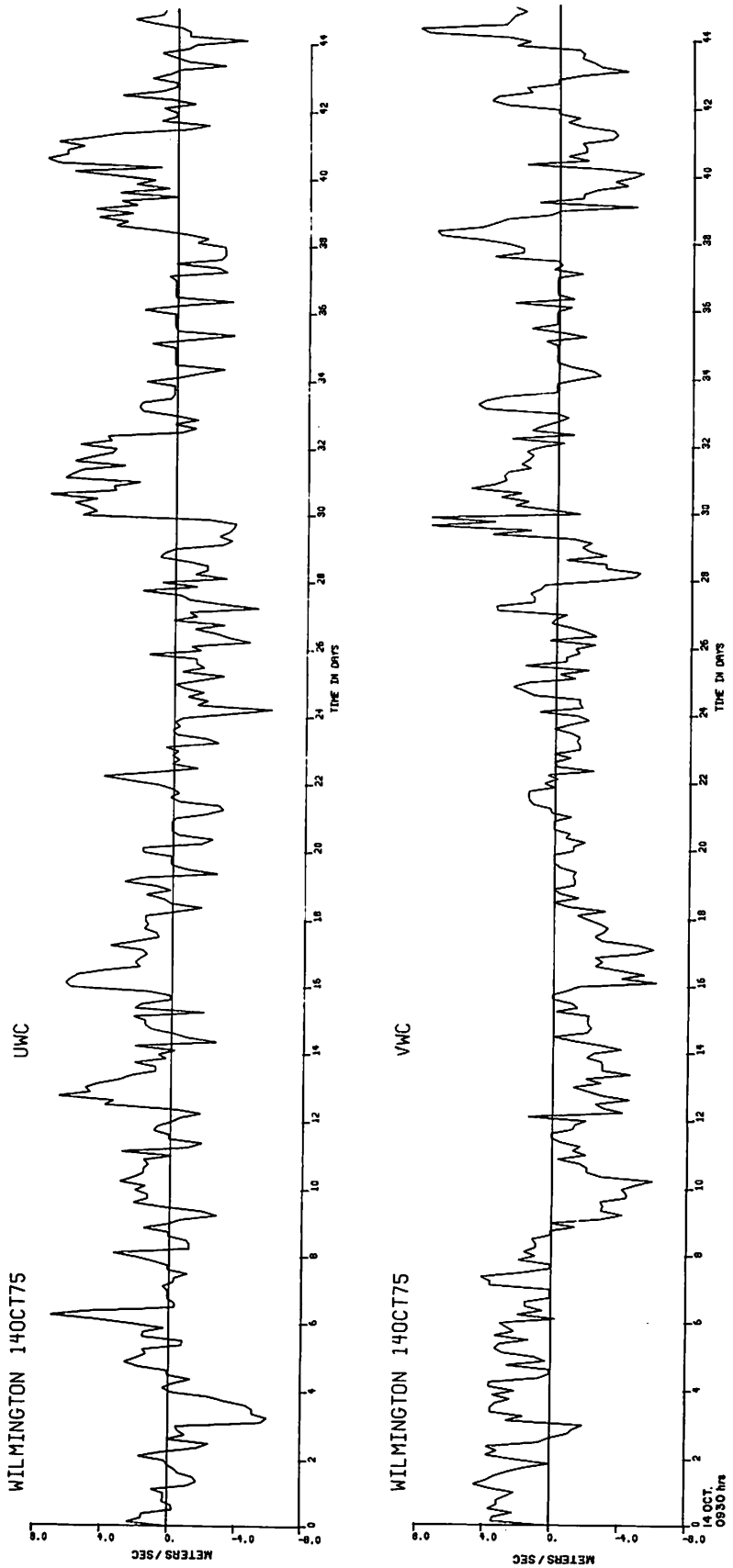

Figure 114 Unfiltered wind velocity components at Wilmington, Oct-Dec 1975

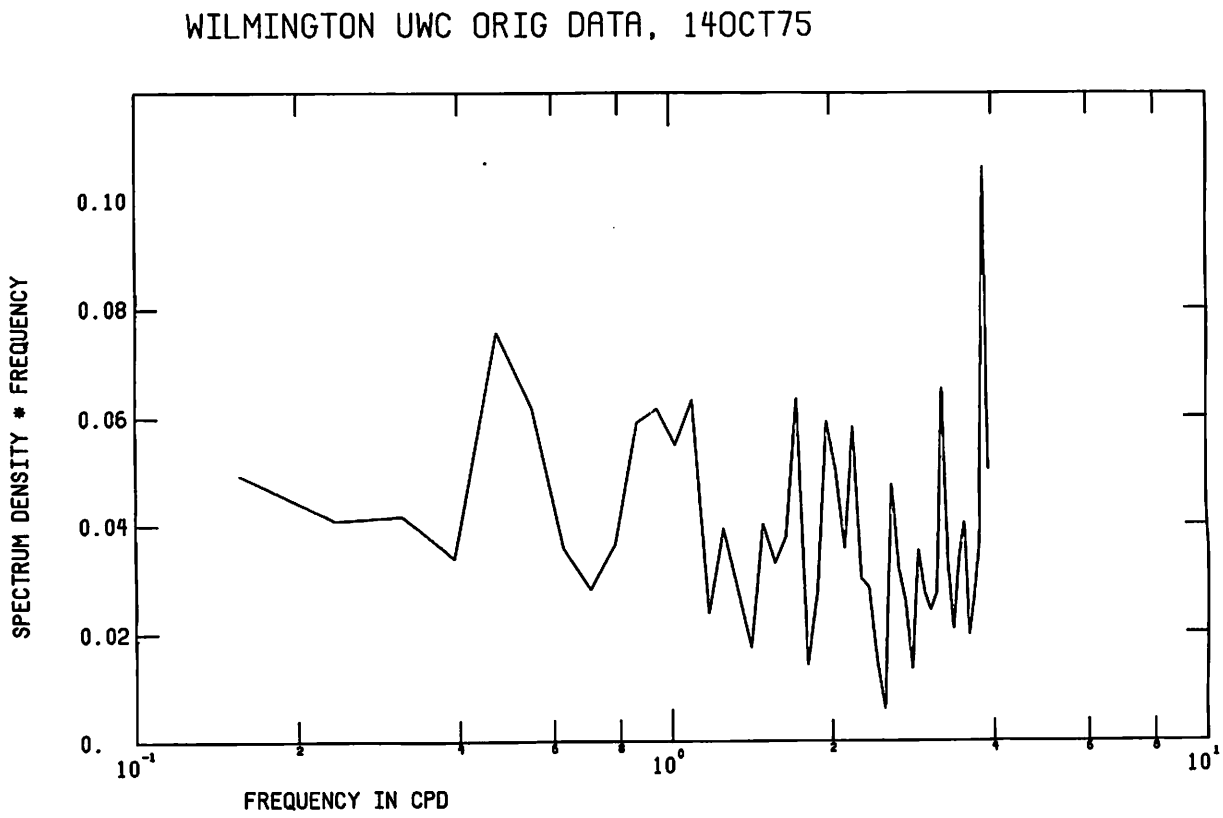

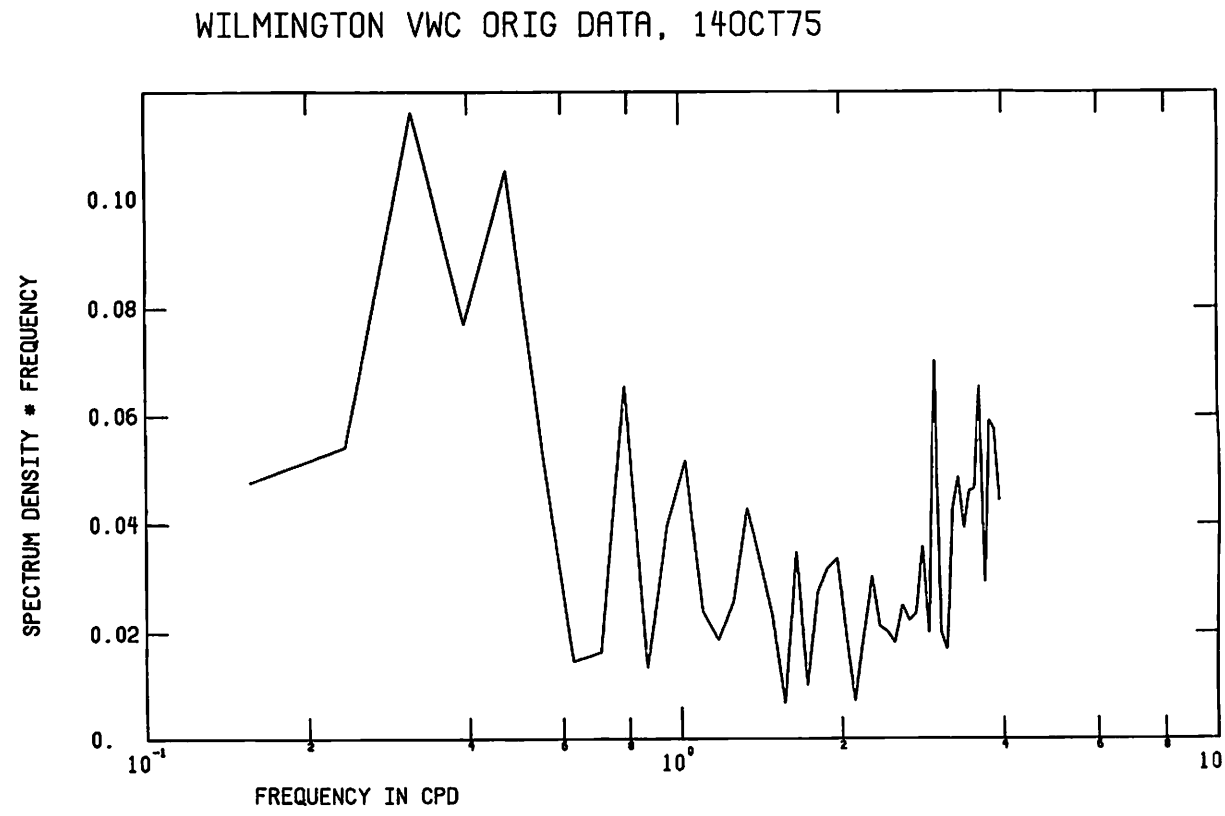

Figure 115 FFT of unfiltered wind velocity components at Wilmington, Oct-Dec 1975

VIII. Intravariable Comparisons Between Current and Meteorological Data

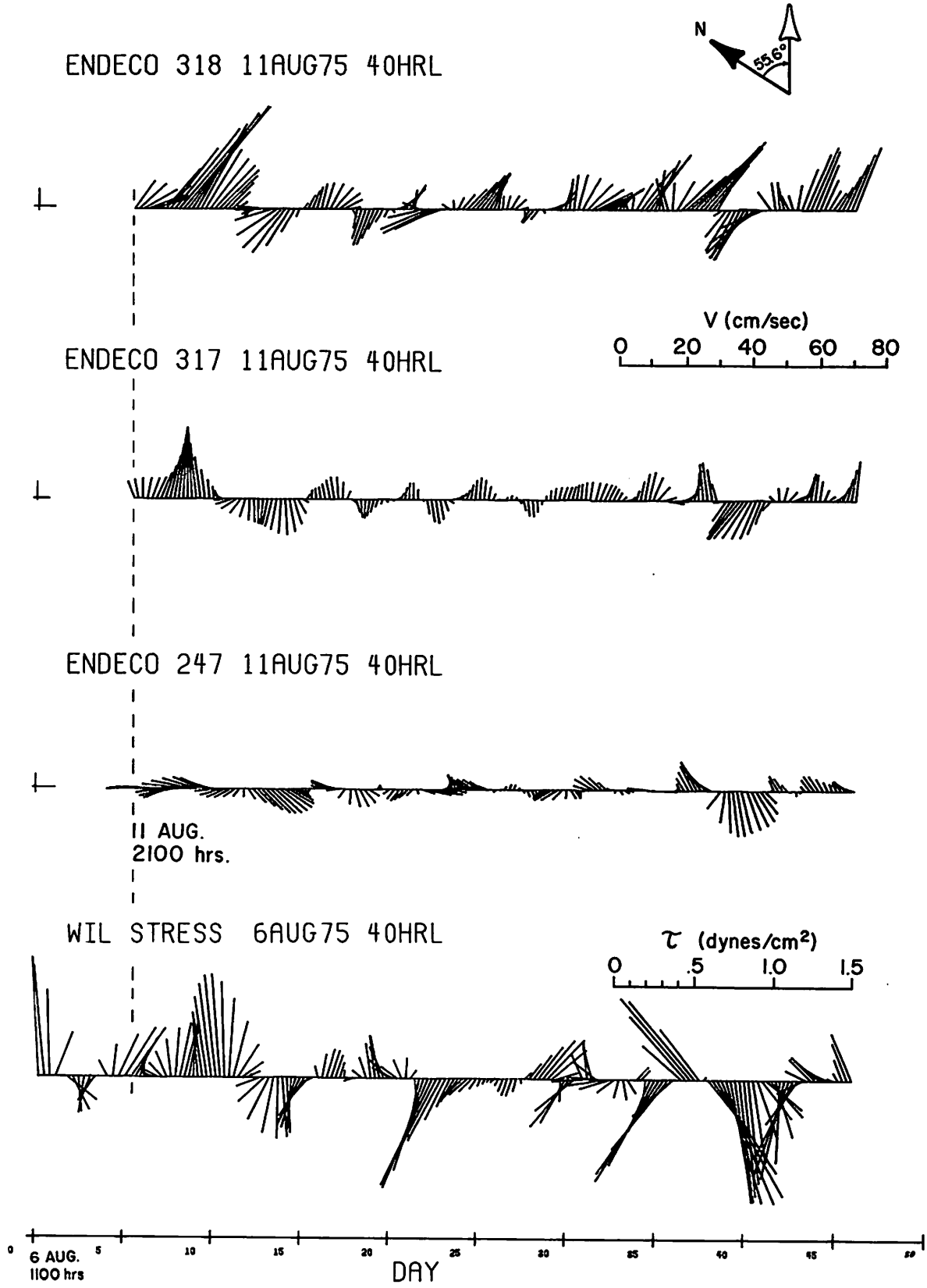

Figure 116 Comparison of low pass current vectors from meters Al_{top}, Al_{bot}, Bl_{bot} and the low pass wind stress vector at Wilmington, Aug - Sept 1975

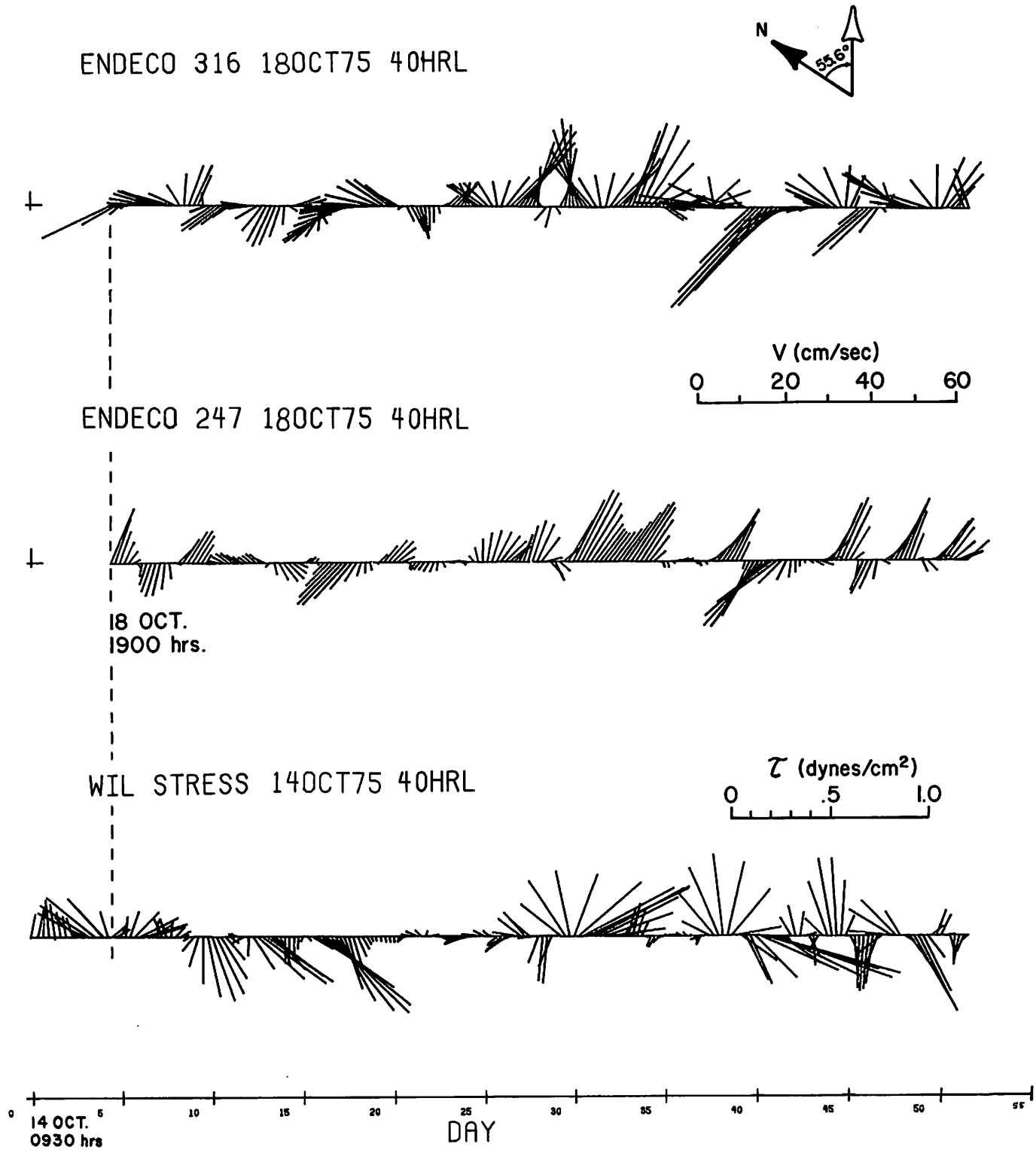

Figure 117 Comparison of low pass current vectors from meters $A2_{top}$ and $A2_{bot}$ and the low pass wind stress vector at Wilmington, Oct - Dec 1975

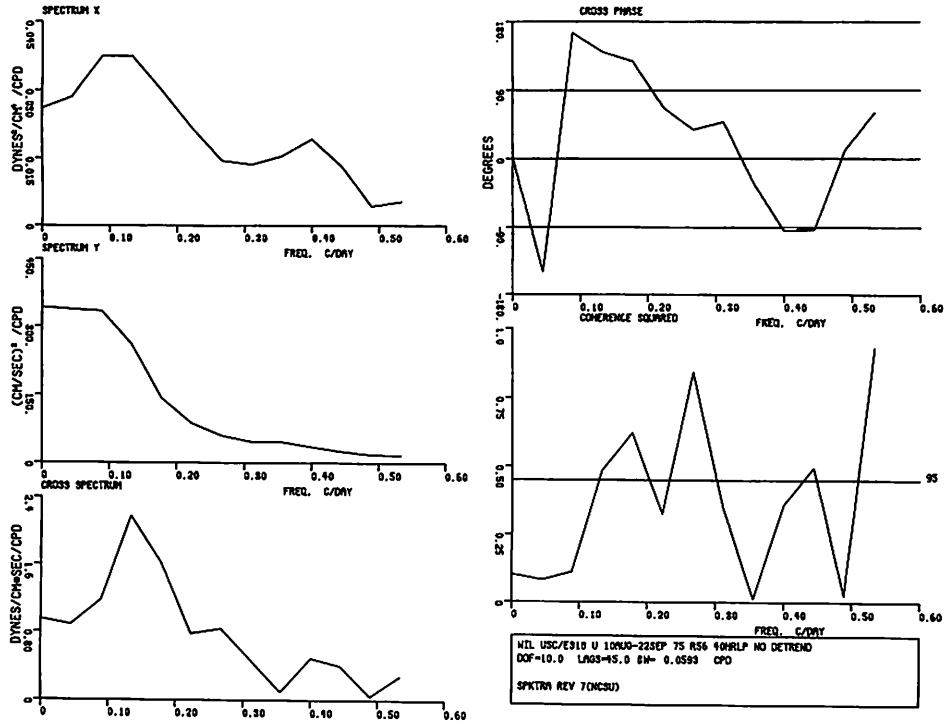

Figure 118 Spectra of the low pass wind stress u component at Wilmington and the low pass current velocity u component from meter Al_{top} Aug-Sept 1975

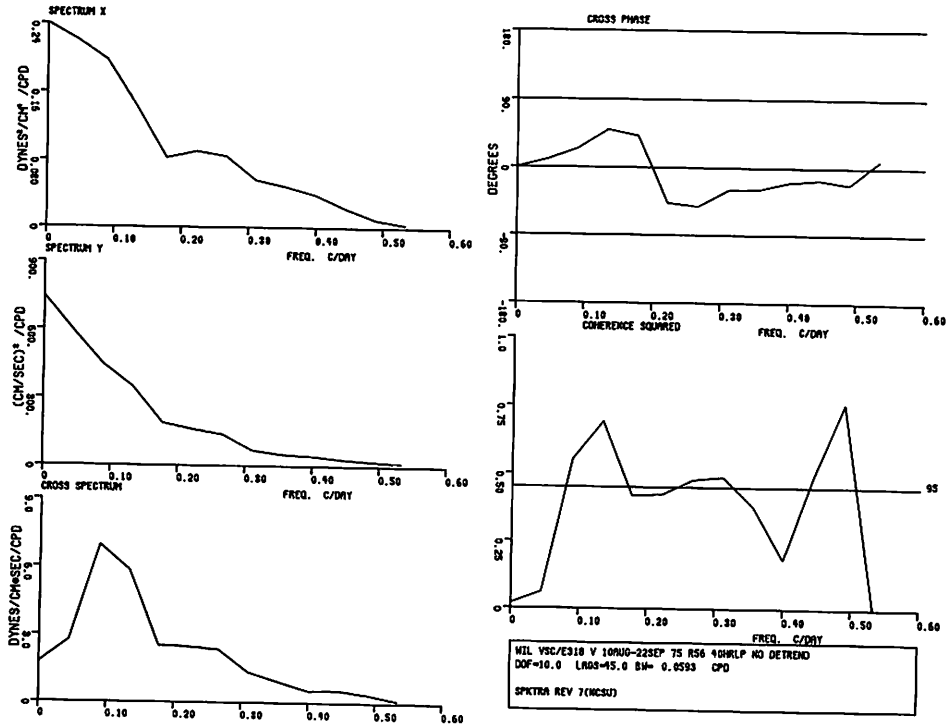

Figure 119 Spectra of the low pass wind stress v component at Wilmington and the low pass current velocity v component from meter Al_{top} Aug-Sept 1975

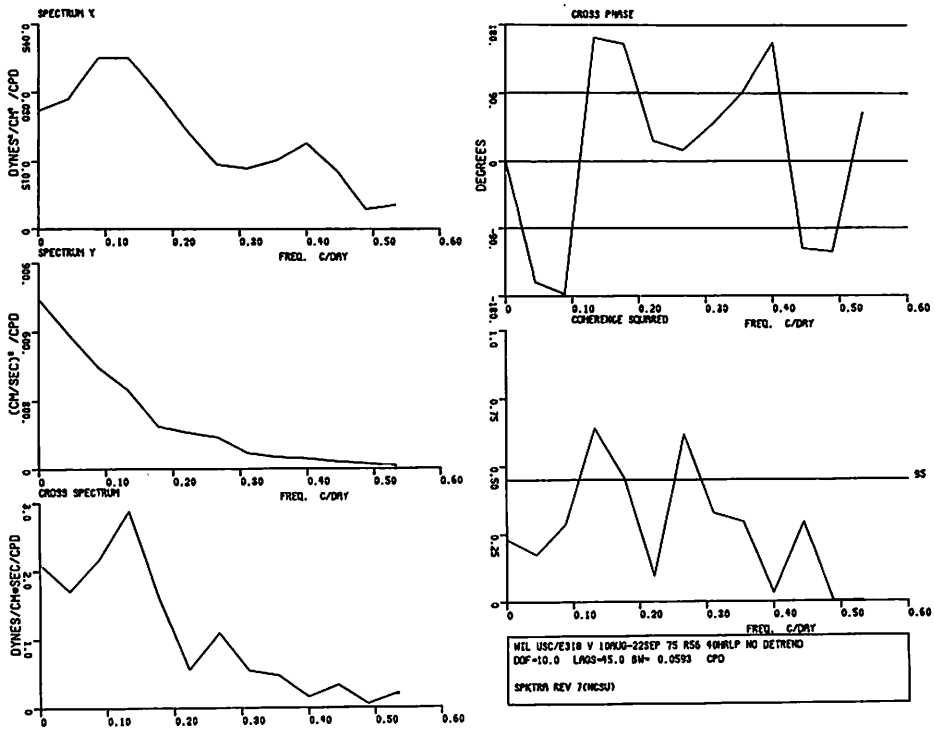

Figure 120 Spectra of the low pass wind stress u component at Wilmington and the low pass current velocity v component from meter Al_{top} Aug-Sept 1975

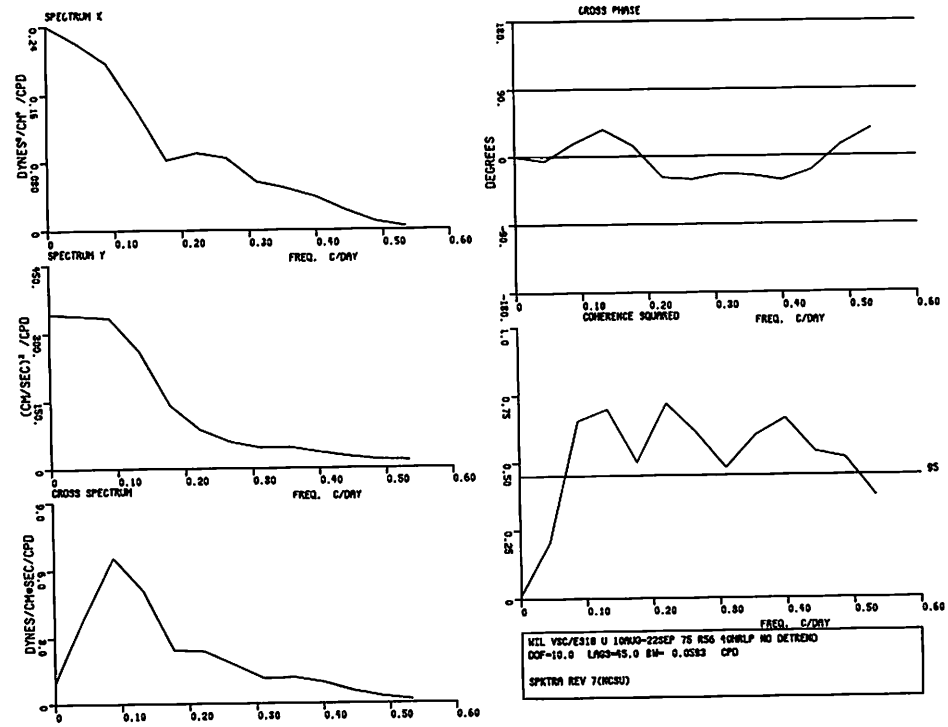

Figure 121 Spectra of the low pass wind stress v component at Wilmington and the low pass current velocity u component from meter Al_{top} Aug-Sept 1975

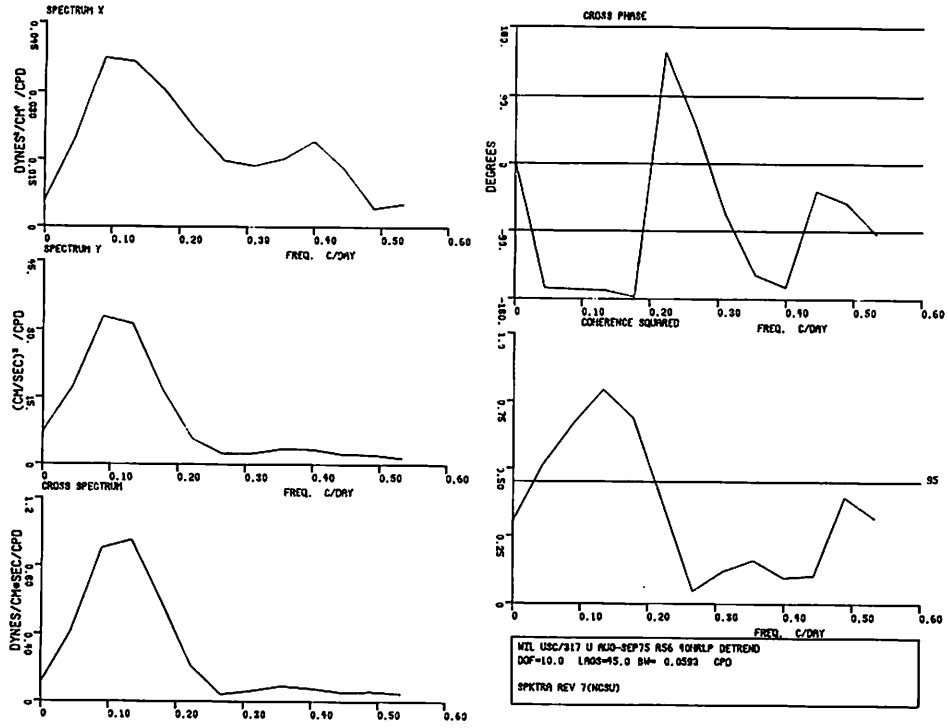

Figure 122 Spectra of the low pass wind stress u component at Wilmington and the low pass current velocity u component from meter Al_{bot} Aug-Sept 1975 (detrended)

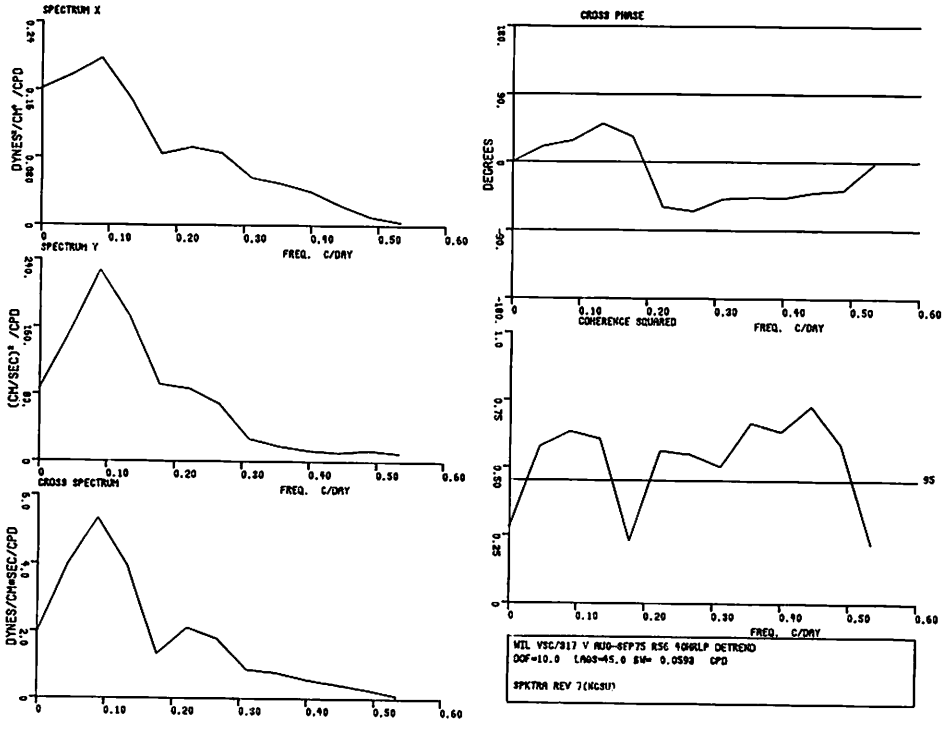

Figure 123 Spectra of the low pass wind stress v component at Wilmington and the low pass current velocity v component from meter Al_{bot} Aug-Sept 1975 (detrended)

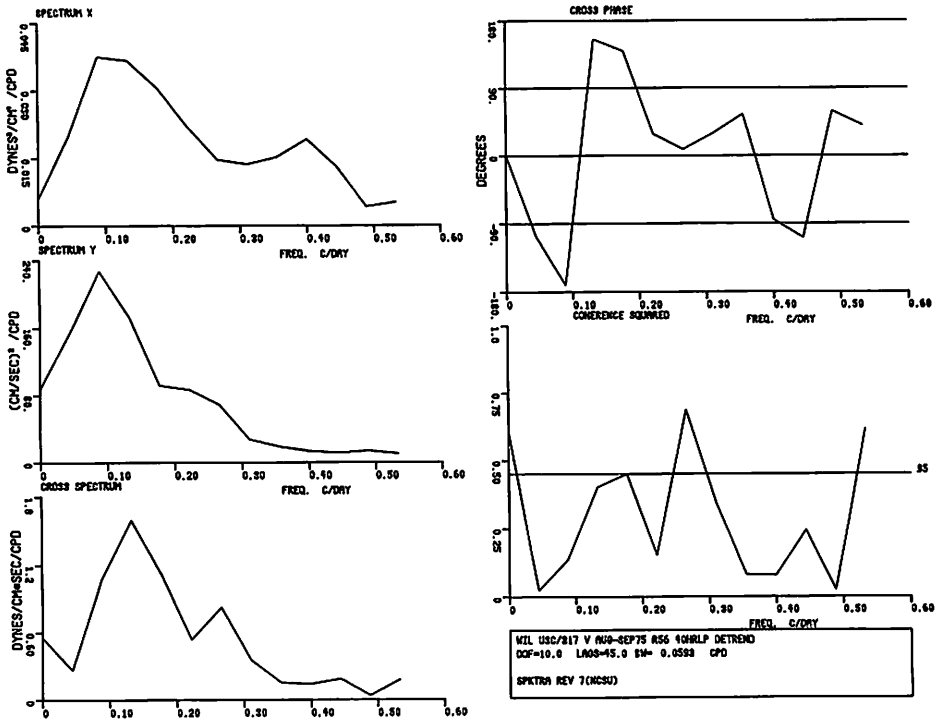

Figure 124 Spectra of the low pass wind stress u component at Wilmington and the low pass current velocity v component from meter Al_{bot} Aug-Sept 1975 (detrended)

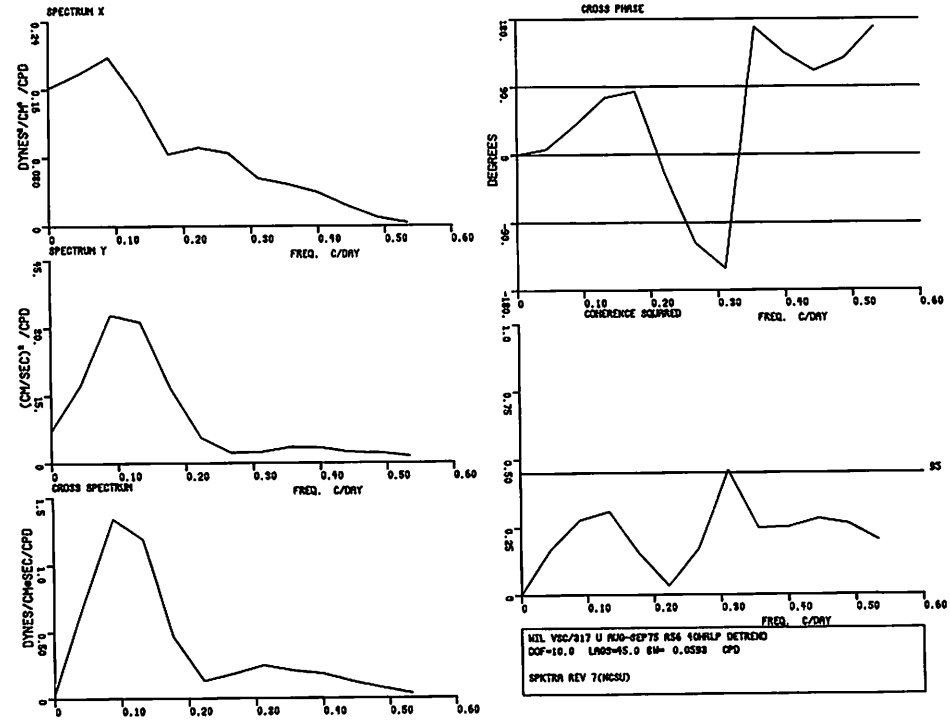

Figure 125 Spectra of the low pass wind stress v component at Wilmington and the low pass current velocity u component from meter Al_{bot} Aug-Sept 1975 (detrended)

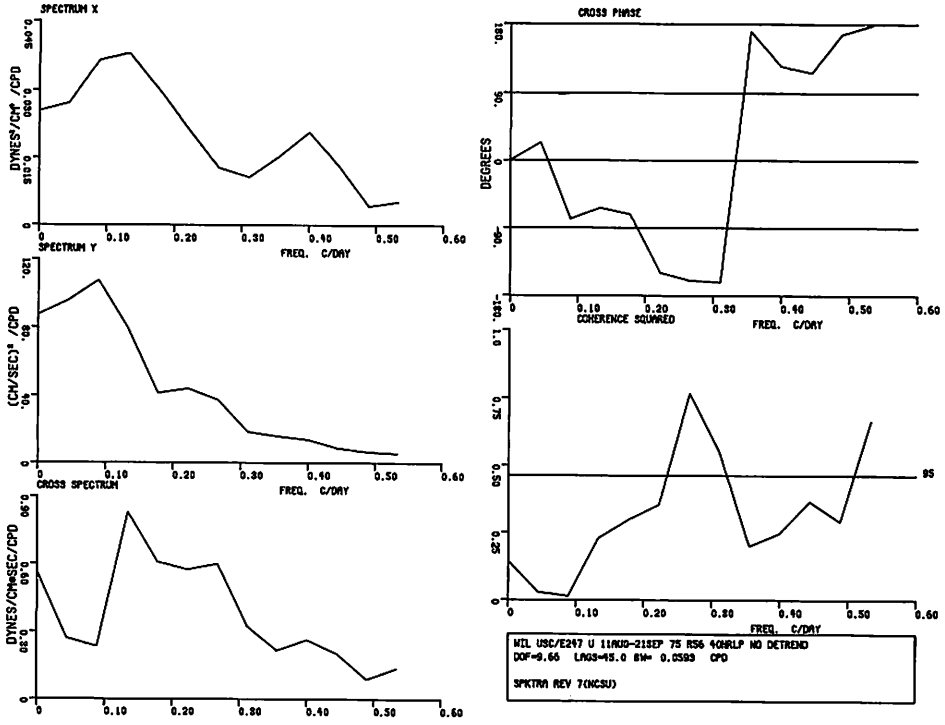

Figure 126 Spectra of the low pass wind stress u component at Wilmington and the low pass current velocity u component from meter Bl_{bot} Aug-Sept 1975

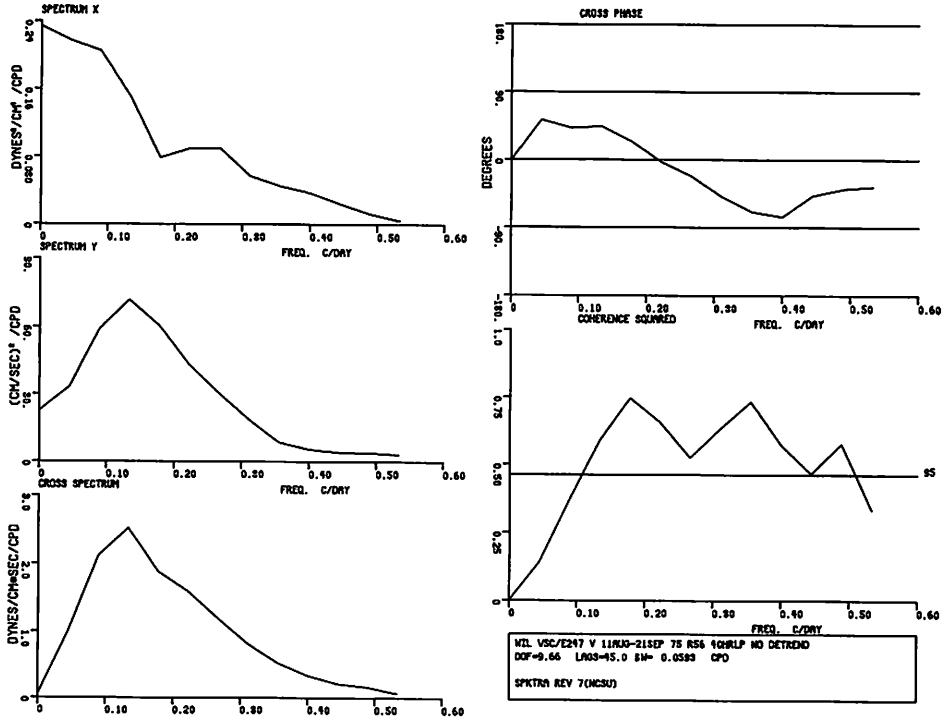

Figure 127 Spectra of the low pass wind stress v component at Wilmington and the low pass current velocity v component from meter Bl_{bot} Aug-Sept 1975

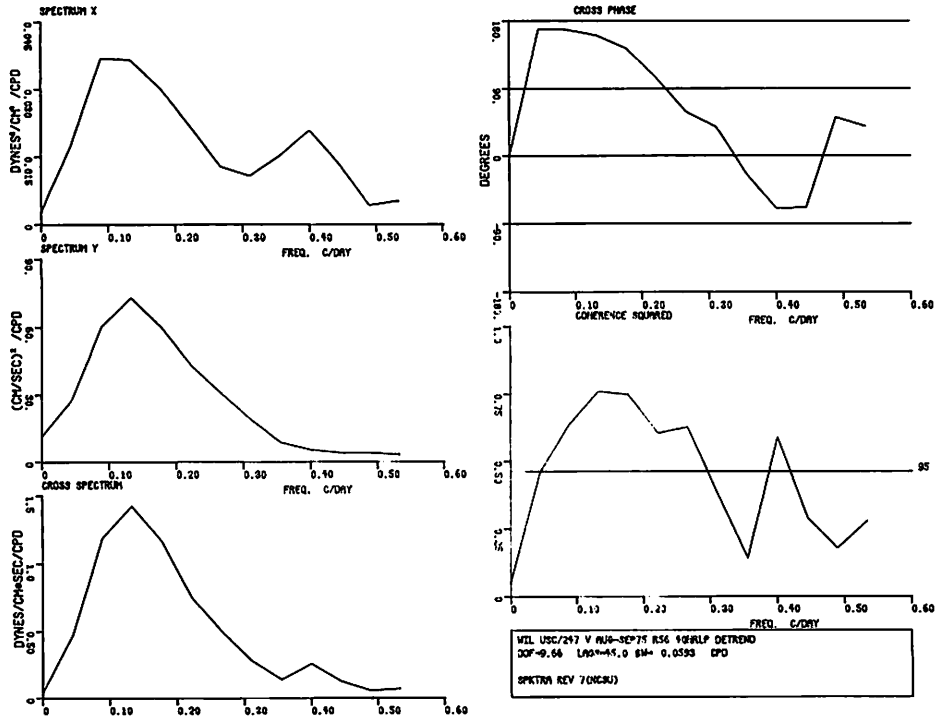

Figure 128 Spectra of the low pass wind stress u component at Wilmington and the low pass current velocity v component from meter Bl_{bot} Aug-Sept 1975 (detrended)

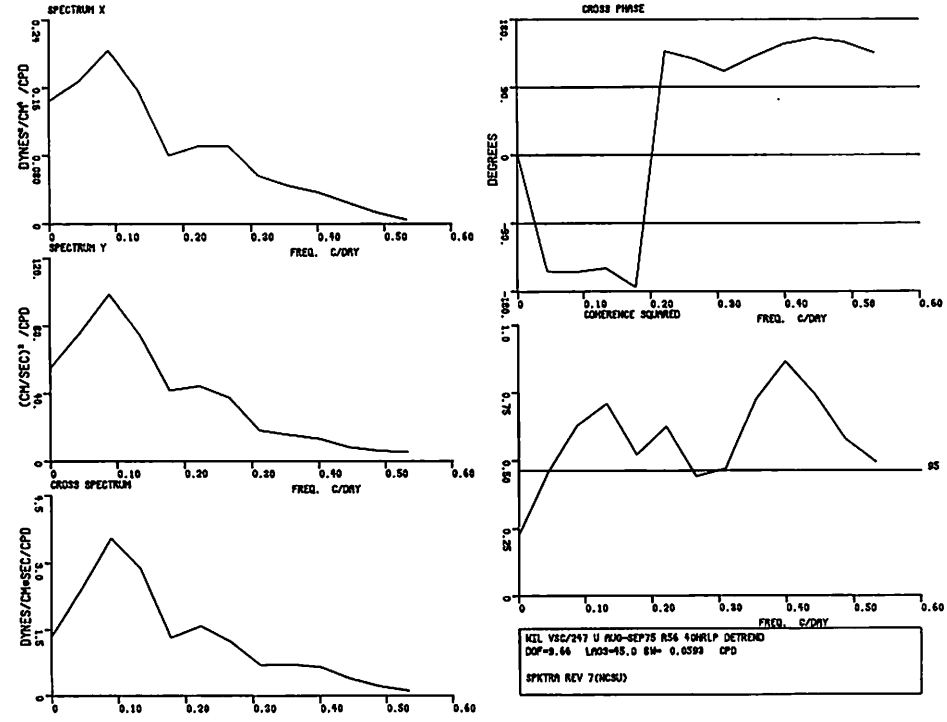

Figure 129 Spectra of the low pass wind stress v component at Wilmington and the low pass current velocity u component from meter Bl_{bot} Aug-Sept 1975 (detrended)

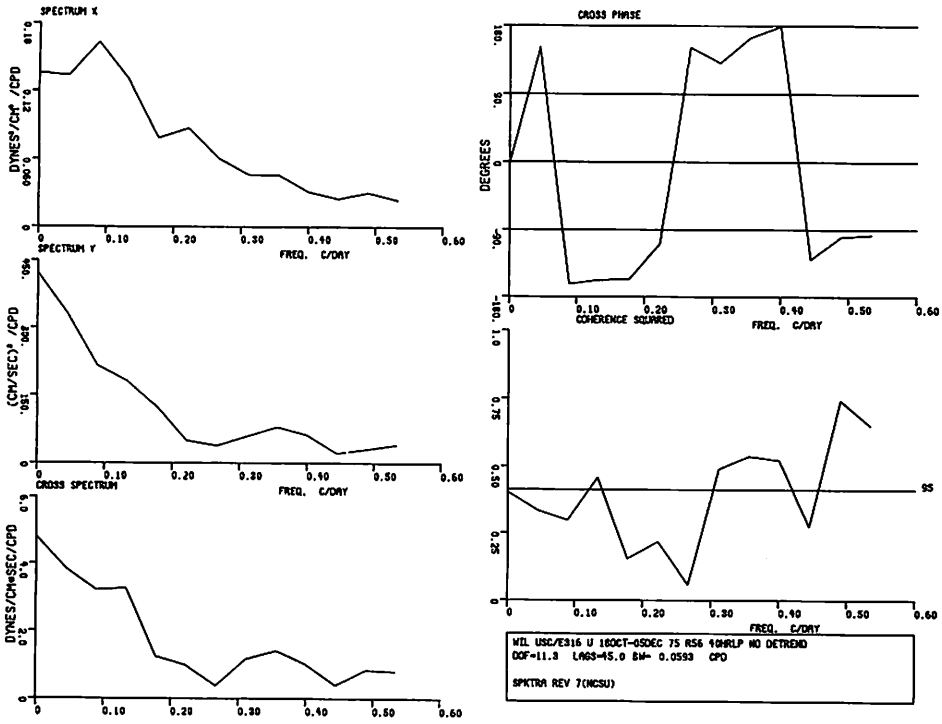

Figure 130 Spectra of the low pass wind stress u component at Wilmington and the low pass current velocity u component from meter $A2_{top}$ Oct-Dec 1975

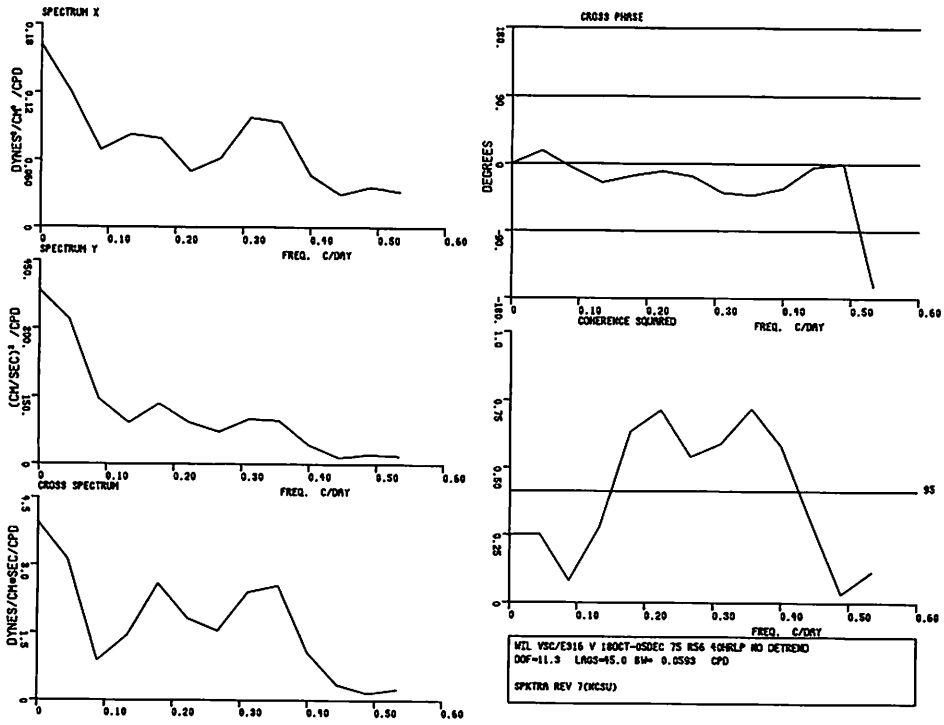

Figure 131 Spectra of the low pass wind stress v component at Wilmington and the low pass current velocity v component from meter $A2_{top}$ Oct-Dec 1975

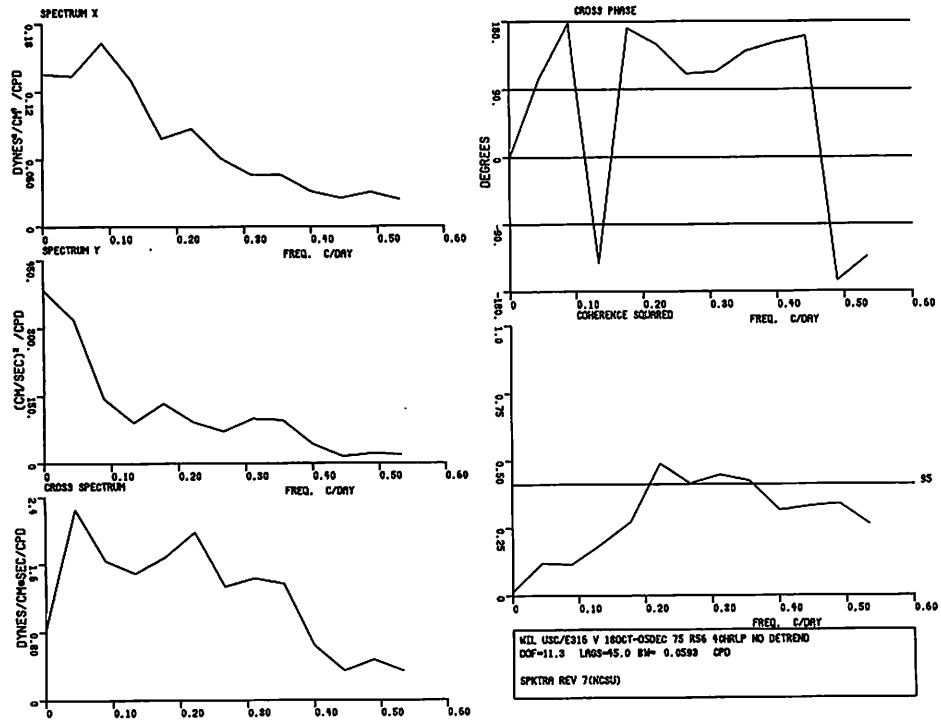

Figure 132 Spectra of the low pass wind stress u component at Wilmington and the low pass current velocity v component from meter $A2_{top}$ Oct-Dec 1975

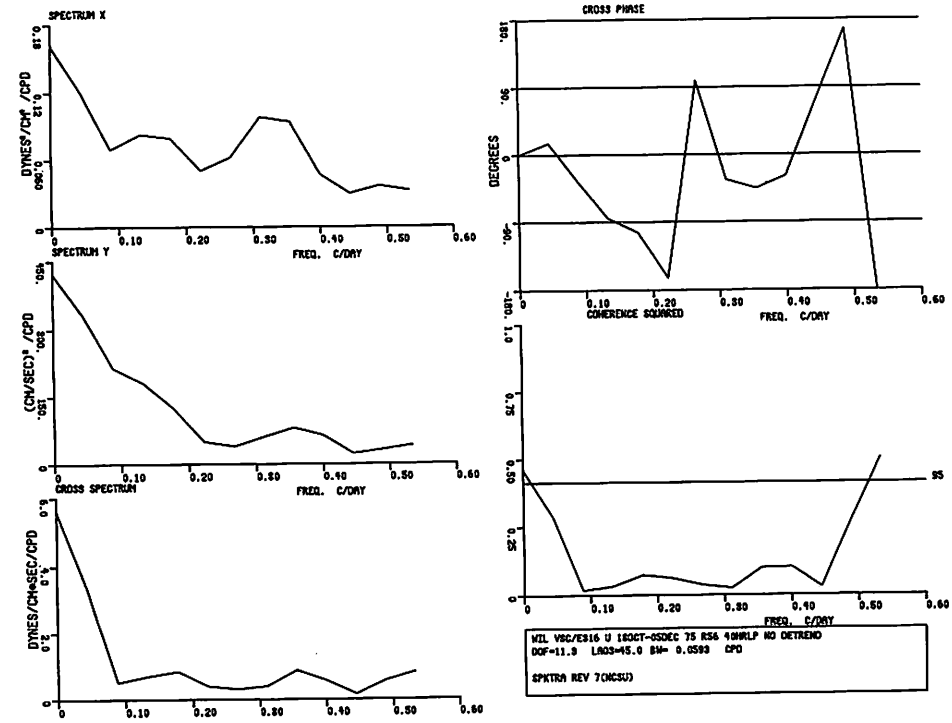

Figure 133 Spectra of the low pass wind stress v component at Wilmington and the low pass current velocity u component from meter $A2_{top}$ Oct-Dec 1975

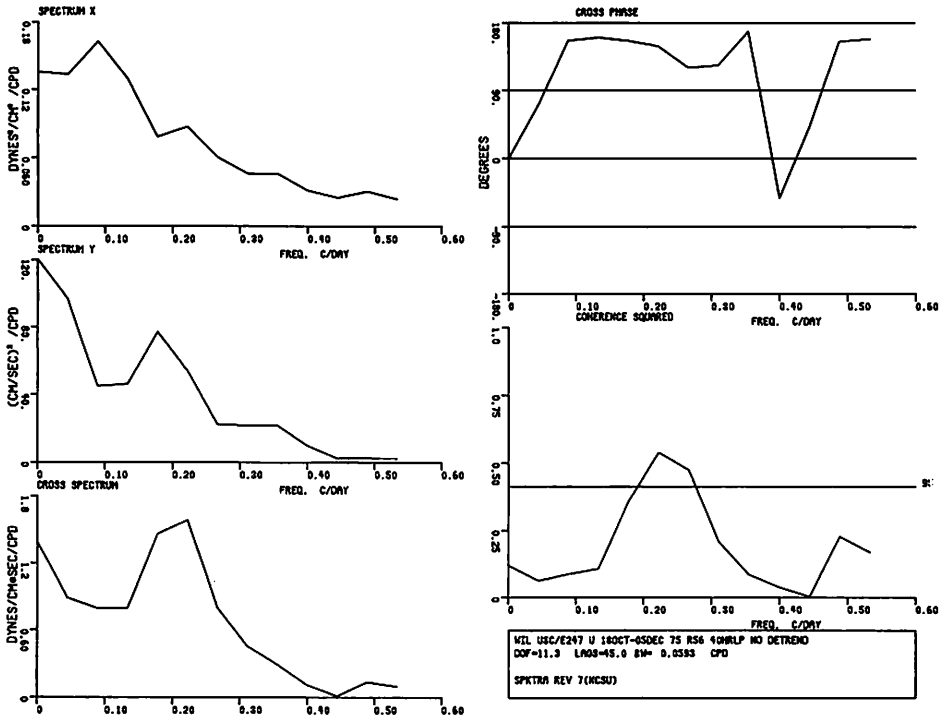

Figure 134 Spectra of the low pass wind stress u component at Wilmington and the low pass current velocity u component from meter $A2_{bot}$ Oct-Dec 1975

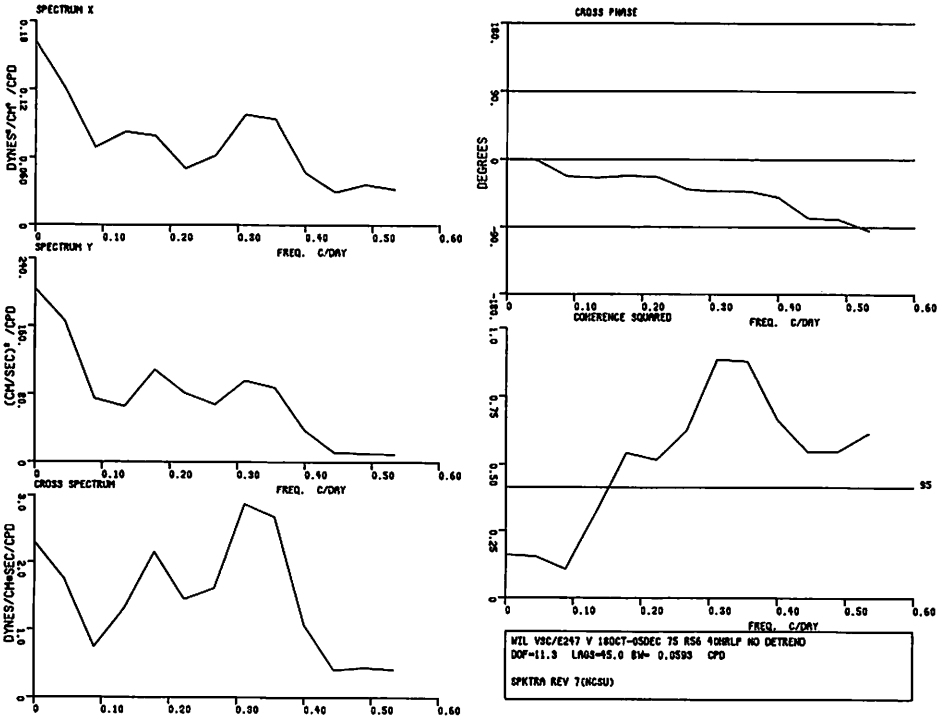

Figure 135 Spectra of the low pass wind stress v component at Wilmington and the low pass current velocity v component from meter $A2_{bot}$ Oct-Dec 1975

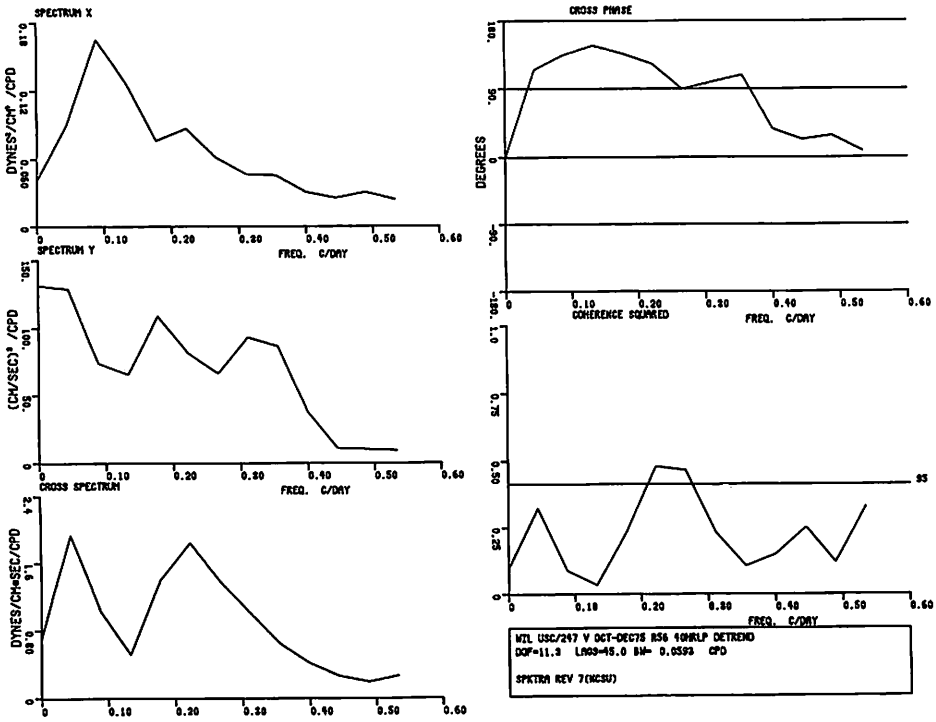

Figure 136 Spectra of the low pass wind stress u component at Wilmington and the low pass current velocity v component from meter $A2_{bot}$ Oct-Dec 1975 (detrended)

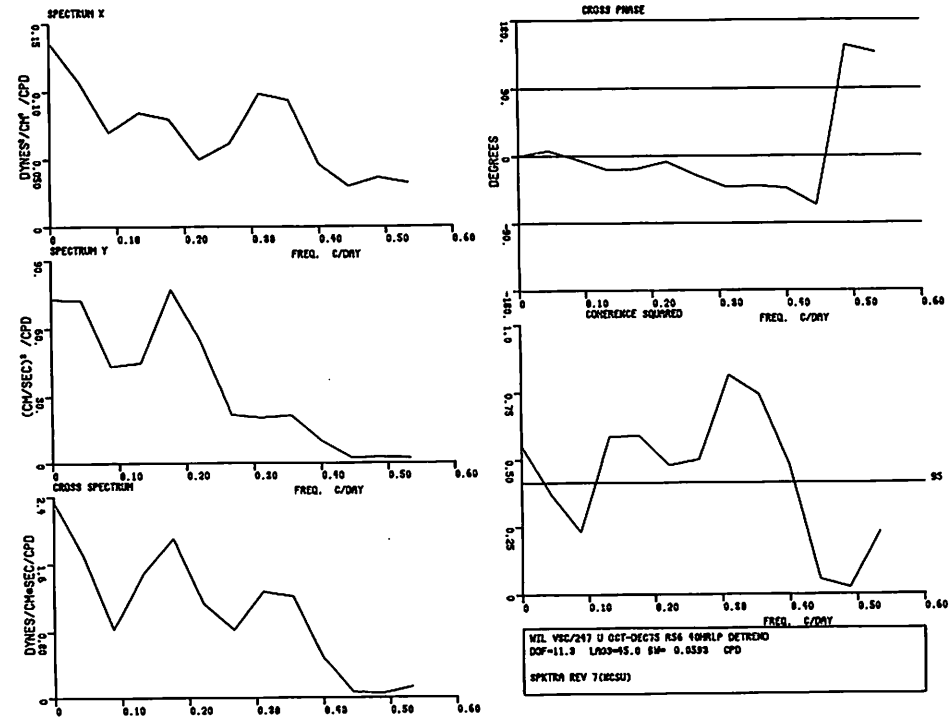

Figure 137 Spectra of the low pass wind stress v component at Wilmington and the low pass current velocity u component from meter $A2_{bot}$ Oct-Dec 1975 (detrended)

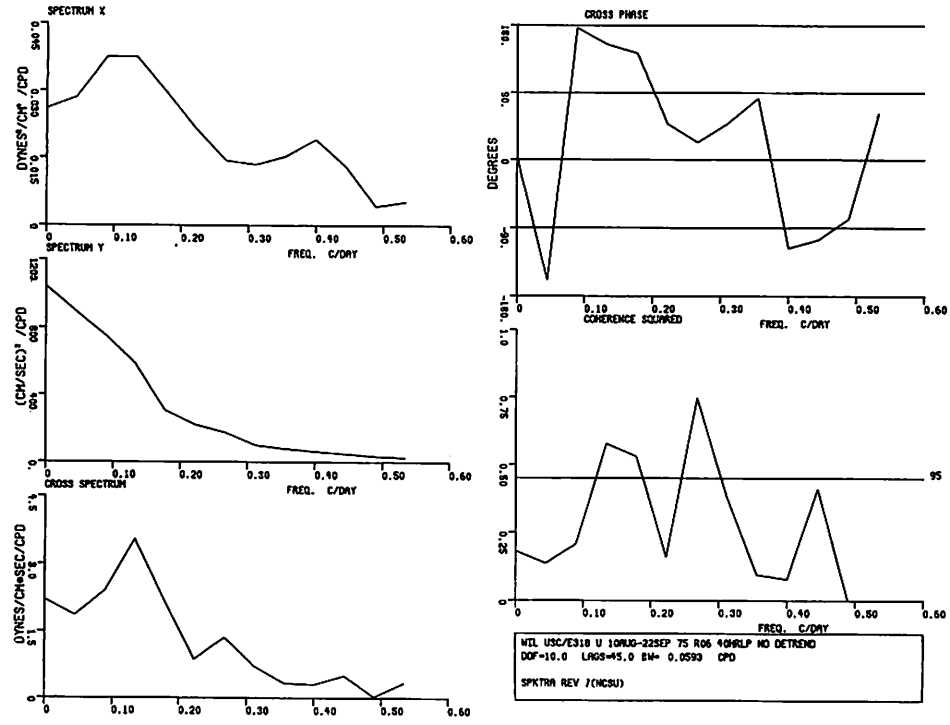

Figure 138 Spectra of the low pass wind stress u component at Wilmington and the low pass current velocity u component from meter Al_{top} (Principal Axis = 06°), Aug-Sept 1975

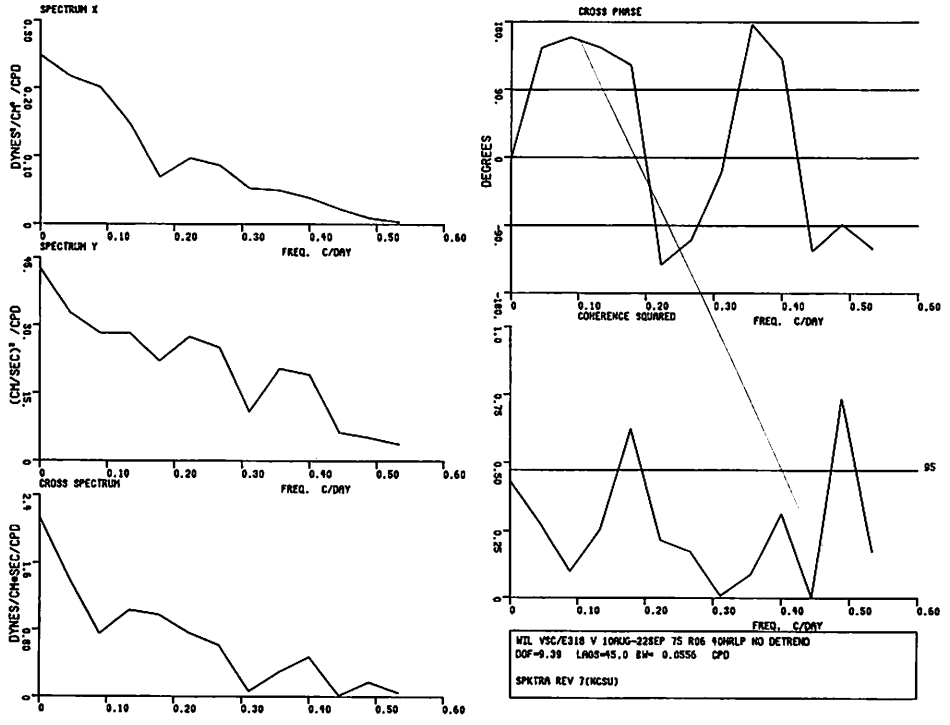

Figure 139 Spectra of the low pass wind stress v component at Wilmington and the low pass current velocity v component from meter Al_{top} (Principal Axis = 06°), Aug-Sept 1975

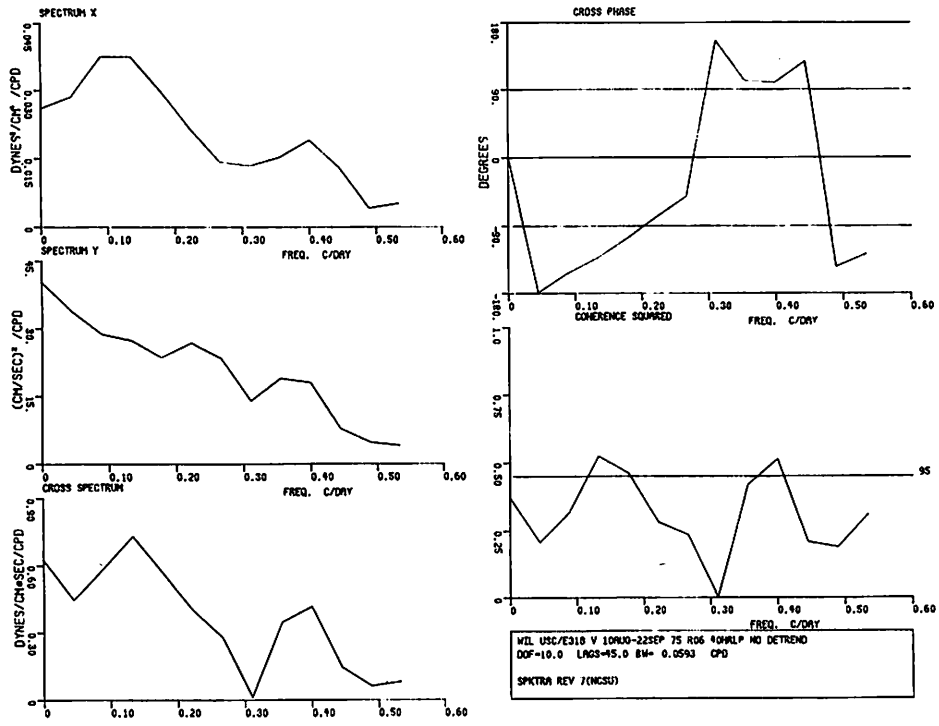

Figure 140 Spectra of the low pass wind stress u component at Wilmington and the low pass current velocity v component from meter Al_{top} (Principal Axis = 06°), Aug-Sept 1975

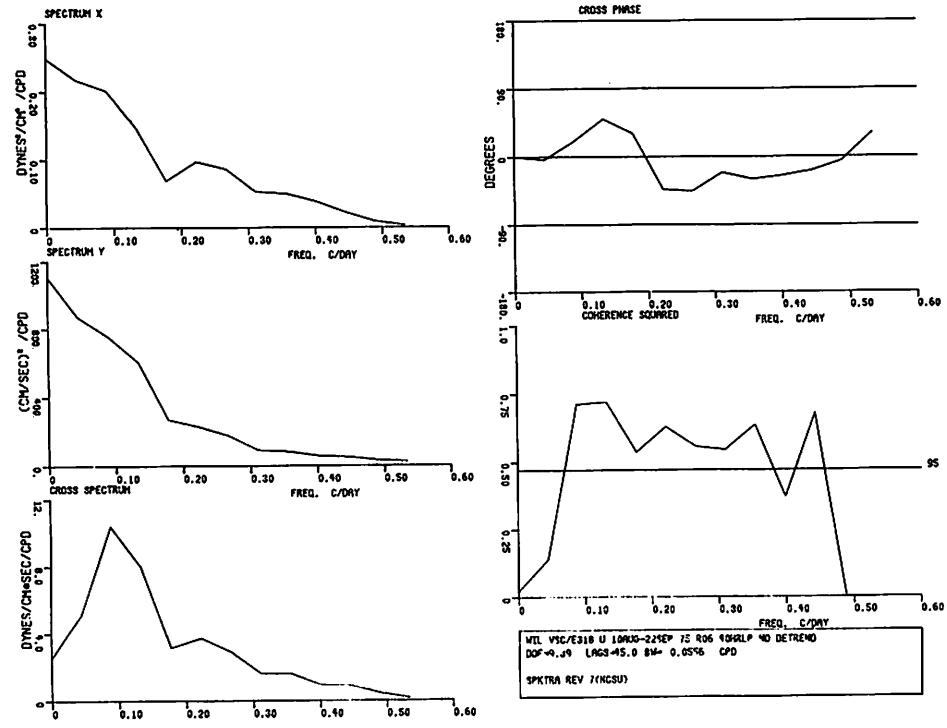

Figure 141 Spectra of the low pass wind stress v component at Wilmington and the low pass current velocity u component from meter Al_{top} (Principal Axis = 06°), Aug-Sept 1975

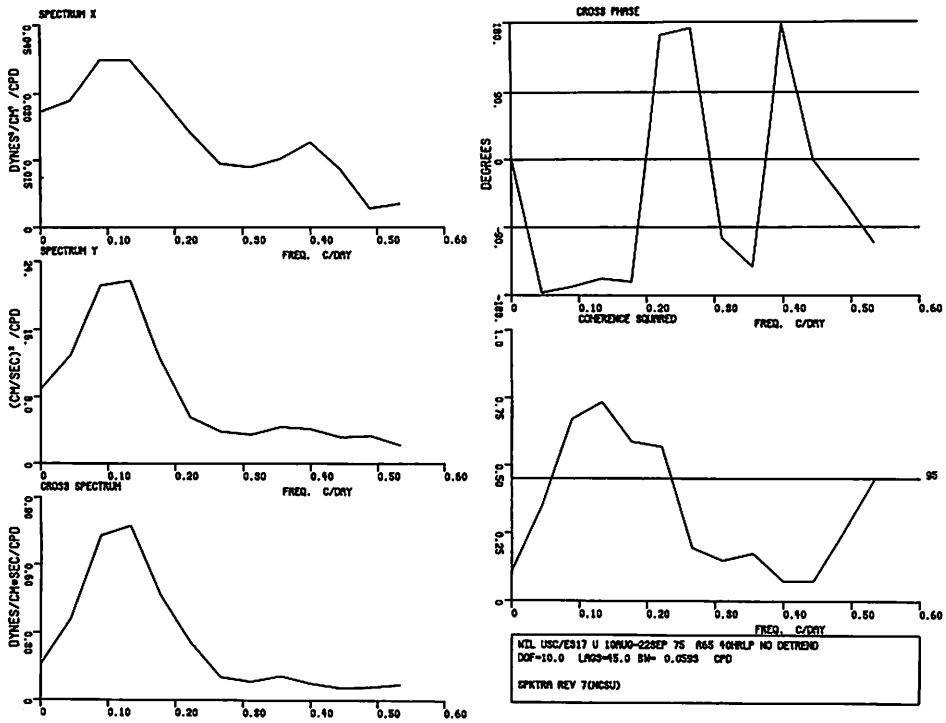

Figure 142 Spectra of the low pass wind stress u component at Wilmington and the low pass current velocity u component from meter Al_{bot} (Principal Axis = 65°), Aug-Sept 1975

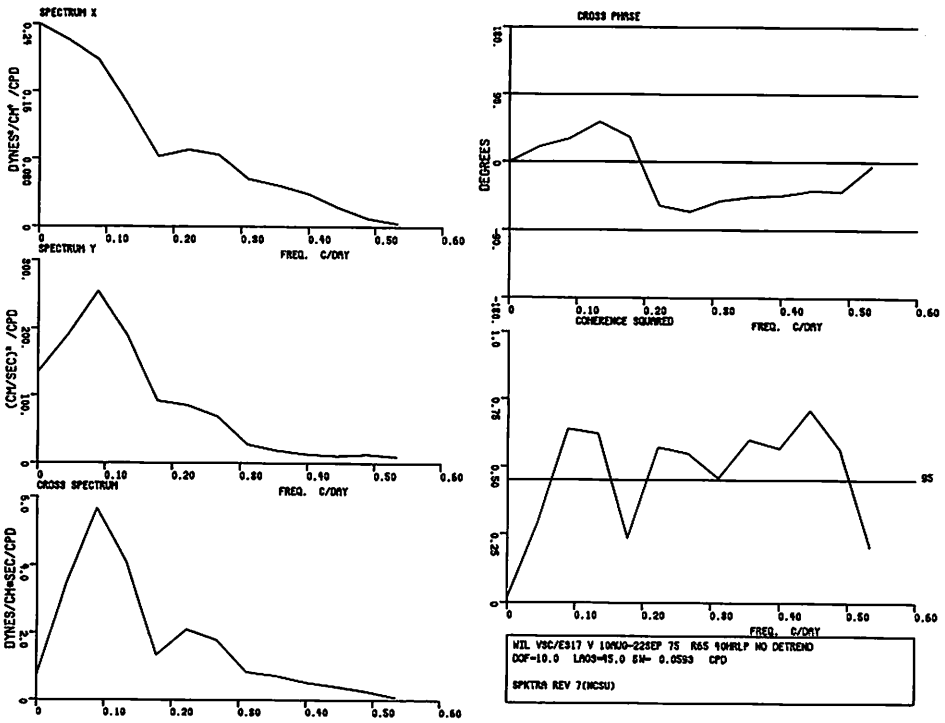

Figure 143 Spectra of the low pass wind stress v component at Wilmington and the low pass current velocity v component from meter Al_{bot} (Principal Axis = 65°), Aug-Sept 1975

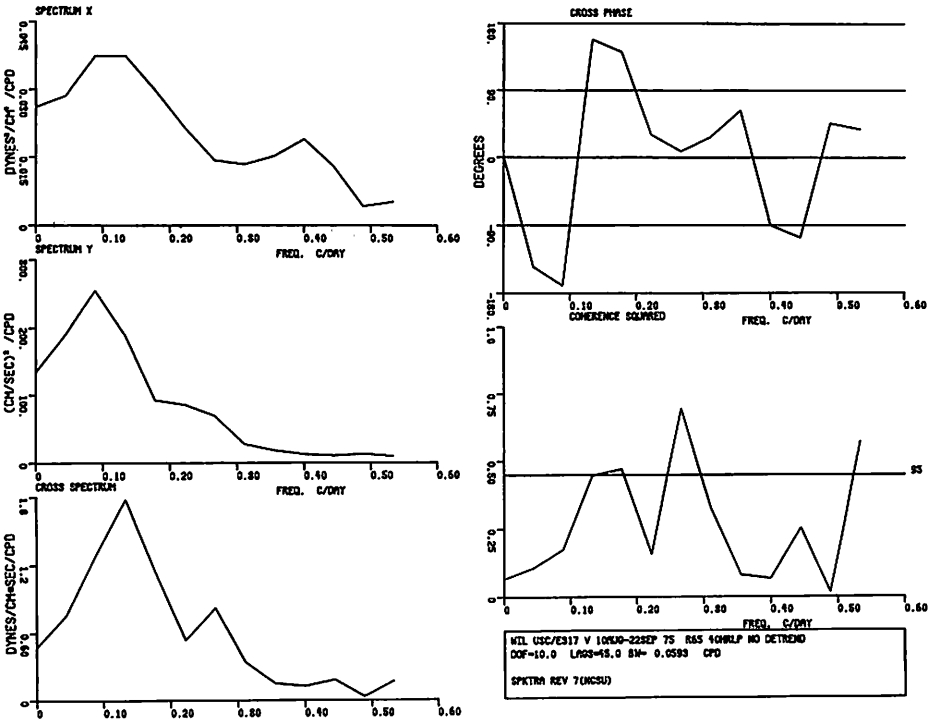

Figure 144 Spectra of the low pass wind stress u component at Wilmington and the low pass current velocity v component from meter Al_{bot} (Principal Axis = 65°), Aug-Sept 1975

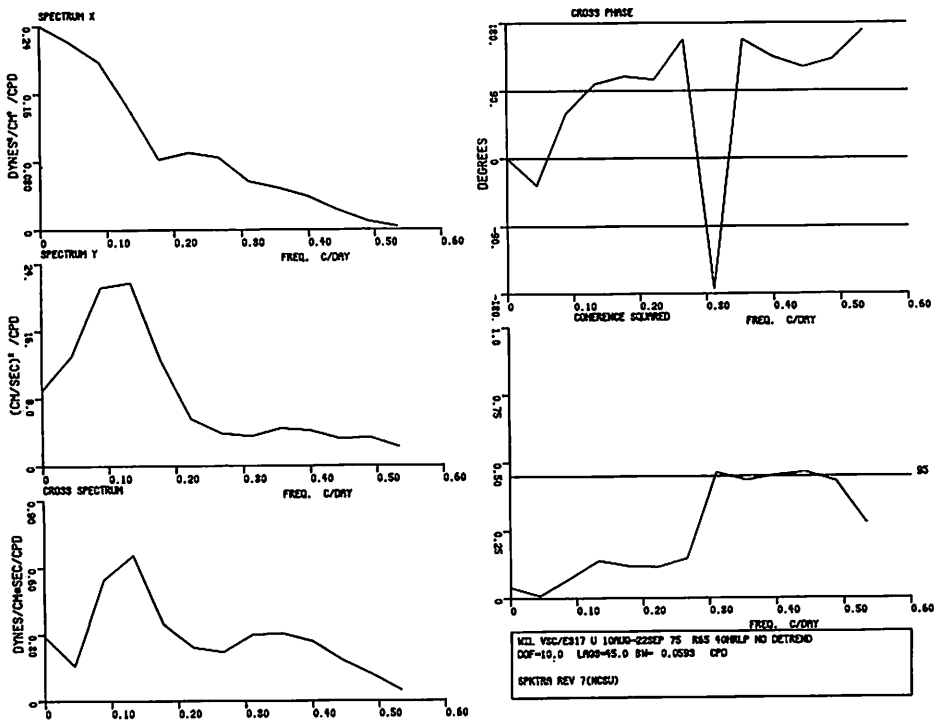

Figure 145 Spectra of the low pass wind stress v component at Wilmington and the low pass current velocity u component from meter Al_{bot} (Principal Axis = 65°), Aug-Sept 1975

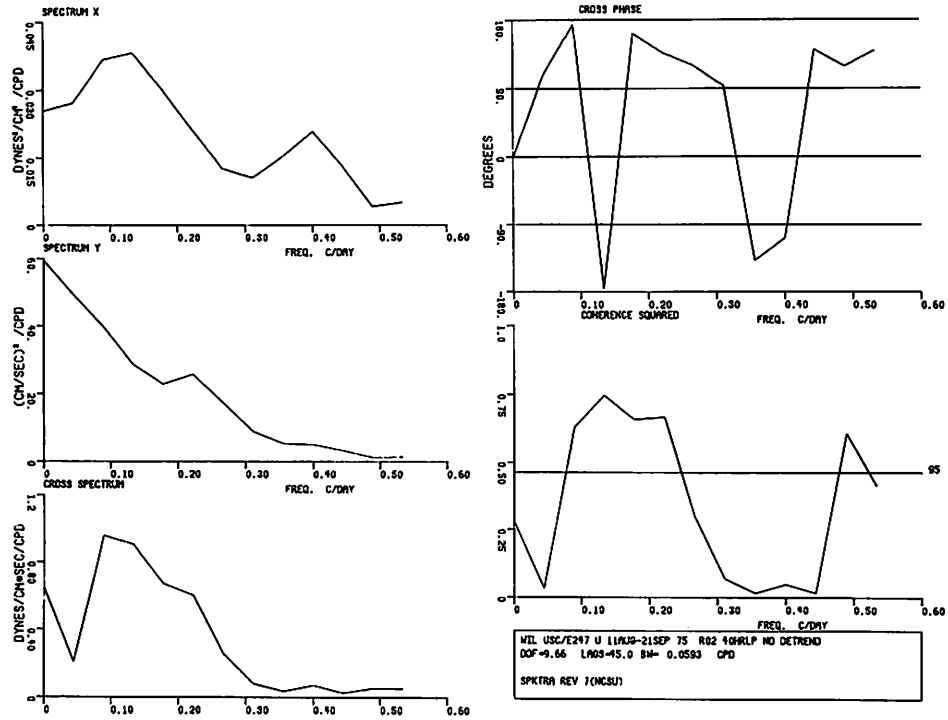

Figure 146 Spectra of the low pass wind stress u component at Wilmington and the low pass current velocity u component from meter Bl_{bot} (Principal Axis = 02°), Aug-Sept 1975

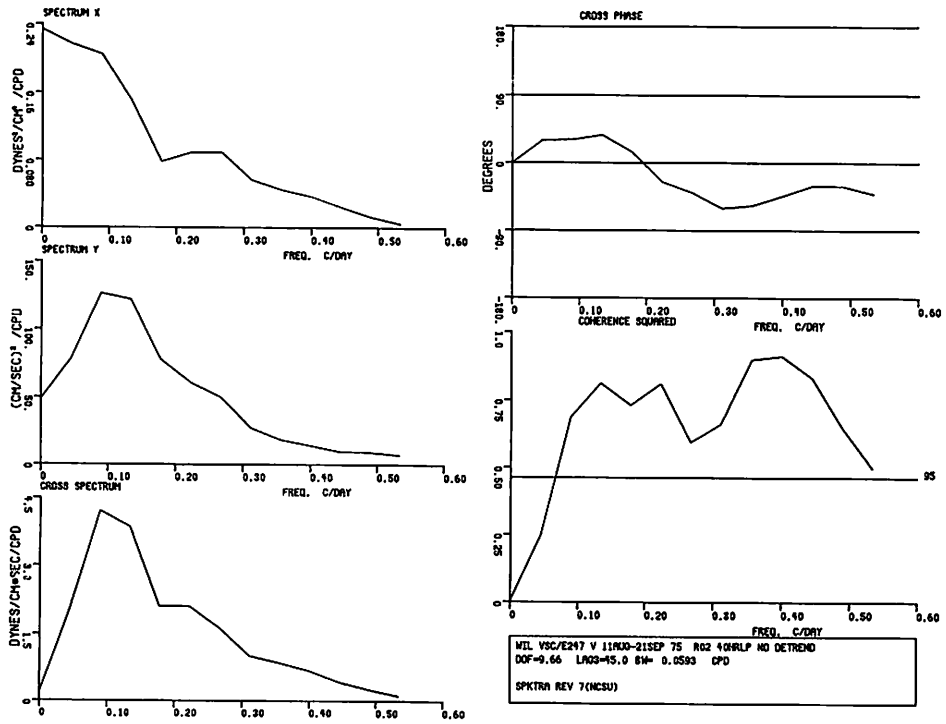

Figure 147 Spectra of the low pass wind stress v component at Wilmington and the low pass current velocity v component from meter Bl_{bot} (Principal Axis = 02°), Aug-Sept 1975

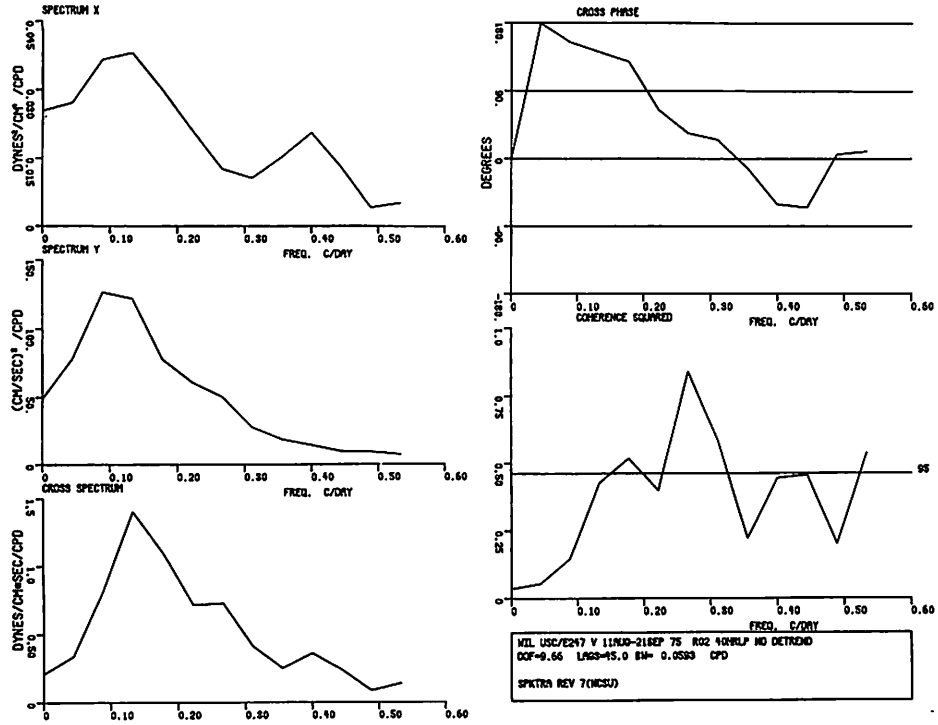

Figure 148 Spectra of the low pass wind stress u component at Wilmington and the low pass current velocity v component from meter Bl_{bot} (Principal Axis = 02^{o}), Aug-Sept 1975

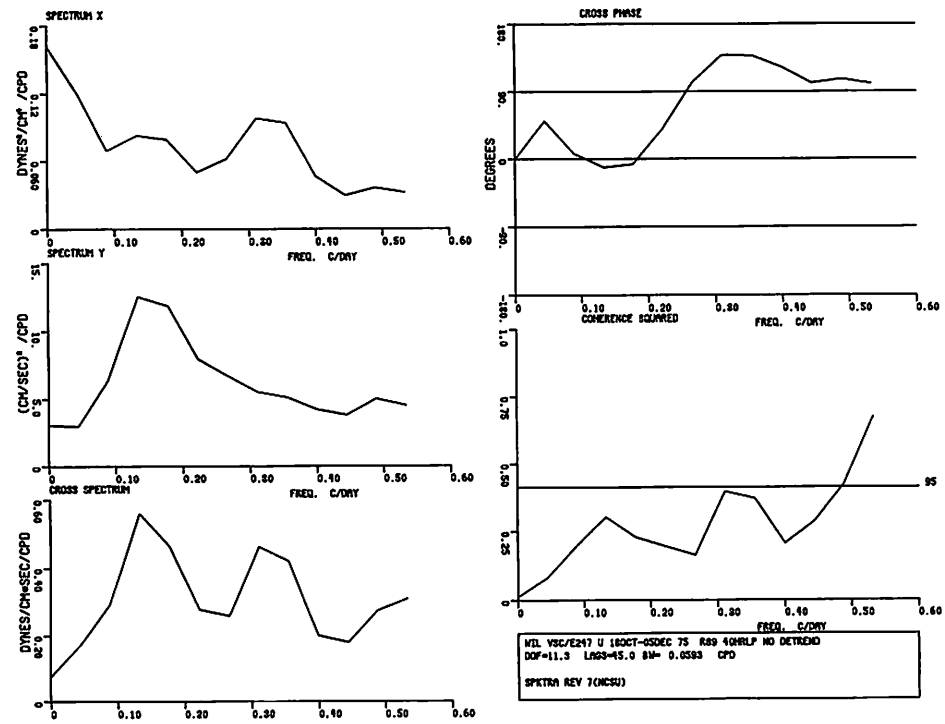

Figure 149 Spectra of the low pass wind stress v component at Wilmington and the low pass current velocity u component from meter Bl_{bot} (Principal Axis = 02^{o}), Aug-Sept 1975

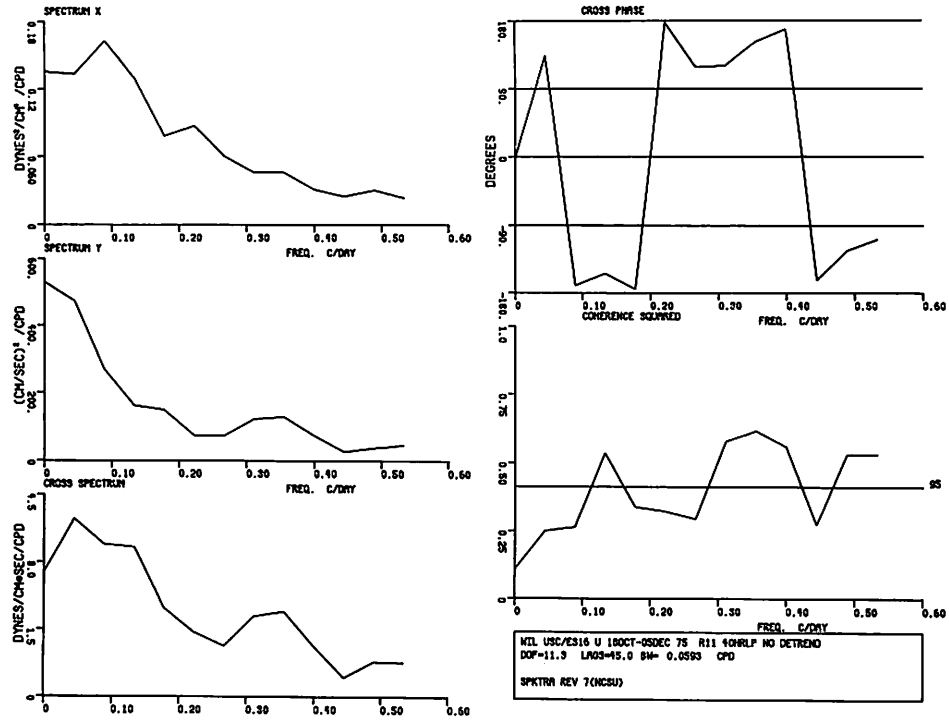

Figure 150 Spectra of the low pass wind stress u component at Wilmington and the low pass current velocity u component from meter $A2_{top}$ (Principal Axis = 11°), Oct-Dec 1975

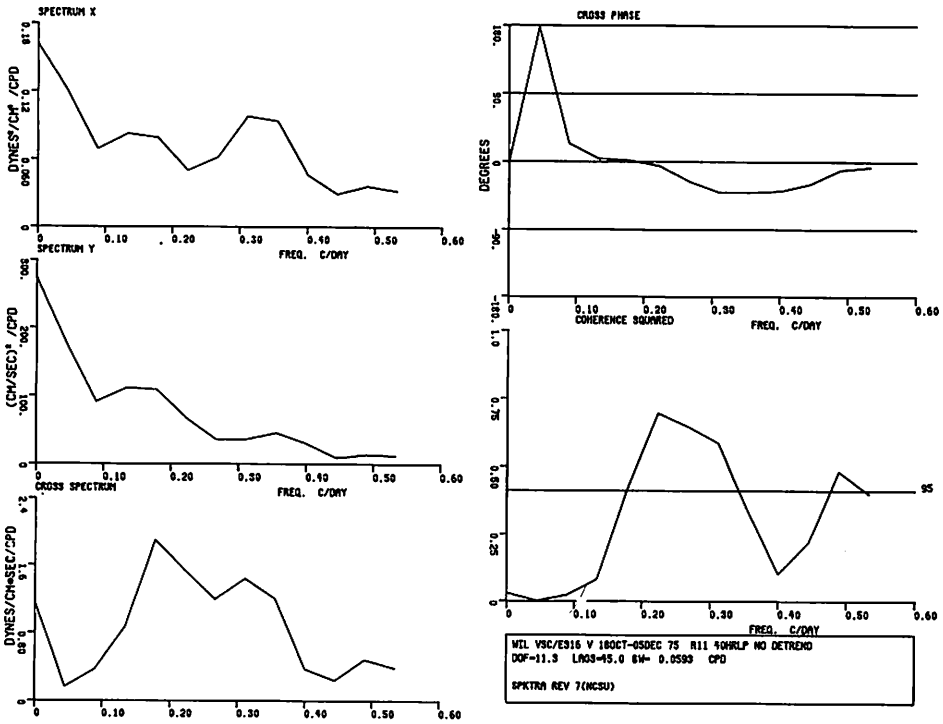

Figure 151 Spectra of the low pass wind stress v component at Wilmington and the low pass current velocity v component from meter $A2_{top}$ (Principal Axis = 11°), Oct-Dec 1975

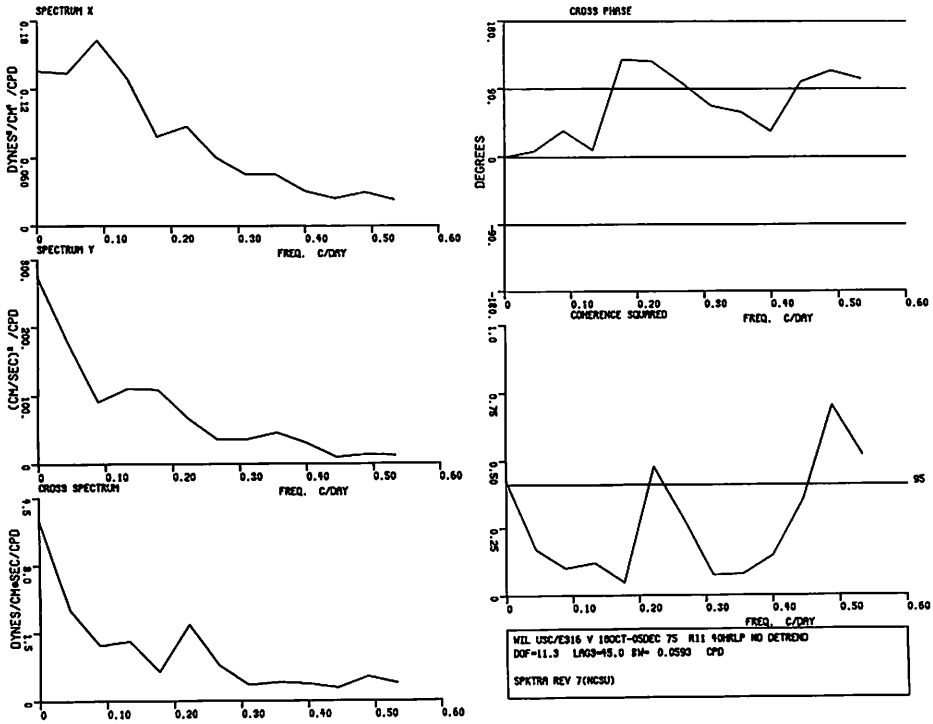

Figure 152 Spectra of the low pass wind stress u component at Wilmington and the low pass current velocity v component from meter $A2_{top}$ (Principal Axis = 11°), Oct-Dec 1975

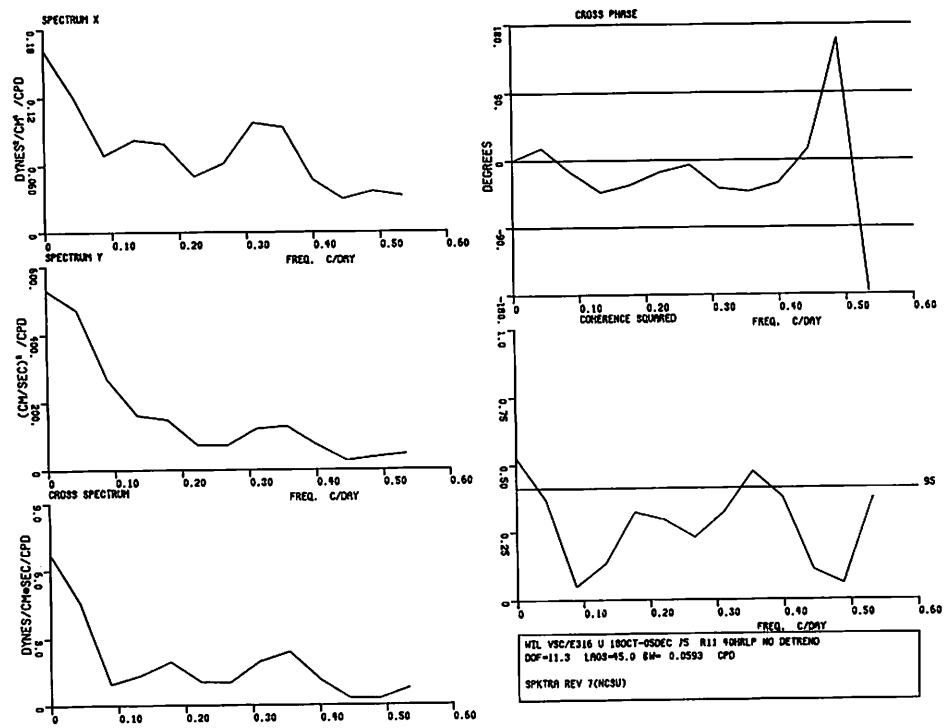

Figure 153 Spectra of the low pass wind stress v component at Wilmington and the low pass current velocity u component from meter $A2_{top}$ (Principal Axis = 11°), Oct-Dec 1975

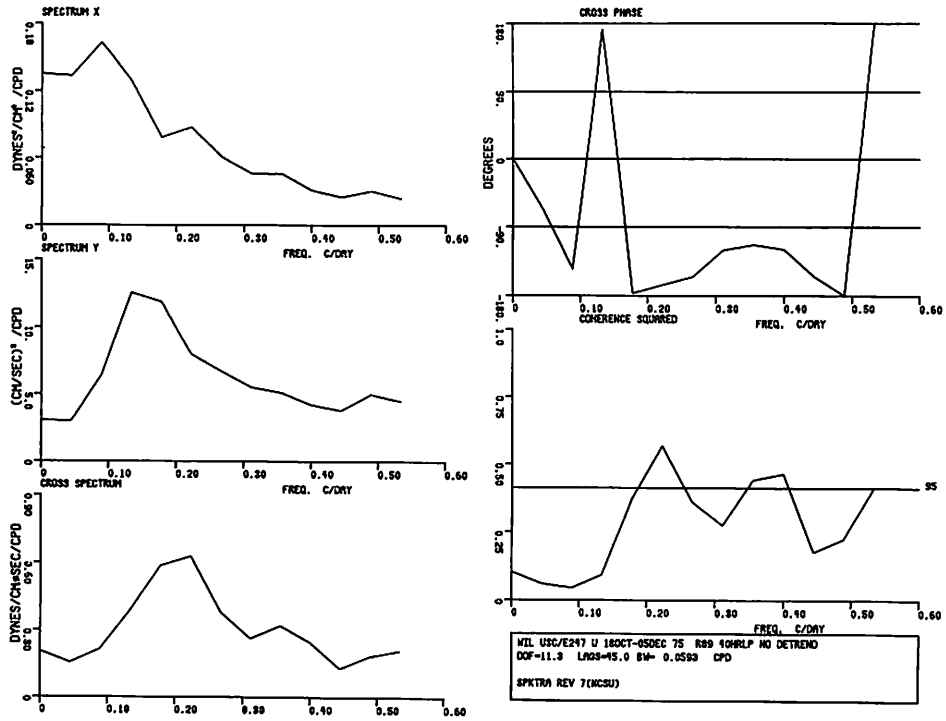

Figure 154 Spectra of the low pass wind stress u component at Wilmington and the low pass current velocity u component from meter $A2_{bot}$ (Principal Axis = 89^{o}), Oct-Dec 1975

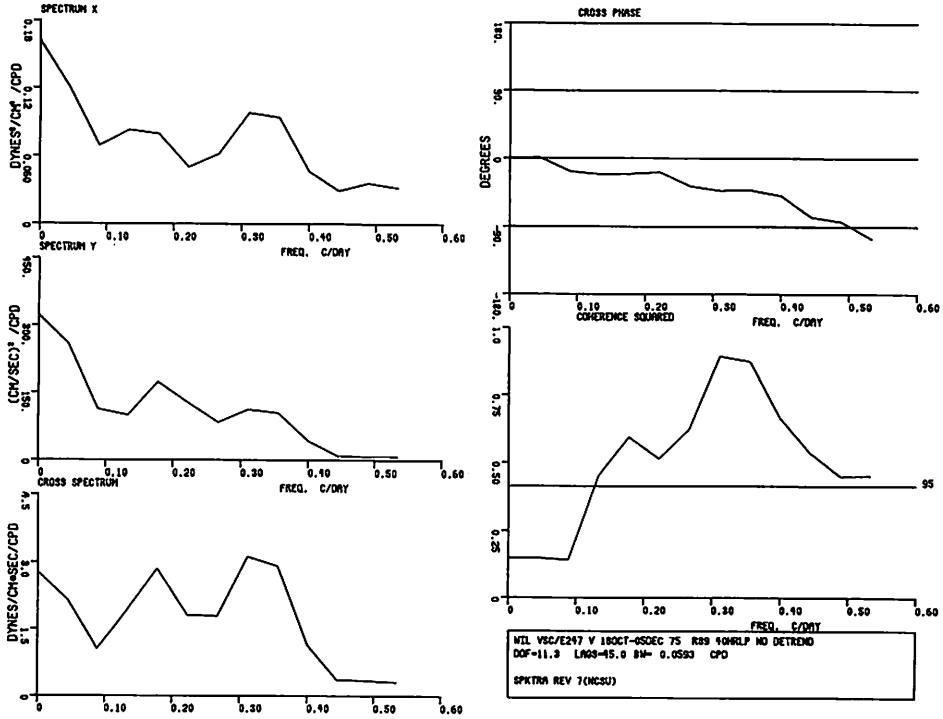

Figure 155 Spectra of the low pass wind stress v component at Wilmington and the low pass current velocity v component from meter $A2_{bot}$ (Principal Axis = 89^{o}), Oct-Dec 1975

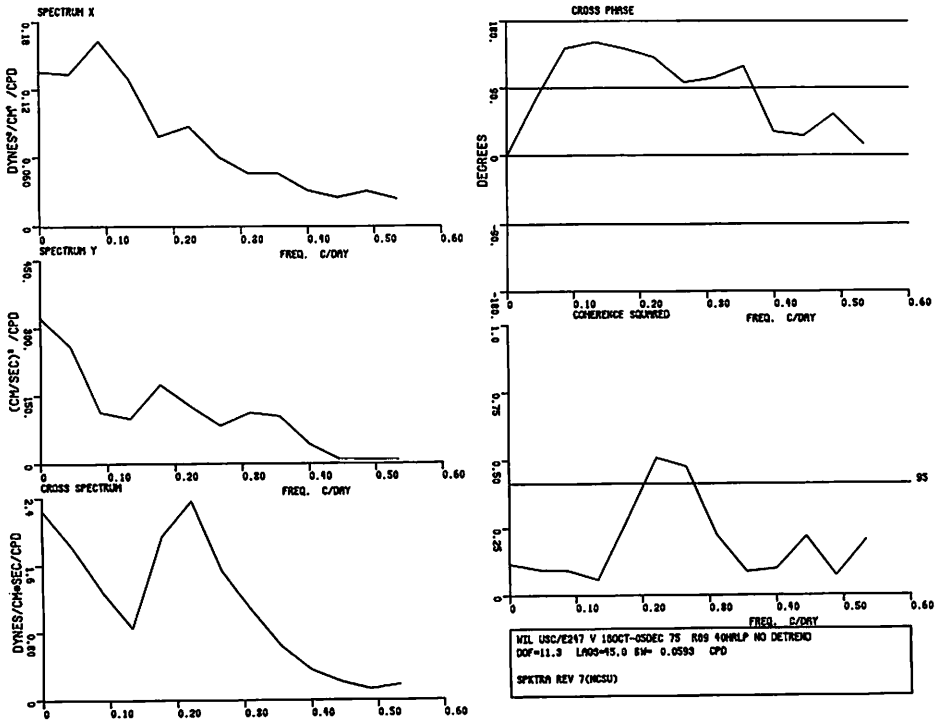

Figure 156 Spectra of the low pass wind stress u component at Wilmington and the low pass current velocity v component from meter $A2_{bot}$ (Principal Axis = 89°), Oct-Dec 1975

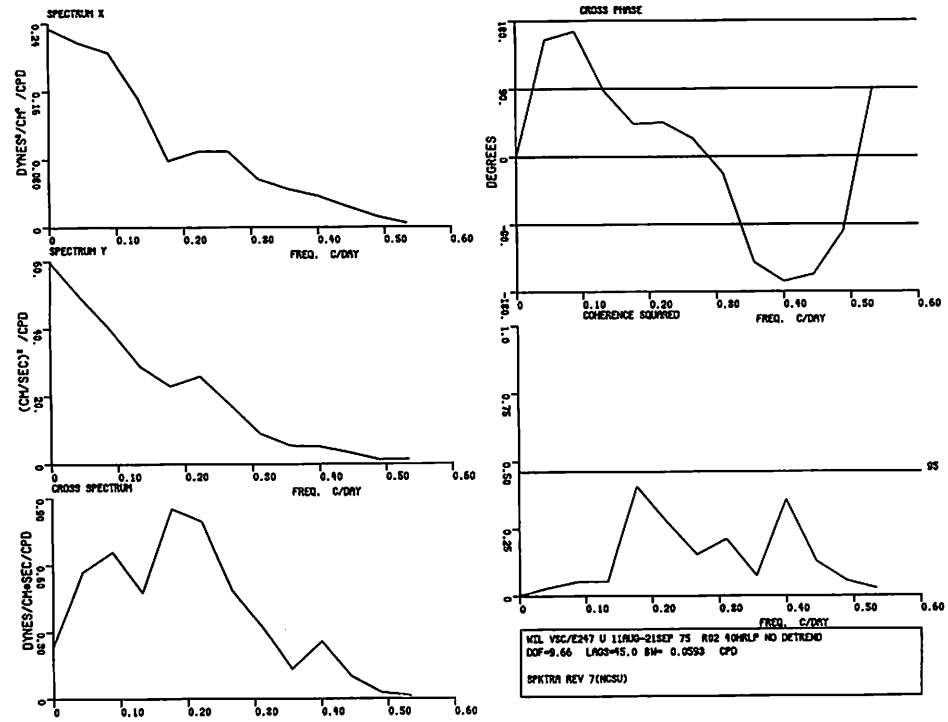

Figure 157 Spectra of the low pass wind stress v component at Wilmington and the low pass current velocity u component from meter $A2_{bot}$ (Principal Axis = 89°), Oct-Dec 1975

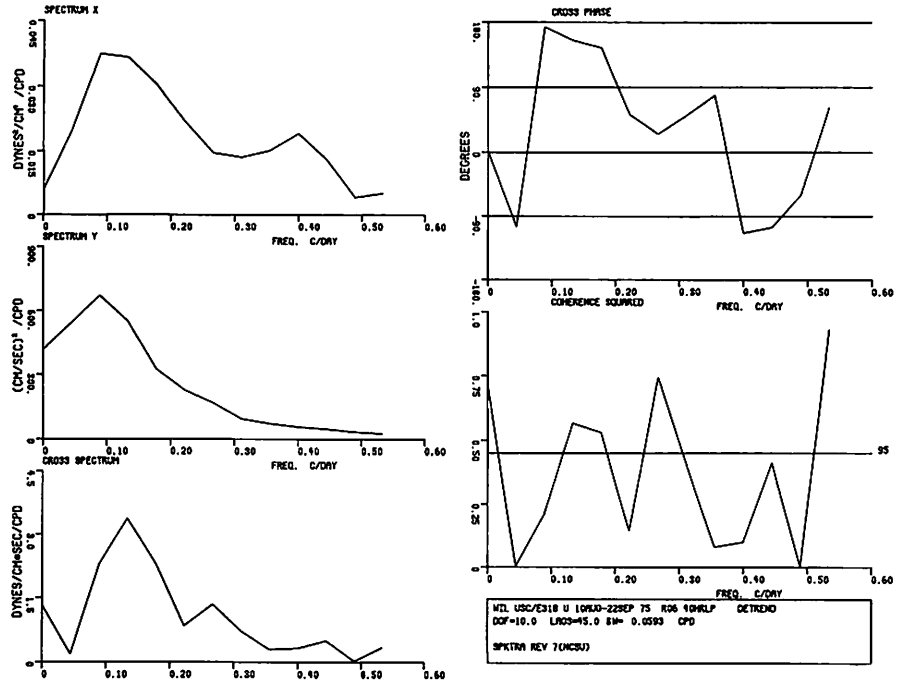

Figure 158 Spectra of the low pass wind stress u component at Wilmington and the low pass current velocity u component from meter Al_{top} (Principal Axis = 06°), Aug-Sept 1975 (detrended)

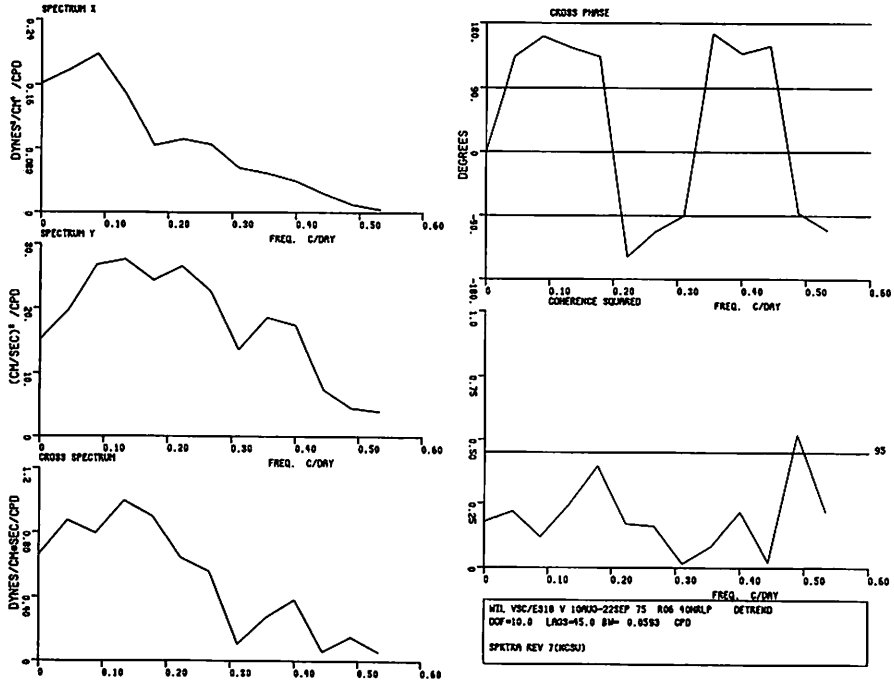

Figure 159 Spectra of the low pass wind stress v component at Wilmington and the low pass current velocity v component from meter Al_{top} (Principal Axis = 06°), Aug-Sept 1975 (detrended)

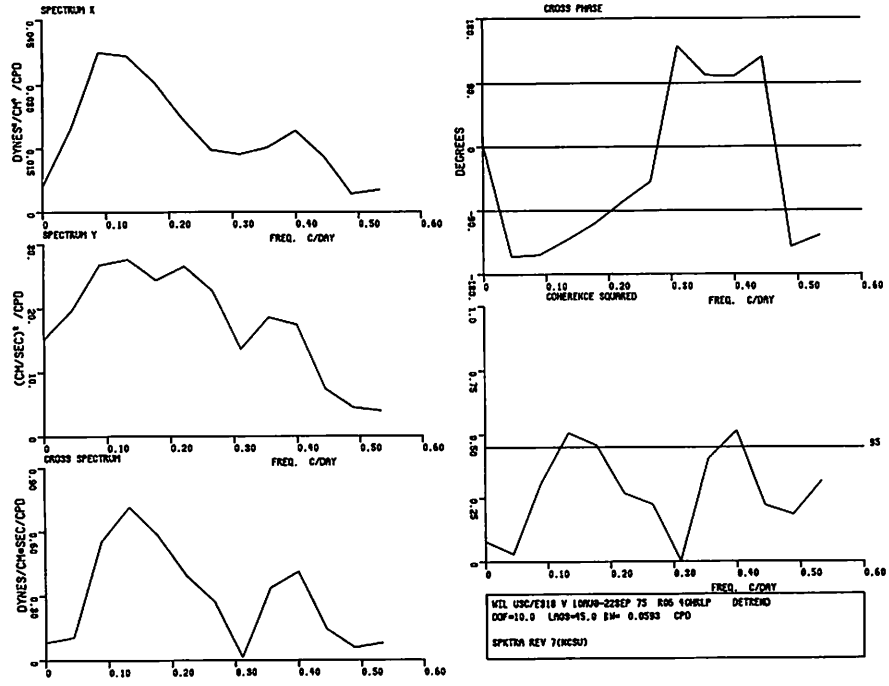

Figure 160 Spectra of the low pass wind stress u component at Wilmington and the low pass current velocity v component from meter Al_{top} (Principal Axis - 06°), Aug-Sept 1975 (detrended)

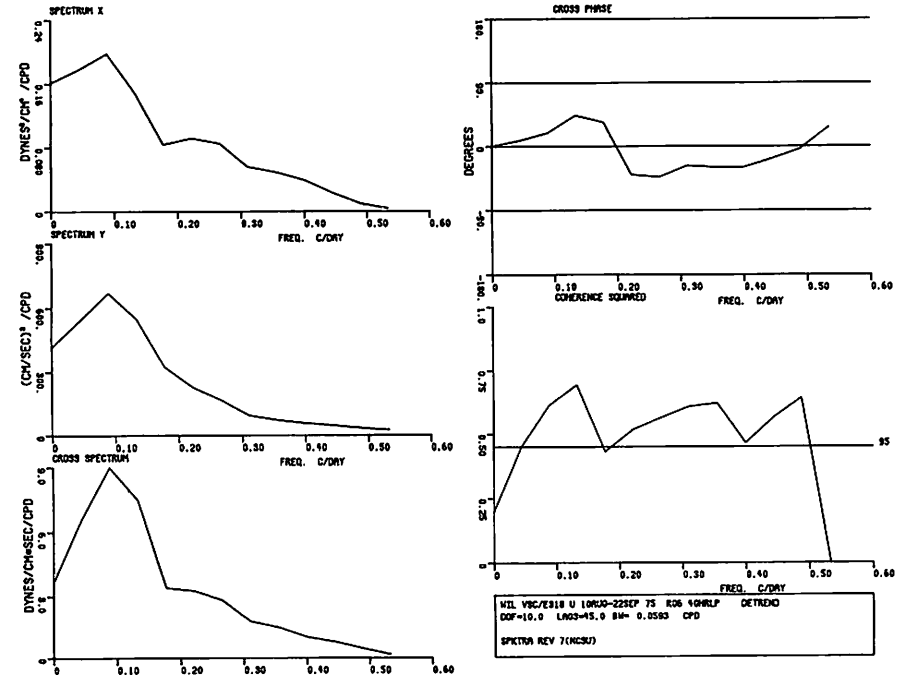

Figure 161 Spectra of the low pass wind stress v component at Wilmington and the low pass current velocity u component from meter Al_{top} (Principal Axis = 06°), Aug-Sept 1975 (detrended)

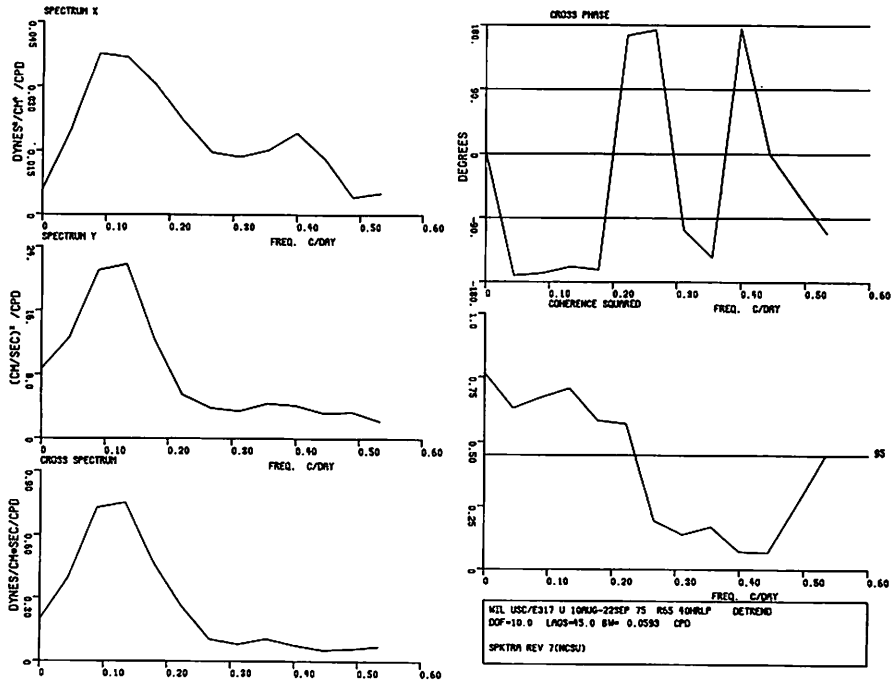

Figure 162 Spectra of the low pass wind stress u component at Wilmington and the low pass current velocity u component from meter Al_{bot} (Principal Axis = 65^{o}), Aug-Sept 1975 (detrended)

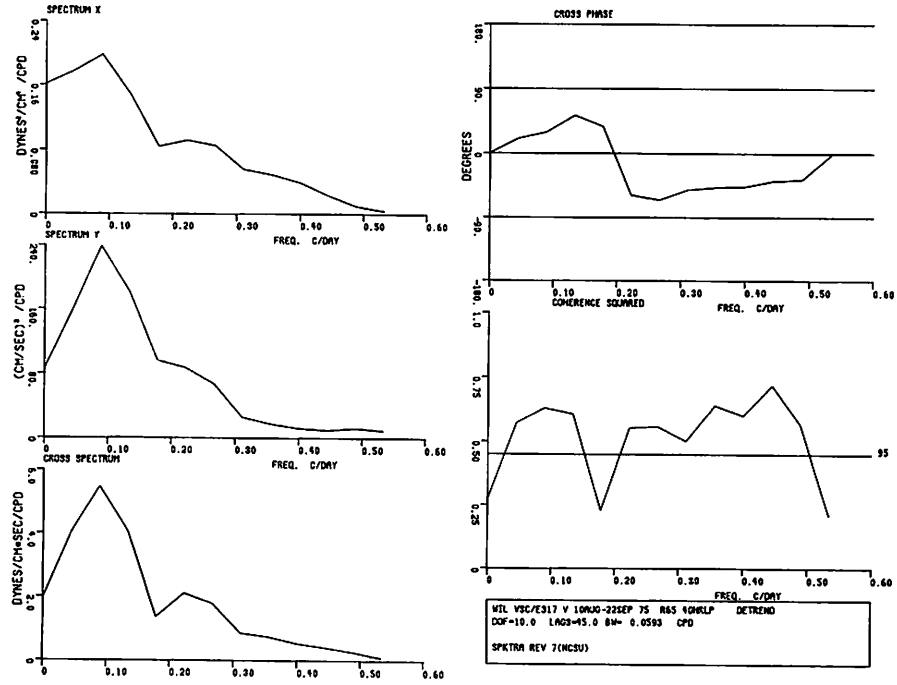

Figure 163 Spectra of the low pass wind stress v component at Wilmington and the low pass current velocity v component from meter Al_{bot} (Principal Axis = 65^{o}), Aug-Sept 1975 (detrended)

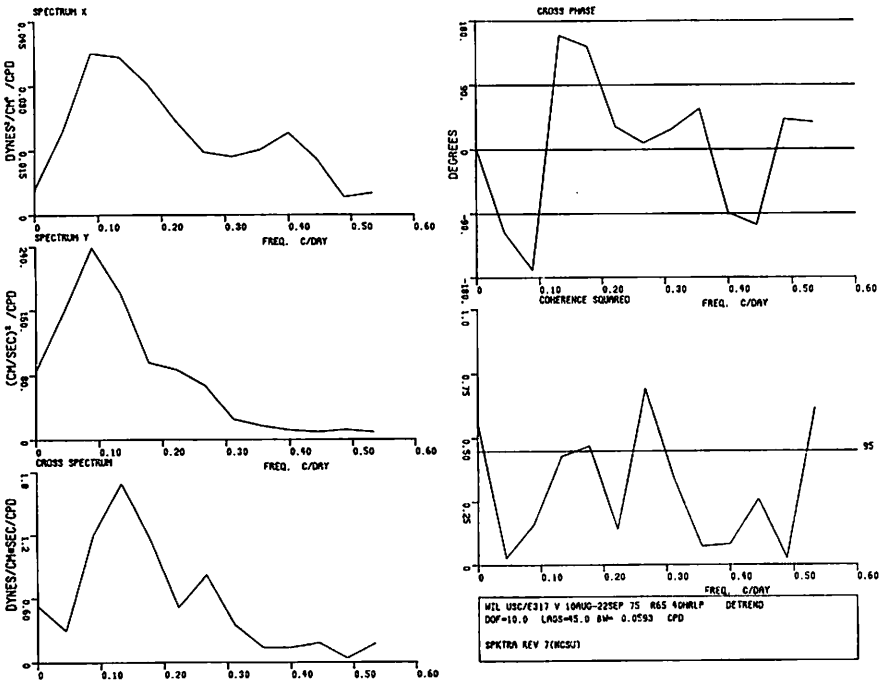

Figure 164 Spectra of the low pass wind stress u component at Wilmington and the low pass current velocity v component from meter Al_{bot} (Principal Axis = 65°), Aug-Sept 1975 (detrended)

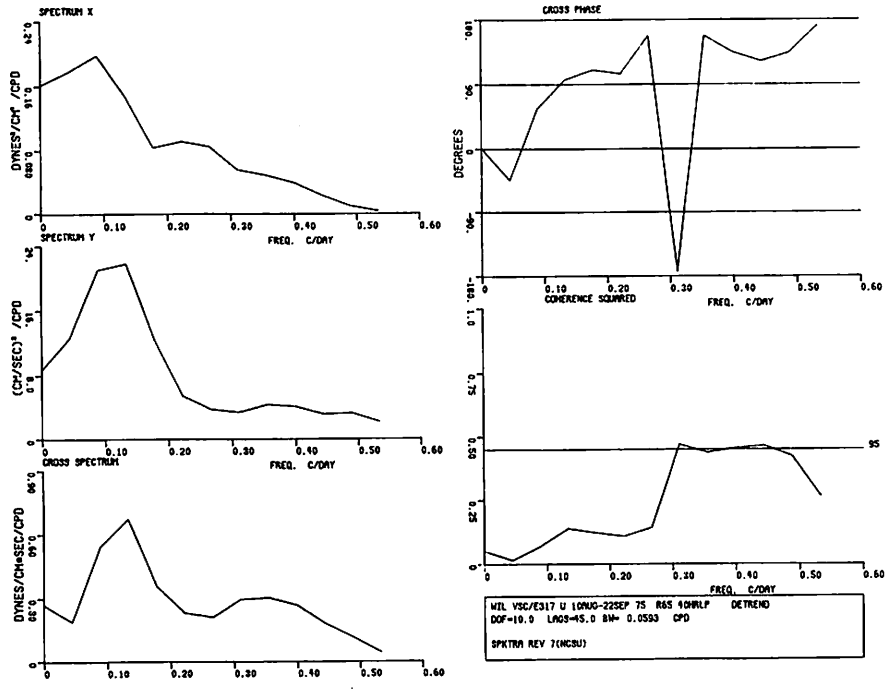

Figure 165 Spectra of the low pass wind stress v component at Wilmington and the low pass current velocity u component from meter Al_{bot} (Principal Axis = 65°), Aug-Sept 1975 (detrended)

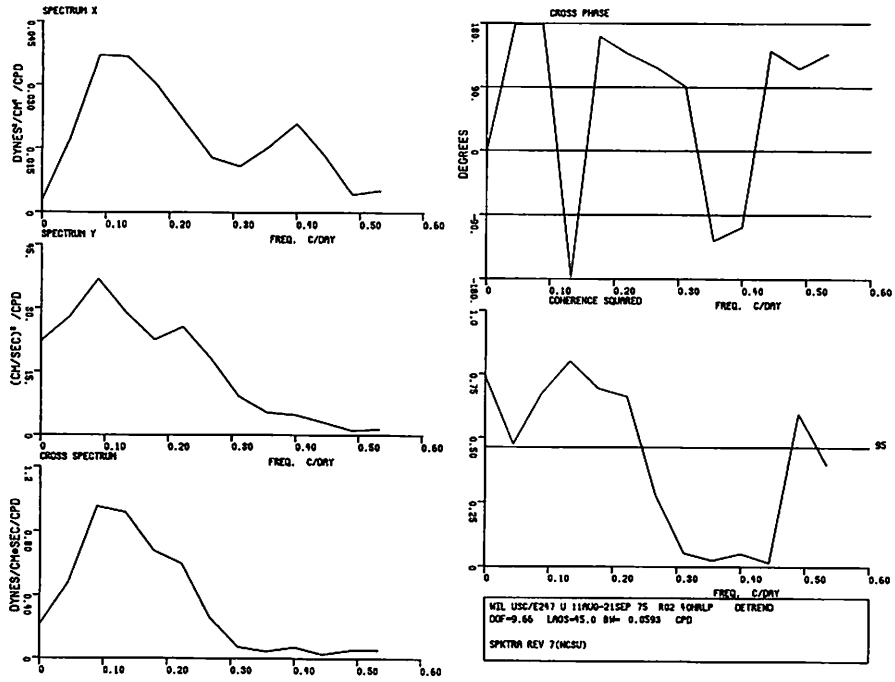

Figure 166 Spectra of the low pass wind stress u component at Wilmington and the low pass current velocity u component from meter Bl_{bot} (Principal Axis = 02^{o}), Aug-Sept 1975 (detrended)

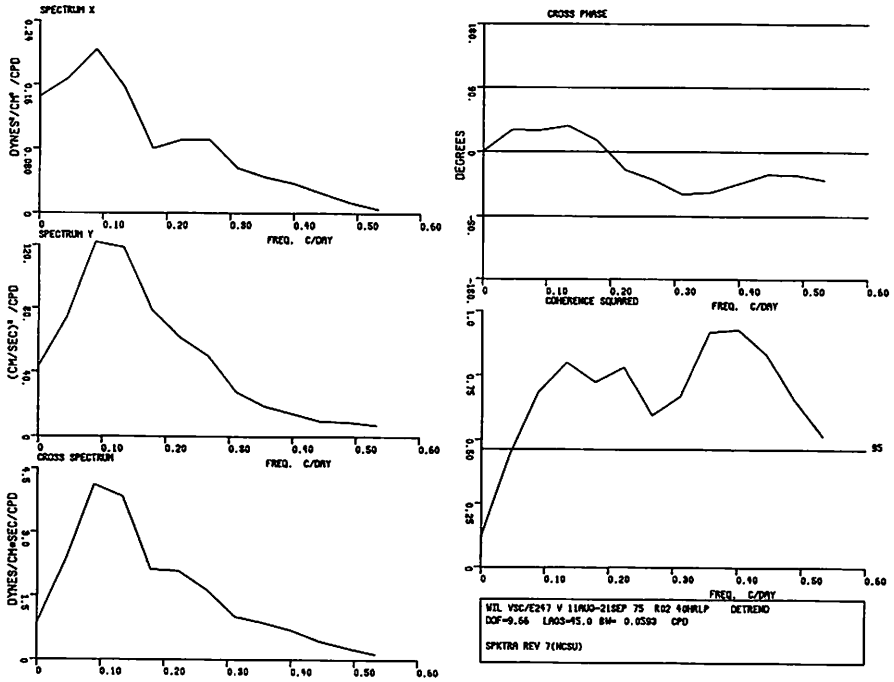

Figure 167 Spectra of the low pass wind stress v component at Wilmington and the low pass current velocity v component from meter Bl_{bot} (Principal Axis = 02^{o}), Aug-Sept 1975 (detrended)

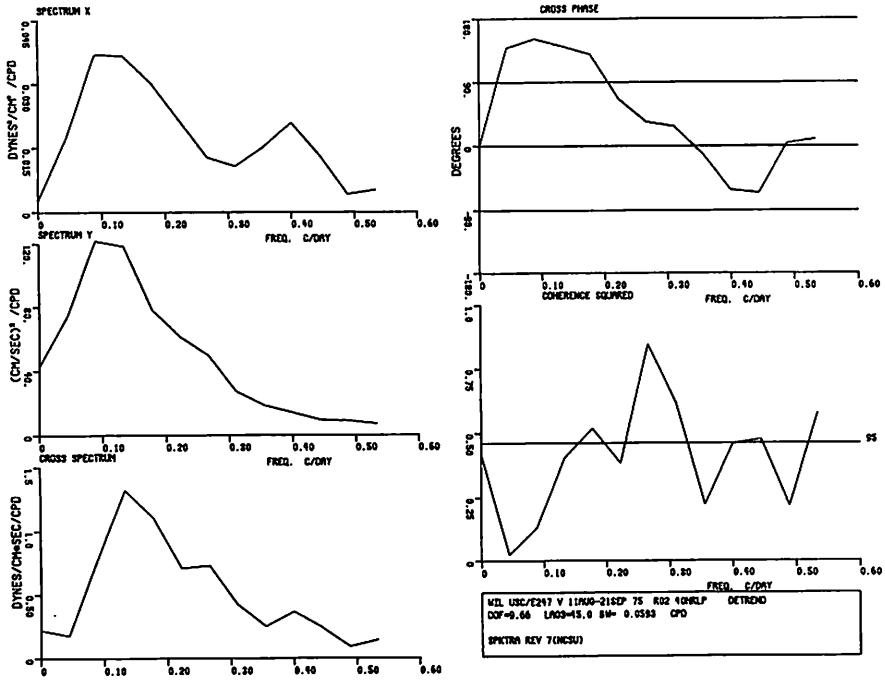

Figure 168 Spectra of the low pass wind stress u component at Wilmington and the low pass current velocity v component from meter Bl_{bot} (Principal Axis = 02°), Aug-Sept 1975 (detrended)

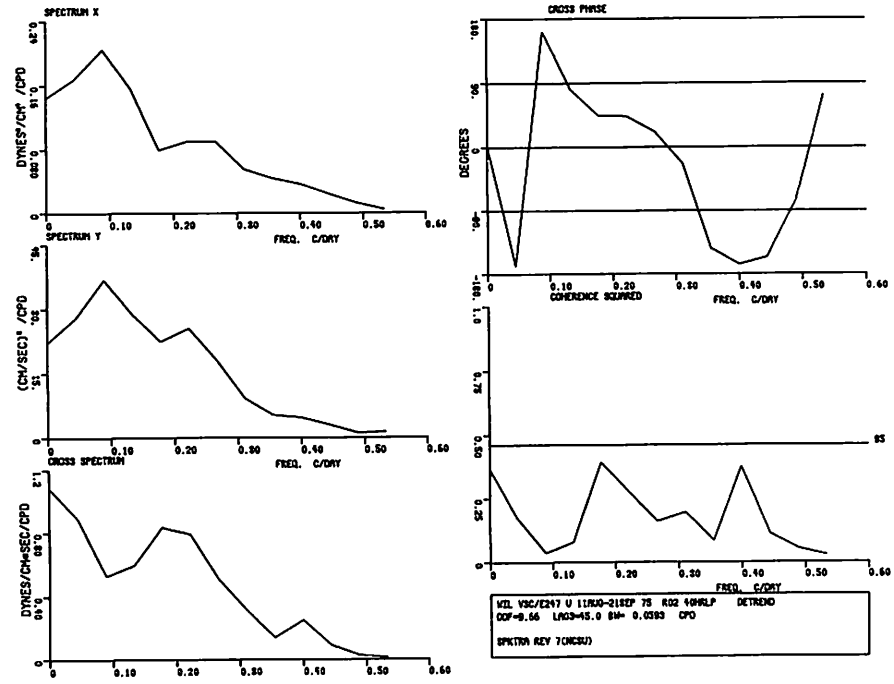

Figure 169 Spectra of the low pass wind stress v component at Wilmington and the low pass current velocity u component from meter Bl_{bot} (Principal Axis = 02°), Aug-Sept 1975 (detrended)

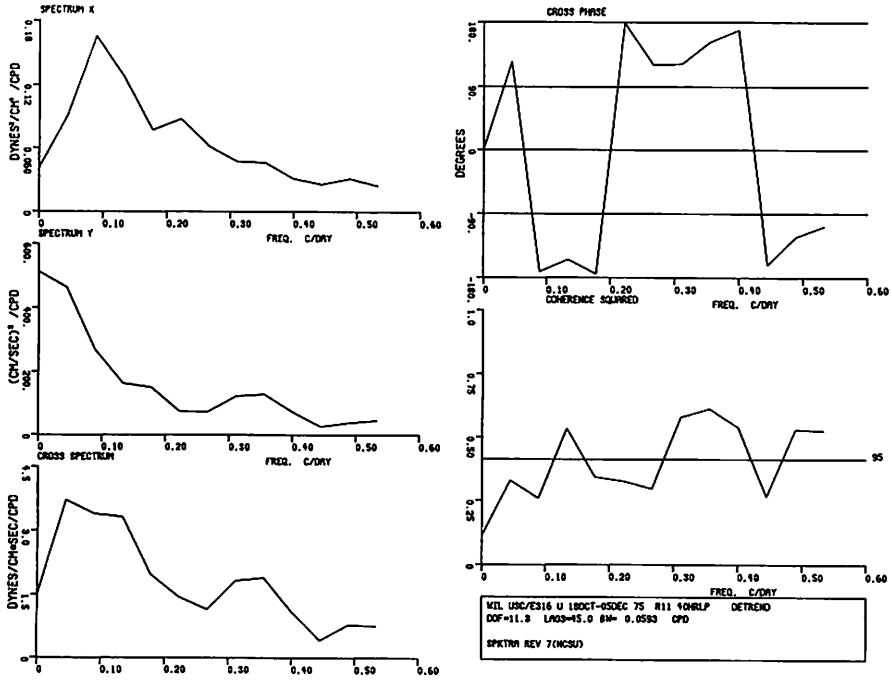

Figure 170 Spectra of the low pass wind stress u component at Wilmington and the low pass current velocity u component from meter $A2_{top}$ (Principal Axis = 11^{o}), Oct-Dec 1975 (detrended)

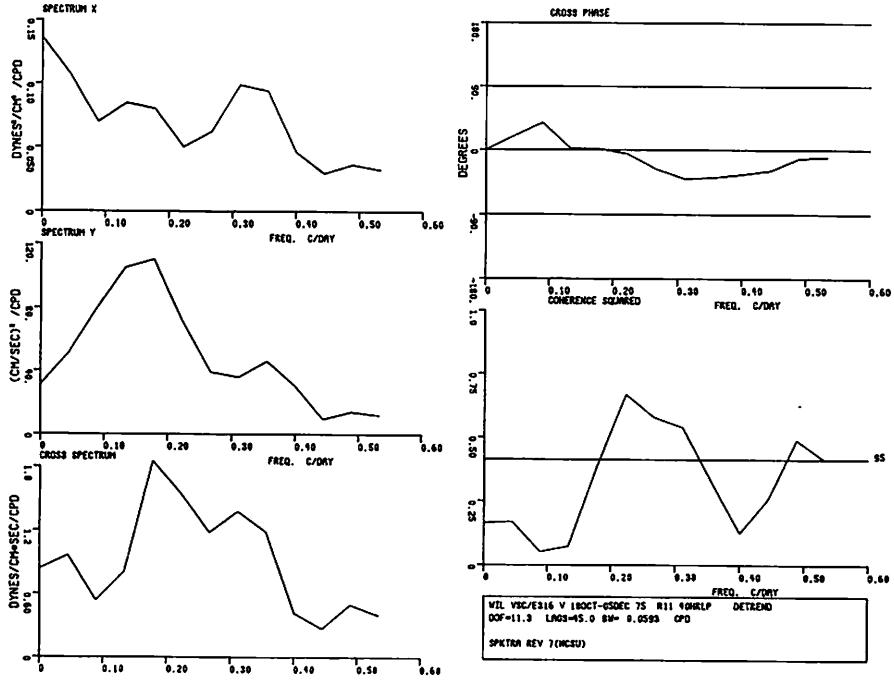

Figure 171 Spectra of the low pass wind stress v component at Wilmington and the low pass current velocity v component from meter $A2_{top}$ (Principal Axis = 11^{o}), Oct-Dec 1975 (detrended)

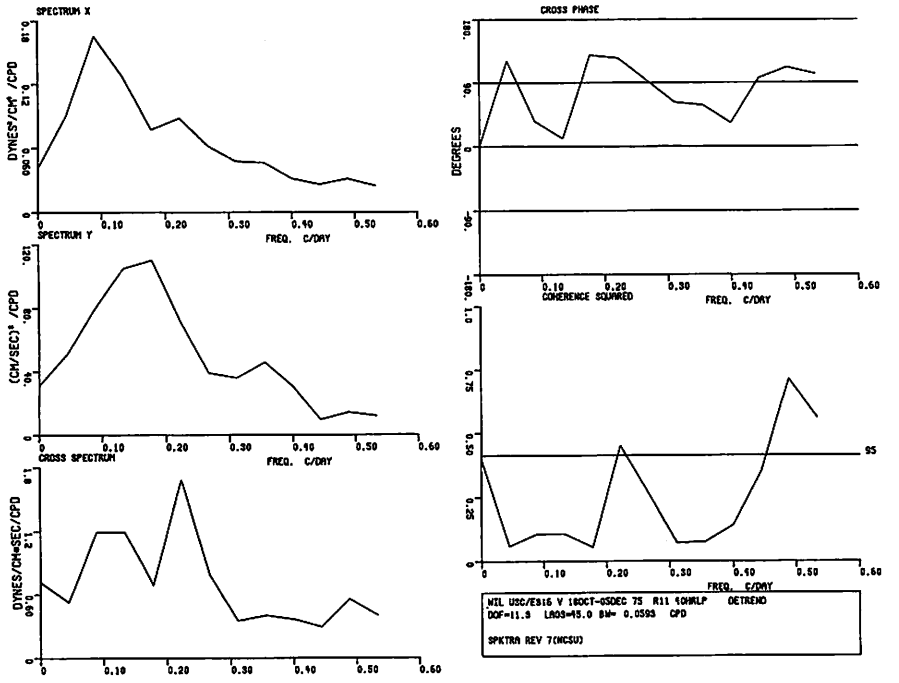

Figure 172 Spectra of the low pass wind stress u component at Wilmington and the low pass current velocity v component from meter $A2_{top}$ (Principal Axis = 11°), Oct-Dec 1975 (detrended)

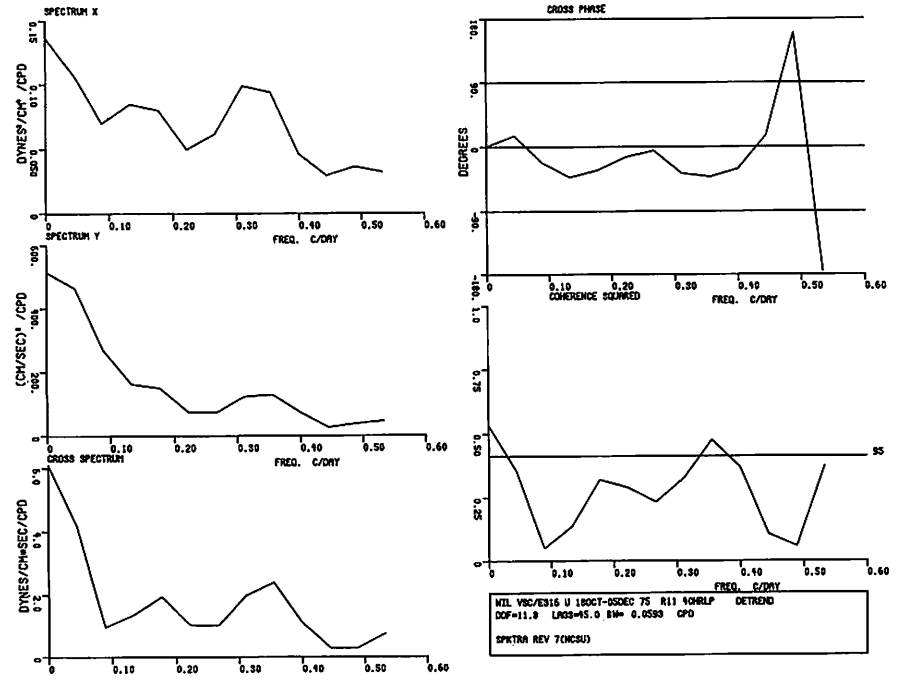

Figure 173 Spectra of the low pass wind stress v component at Wilmington and the low pass current velocity u component from meter $A2_{top}$ (Principal Axis = 11°), Oct-Dec 1975 (detrended)

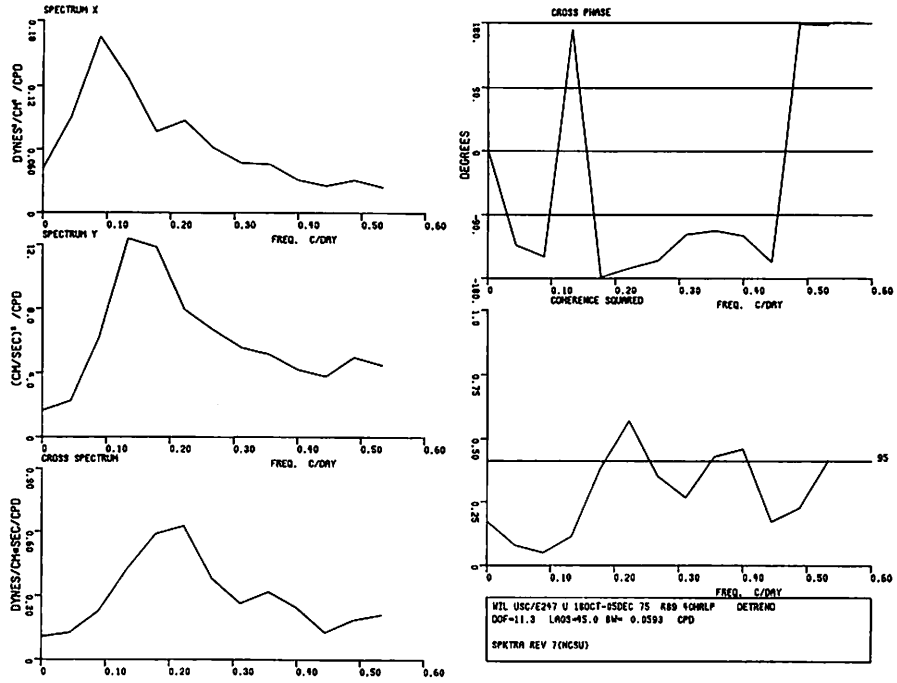

Figure 174 Spectra of the low pass wind stress u component at Wilmington and the low pass current velocity u component from meter $A2_{bot}$ (Principal Axis = 89^{o}), Oct-Dec 1975 (detrended)

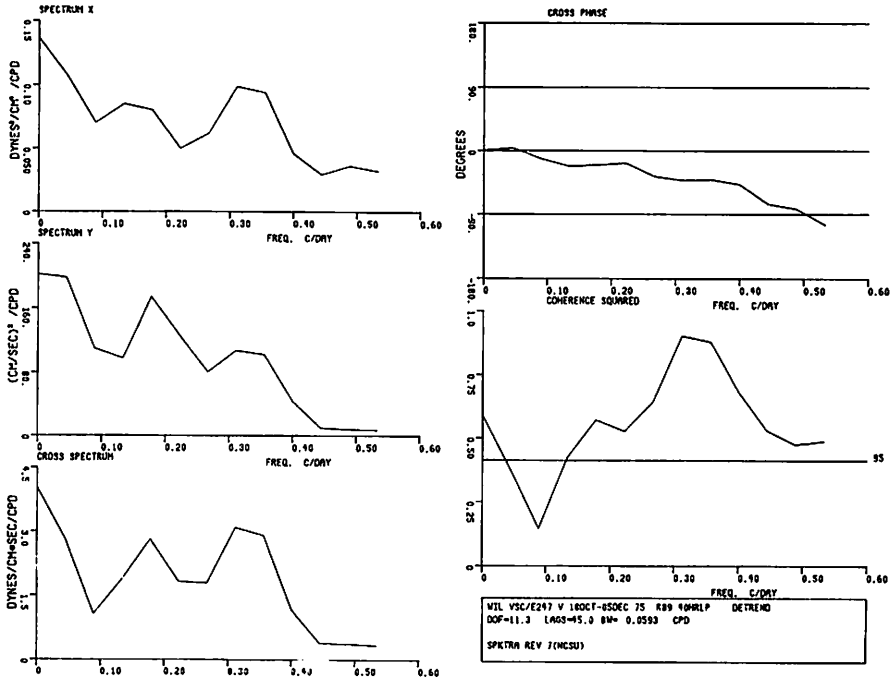

Figure 175 Spectra of the low pass wind stress v component at Wilmington and the low pass current velocity v component from meter $A2_{bot}$ (Principal Axis = 89^{o}), Oct-Dec 1975 (detrended)

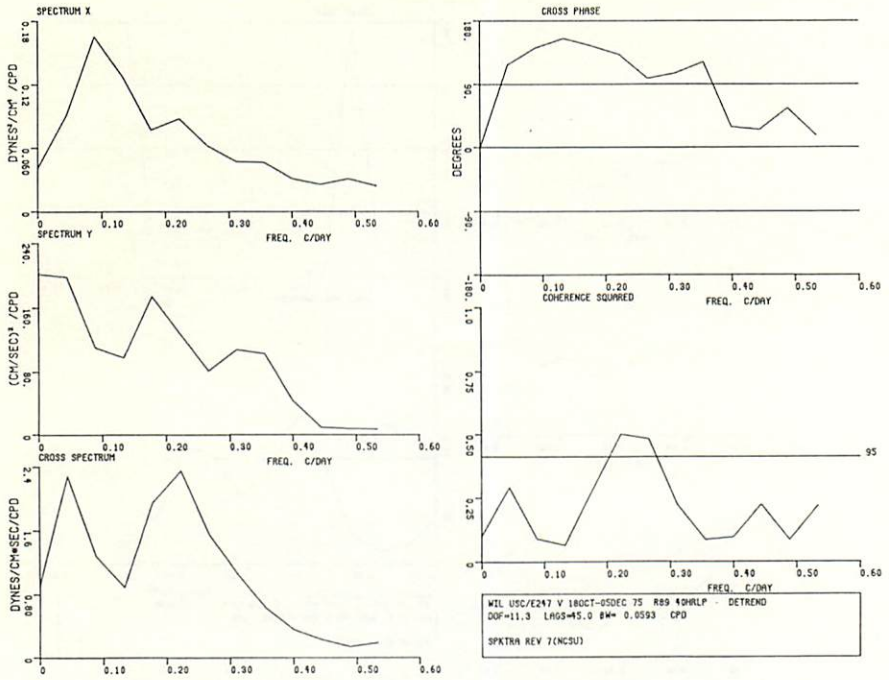

Figure 176 Spectra of the low pass wind stress u component at Wilmington and the low pass current velocity v component from meter $A2_{bot}$ (Principal Axis = 89°), Oct-Dec 1975 (detrended)

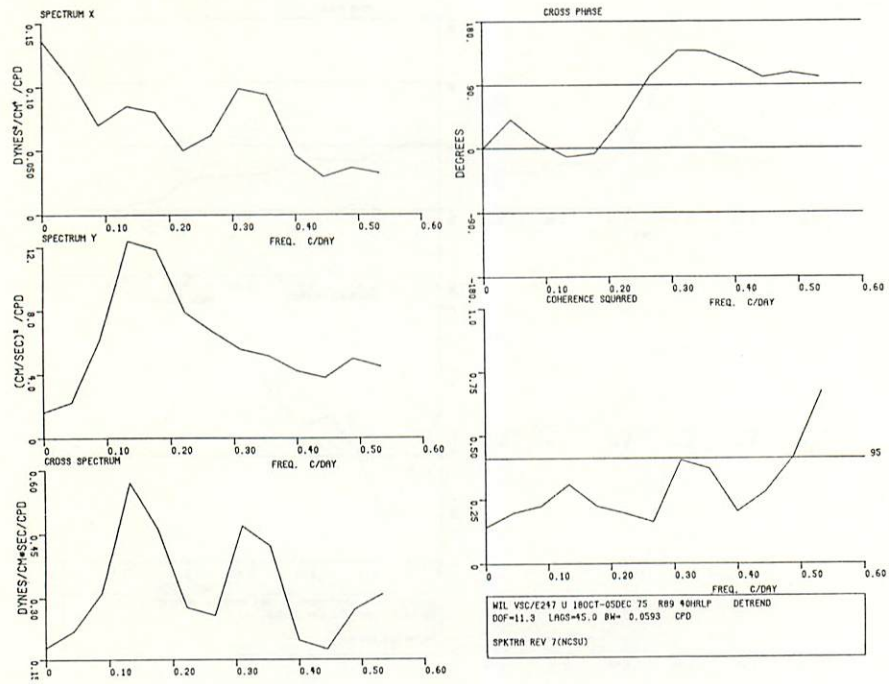

Figure 177 Spectra of the low pass wind stress v component at Wilmington and the low pass current velocity u component from meter $A2_{bot}$ (Principal Axis = 89°), Oct-Dec 1975 (detrended)

IX. Coastal Sea Level Data

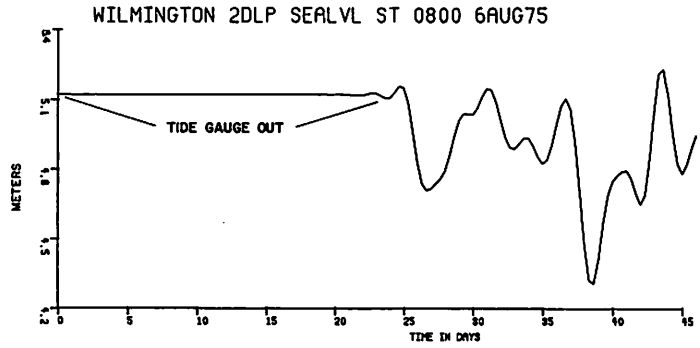

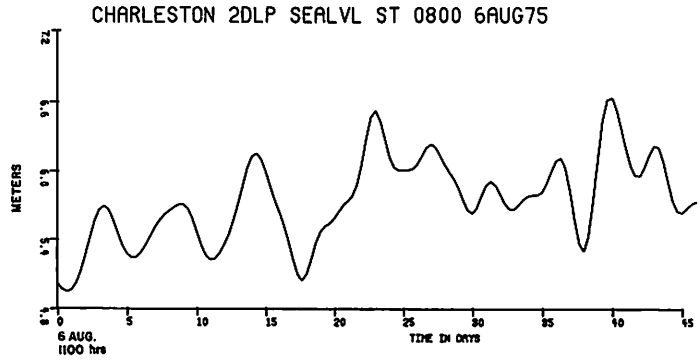

Figure 178 Low pass sea level at Wilmington, N.C. Charleston, S.C. Aug-Sept 1975

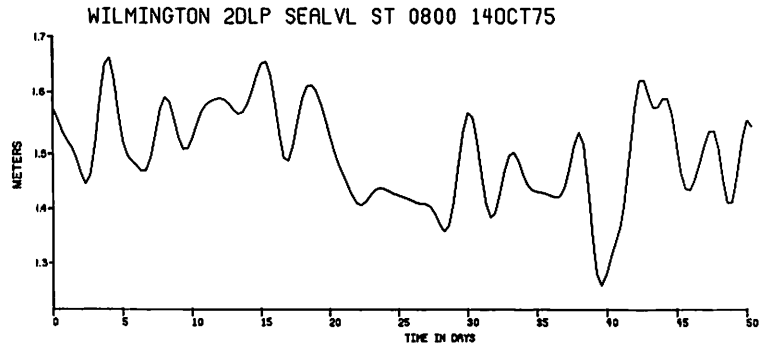

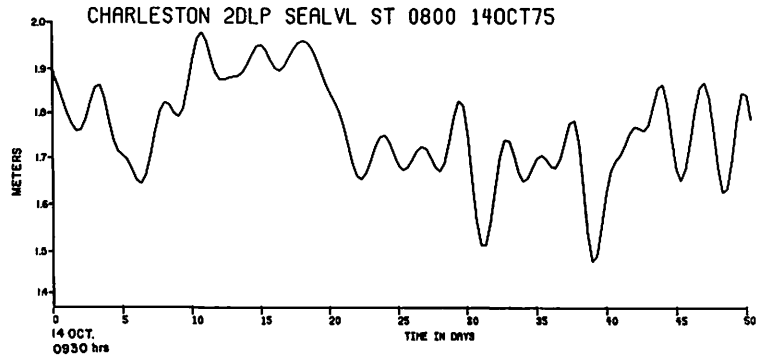

Figure 179 Low pass sea level at Wilmington, N.C. Charleston, S.C. Oct-Dec 1975

X. Temperature Data

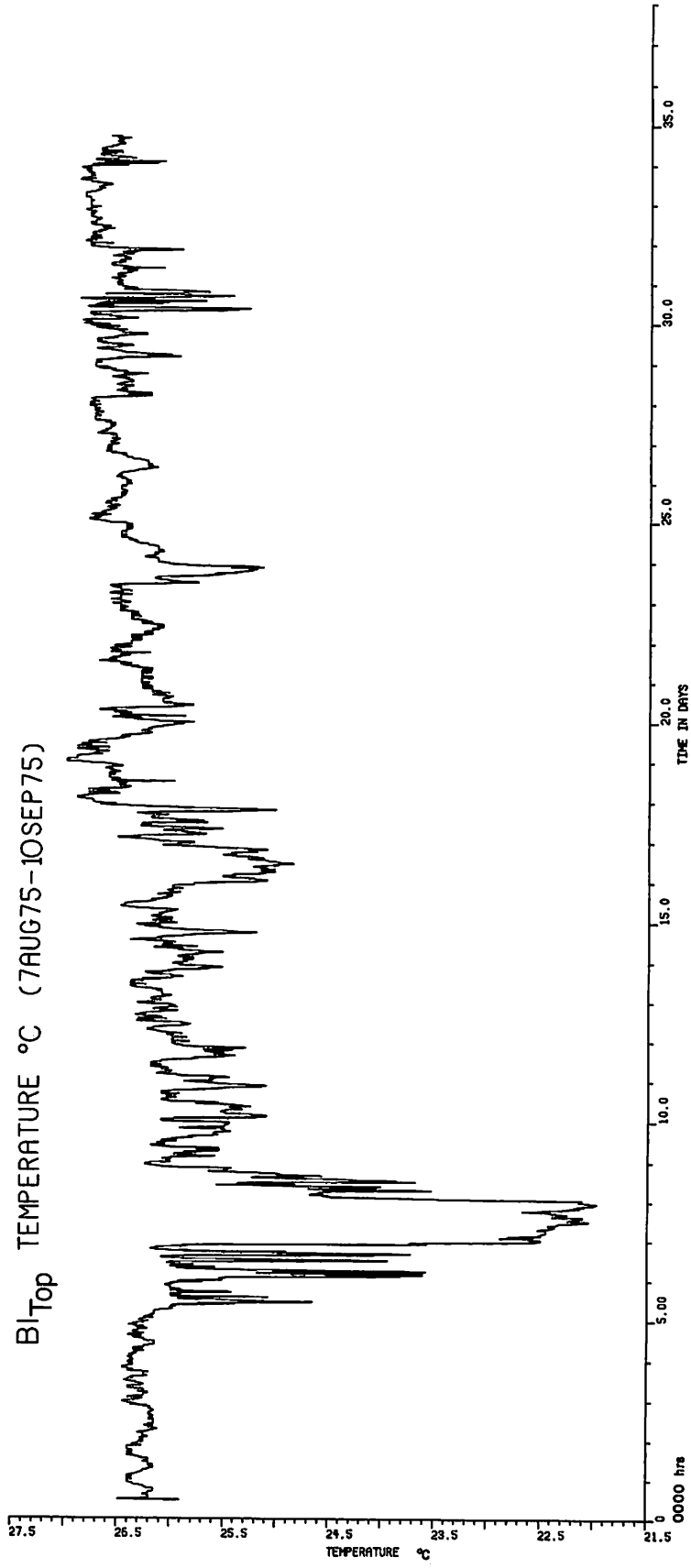

Figure 180 Unfiltered temperature from Bl_{top} thermograph

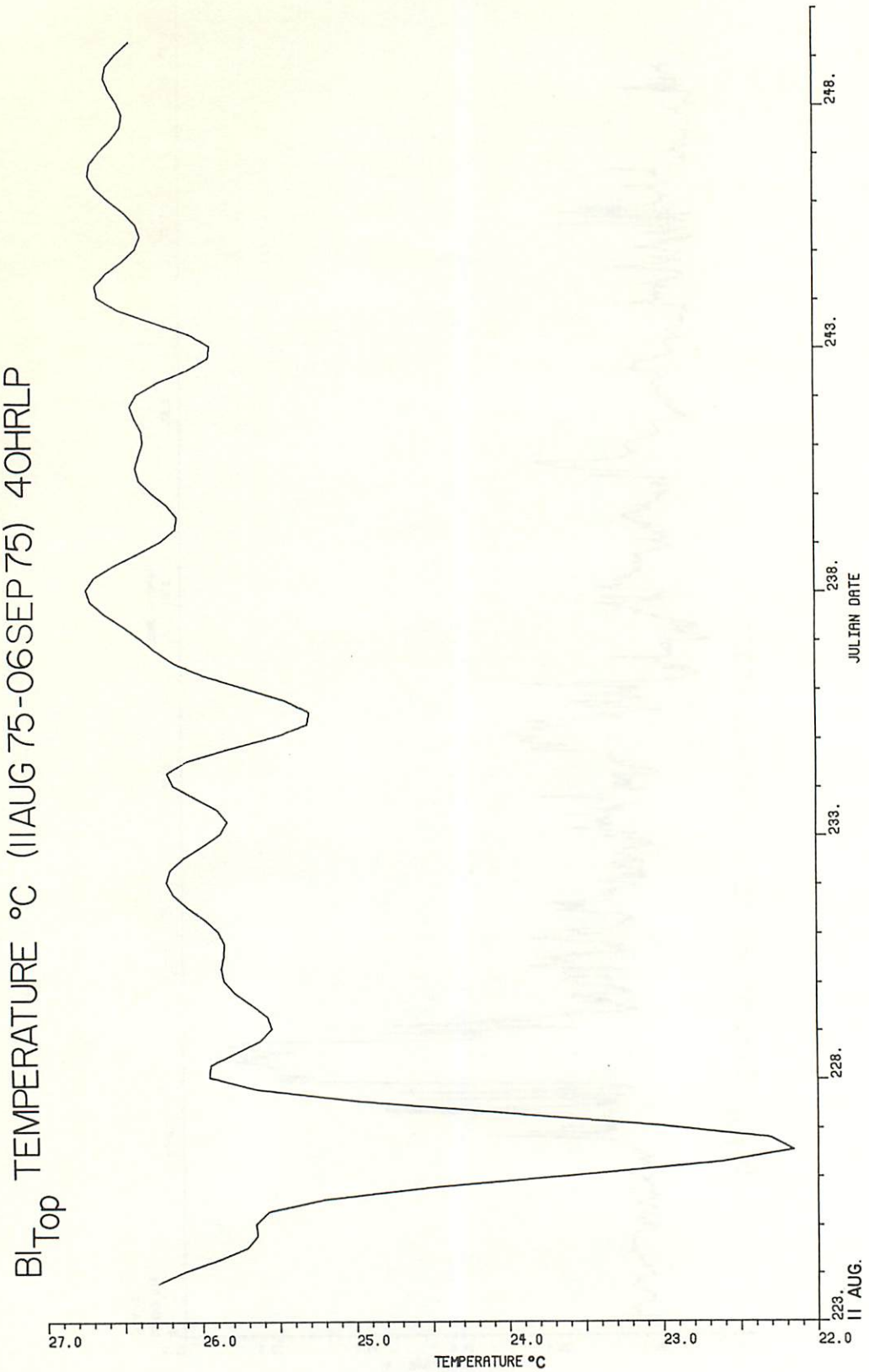

Figure 181 Low pass temperature from Bl_{top} thermograph

XI. Case Study

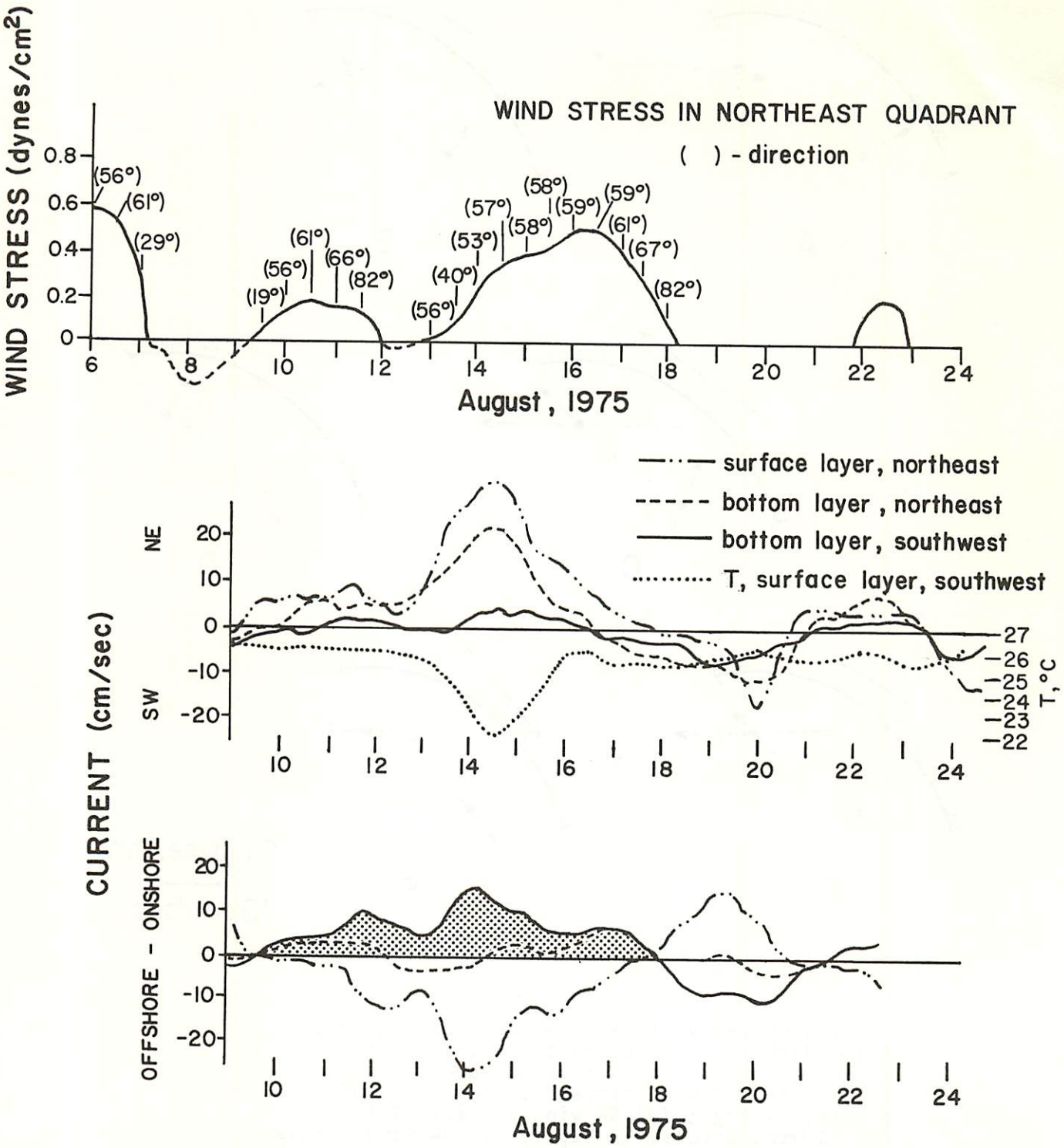

Figure 182 Case study of bottom intrusion during period Aug 9-24, 1975

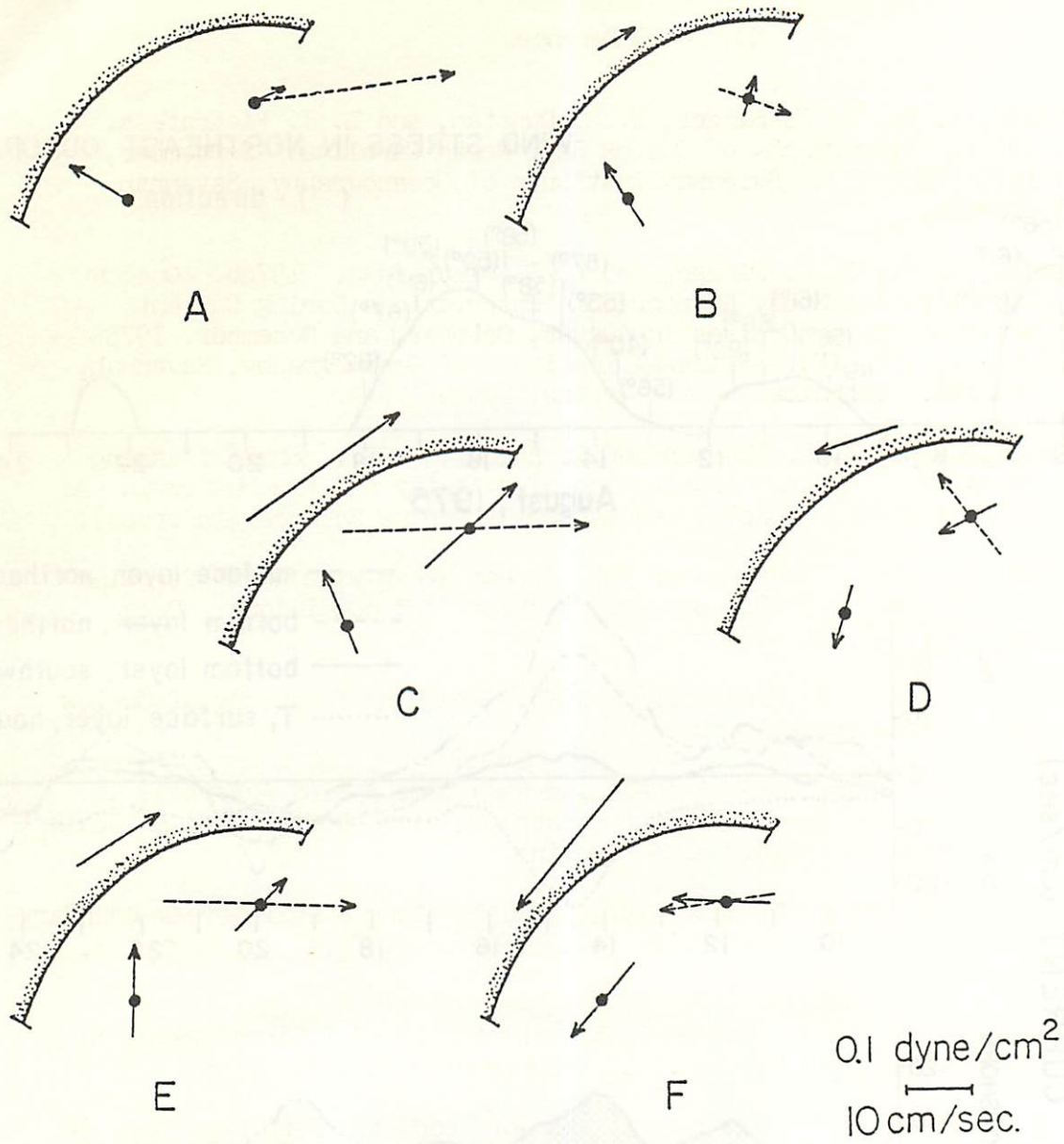

Daily averaged vectors of wind stress squared (Cape Hatteras) and currents during specific events of wind. (a) 42-day average currents (only); (b) NE wind stress, 12 Aug.; (c) NE wind stress, 14 Aug.; (d) SW wind stress, 19 Aug.; (e) NE wind stress, 12 Sept.; (f) SW wind stress, 14 Sept. Wind stress vectors are depicted northwest of the shoreline in each illustration except the first. In (a), multiply vector lengths by 0.05 for true speeds. Dotted arrows represent currents at 10 meters depth; solid arrows represent currents at 25 meters depth.

Figure 183 Daily averaged vectors of wind stress squared (Cape Hatteras) and currents during specific events of wind

XII. References

Atkinson, L. P., J. J. Singer, W. M. Dunstan, and L. J. Pietrafesa. 1976a. Hydrography of Onslow Bay, North Carolina: September, 1975 (OBIS II). Skidaway Institute of Oceanography, Savannah Georgia.

Atkinson, L. P., J. J. Singer, and L. J. Pietrafesa. 1976b. Onslow Bay Intrusion Study Hydrographic Observations During Current Meter Servicing Cruises in August, October, and December, 1975 (OBIS I, III, IV). Skidaway Institute of Oceanography, Savannah, Georgia. Technical Report Series, Number 76-4.

Atkinson, L. P., J. O. Blanton and E. Haines. 1977. Shelf flushing rates based on the distribution of salinity and freshwater in the Georgia Bight. Coastal and Estuarine Marine Science (in press).

Blanton, J. 1971. Exchange of Gulf Stream Water with North Carolina shelf water in Onslow Bay during stratified conditions. Deep Sea Res., 18, 167-178.

Blanton, J. and L. J. Pietrafesa. 1978. Flushing frequency of Onslow Bay. (Manuscript in press).

Brooks, D. A. 1976. FESTSA (Fast and Easy Time Series Analysis) at NCSU. Center for Marine and Coastal Studies, North Carolina State University, Raleigh, North Carolina.

DeRycke, R. J. and P. K. Rao. 1973. Eddies along a Gulf Stream boundary from a very high resolution radiometer. J. Phys. Oceanogr., 3, 490-492.

Fofonoff, N. P. 1969. Spectral characteristics of internal waves in the Ocean. Deep Sea Res., 16 (supplement), 59-72.

Lee, T. N. 1975. Florida current spin-off eddies. Deep Sea Res., 22 (11), 753-765.

Legeckis, R. 1975. Applications of synchronous meteorological satellite data to the study of time dependent sea surface temperature changes along the boundary of the Gulf Stream. Geophys. Res. Lett., 2 (10), 435-438.

Mooers, C.N.K. 1970. The interaction of an internal tide with the frontal zone of a coastal upwelling region. Ph.D. thesis, Oregon State University.

Mysak, L. A. and B. V. Hamon. 1969. Low-frequency sea level behavior and continental shelf waves off North Carolina. J. Geophys. Res., 74 (6), 1397-1405.

Pietrafesa, L. J. 1974. Wind Wave Studies in Onslow Bay; A Research Proposal Submitted to Sea Grant.

Pietrafesa, L. J. and L. P. Atkinson. 1975. Continental Shelf Processes Affecting the Oceanography of the South Atlantic Bight; a Research Proposal Submitted to Energy Research and Development Administration.

Pietrafesa, L. J., D. A. Brooks, L. P. Atkinson, R. D'Amato and J. Bane, 1976. Preliminary Data Report, Physical/Dynamical Observations Made in Onslow Bay; Summer, Fall and Winter, 1975. Center for Marine and Coastal Studies, North Carolina State University, Raleigh, North Carolina.

Singer, J. J., L. P. Atkinson, W. S. Chandler and P. G. O'Malley. Hydrographic observations in Onslow Bay, North Carolina: July-August 1976 (OBIS V), Data Graphics. Georgia Marine Science Center Technical Report 77-6.

Stefansson, U., L. P. Atkinson and D. Bumpus. 1971. Hydrographic Properties and Circulation of the North Carolina Shelf and Slope Waters. Deep-Sea Res. 18:383-420.

Strong, A. E. and R. J. DeRycke. 1973. Ocean current monitoring employing a new satellite sensing technique. Science, 182(4111), 482-484.

Stumpf, H. G. and P. K. Rao. 1975. Evolution of Gulf Stream eddies as seen in satellite infrared imagery. J. Phys. Oceanogr., 5(2), 388-393.

Von Arx, W. S., D. F. Bumpus, and W. S. Richardson. 1955. On the fine structure of the Gulf Stream front. Deep Sea Res., 3, 46-65.

Webster, F. 1961. A description of Gulf Stream meanders off Onslow Bay. Deep Sea Res., 8, 130-143.